2008

Mechanics and mechanisms of surface damage in Al-Si alloys under ultra-mild wear conditions

Ming Chen
University of Windsor

MECHANICS AND MECHANISMS OF SURFACE DAMAGE IN Al-Si ALLOYS UNDER ULTRA-MILD WEAR CONDITIONS

by

MING CHEN

A Dissertation
Submitted to the Faculty of Graduate Studies
through the Engineering Materials Program
in Partial Fulfillment of the Requirements for
the Degree of Doctor of Philosophy
at the University of Windsor

Windsor, Ontario, Canada
2008

Your file Votre référence
ISBN: 978-0-494-47095-4
Our file Notre référence
ISBN: 978-0-494-47095-4

DECLARATION OF CO-AUTHORSHIP

I hereby declare that this thesis incorporates material that is result of joint research, as follows:

This thesis incorporates the outcome of a joint research undertaken in collaboration with Dr. X. Meng-Burany under the supervision of professor A. T. Alpas. The collaboration consists of the provision of FIB and TEM micrographs (e.g., **Figs. 9** to **10** in **Chapter 5** and **Figs.11** to **12** in **Chapter 6**). The interpretation of these micrographs and their analyses were performed by the author.

I am aware of the University of Windsor Senate Policy on Authorship and I certify that I have properly acknowledged Dr. X. Meng-Burany's contribution to my thesis, and have obtained written permission from Dr. X. Meng-Burany to include the above material(s) in my thesis.

I declare that, to the best of my knowledge, my thesis does not infringe upon anyone's copyright nor violate any proprietary rights and that any ideas, techniques, quotations, or any other material from the work of other people included in my thesis, published or otherwise, are fully acknowledged in accordance with the standard referencing practices. Furthermore, to the extent that I have included copyrighted material that surpasses the bounds of fair dealing within the meaning of the Canada Copyright Act, I certify that I have obtained a written permission from the copyright owner(s) to include such material(s) in my thesis.

I declare that this is a true copy of my thesis, including any final revisions, as approved by my thesis committee and the Graduate Studies office, and that this thesis has not been submitted for a higher degree to any other University of Institution.

ABSTRACT

Al-Si alloys intended for use in engine components must operate under ultra-mild wear (UMW) conditions to fit an acceptable amount of wear during a typical vehicle life. This study simulated surface damage in a UMW regime on five chemically etched Al-Si alloy surfaces using a pin-on-disc tribometer at low loads (0.5-2.0 N) under boundary lubricated conditions. The five alloys contained 11 to 25 wt.% Si and differed in matrix hardness, silicon particle morphology, and size. The mechanisms leading to the UMW damage and the role that the matrix hardness and microstructure play on said mechanisms were studied. Quantitative measurement methods based on statistical analysis of particle height changes and material loss from elevated aluminum using a profilometer technique were developed and used to asses UMW.

The Greenwood and Tripp's numerical model was adapted to analyze the contact that occurred between Al-Si alloys with silicon particles protruding above the aluminum and steel balls. The estimation of the real contact pressure applied to the silicon particles was used to rationalize the damage mechanisms.

The UMW mechanisms consisted of i) abrasive wear on the top of the silicon particle surfaces; ii) sinking-in of the silicon particles; iii) piling-up of the aluminium around sunken-in particles and vi) wear of the aluminium by the counterface, which eventually led to the initiation of UMW-II. Increasing the size or areal density of silicon particles with small aspect ratios delayed the onset of UMW-II by providing resistance against the silicon particles sinking-in and the aluminum piling-up. The UMW wear rates, however, began to decrease after long sliding cycles once an oil residue layer supported by hardened ultra-fine subsurface grains formed on the deformed aluminium matrix. The

layer formation depended on the microstructure and applied load. Overall experimental observations suggested that Al-11% Si with small silicon particles exhibited optimal long-term wear performance.

To

my husband Mingwu Bai

my daughter Yanhua Bai

my son Jeffrey Bai

ACKNOWLEDGEMENT

I would *first* sincerely thank Dr. Ahmet T. Alpas, my advisor for accepting me as his student and giving me continuous support and encouragement throughout my study at the University of Windsor. Dr. Alpas has devoted his tremendous time and energy in teaching me to conduct scientific study with positive thinking and write good quality scientific report with his wisdom and great patience. I am also deeply grateful to Dr. Thomas Perry, my co-advisor from General Motor Corporation for his teaching, guidance and supervision using his knowledge and industrial experience. The learning from them and the working on experimental explorations under their guidance are both enjoyable and rewarding.

I would like to sincerely thank my committee members for taking time from their busy schedules to read my dissertation and help me to improve the final version of the dissertation.

I can not say enough thanks to Dr. Xianying Meng-Burany for helping me to characterize the worn surface and subsurface of my samples using FIB and TEM. Her excellent work helped me obtain in-depth insight into the experimental observations.

I am indebted to Dr. M. Elmadagli, previous research associate of IRC in Tribology of Lightweight Materials. He gave me lots of valuable help and his involvement in this research at the beginning helped me overcome many difficulties and keep moving forward.

I would like to express my gratitude to Mr. J. Robinson, Mr. P. Sequin and the members of the Technical Support Center for their technical assistance, Ms. B. Denomey

and Ms. Q. Tu (previous secretary of IRC) for their administrative assistance during my study. Special thanks to Dr. S. Akarca, and Mr. M. Shafiei, previous and present research coordinator of IRC for their support.

I am grateful to all the previous and current student fellows at IRC in Tribology of Lightweight Materials for their help and friendship. In particular, I would like to thank A. Abougharam for his help of transportation to the GM research facility and helping me conduct nano-hardness measurements on my samples when I was not able to go there. S. Pratibha and F. Sen are also greatly appreciated for their helping me when I was revising my dissertation.

Dr. M. Lukitsch from General Motor Limited is acknowledged for his help with the nanoindentation measurements.

The financial support from NSERC and General Motors of Canada is greatly appreciated. I also would like to acknowledge the Doctorial Tuition Scholarship provided by the University of Windsor.

I especially want to express my deep thanks to my previous mentor, Prof. Koji Kato, at Tohoku University in Japan (now at Nihon University) for his great inspiration. He has played a vital role in helping me achieve the present stage.

Last but not the least; I am deeply gratitude to my mother, father-in-law, sister, and brothers for their support with their encouragement, patience, and sacrifice. The backbone support from my husband, Mingwu Bai, my daughter, Yanhua Bai, and my son, Jeff Bai with their love, sacrifice, and patience is always the core, which helped me to reach the final step.

TABLE OF CONTENTS

LIST OF ABBREVIATIONS

MW	**Mild wear**
SW	**Severe wear**
UMW	**Ultra-mild wear**
UMW-I	**The first UMW regime**
UMW-II	**The second UMW regime**
UMW-III	**The third UMW regime**
MW-1	**The first regime of mild wear**
MW-2	**The second regime of mild wear**
ZDDP	**Zinc dialkyl-dithiophosphates**
XPS	**X-ray Photoelectron Spectroscopy**
XANES	**X-ray Absorption Near Edge Structure**
EDS	**Electron diffraction spectrum**
TEM	**Transmission electron microscopy**
FIB	**Focused ion beam**
COF	**Coefficient of friction**
C	**Coarse silicon particles**
F	**Fine silicon particles**
WT	**Wear track**
HV	**Vickers hardness**
HB	**Hardness in Brinell scale**
RH	**Relative Humidity**
RNT	**Radionuclide technique**
SD	**Sliding direction**

LIST OF TABLES

LIST OF FIGURES

NOMENCLATURE

The parameters are listed in the order as they appear in the equations listed in the text.

$h_{\min}$ = the minimum lubricant film thickness

σ^* = the r.m.s roughness of the two surfaces ($\sigma^{*2} = R_{q1}{}^2 + R_{q2}{}^2$)

λ = severity of asperity interactions in lubricated sliding ($\frac{h_{\min}}{\sigma^*}$)

E^* = the composite elastic modulus of two contact surfaces

E_{Al-Si} = the elastic modulus of Al-Si alloys and given by

$$E_{Al-Si} = E_{Si} w_{Si} + E_{Al}(1 - w_{Si})$$

w_{Si} = the weight fraction of silicon phase

ν_{Al-Si} = the Poisson's ratio of Al-Si alloys

R = the radius of the counterface ball

α and η_0 = viscosity constants of oil

$$\alpha \approx (0.6 + 0.965 \log_{10} \eta_0) \times 10^{-8}$$

R_{q1} = the r.m.s roughness values for the top surface measured

R_{q2} = the r.m.s roughness values for the bottom surface measured

dN = the expected number of contacts

dA_r = the real area of contact

$d\Psi$ = an element of surface

dP = the total load

z = the silicon particle height

R_p = the equivalent curvature radius of the silicon particle tips

$\phi(z)$ = the height distribution function

$F_0(h)$ = parabolic cylinder function, n = 0

$F_1(h)$ = parabolic cylinder function, n =1

$F_{3/2}(h)$ = parabolic cylinder function, n = 3/2

η = the density of the silicon particles

$\eta d\psi$ = the number of silicon particles per unit area The term

$\eta(R_p\sigma)$ = the area density of the silicon particles (measured using quantitative metallography)

σ = the standard deviation of silicon particle height

$p(r)$ = the apparent contact pressure distribution

u = the separation of the nominal surfaces at the position of a particular particle

$w(r)$ = the displacement of the nominal surfaces at r

h = dimensionless separation of the nominal surfaces at the position of a particular particle (u/σ)

$K(\xi)$ = the complete elliptic integral of the first kind of modulus ξ

w^* = dimensionless displacement (w/σ)

u^* = dimensionless displacement (u/σ)

d^* = dimensionless separation (d/σ)

ρ = radial distance $(r/\sqrt{2R\sigma})$

p^* = dimensionless pressure $(p/(E^*\sqrt{\sigma/8R}))$

μ = surface parameter which is related with particle distribution, size, and density $(=\frac{8}{3}\eta\sigma\sqrt{2RR_p})$

$q^*(\rho)$ = the Hertzian pressure

$q^*(0)$ = the maximum Hertzian contact pressure

a^* = the effective contact radius

T = the dimensionless total load

W = the actual load

P_r = is real contact pressure (dP/dA_r)

CHAPTER 1 INTRODUCTION

The growing demand to improve fuel economy, triggered by concerns about energy usage and global warming has a significant effect on the selection of the materials used for the automotive industry [1-2]. In this respect, lightweight materials, in particular, 300 series Al-Si alloys are experiencing increasing use in the manufacturing of engine components. Their high strength to weight ratio, good formability, good corrosion resistance and recycling potential make these alloys an ideal choice [3].

Considerable efforts have been made to understand the sliding wear properties of Al-Si alloys. Most laboratory-scale wear tests revealed that Al-Si alloys display complex tribological behaviour even when tested under dry sliding conditions. One common observation is that they all show two distinct wear regimes, namely "mild wear" (MW) and "severe wear" (SW). The wear rates in the MW regime fall between 10^{-4} and 10^{-3} mm^3/m, while SW rates were greater than 10^{-3} mm^3/m, typically 10^{-2} to 1. The transition between these regimes is abrupt and tends to coincide with a specific combination of testing conditions. The wear micro-mechanisms that control each regime's wear rates are significantly different. MW rates are primarily controlled by surface oxidation, plastic deformation and material transfer, while SW rates are typically a result of large-scale plastic deformation and metallic melting. The MW regime is further divided into two sub-regimes; the first mild wear regime (MW-1) is attributed to oxidative wear, and the second mild wear regime (MW-2) is primarily related to delamination wear [4-6]. While wear rates are stable in the MW regime, an accelerated increase in wear rates is observed in the SW regime, and as a result of seizure, a catastrophic form of tribological failure

always follows. Therefore neither wear rates, nor the mechanisms that control them can be extrapolated to the other.

MW, when observed under laboratory conditions, roughly simulates the sliding wear of automotive components that operate under dry contact---such as brake assemblies or a piston-engine bore system (in the case of a cold start, where oil starvation may lead to metal-on-metal contact). Metal-to-metal contact and scuffing in Al-Si alloys is closely related to SW [7-8] ---one of the extreme cases that should be considered in tribological design.

Most of the sliding surfaces in engines operate in an environment that includes engine oil in order to reduce friction and wear. Lubrication is often characterized as hydrodynamic, mixed or boundary lubrication depending on the magnitude of $\eta v/P$, where η is the viscosity of the lubricant, v is the sliding speed, and P is the applied load. In a hydrodynamic regime, the two sliding surfaces are completely separated by the lubricant film, and the applied load is carried by the film. No solid-to-solid contact should occur. Accordingly, in this region, friction is essentially caused by the shearing of the film, prompting an extremely low coefficient of friction with no wear and no surface damage. Hydrodynamic lubrication generally happens when the sliding surfaces are smooth and idealized (minimal surface roughness), the sliding speed is high and the normal load is small.

Mixed lubrication starts when the fluid film between the two sliding surfaces becomes thinner. In this regime the applied load is carried by both the fluid film and the asperities on the solid surfaces. Mixed lubrication is characterized by a sharp rise in the coefficient of friction as $\eta v/P$ decreases. When the $\eta v/P$ drops to a sufficiently low value, the lubrication regime transitions to a boundary lubrication region where the coefficient

of friction reaches a maximum value.

In a boundary lubrication regime, the fluid film has been squeezed out of the interface, the load, therefore, is carried by the surface asperities rather than by the lubricant. But the friction and wear behaviours under boundary lubricated conditions are not the same as those observed in dry sliding conditions. Generally, the solid films that are formed on one or both surfaces through a chemical absorption, a physical absorption, or a tribo-chemical reaction play a key role in the friction and wear in a boundary lubrication regime. Friction and wear in boundary lubricated conditions does not primarily depend on bulk material properties, but rather on the film properties and the mechanisms by which the films are generated, as well as the detachment and reformation of the films [9]. Many engineering applications like piston-cylinder bore assemblies and transmissions run in the boundary lubrication regime.

A more general concern is the actual lubricated tribological performance of piston-cylinder bore assemblies for extended durability applications. Wear should not exceed a few nanometers per hour for the long-term durability of cylinder bore surfaces, as revealed in radiotracer experiments run in conventional cast-iron engines [10]. Accordingly, lightweight Al-Si alloys used in engine components must be able to satisfy the same durability conditions.

Extremely minimal wear rates define a new regime in which wear rates are typically smaller than 10^{-6} mm^3/m or at least an order of magnitude smaller than the MW range. This regime can be referred to as the ultra-mild wear (UMW) regime, and is not readily simulated under laboratory conditions. The wear rates tend to be below the sensitivity limits of mass, volume and dimensional change measurements used to measure wear rates in MW and SW. Furthermore, no obvious surface damage occurs in the UMW

regime that could be considered comparable to what results from plastic deformation and material transfer [11], so new experimental techniques must be developed to quantify the damage in UMW.

These difficulties have made laboratory-scale research on UMW in Al-Si alloys almost non-existent compared to the large body of studies conducted on MW and SW. UMW is believed to have been first achieved in an A 390 (Al-18.5% Si) under an argon atmosphere against 52100 steel [12] using a block-on-ring configuration. However, this environment did not simulate engine conditions, and the low wear rates could not be maintained for a long sliding distance. Dienwiebel et al. [13] performed a study on an Al-Si cylinder bore surface running under the similar working and loading conditions but using a novel measurement technique radionuclide-technique (RNT) for ultra low wear, Auger electron spectroscopy (AES) and focus ion beam (FIB). Results addressing the microstructural changes induced by the corresponding sliding wear at the contact surface and subsurface adjacent to the contact surface were far from comprehensive, and additional research in this area is needed.

The main purpose of this research is to simulate the surface damage that occurs to Al-Si engine components under normal running conditions—(UMW) regime—by performing laboratory-scale wear tests on Al-Si alloys at light loads and under boundary lubricated conditions. The UMW regime is defined as surface damage accompanied by zero material loss, or immeasurable material loss, at least not measurable using a conventional mass loss-based measurement. Our experimental observations show that, like the MW regime identified in Al-Si alloys, the UMW regime can be divided into three sub-regimes. The first UMW sub-regime, designated as UMW-I, is characterized by zero material loss from the aluminum matrix, with only the top Si particle surface suffering

abrasive wear. Fracture and fragmentation of silicon can occur in UMW-I. Sinking-in of silicon particles into the aluminum matrix is also often observed in UMW-I, this can lead to piling up of aluminum around the sunken-in material. Material loss becomes measurable from the elevated aluminum matrix in the second UMW sub-regime (UMW-II). The third sub regime of UMW is designated as UMW-III and has two characteristic features: the material loss decreases and an oil residue layer forms on the contact surface after sliding long cycles. A new methodology that uses an optical surface profilometer to detect morphological changes on the contact surfaces was developed and used to quantitatively evaluate the damage to the silicon particles and very small wear rates from the aluminum matrix. The wear rates are controlled by mechanisms that differ from those encountered in high wear regimes, so it is essential to examine the micro-mechanisms that lead to the UMW wear damage. This is achieved using a series of analytical microscopical measurements, which helps to determine the metallurgical basis of UMW.

A full understanding of the contact that occurs between solids is required to comprehend adhesion, friction, lubrication, and wear, all of which have motivated extensive theoretical studies. For rough solids, two major methods employed to gain such an understanding are FEM and numerical analysis, following the Greenwood and Williamson's model [14-15]. Contact mechanics-related studies on Al-Si alloys have rarely been reported. In this research, all Al-Si alloy surfaces are chemically etched to expose the top portions of silicon particles, and hence, apply the load directly on the silicon particles---a configuration that is expected to simulate actual engine bore surfaces.

Estimating the contact pressure applied to the exposed Si particles is crucial in order to gain a realistic understanding of the way they respond mechanically to the applied load. To achieve this, the Greenwood and Tripp's numerical contact model,

which considers silicon particles as load-carrying "asperities", is adapted to estimate the real contact pressure---taking into account the silicon particle height distribution and size. The contact mechanics analysis establishes the pressure distributions, estimates the maximum contact pressures applied on the Si particles, and hence, facilitates an understanding of the reasons behind the observed damage processes, such as the embedding of particles into the matrix, or their fracture.

This study considers commercial and experimental cast alloys containing different silicon amounts (11 to 25 wt. % Si), matrix hardnesses, Si particle morphologies and sizes. A selection of Al-Si alloys with different matrix hardnesses and microstructures is intended to establish correlations between their sliding wear performance and specific silicon and aluminum property details.

This dissertation is organized in the following way: **Chapter 2** provides a literature survey on: i) the sliding wear properties of Al-Si alloys under dry sliding conditions; ii) the sliding wear characteristics of Al-Si alloys under lubricated conditions; and iii) the wear damage of engine components. **Chapter 3** gives the details of the materials tested, followed by descriptions of the experimental procedures developed to achieve UMW, including the pin-on-disc machine, wear test conditions, and the procedures used to evaluate the test results. **Chapter 4** analyzes the contact pressure applied to the protruded silicon particles by adapting Greenwood and Tripp's numerical model. **Chapter 5** identifies UMW mechanisms using a binary Al-Si alloy, then examines the effects of matrix hardness and microstructure (in terms of silicon particle morphology and size) on said mechanisms. **Chapter 6** illustrates surface damage evolution with sliding cycles and applied loads to capture the transition from UMW-I to UMW-II and finally to UMW-III. The mechanisms and microstructural effects responsible for these

transitions are identified through the examination of the evolution of sliding-wear induced microstructural changes at the contact surface and adjacent to the contact surface in Al-Si alloys during the surface damage process in UMW. **Chapter 7** summarizes and concludes the dissertation.

CHAPTER 2 LITERATURE SURVEY

2.1. Introduction

The first section of this chapter reviews the current literature on the wear characteristics of Al-Si alloys under dry sliding conditions, with a brief introduction of how Al-Si alloys are currently used for combustion engine components followed by a review of the wear mechanisms. The review consists of a summary of wear regimes, the formation of tribolayers, and the effect of silicon percentage and morphology on Al-Si alloy wear properties. A summary of dry sliding tests performed under laboratory conditions to determine wear regimes (mild and severe wear) is also provided. The second section of this chapter reviews the literature on Al-Si alloy sliding wear behaviour under lubricated conditions. This section includes a review of engine lubricants and an explanation of the major additive, ZDDP's effect on wear reduction. The third section of this chapter introduces internal combustion engine wear damage and reviews the current literature on aluminum engine-related wear—including an introduction to the major surface preparations for Al-Si engine surfaces.

2.2. Dry Sliding Wear Behaviour of Aluminum Silicon Alloys

2.2.1. Engine-Grade Al-Si Alloys and Their Properties

The use of lightweight materials like titanium, cast Al-Si and magnesium alloys, as well as aluminum-based composites is becoming popular in motor vehicles and other types of transportation. However, these lightweight materials tend to exhibit poor wear resistance, and so the aerospace industry uses sophisticated coatings to prevent the wear

of their lightweight components. In order for wear resistant components to benefit the automotive industry, they must be affordable in high volume production. This has been attempted using low-carbon steel thermal-sprayed coatings on Al-Si cylinder bore surfaces [16], as well as by using aluminum-based MMC's to make engine components [17]. The costs associated with these lightweight material processing techniques, however, remain too high. Casting new wear resistant Al-Si alloys, therefore, is the optimal choice for replacing traditional cast iron engine components to reduce fuel consumption and improve a vehicle's environmental emission performance.

Al-Si alloys can be divided into three categories based on silicon percentage—eutectic, hypoeutectic, and hypereutectic. The Al-Si binary system shown in **Fig. 2.1** forms a eutectic at 12.6 wt% silicon at 577°C [18]. Aluminum alloys with 5-20 wt% silicon are commonly used, and hypoeutectic alloys—such as 319 and A380—contain 5-10 wt% Si, which is below the eutectic composition, while hypereutectic alloys like A 390 have 14-20 wt% Si—with silicon percentages that fall above eutectic compositions. The very low solubility of silicon in an aluminum means that Al-Si alloys contain virtually pure aluminum and silicon as either a primary or eutectic phase, depending on whether the silicon percentage is greater or less than the eutectic point (12.6% Si) and the cooling rate, and the concentration of modifiers. Commercial Al-Si alloys often contain major alloying elements like Cu, Fe, Mn and Mg. **Table 1** lists the compositions of three commercial Al-Si alloys, 380, 319, and A 390. Fe generally exists as an impurity that is considered detrimental to the mechanical properties of aluminum alloys due to the precipitation of Al_5FeSi. Therefore, manganese is added to the Al-Si alloy to promote the formation of $Al_{15}(Mn,Fe)_3Si_2$, which has a compact morphology and does not initiate cracks in cast Al-Si alloys to the same extent as Al_5FeSi. Copper and magnesium are

often added as alloying elements to increase the strength and hardenability of Al-Si alloys, through precipitation hardening during an aging treatment. Magnesium also reduces the detrimental effects of impurities like iron. The impurities and alloying elements partly go into solid solution in the matrix and partly form intermetallic phases during solidification [19].

Fig. 2.2 [19] illustrates the typical microstructures for these three casting Al-Si alloys. Si particles appear as platelets or needle-like in hypoeutectic Al-Si alloys 380 and 319, while hypereutectic A 390 contains both the block-like primary Si phase and platelet or needle-like eutectic Si particles. Commercial Al-Si alloys usually also have intermetallic compounds like $Al_{15}(Fe, Mn)_3Si_2$, $Al_5Mg_8Cu_2Si_6$ and $CuAl_2$ as secondary phases (indicated in **Figure 2.2)**.

Typical mechanical properties of these three alloys summarized in **Table 2.2** indicated that the mechanical properties especially ductility are dependent on the silicon percentage in Al-Si alloys, which influences the microstructure of the alloys [20]. The silicon particle size, morphology, and distribution can be improved by different processing technique, heat treatment, or by the addition of grain refiners and modifiers such as sodium, phosphorus, and rare earth elements, such as strontium [19]. This will be reviewed in **Section 2.2.6**.

Hypoeutectic Al-Si alloys boast excellent casting properties, thermal conductivity and machinability [20]—the main reasons these kinds of Al-Si alloys (319 and A 380 series) have seen extensive use in the automotive industry as cylinder blocks, cylinder heads, and pistons [21] Hypoeutectic Al-Si alloys also exhibit poor wear and scuffing resistance, however, so that engine blocks made from hypoeutectic Al-Si alloys must be paired with cast iron cylinder liners [22]. The cast iron liners found in aluminum engine

blocks add unwelcome weight that, in turn, decreases thermal conductivity and increases production costs. The development of linerless Al-Si engine blocks with higher Si content is expected to solve this problem. **Fig. 2.3** shows an example of one of GM's linerless engine blocks made from an Al-Si alloy containing 12 wt.% Si.

Cast hypereutectic Al-Si alloys, like cast A390 with 16-19 wt% Si, developed by General Motors Corporation for the Chevrolet Vega engine blocks in the early 1970s [1, 23, 24]—have demonstrated excellent wear resistance. The block surfaces were etched with 10% NaOH so that silicon particles would protrude above the aluminum surface—reducing wear damage to the aluminum matrix. Hypereutectic Al-Si alloys, however, experience deterioration of both castability and machinability due to the large, unevenly distributed primary silicon particles (unavoidable in hypereutectic alloys) [25]. With this in mind, extensive efforts have been made to reduce primary silicon particle size, as well as to improve their distribution using special processing techniques—such as powder metallurgy (PM) and spray forming—to improve the distribution of fine, primary silicon particles in hypereutectic Al-Si alloys.

The PM process, which includes the atomization of molten metal followed by hot extrusion or hot isostatic pressing and sintering [26], is one method of producing hypereutectic Al-Si alloys with a high silicon percentage that showcase a refined and homogenous dispersion of hard silicon particles in comparison with cast components. Honda uses a rapidly solidified PM aluminum alloy containing 17% Si, 5% Fe, 3% Cu, 1% Mg and 0.5% Mn to manufacture cylinder liners for motorcycle engines. It is the finely dispersed hard Si particles, as well as the intermetallic compounds embedded in the aluminum matrix, that give this alloy increased wear resistance [27]. Casellas et al. [28] studied the microstructural effects of the PM technique on the wear resistance of Al-Si

alloys containing 14% Si using a pin-on-disc machine. The authors reported that PM produced Al-Si alloys exhibited slightly higher wear resistance than similar cast Al-Si alloys. Kiyota et al. [29] developed a series of Al-Si alloys using PM processes with a silicon percentage that varied from 10 to 30% and incorporated the following elements: 5-15 wt% nickel, 3-15 wt% iron or 5-15 wt% manganese. Hot-extruded PM products have finely dispersed silicon particles with a size <15 μm, and intermetallics with a size <20 μm. The authors concluded that Al-Si parts produced by the power metallurgical method exhibited superior high-temperature properties that made them suitable for use as cylinder liner material in aluminum cylinder blocks. Even though Al-Si alloys produced using the PM process exhibit good wear resistance, this production method is sophisticated, which makes it difficult to meet automotive industry productivity requirements—due to the complicated shapes of engine components.

The spray forming process is another way of addressing low ductility and limited workability problems caused by the distribution of coarse and non-uniform primary Si particles. In this technique, the melt is atomized by a high-pressure gas jet to generate a spray of micron-sized droplets that are subsequently deposited on a stationary or movable substrate and left to consolidate into an ingot, as illustrated in **Fig. 2.4a**. The ingot is then formed into tubing that can be cut into cylinder liners by an extrusion process. The spray compacted billets are then extruded into tubes and machined to achieve the final dimensions of the cylinder liner inserts [30-31]. The effects of rapid solidification during spray deposition lead to chemical and microstructural homogeneity, combined with a refinement in grain size and second phase particle size [32, 33]. PEAK, a German company, introduced the spray forming process to make a hypereutectic Al-Si alloy with

a composition of Al-25% Si-4%Cu-Mg (wt%), which is called SILITEK. **Fig. 2.4b** shows that the silicon particles in SILITEK are fine and distributed uniformly. Spray formed Al-Si alloy cylinder liners made from SILITEK have been used in Daimler-Benz automotive engines [30, 34].

In summary, hypoeutectic Al-Si alloys have excellent castability and machineablity, but exhibit poor wear resistance. Hypereutectic Al-Si alloys processed by the above mentioned special techniques, on the other hand, demonstrate much better wear resistance with improved machinability and castability thanks to the uniformly distributed small silicon particles. Both spray forming and the PM process, however, require special techniques and several distinctive intermediate steps—compared to conventional casting processes. The cost associated with spray forming and PM is high, so providing lightweight Al-Si alloys with the required wear resistance, castability, machinability and cost affordability continues to be a challenge for the automotive industry.

2.2.2. Wear Regimes

Lim and Ashby [35] constructed an empirical wear map for steel-on-steel by summarizing the wear rate and wear mechanism data for steel included in the literature, then modeling with a theoretical analysis to calibrate the experimental data (**Fig. 2.5**). In this plot, the wear rate is normalized by dividing by the worn surface nominal apparent contact area (A_n). The pressure is normalized by dividing by nominal apparent contact area of the wearing surface (A_n) and the room temperature hardness (H_0), and the sliding velocity is normalized by dividing by the velocity of heat flow (the ratio of the radius of the circular nominal contact area, r_0, to the thermal diffusivity, a). The result is a more global diagram of how materials in relative motions behave when they encounter different

sliding conditions—providing relationships between various dominant wear mechanisms that occur under different sliding conditions, as well as anticipated wear rates. **Figure 2.5** illustrates the three wear regimes—ultra-mild wear (UMW), mild wear (MW) and severe wear (SW)—that appear when steel slides against steel counterfaces under dry sliding conditions.

"Mild wear" (MW) and "severe wear" (SW) have been the two most frequently reported wear regimes in Al-Si alloys sliding against a steel counterface under dry-sliding conditions [4, 36 -39]. MW generally occurred at a relatively low applied load, with the MW regime's wear rate falling between 10^{-4} and 10^{-3} mm^3/m while severe wear occurred at a high load, high temperatures and high sliding velocity—prompting a volumetric wear loss rate of $\geq 10^{-2}$ mm^3/m. **Fig. 2.6** indicates that the transition between mild (oxidative) and severe (metallic) wear generally occurred when the applied normal load was above 30-100 N [4]. A closer look at the results presented in **Fig. 2.6** reveals that the transition from MW to SW occurs at 30 N in the binary alloy Al-16% Si. The transition load increased to approximately 80 N in the alloy Al-16% Si containing 2% Cu, but when 1% Ni and 1% Fe were added to the Al-16% Si-Cu, the transition load increased only slightly. As the literature survey presented in **Section 2.2.1** explained, Cu is generally added to Al-Si alloys to increase their matrix hardness through precipitation hardening—suggesting that the transition load increased alongside the matrix hardness. The effect of Si percentage on transition load will be reviewed in **Section 2.2.5**. On the other hand, Zhang and Alpas [38] reported the transition from MW to SW was dependent on both the applied normal load and the sliding speed (**Fig. 2.7**)—occurring at a lower load with an increasing sliding speed. For example, the transition load of 230 N at 0.4 m/s decreased to 9.0 N when the sliding speed was increased to 5.0 m/s. The study also showed that the

transition from mild to severe wear was related to the surface contact temperature, so that when the bulk surface temperature (T_b) exceeded the critical temperature (0.4 T_m), severe wear occurred (where T_m is the melting temperature of the alloy). It also infers that transition load is affected by matrix hardness, specifically the material softening caused by recrystallization at high loads and high sliding speeds.

It is well known that a material's tribological properties are often influenced by test conditions like humidity, atmosphere and sliding counterfaces [40-41], but most of the previous Al-Si alloy experiment results were achieved in ambient air sliding against an iron-based counterface. Changing the experimental conditions is also expected to change the sliding wear behaviour of Al-Si alloys. Elmadagli et al. [6] studied the sliding wear behaviour of A390 (18.5% Si), Al-25% Si and 383 (8% Si) using a ring-on-block in a controlled, dry air environment (5% RH). The authors reported that the transition from mild to severe wear existed in all the alloys tested under testing conditions, but that two wear sub-regimes—i.e. the first and second mild wear sub-regimes—were identified in the three tested alloys (**Fig. 2.8**). There was a short transition from 35 to 60 N between these two sub-regimes, which were differentiated by a wear rate transition from 80 to 250%. In addition, the wear rate for the mild wear regime was stable, increasing linearly with an increase in sliding distance, while the wear rate for the severe wear regime was unstable, showing an exponential increase with sliding distance. The above differences in the wear rates might be taken to be the reason for existence of two distinctive wear regimes in Al-Si alloys.

Elmadagli and Alpas [12] also explored the effects of counterface and atmosphere on the sliding wear behaviour of Al-18.5% Si by changing the atmosphere, humidity and counterface. A new wear regime called ultra-mild wear—in which the wear rate was an

order of 10^{-5} mm^3/m—was achieved in Al-Si alloy at loads below 10 N when the sliding tests were performed on the Al-18.5% Si in an argon atmosphere sliding against a 52100 steel counterface. Ultra-mild wear was also achieved when sliding tests were conducted in dry air (5% RH) but against a DLC-coated steel counterface (**Fig. 2.9**). The wear rate for the ultra-mild wear regime was an order of magnitude lower than that measured for the mild wear regime at loads below 10 N. A similar UMW regime was reached in a study performed by Zhang and Alpas [17] in a 2024 Al reinforced with 20% Al_2O_3 particles when the test was run at a sliding speed of 0.1 ms^{-1} and a normal load of 0.5 N (**Fig. 2.10**). This suggests that Si and Al_2O_3 particles tend to carry applications at low sliding speeds and loads to prevent the aluminum from being damaged. It might also be attributed to the constraint effect of load carrying hard particles on subsurface plastic deformation under sliding contact at low loads.

2.2.3. Wear Mechanisms

As the review presented above indicates, mild and severe wear display a significant difference in wear rate. This can be understood by identifying the mechanisms operating in the different wear regimes. An examination of the worn surfaces paired with a characterization of the wear debris is both crucial and instructive for identifying wear mechanisms. Extensive studies have been performed to identify the wear mechanisms of Al-Si alloys under dry sliding conditions [36-37, 42-44]. The mechanisms that operate in dry sliding wear of Al-Si alloys have been summarized in wear mechanism maps by Antoniou and Subramanian [45], and Liu [46] by adopting a similar approach to Lim and Ashby [35], using wear rate and wear mechanism data for aluminum alloys from literature (**Fig.2.11**). As **Fig. 2.11** illustrates wear mechanisms identified in Al-Si alloys

consist of oxidative wear, delamination wear, severe plastic deformation wear and seizure. At low applied loads and sliding speeds, the dominant wear mechanism was the oxidation of Al-Si alloys. While delamination or metallic wear—the formation of metallic debris—was the dominant SW mechanism. However, conflict exists regarding Al-Si alloy wear mechanisms in the MW regime. Such controversy can be attributed to the fact that a range of different alloy compositions were tested using experimental procedures perfected by various researchers.

A Study performed by Clarke and Sarkar [39] on an Al-6.2% Si revealed that mutual material transfer between the two contact surfaces was an important feature of all sliding wear regimes. This material transfer mostly occurred to the Al-Si alloys due to its lower yield stress. They suggested that a shear transfer mechanism was dominant in both wear regimes. The authors proposed that delamination was the dominant mechanism in the mild wear regime of eutectic and hypereutectic alloys. Asperity interaction, gross plastic deformation and ductile fracture were the major mechanisms that prompted seizure conditions.

Biswas et al. [36] proposed that mild wear was characterized by the in situ formation of a protective, iron-rich, compacted layer while severe wear was initiated when the protective layer was removed by plastic deformation at the subsurface. Similar observations were made by Shivanath [5] in the dry sliding of hypereutectic, eutectic and hypoeutectic alloys against a steel counterface in the mild wear regime.

Two wear mechanisms, oxidative and metallic wear, were identified by Beeseley and Eyre [43] in the dry sliding of aluminum alloys containing 1-8% Cu and zinc. Oxidative wear occurred at low applied loads and was characterized by the formation of protective surface films, which were observed on both the Al-Si surface and the

counterface. But the films were broken up at the onset of severe wear by the plastic deformation at high load and sliding speed. Microprobe analysis revealed that in the case of aluminum sliding against iron, the surface films consisted of oxides and an Al/Fe intermetallic compound. Wear occurred firstly by oxidation of the asperities and then secondly by fracture and compaction of the oxidized wear debris into this layer. Beeseley and Eyre's [43] definition of the oxidative wear process is supported by Razavizadeth and Eyre [42]. Metallic wear became the dominant wear process at the higher applied loads. The Al-Si alloy surfaces were characterized by plastic deformation and fracture, and significant transfer of material between the sliding surfaces and wear debris formation. The large amount of plastic deformation and higher wear rate prevented the formation of an oxide layer.

However, Antoniou and Borland [44] reported that oxidation did not play a significant role in the mild wear of Al-Si alloys. While a dark surface layer and a subsurface deformation region with silicon particle fragmentation and fine equiaxed debris were observed, their examination did not reveal the presence of iron oxide and Al-Fe intermetallic compounds. The authors proposed that mechanisms that operated at low loads could be categorized as deformation, compaction and fracture while ones that operated at high loads featured debris that was predominantly formed by a ductile shear mechanism, namely, at higher applied loads a delamination wear mechanism was inferred. The observations made by Reddy et al. [47] supported those of Antonio and Borland [44], the worn surface was characterized by the formation of an iron-rich compacted debris layer at low loads but the presence of oxidation film. Wear debris formed in this regime was a result of abrasion and cracking of this protective layer.

SEM observations of the worn surfaces of a wrought aluminum alloy (6061 Al)

under unlubricated conditions conducted by Zhang and Alpas [38] revealed the presence of two types of wear debris—fine equiaxed particle debris (0.5 –5.0 in diameter) and large, plate-like debris—in the mild wear regime. They suggested that the fine equiaxed particles agglomerated further—forming dark aggregates. EDS and XRD analysis showed that the wear debris particles consisted of an aluminum oxide phase with a partly amorphous structure and elemental iron. With this in mind, the authors proposed that mild wear was caused by the delamination or spalling of the mechanically mixed layers—which were discontinuous—allowing fresh metal-to-metal contact that prompted oxidation and iron transfer to occur concurrently. The worn surfaces in the severe wear regime had a shiny, metallic appearance that indicated heavy surface and subsurface damage. Cross-sectional SEM studies performed below the worn surfaces suggested that the thin, plate-like wear debris generated in the severe wear regime were not a result of the delamination of a mechanically mixed layer. This debris was caused by the direct detachment of bulk aluminum due to subsurface crack initiation and propagation. The authors suggested that the thick, plate-like wear debris observed in the severe wear regime was attributed to thermal softening, because the flash temperature reached a critical value of 0.4Tm (where T_m is the melting temperature of the alloy).

Wilson and Alpas [48] systematically investigated the effects of testing conditions on wear mechanisms in an A356 alloy sliding against 52100 steel using a block-on-ring testing machine in an ambient air atmosphere. A wear mechanism map was then constructed (**Fig. 2.12**). Applied test loads and sliding speeds varied from 0.2 to 400N and 0.1 to 5 m/s, respectively. They found that when the flash temperature (T_f) exceeded a critical value, a mild wear transition from mechanical mixing/oxidation wear to delamination wear occurred. The debris generated in the mixing/oxidation wear regime

was black and powdery in nature. While metallic flake or plate debris was produced in the delamination wear regime. But **Fig. 2.12** indicates that the wear rates in the delamination regime are similar to those in the mixing/oxidation regime. It infers that the onset of metallic transfer is not necessarily associated with high wear rates in Al-Si alloys. The authors proposed that the heavily sheared, plate-like delamination wear debris produced at a critical sliding speed and flash temperature was attributed to non-isothermal type shear localization in the alloy.

Elmadagli and Alpas [49] illustrated how sliding wear in both mild wear sub-regimes (MW-1 and MW-2) was prompted by the formation of tribolayers. The authors found that tribolayers formed in MW-1 at a faster rate with a more significant amount of material transfer than the tribolayers formed in MW-2. This suggests that higher wear rates in the MW-2 regime were due to the easy spallation of thick tribolayers generated in MW-2, as well as the extrusion of exposed aluminum surfaces over the tribolayer. Wilson and Alpas [48] also observed that two sub-regimes existed in the mild wear regime of an A356 alloy sliding against 52100 steel. The mechanisms operating in these sub-regimes differed—from a mixing/oxidation sub-regime at low speeds where the worn surfaces were covered by tribolayers to a sub-regime where delamination at higher speeds led to the removal of material next to the contact surfaces.

Elmadagli and Alpas [12] used EDS to examine the worn surfaces and sub surfaces of Al-18.5% Si generated in a UMW regime, UMW was reached under two test conditions—an argon atmosphere and sliding against a DLC-coated counterface in air. Their results indicated that the surface layer's composition changed from iron-rich transfer films to aluminum-rich tribolayers when the sliding distance was increased. The iron-rich layer was hard and brittle, and exhibited easy spallation. The authors attributed

the decrease in UMW wear rate to the continuous coverage provided by the aluminum-rich layer. The analysis of the worn surface generated in air while sliding against a graphitic DLC-coated counterface revealed no iron-rich oxidized tribolayer, and the corresponding wear rates and the coefficient of friction were lower than those obtained for the tests against an uncoated 52100 steel counterface.

The UMW obtained by Zhang and Alpas [17] for 6061 Al-20 vol.% Al_2O_3 sliding against SAE 52100 bearing steel exhibited a different scenario. The authors reported that at 3.0 N and a sliding speed of 0.2 m/s, the worn surface exhibited Al_2O_3 particulates standing proud of the aluminum matrix. The exposed particulates caused abrasive damage to the steel counterface during sliding, and the worn steel fragments were then transferred to the composite surface to form a protective, iron-rich transfer layer that tended to oxidize—producing a reddish-brown Fe_2O_3. The iron-oxide also featured a low friction coefficient, providing an in situ lubricating effect. This type of inconsistent identification of UMW mechanisms in the two sliding contact systems might be attributed to different matrix compositions, mechanical behaviours between Si particles and Al_2O_3, testing atmospheres and the counterfaces used in the two studies.

2.2.4. Tribolayers

The finely-mixed tribolayer usually formed on the wear tracks has been named the mechanical mixed layer (MML). The MML exhibits a different chemical composition and material structure compared to the material away from the surface. It arises from plastic deformation, material transfer and mechanical mixing induced by sliding contacts [50, 51]. As a result, investigations of the transfer, mixing and associated chemical and mechanical processes that occur during the dry sliding of Al alloys and other ductile

materials have been given great attention. Longitudinal SEM and TEM observations of cross-sections of worn surfaces, in addition to micro-hardness measurements for the subsurface have been the most commonly used methods for investigating tribolayers [51-52]. Tribolayers have been commonly observed on contact surfaces generated in the mild wear regime of aluminum-based composites, and Al-Si alloys, when they slid against a steel counterface in an ambient environment [5, 36, 43, 50-55]. Controversy surrounds the exact composition of UMW layers.

Longitudinal SEM observations of worn surfaces of A356 Al-10% SiC-4% Gr and A356 Al-5% Al_2O_3-3% Gr performed by Riahi et al. [55] revealed that a protective tribolayer was formed at nearly all sliding speeds and loads in mild wear regimes for both composites. EDS analysis revealed that the topmost part of the tribolayer consisted of iron-rich layers, while the rest was made up of fractured SiC and Al_3Ni particles and thin graphite films with a thickness of about 30-50 μm and which were elongated over long distances in the direction of sliding. The average microhardness of the tribolayers was considerably higher than that of the bulk material, and their formation increased the surface hardness significantly—playing an important role in delaying the mild-to-severe wear transition in aluminum matrix composites. They also showed, however, that abrasive wear caused by the fractured hard intermetallic and ceramic particles in the tribolayers acted as either two- or three-body abrasives against the steel counterface—increasing the severity of scuffing.

Li and Tandon [52, 56-57] systematically characterized the MML that was generated during the sliding wear of an A356 Al-Si casting alloy by using SEM, TEM, XRD and Mössbauer spectroscopy techniques. SEM observations of collected wear debris revealed two types of morphology—ultrafine equiaxed particles at low loads and a

mixture of fine equiaxed particles and plate-like flakes at high loads. EDS analysis revealed that the ultrafine structure consisted of the original materials—α-Al and α-Fe—from counterface materials. They reported that the debris contained a significant amount of iron, and that the amount of elemental iron in the debris increased with an increasing load—inferring more material transfer from the counterface. The elemental iron was mostly present in the aggregates with ultrafine particles. The formation of the plate-like debris particles was attributed to the detachment of the MML from the worn surface of an Al alloy and the Al composite. They proposed that the MML was formed by an extensive mechanical mixing process—such as fracture, fragmentation and repeated transfer and compaction—that occurred between two contact surfaces during sliding wear.

Elmadagli and Alpas [12, 49] conducted investigations on the worn subsurfaces of Al-18.5% Si sliding against 52100 at 10 N in a controlled dry air environment (5% RH), as well as in an argon atmosphere. Cross-sectional SEM observations revealed that a tribolayer was usually present on the worn surfaces generated under various testing conditions. The tribolayer and the damage zone below it, however, varied with the testing conditions. Their results indicated that iron transfer from the steel counterface to the silicon particles on the contact surfaces initiated the formation of tribolayers. Li and Elmadagli [58] characterized the tribolayer generated during dry sliding tests in air and argon atmospheres by using SEM, electron probe micro-analyzer (EPMA), focused ion beam (FIB) and TEM. They discovered that the tribolayer that formed in air contained significant amounts of iron, aluminum and oxygen, while a much less significant amount of oxygen and iron were detected in the tribolayer formed in argon. The microstructures of the tribolayer formed under the two test conditions shown in **Fig. 2.13** proved to be different. The authors reported that the tribolayer that formed in air was severely

fractured, and they attributed its brittleness to the high amount of oxygen. The tribolayer formed in argon, however, contained amorphous oxides mixed with ultra fined-grain aluminum (100 nm) and silicon, which reduced the A390 wear rates under such testing conditions. They also found that the aluminum beneath the tribolayer was refined in both test conditions, due to severe subsurface plastic deformation.

These contradictory characterizations of the chemical composition of the tribolayer formed in the MW regime might be a result of different testing conditions like humidity or the applied loads used in the various studies.

It must be emphasized that except for the change in the tribolayer's composition, the aluminum grain size in this layer is refined significantly, which are caused by large scale plastic deformation during sliding contacts of ductile materials with counterfaces. Hammerbergs et al. [59] confirmed these kinds of microstructural changes using molecular dynamics simulations from one pure, single crystal of copper sliding against another. Such significant changes in material microstructure and composition are expected to increase the wear resistance of ductile materials like aluminum alloys once the layer is formed on contact surfaces.

2.2.5. The Effect of Silicon Percentage on the Wear of Al-Si Alloys

An increase of silicon was traditionally expected to improve the wear resistances of aluminum alloys in the mild wear regime. Numerous experimental observations have indicated that the transition load at which wear changed from mild to severe increased along with an increase in silicon content [4, 60-62]. Silicon is also considered as an anti-seizure agent [61]. However, a unanimous conclusion regarding the role of silicon content on the wear resistance cannot be drawn from previous results on dry sliding. This can be

attributed to the range of test conditions used by various researchers—from geometry, sliding speed and applied load to microstructures and environment.

Bai Pramila and Biswas [62] reported that Si additions (4 to 24% Si) improved the wear resistance of Al-Si alloys, but that no linear relationship between wear rate as a function of Si content was ever found. Observations made by Shivanath et al. [4], however, regarding the wear of sand and chill cast Al-Si binary alloys (4 - 20% Si) showed that the MW rate (oxidative wear rate) was generally independent of silicon content or silicon particle size. The Al-Si alloys containing approximately 12% Si exhibited the highest wear rates.

These findings were contradicted in a study published by Clarke and Sarkar [63], where it was reported that the wear resistance of Al-Si alloys increased with the increase of the silicon percentage up to a near eutectic composition (13 wt% Si), then the wear rate increased along with the Si percentage thereafter (**Fig. 2.14**). This suggested that—regarding wear and load-carrying capability—a near-eutectic alloy would be ideal. They reported that hypereutectic alloys exhibited poor wear resistance compared with hypoeutectic alloys, and it was concluded that the beneficial effect of silicon was to decrease the propensity to seizure. High silicon alloys, however, wore down even hard steel counterfaces. Similar results were reported by Mohammed et al. [64] when they investigated the wear of Al-Si alloys containing 3–22% Si sliding against steel under dry sliding conditions. The results indicated that the adhesive wear rate in aluminum alloys was reduced by the addition of silicon until a minimum value close to eutectic composition had been reached. The further addition of silicon increased the wear rate. However, Andrew et al. [61] showed that the wear rate decreased considerably when the volume fraction of the primary silicon phase was increased.

Wang et al. [65] investigated the effect of Si content on the dry sliding wear behaviours of spray-deposited Al-Si alloys containing 12, 20 and 25% Si using a pin-on-disk machine at normal loads of 8.9, 17.8, 26.7 and 35.6 N. Their results indicated that at a low load (8.9 N), the wear rate of the spray-deposited Al-Si alloy decreased with an increase in Si content, and the dominant wear mechanism was oxidative wear. At a high load (35.6 N), the spray-deposited Al-20Si exhibited wear resistance that was superior to the Al-25Si and Al-12Si alloys, with a dominant wear mechanism of delamination and third-body abrasion. This suggested that the wear resistance did not increase linearly along with the increase in silicon percentage. An optimum silicon percentage is expected in Al-Si alloys, so too many silicon particles might cause more abrasive wear to the counterface that, in turn, increases the wear of the Al-Si alloys.

Elmadagli and Alpas [6] initially conducted a parametric study of the relationship between the microstructure and wear resistance of Al-Si alloys in a controlled air atmosphere (5% RH) using pair wise comparisons. Pair wise comparisons generally refer to any process that compares entities in pairs to judge which of each pair is preferred, or displays a greater amount of some quantitative property. In order to use this method, two alloys were selected, in which only one microstructural feature showed significant difference. The sliding wear tests were performed on three commercial Al-Si alloys, die cast 383 (9.5 wt.% Si), A390 (18.5 wt.%) and a spray-cast alloy with 25 wt% Si, all in a controlled dry atmosphere. The as-cast 383 was solution-treated at 480 ^{o}C for 36 hours in order to change the Si particle shape and hardness while maintaining the other parameters within a reasonably close range. A power-law relationship between wear rate, W, and applied load, L, was established

$$W = CL^n \tag{2.1}$$

where C and n were the wear coefficient and the wear exponent,, respectively. It proved that increasing the silicon percentage from 9 to 25% slightly reduced wear coefficients, but increased the transition load of the first mild wear sub-regime by 140%.

It should be noted that Si particles and aluminum matrix have significantly different mechanical properties. The Si particles in Al-Si alloys are supported by the aluminum matrix, making the mechanical response of Si particles to the applied load important for understanding the wear behaviours of Al-Si alloys, especially at low applied loads (helpful for understanding contradictory findings reported by various researchers). The way Si particles mechanically respond to applied loads will change accordingly based on different testing procedures, matrix compositions (matrix hardnesses) and a variety of processing techniques for producing a range of Si particle sizes and morphologies in Al-Si alloys.

2.2.6. The Effect of Silicon Particle Morphology on the Wear of Al-Si Alloys

The silicon particle morphology in an Al-Si alloy changes in relation to the silicon percentage and processing techniques used to develop it. Eutectic Si particles are generally needle-like or platelet like, while primary Si particles are block-like [19]. Sodium, sulfur, phosphorous and rare earth elements like Sr are traditionally used to modify eutectic and coarse primary Si particle morphology by influencing the nucleating and growth processes of coarse Si particles [66-68]. Si particle morphology also can be modified by increasing cooling speed of casting and solution heat treatment. Elmadagli [69] modified the silicon particle shape in the 383 alloy by solution heat treatment at 480°C for 36 hours and followed with a hot water quenching at 80°C. After the solution

heat treatment and water quenching, the 383's needle-like Si particles with a sphericity of 0.2 were forced into round shapes with a sphericity of 0.5. Extensive studies of the effect of Si particle morphology on the wear of Al-Si alloys have been conducted, and they indicate that Al-Si alloys with spheroidized Si particles (smaller aspect ratio) exhibit better wear resistance in the MW regime, namely, at relatively low applied loads, in comparison with the Al-Si alloys with large aspect ratio Si particles [69-73].

Pair wise comparison performed by Elmadagli and Alpas [6] for a 383 alloy with 9.5 % Si indicated that a decreasing silicon particle aspect ratio reduced the wear coefficient of the first mild wear sub-regime, C_1, and increased the load, L_1, at which the transition from MW-1 to MW-II initiated. C and L were described in **Equation 2.1** (**Section 2.2.5**). When the aspect ratio was reduced from 3.75 to 1.98 by solution heat treatment at 480 °C for 36 hours, C_1 was decreased by 25% and L_1 was increased by 25%.

Riahi et al. [71-72] investigated the scuffing resistances of two eutectic Al-Si alloys, etched by 10% NaOH, containing 12% Si but with different morphologies. The results showed that the alloy containing smaller aspect ratio second particles exhibited better scuffing resistance. The authors attributed this to the different fracture behaviours of the two types of secondary Si-rich particles. They found that the Si-rich particles with larger aspect ratios were more likely to be fractured at their roots, while the particles with smaller aspect ratios tended to fracture from their edges. The fracture behaviour of Si-rich particles with different morphologies found in Al-Si alloys that had been subjected to sliding contact was analyzed using a flexure formula. The authors derived an equation to compute the maximum tensile stress, incorporating the coefficient of friction at the root of a Si-rich phase with a rectangular shape:

$$(\sigma_{\max})_{k_1} = (\frac{6}{\sqrt{1.8}})\frac{h_{ph}\sqrt{P}(\mu\sqrt{H_m})}{t^2} \tag{2.2}$$

where σ_{max} is the maximum tensile stress at the root of the Si-rich particle with an aluminum matrix, μ is the coefficient of friction, t is the thickness of a particle with a rectangular shape, H_m is the matrix hardness measured and h_{ph} is the height of the protruded particle section. At a given applied load of 0.1 N, μ=0.1, t =3 μm and when the particle stood proud of the matrix by 7.5 μm, the estimated σ_{max} could reach as high as 2.35 GPa. But in **Equation 2.2** the factor of a particle shape—aspect ratio is not included—the conclusion that the particles with smaller aspect ratios exhibited smaller σ_{max} in comparison with the particles with larger aspect ratios cannot be drawn accordingly. An equation to calculate the critical particle thickness, t_c, was obtained by combining the fracture toughness of the particles with **Equation 2.2**:

$$t_c = \left[3.2\sqrt{P}h_{ph}\sqrt{\pi c}(\mu\frac{\sqrt{H_m}}{K_{Ic}})\right]^{1/2} \tag{2.3}$$

where K_{Ic} is the fracture toughness of the Si-rich particles and $2c$ represents the semi-circular cracks formed by the Vickers indenter. Following this equation, the particle with $t < t_c$—namely with a larger aspect ratio—will be subjected to fracture.

2.2.7. Summary of Literature on the Dry Sliding Wear of Al-Si Alloys

The literature survey presented above indicates that extensive laboratory-scale studies have been performed on Al-Si alloys in an effort to understand their sliding wear characteristics under dry sliding conditions—circumstances that tend to belong to "mild" and "severe" wear regimes. The main results can be summarized as follows:

1. Two different wear regimes occur when Al-Si alloys slide against iron-based counterface materials. "Mild" wear is characterized by a relatively low wear rate as well as the formation of tribolayers, the oxidation of aluminum, material transfer and back transfer. "Severe" wear is characterized by a high wear rate, severe plastic deformation of the contact surface, material transfer and high contact surface temperature. "Ultra-mild" wear is reached when sliding tests are performed under special test conditions, like a changing environmental atmosphere and a variety of counterface materials.
2. The worn surfaces of Al-Si alloys—obtained after sliding tests are performed in a mild wear regime—feature a tribolayer, a mixture of transferred materials, fragmented Si particles, oxidized aluminum and iron and plastically deformed aluminum with ultra-fine grain sizes. The presence of these elements significantly affects the wear resistance of Al-Si alloys.
3. The wear resistance of Al-Si alloys is also affected by silicon content, which is also related to testing conditions. It is generally accepted that the transition load to severe wear increases with the Si content.
4. Al-Si alloys with small aspect ratio Si particles exhibit better wear resistance in the mild wear regime in terms of wear rate and transition load. Decreasing the Si particle aspect ratio or increasing the Si particle sphericity prompts a decrease in the wear rate and an increase in the transition load.

Under normal running conditions, however, engine components in cylinder block assemblies operate under lubricated conditions, so that a comprehensive understanding the sliding wear behaviours of Al-Si alloys under lubricated conditions—especially under engine oil or lubricants containing additives used in engine oil—is essential to better use

Al-Si alloys as engine components.

2.3. Wear Properties of Al-Si Alloys under Lubricated Conditions

2.3.1. Engine Lubricant and Its Additives

A formulated automotive engine lubricant commonly contains base oil and a mixture of various additives intended to work in internal combustion engine chambers—and are subjected to a wide range of fuels. Engine lubricant is used to minimize wear, improve efficiency and prolong engine life [74]. The additives in engine oil act as defoamers, viscosity improvers, flash-point depressants, antiwear and extreme pressure additives, detergents and dispersants. Tribologists continue to focus on creating new, more environmentally responsible engine additives that meet the increasingly tight requirements of ecological emissions.

Due to extreme working condition, the engine lubricants interact with the combustion products, which results in their contamination and oxidation in addition to the formation of deposits on contacting and rubbing surfaces that lead to corrosion and wear. The most effective class of antiwear and antioxidant additive used in engine oil has been zincdialkyl(aryl)-dithiophopshates or ZDDPs (**Fig. 2.15**) [75]. So far, extensive research has been performed using a wide range of surface analytical techniques like XPS, infra-red absorption spectroscopy (IR spectroscopy) and X-ray absorption near edge (XANES) technique [76-77] to better understand the lubrication properties of ZDDPs, including the chemical characterization of ZDDP films. XPS is a quantitative spectroscopic technique that measures the elemental composition, chemical and electronic states of the elements from the surface of a material. XPS spectra are obtained by irradiating a material with a beam of aluminum or magnesium X-rays from the top 1 to 10 nm of the material being

analyzed in ultra-high vacuum (UHV) conditions. IR spectroscopy is a measurement that involves collecting absorption information and analyzing it in the form of a spectrum. The frequencies at which absorptions of IR radiation ("peaks" or "signals") occur can be correlated directly to bonds within the compound being analyzed—making it useful for identifying organic and organometallic molecules. XANES is also a type of absorption spectroscopy that quantitatively determines the composition of a mixture of species while remaining strongly sensitive to the chemical information— valence, charge transfer and the oxidation state of the absorbing atom. It covers a region of x-ray absorption spectrum with ~ 50 eV of the absorption edge [77-78].

The majority of rubbing systems that have been investigated are steel and cast iron, and ZDDP has proven beneficial in preventing wear in these systems [79]. It is a widely accepted belief that ZDDPs breaks down in the combustion chamber to create sacrificial films through a tribo-chemical reaction under high temperature and pressure—characteristics that are responsible for minimizing the asperity contact that eventually leads wear. This film is commonly referred to as an antiwear film, and is composed of various amounts of zinc, phosphorous, sulfur and oxygen [80]. The effect of ZDDP on aluminum alloys, however, is not clear.

2.3.2. Sliding Wear Properties of Al-Si Alloys Under Lubricated Conditions

A minimal amount of investigation has been performed on the lubrication of Al-Si alloys—compared to the research efforts made to understand the wear properties of Al-Si alloys under dry sliding conditions. Some of the research focused on the tribology of Al-Si alloys under fully formulated engine oil lubricated conditions or a polymer-based lubricant [13, 81-83], while the majority tested whether or not ZDDP also acts as an anti-

wear additive in Al-Si alloys [84-89].

Timmermans et al. [81] studied the wear behaviour of a hypereutectic P/M Al-Si alloy sliding against steel under fully lubricated conditions with SAE 15W50 engine oil as a lubricant. The tests were conducted at 150°C and the wear test data indicated that the wear volume of the tested alloy was reduced by using engine oil as a lubricant. The presence of engine oil ingredients on the worn surface was examined, indicating that the engine oil used during testing effectively protected the surfaces from wear damage. Hu et al. [82] used XPS, FT-IR and thermal gravimetric (TG) analyses to investigate the tribo-chemical behaviour of Al-Si alloys with 12% Si sliding against itself while lubricated by ethyleneglycol and amines that included ethanolamine, ethylenediamine and triethylenetetramine. The authors found that triethylenetetramine displayed the best anti-wear ability in the Al-Si alloy tested when it was sliding against itself, while the amines exhibited superior anti-wear performance when compared with ethyleneglycol. Wear tests performed by Das et al. [83] on a eutectic Al-Si alloy (12.3% Si) in boundary lubricated conditions, however, indicated that the engine oil with additives reduces friction, but increases wear compared with base oil.

The reported results on the lubrication effect of ZDDP on Al-Si alloys are contradict and far from comprehensive. Wan et al. [84] investigated the wear properties of an aluminum alloy containing ~ 0.5% Si sliding against steel under boundary lubricated conditions with base oil plus a mixed alkyl-chain ZDDP—with a concentration that varied up to 5%—as lubricants. The study showed that the coefficient of friction was not altered by an increase in the concentration of ZDDP while an increase in wear rate occurred at 5% ZDDP concentration. They concluded that ZDDP does not improve the wear properties of aluminum alloys because the films formed tend to be fragile and easily

displaced. The authors suggested that chemical corrosive wear is the dominant mechanism for the tested aluminum alloy. Similar observations were reported by Neville et al. [85]. The authors showed that addition of ZDDP or MoDTC did not show an obvious antiwear effect, as neither the coefficient of friction, nor wear of Al-23% Si rubbed against cast iron at 100°C was much different than the behavior of the same Al-Si alloy rubbed in base oil.

The following research information indicates that ZDDP can act as an anti-wear additive for Al-Si alloys. Kawamura et al. [86] performed sliding wear tests on A390 (with ~ 18% Si) under drip-supplied lubricated conditions using paraffinic base oil with phosphate, phosphite and ZDDP additives. The worn surfaces were examined by electron probe microanalysis (EPMA). The authors found that all the tested additives exhibited good anti-wear properties, regardless of the type of alkyl group used. Konishi et al. [87] conducted wear tests on self-mated A390 tribo-pairs under fully-flooded lubricated conditions of mineral oil containing 2 wt.% ZDDP and synthetic base oil using a pin-on-disk tester. The study revealed that the base oil was important to the performance of the ZDDP, and that the wear rate was reduced by one to two orders of magnitude when ZDDP was added to the base oil compared to testing with the base oil alone. Most importantly, they found zinc, phosphorous and sulfur present on the worn surface, which they attributed to the formation of a protective film containing ZDDP. Fuller et al. [88] tested A6061 sliding against A6061 and A390/A390 while lubricated with base oil containing 1.2 wt.% ZDDP using a reciprocating cylinder-on-block tribometer at loads that varied between 30 and 100N at 60°C. The examination of the wear scars using XANES analysis revealed the presence of sulfur and phosphorous—decomposed from the ZDDP. The authors firstly found that the ZDDP tribo-films formed on the aluminum

alloys are essentially identical (chemically) to those formed on steel—polyphosphate structure—but their generation only occurs after an extended rubbing period (30+ minutes). Similar findings were achieved by Nicholls et al. [89]. They also used XANES spectroscopy to investigate the ZDDP films generated on the sliding surfaces of A319/A319 and A319/52100 steel in boundary lubricated conditions. The P L-edge and P K-edge spectra obtained from said XANES analysis (**Fig. 2.16**) reveals that the films formed on the A6061 and A319 aluminum are very similar to that formed on steel, with a strong peak at 2152 eV being representative of polyphosphate glass. $Zn_4P_6O_{19}$, is also present in the wear scars of aluminum alloys. The authors found three other species in the wear tracks—a phosphide, unreacted ZDDP and the linkage isomer—all of which varied with rubbing time. They also learned that an increase in rubbing time applied to the A319/52100 steel series increased the amount of polyphosphate and unreacted ZDDP while the LI species and phosphide decreased. The authors attributed this to the beneficial effect of silicon particles, which provide a rigid surface, on the formation of an anti-wear film—namely polyphosphate. This was further verified by the results obtained from lubricated wear tests performed by Nicholls et al. [90] on A390 (containing > 18% Si) under conditions similar to a cylinder/bore system. The tests were conducted at 60 N with a corresponding Hertzian contact pressure of 264 MPa at 60°C using MCT-10 base oil with 1.2 wt.% commercial ZDDP concentrate. They found that oxides of both aluminum and silicon, as well as a fairly thick zinc polyphosphate film, formed on the surface of A390 after sliding tests. X-PEEM micro-chemical analysis and AFM and SEM imaging showed that ZDDP anti-wear pads tended to form on the silicon surfaces, and these pads were similar to those formed on steel. The modulus of the anti-wear pads was measured using a nano-indentation tester, and the results showed that the films formed on the A390

and steel surfaces were identical. These promising results provide new insight into the lubrication process of Al-Si alloys with a high Si percentage and encouraging a better understanding of wear damage in Al-Si alloys working under conditions similar to a cylinder/bore engine component.

The controversy about ZDDP's anti-wear effect on Al-Si alloys suggests that XPS is not sensitive enough to detect the tribochemical reaction film that forms on the Al-Si alloys, and tribo-film formation mechanisms in Al-Si alloys are yet to be better understood. It is also important to note that the anti-wear effects of ZDDP usually appear to be obvious in hypereutectic Al-Si alloys at high testing temperatures or during extended periods.

2.4. Engine Component Wear Damage

2.4.1. Brief Introduction to Friction and Wear in Automotive Engines

Fig. 2.17 provides a schematic view of the reciprocating internal combustion engine [2]—the most important motor vehicle component. Friction loss accounts for approximately 40% of the total energy consumption developed by an automotive engine [91]. If powertrain friction loss is the only consideration, then it is the piston and piston ring assembly that contribute the most to the total engine friction and wear in a powertrain system. It is estimated that the sliding of the piston rings and piston skirt against the cylinder wall amounts to approximately 50 to 70% of the cylinder block assembly's friction loss within a powertrain system [92]. As a result, extensive theoretical and experimental investigations have been performed to understand and evaluate the wear damage sustained by an engine block assembly [93]. The principal factors influencing the wear of an engine block assembly are—engine working parameters like speed,

temperature, load and frequency and engine lubricant conditions like gas cleanliness, corrosion, surface finish and lubricant quantity [94]. Abrasive wear, corrosive wear and scuffing are considered the three most serious wear types sustained by engine blocks.

Abrasion occurs when hard particles present on two moving surfaces. These particles scratch the softer surface, ultimately prompting material removal. This type of abrasive wear causes multiple problems, from dimensional changes to leakage and low engine efficiency. The two most common types of abrasive wear are two-body and three-body abrasion. Two-body abrasion occurs when a rough, hard surface slides against a relatively soft opposing surface—damaging the soft surface by plowing or micromachining. Three-body abrasion occurs when hard, rough particles become trapped between two sliding surfaces [95]. In such a situation the greater the difference in hardness between the particles and the contact surface, the more easily the contact surface is damaged.

Corrosion is defined as a destructive process prompted by chemical or electrochemical reactions. Corrosion happens at the anode with either the release of hydrogen gas or the formation of hydroxyl ions at the cathode. These hydroxyl ions may react with metal ions that have been dissolved at the anode to form metal hydroxides or hydrated oxides [96]. Internal combustion engine components—as well as the engine oil itself—are subject to moisture accumulation caused by natural condensation. The oil film deteriorates during long running periods when accumulated moisture interacts with the surface beneath the oil. The engine surface corrodes when accumulated moisture in the engine oil reacts with deposits in the same oil that developed previously during engine operation—causing pitting and, finally, material loss. The synergistic effect of wear and corrosion is, however, detrimental even in engineering applications—especially in cases

where corrosion is also responsible for the wear of metallic components like piston rings and cylinder walls. Generally, the total wear rate when corrosion is present is larger than in dry conditions because of the combined action of mechanical and electrochemical mechanisms [97].

Scuffing is usually characterized by a dramatic friction increase and rapid rise in temperature that accelerates lubricant degradation—causing the two scuffed surfaces to vibrate noisily or even seizure. With this in mind, scuffing is considered the most problematic type of engine damage. Cylinder block assembly—especially between the piston ring and the cylinder bore—is where scuffing is most commonly observed in automotive engines [7]. While scuffing mechanisms are not fully understood due to the complexity of the material systems involved, as well as the diversity of machine operation conditions, it is generally accepted that scuffing at the contact surface is either the result of lubrication breaking down or of the contact surface reaching a critical temperature. Scuffing and its prevention are subject to operating conditions and the physical and chemical interactions of the rubbing system—including the duration, the materials, the surface preparation and the lubricants in the working system [8].

2.4.2. Review of the Literature on Al-Si Engine Related Wear

With the increased use of Al-Si alloys as engine components, issues regarding the friction and wear of engine components made from Al-Si alloys have been given great attention. Ye et al. [98] investigated the scuffing resistance of A390 (KS 281.1P for 1.91 Saturn L-4 engines) without coating, with a nickel-phosphorus plated coating with 4 vol% boron nitride particles (NNC), a tin plating, or a polyamideimide-based CPC with about 15 vol.% graphite particles (D-10). They used a piston-scuffing apparatus that simulates

the relative motion between piston and cylinder. The study also observed the effect of piston skirt surface texture and cylinder bore surface roughness on contact between the two parts, as well as investigating the microstructures and morphological features of surface and near-surface materials. During the course of the study, severe plastic flow, cracking that followed the direction of motion, spalling and the transfer of mutual materials were all observed. The authors reported that aluminum transfer to the liner surface was predominant during mutual material transfer. They attributed the final macro-scuffing of the piston material to surface strength deterioration prompted by local high temperature, plastic deformation and fatigue cracks found in the substrate. Using both the tin plating and the NCC-coating together did not significantly improve scuffing resistance.

Yu [11] conducted a failure analysis of scuffed, linerless Al-Si automotive engine blocks subjected to sliding wear. Five types of wear damage were identified—'Virgin area', 'Normal wear', 'burnishing wear, 'Comet area (Abrasive wear)' and 'Severe wear' (**Fig. 2.18**). The virgin area found on a cylinder bore surface has the same surface morphology as the new bore surface. The only damage observed in the virgin area was the fracture of the secondary phases. Compared with the virgin area, the normal wear zone differed in reflectivity and depth of particle fracture. The virgin area appeared highly reflective, while the normal wear zone was dull and mottled—suggesting that a film might be covering the contact surface in a normal wear zone. The silicon particles near the contact surface were fractured to 7 μm, but no obvious topographical changes were detected in either the virgin or the normal wear zone. Both comets and burnishing wear were characterized by abrasive scratches on the contact surfaces that related to the scratching of the hard particles trapped between the piston skirt and the cylinder bore.

Examinations of the surfaces and subsurfaces revealed that severe wear in the form of scuffing was caused by the direct contact of aluminum on aluminum—which was related to severe plastic deformation, fracture and the mixing of hard particles. The authors proposed that a suitable piston skirt design would prevent severe wear.

Yu's identification of wear damage helped explain Al-Si engine wear. If severe wear is prevented by precise design, normal wear would become the only acceptable cylinder block assembly wear damage under long running durations. Without measurable material loss from the contact surfaces, wear rates cannot be depicted using conventional mass or volume loss-based rates. Quantitative representation of the wear in this condition requires a novel approach.

Scherge et al. [99] introduced the fundamental radionuclide-technique (RNT) and applied it to the investigation of engine component wear behaviours. The RNT illustrated in **Fig. 2.19**—including the concentration method and the difference method—is considered suitable for mechanical systems with low wear rates. The location of suspected wear is radioactively labeled via bombardment with heavily charged particles. Consequently, the time dependence of wear is determined by radiation emitted by activated material. RNT provides the advantage of continuous observation and progressive wear measurements taken from the machine parts in service, without having to stop or disassemble the machine. RNT is highly sensitive—capable of resolving wear rates as low as 0.1/nm/h or 1 μg/h. Scherge et al. [99] measured the material removal rate using RNT for a water-cooled, four-cylinder diesel engine with a variety of oils and a range of cylinder wall temperatures under hot test operations (maximum speed at full load). The wear rates seen in the cylinder liner around the top dead center position for the top piston ring (the critical wear zone for diesel engines) when tested below 150 °C under

different formulated oils with a variety of viscosities were below 500 μg/h.

Dienwiebel et al. [13] used RNT to measure the wear rate of an AlSi cylinder bore made from an AlSi17Cu4Mg alloy operating in fully formulated engine oil (Fuchs Titan 5W30). The results revealed a wear rate of approximately 10 to 20 nm/h—depending on the loading conditions. The material loss measured by Dienwiebel et al. [13] was consistent with that measured by Schneider et al. [10] from cylinder bore surfaces in spark-ignition (SI) engines. The authors used a radiotracer method that measured the wear rate at 2 to 20 nm per running hour—an acceptable amount of wear for the typical vehicle's service life. Acceptable wear of the cylinder bore radius in automotive engines during a typical vehicle life of 150,000 km running at 50km/h is $\leq$ 50 μm. It follows that the corresponding material loss rate should not exceed 1 $x10^{-13}$ m/rev or 16 nm/h.

Dienwiebel et al. [13]—apart from measuring the AlSi cylinder bore's material loss using novel techniques—used FIB and AES to examine the worn surface of an AlSi17Cu4Mg engine block after said block had been operating in fired dynamometer testing conditions for approximately 250 hours over the engine's full speed and torque range. The authors reported the presence of a surface layer consisting of a mixture of embedded Si particles and an aluminum matrix. The study also observed that the aluminum between the embedded Si particles appeared to be plastically deformed—suggesting that even though the material removal rate is low in normal running conditions, material surfaces are not free of damage at the microscopic level. The authors attributed these phenomena to friction-induced dispersion hardening. But the authors did not consider the mechanical behaviour of Si particles under sliding contact. The micro-structural changes induced by the normal wear of Al-Si alloy engine bores were far from comprehensive.

In addition, similar to results obtained from sliding tests under lubricated conditions that used engine oil as a lubricant [81], AES elemental composition analysis detected engine oil elements like Ca, O, C and P on the worn cylinder bore surface. While these preliminary observations provide important information about the wear damage suffered by AlSi cylinder bore surfaces, the surface damage mechanisms themselves—operating under conditions similar to the rubbing that occurs between piston ring or piston skirt and cylinder bore surfaces—are far from clear. Additional systematic laboratory-scale studies are expected.

2.4.3. Surface Preparation of Al-Si Engine Component Surfaces

Fig.2.20 shows a SEM image taken from an ALUSIL engine block surface [100]. This illustrates how Al-Si alloys are used in tribological applications; silicon particles stand proud of the aluminum matrix, and hence, carry the load. Surface preparation techniques for cylinder bores in linerless Al-Si engine blocks can delay or speed the development of wear resistant surfaces [1, 22]. Chemical -etching and mechanical honing are the two most common techniques used to prepare the surfaces of Al-Si cylinder bores—exposing the silicon particles that, in turn, lead to the carrying of the applied load.

The conventional chemical-etching technique involves each cylinder bore being machined and honed to the desired dimensions, followed by the application of a chemical etchant (10% NaOH) to the bore surfaces to remove some of the aluminum matrix and expose the silicon phases [22]. This treatment creates a surface in which hard silicon particles carry the load so that there is no contact between the piston rings/skirt and the soft aluminum matrix during engine operation.

The mechanical surface preparation method serves as an alternative to the role of

chemical-etching in improving cylinder bore wear resistance. Mechanical reduction is followed by a polishing process similar to most honing operations—with the exception that the conventional hone stone is replaced by a tool that consists of an abrasive (typically diamond) embedded in a polymer matrix. The soft matrix allows the hard abrasive to yield as it contacts hard phases on the bore surface, yet it is stiff enough to allow some cutting action against the softer aluminum. The surface topography created by a conventional bore honing process followed by a "mechanical reduction" process is similar to that of surfaces prepared by chemical-etching.

At present, published reports on the effects of chemical-etching (10% NaOH) and finishing on the wear properties of Al-Si alloys remain limited. Riahi et al. [71-72] investigated the effect of chemical-etching conditions on the scuffing resistance of eutectic Al-Si alloys—varying the etching time from 5 to 7 minutes. The authors found that etching times lasting longer than 7 minutes resulted in the weakening of the particle/matrix bonding due to the excessive dissolution of matrix material around the particles. This weakening of particle/matrix bonding prompted particles to detach from the contact surface during sliding—resulting in decreased scuffing resistance. They recommended that optimum etching times for the tested Al-Si alloys lay between 5 and 7 minutes. Information comparing of the two types of surface preparation has not been reported yet, leaving it uncertain which surface preparation would provide the optimum surface for the wear resistance of Al-Si alloys.

2.4.4. Remarks

The literature survey above indicates that under normal running conditions—for durability applications—the majority of wear damage experienced by engine cylinder

bore surfaces can be classified as normal wear. Engine bore surfaces do not surfer from obvious surface damage or material loss. Accordingly, Al-Si alloys intended for use making engine components—like cylinder block assemblies—must be able to operate in the ultra-mild wear regime under similar loading conditions [11-12]. Most of the previous laboratory scale tests on Al-Si alloys conducted in "mild" and "severe" wear regimes, and usually tested at high loads under dry sliding conditions, therefore, are more applicable to oil starvation or seizure conditions. In addition, the application of Al-Si alloys in an automotive engine is that Si particle should stand proud of aluminum matrix to prevent aluminum from being damaged. But this was not taken into account in previous studies on sliding wear behaviours of Al-Si alloys. Almost all the tests have been conducted on relatively smooth Al-Si alloy surfaces or the authors did not even mention about the surface preparation.

While the mechanical behaviour of Si particles during sliding contact has hardly been considered in previous studies, Al-Si alloys can be categorized into two component materials and Si particles exhibit a significant difference in their mechanical properties compared to the aluminum matrix. It follows that the mechanical response of the Si particles to the applied load and the interface between the Si particles and the aluminum matrix should both be taken into account and the pressure applied to the Si particles in Al-Si alloys must be estimated in order to fully comprehend the realistic role that Si particles play.

It should also be emphasized that wear processes are nonlinear, and many different mechanisms can be responsible for wear phenomena in various wear regimes. This suggests that knowing what controls wear rates in the mild wear regime does not help explain the wear mechanisms that operate in the ultra-mild regime. Conventional

mass loss-based wear measurement techniques are not suitable to evaluate UMW in laboratory conditions due to the very small amount of material loss. It takes long period of time for the detectable quantities of mass loss to occur during the wear testing. Studying the progression of UMW under laboratory conditions is more challenging than studying mild and severe wear regimes, so a new methodology must be developed to evaluate UMW.

Table 2.1. Chemical compositions for the three major commercial casting Al-Si alloys [20].

Alloy	%Si	%Cu	%Fe	%Mg	%Mn	%Ni	%Zn	%Ti
319	5.5-6.5	3-4	1	0.1	0.5	0.35	1.0	0.25
380	7.5-9.5	3-4	1.3	0.1	0.5	0.5	3.0	-
A390	16-18	4-5	0.5	0.45-0.65	0.1	-	0.1	0.2

Table 2.2. Typical mechanical and thermal properties of the three alloys [20]

Alloy	Tensile strength (MPa)	Yield strength (MPa)	Elongation (%)	Hardness (HB)	Thermal conductivity (W/m.K)
A390	275	180	<1	100	0.32
380	310	150	3.5	75	0.26
319	250	165	2.0	80	0.27

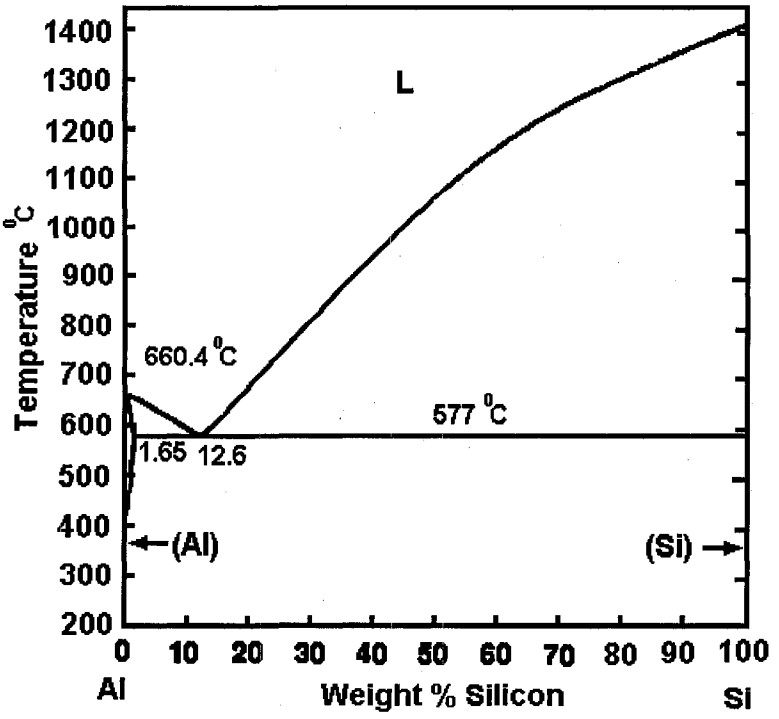

Fig. 2.1. Aluminum-Silicon binary phase diagram [18].

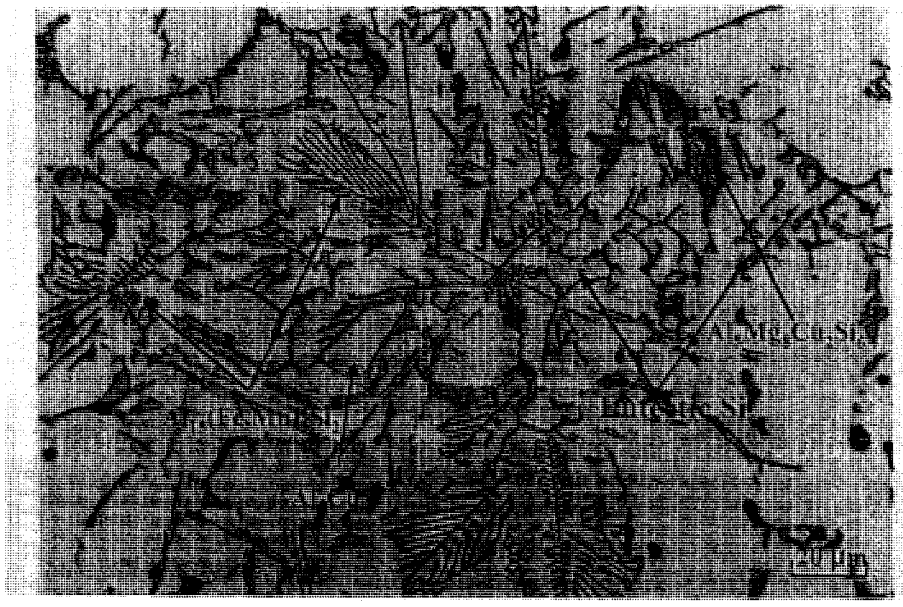

(a)

(b)

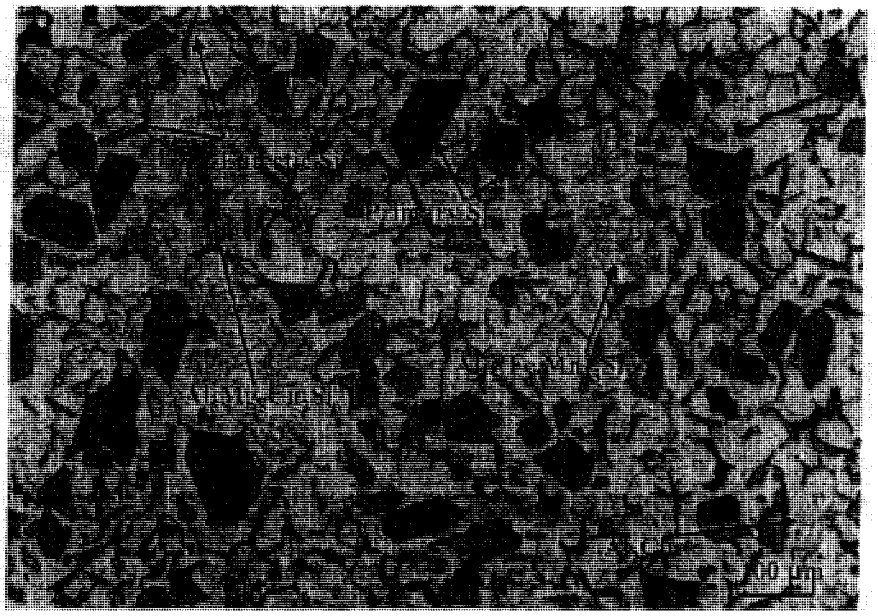

(c)

Fig. 2.2. Typical microstructures of **(a)** hypoeutectic 319, **(b)** hypoeutectic 319 , and **(c)** Hypereutectic A 390 alloy [19].

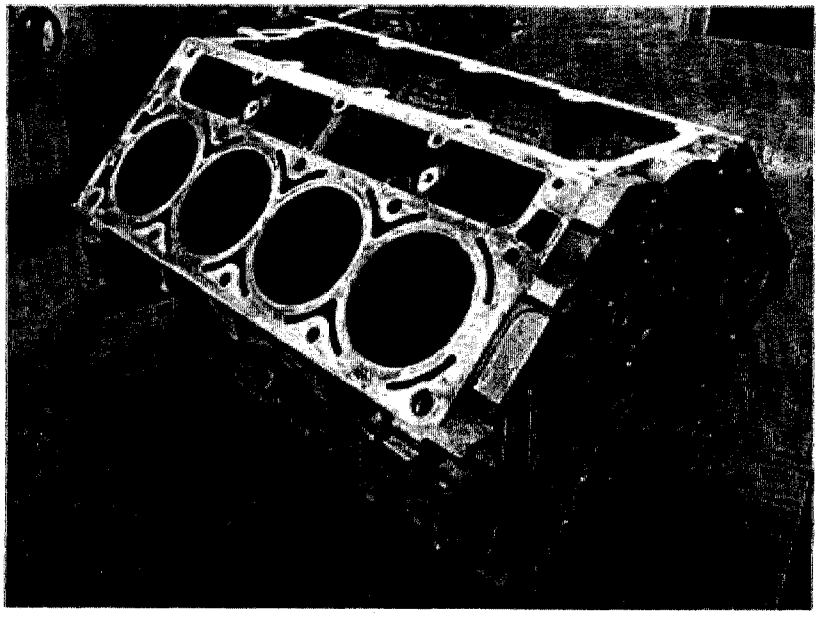

Fig. 2.3. Illustration of a linerless engine block made from an eutectic Al-Si alloy .

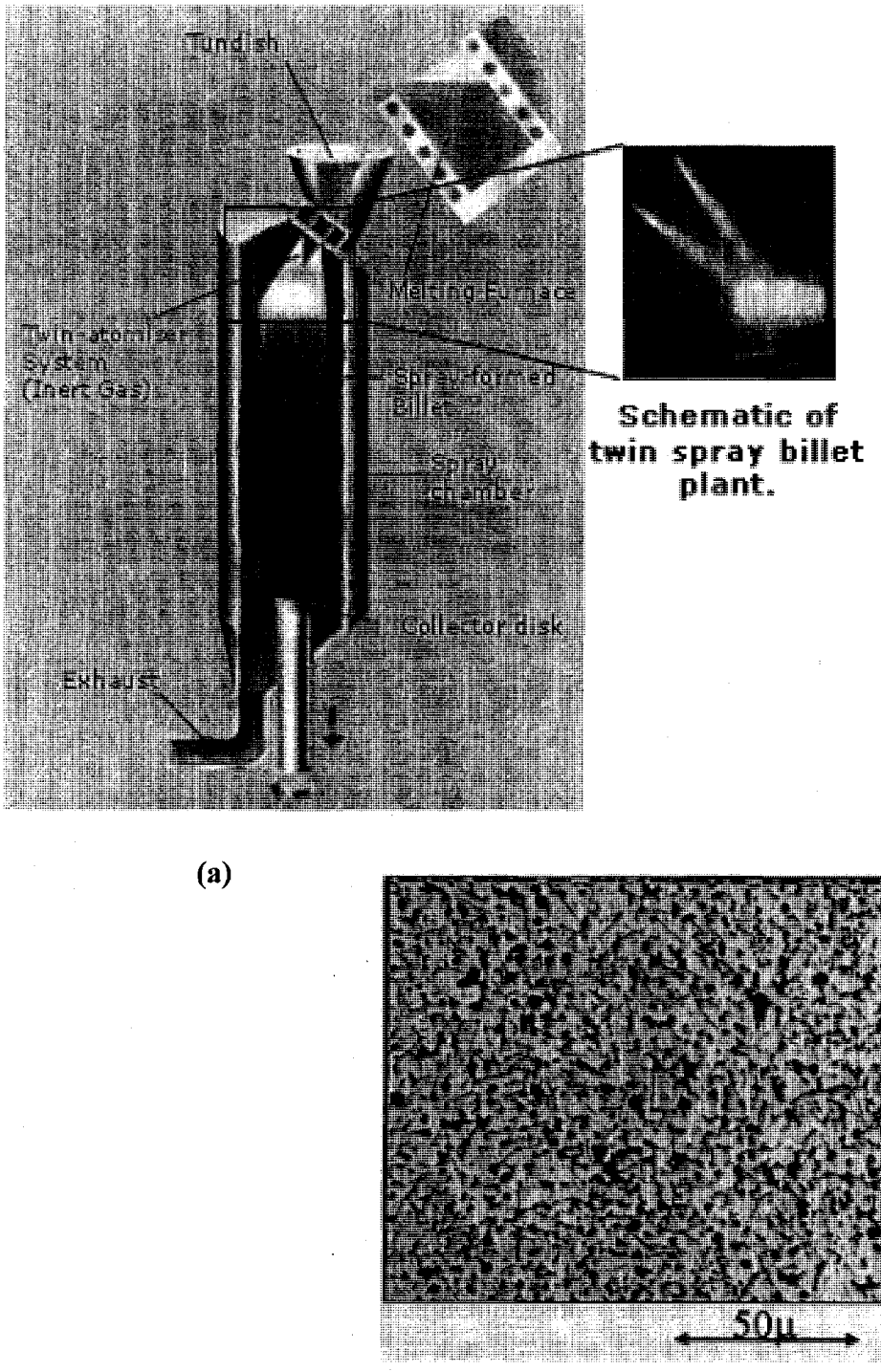

Fig. 2.4. (a) A schematic of Osprey™ spray casting process, and **(b)** and the microstructure of a spray formed hypereutectic Al-Si Alloys (with 21% Si) [30].

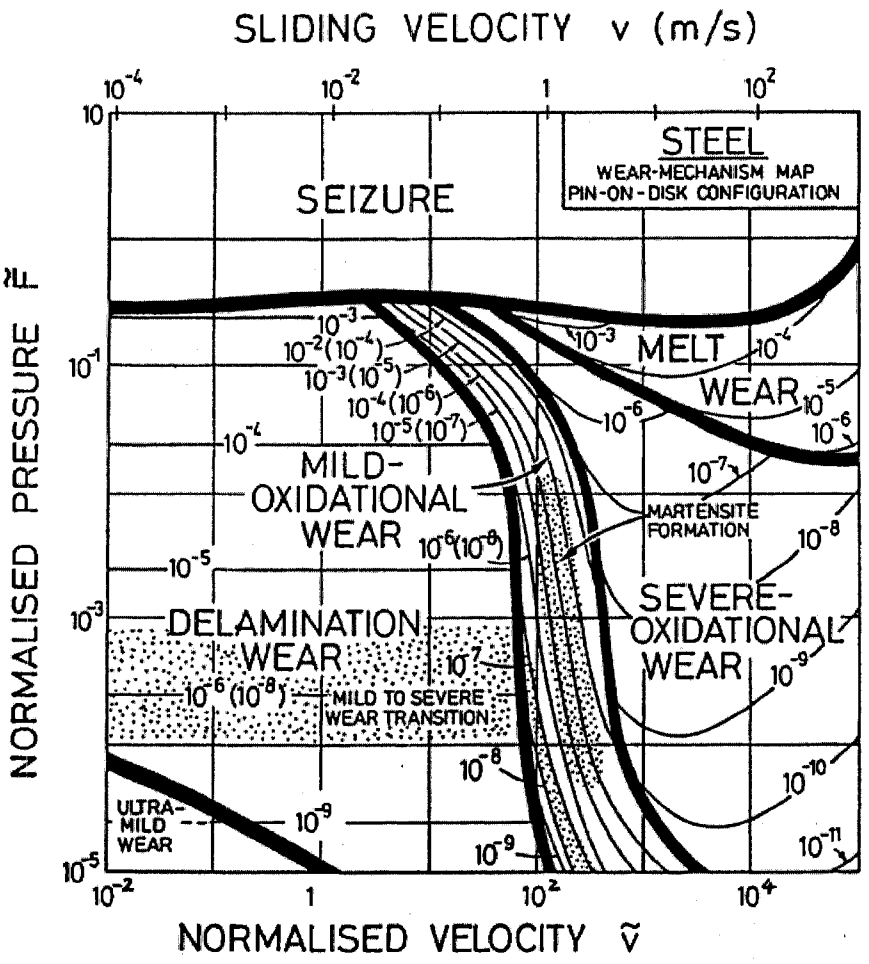

Fig. 2.5. Wear mechanism map for steel [35].

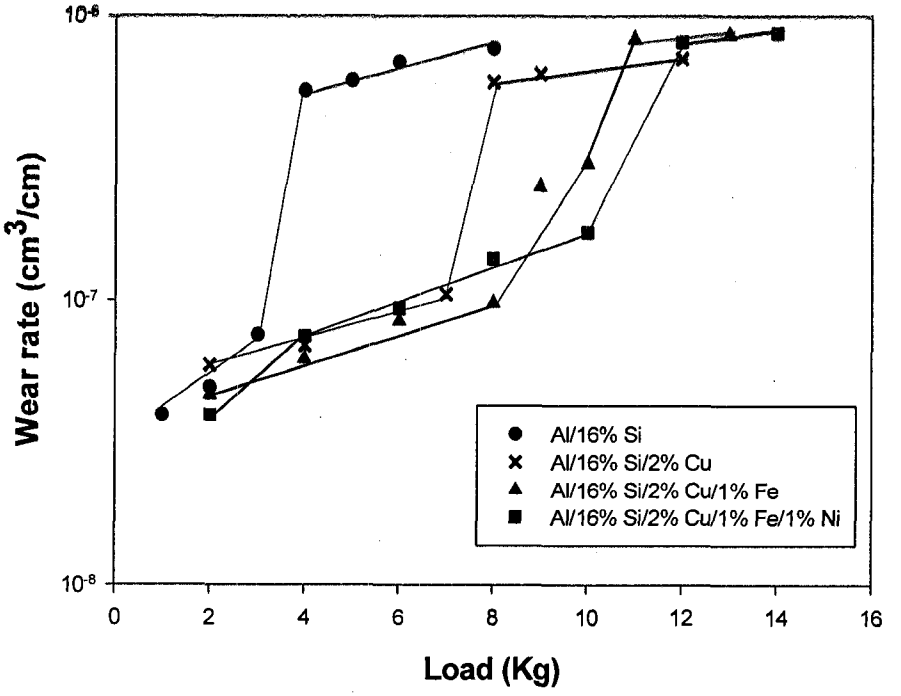

Fig. 2.6. Variations of wear rate of four Al-Si alloys with normal load [4].

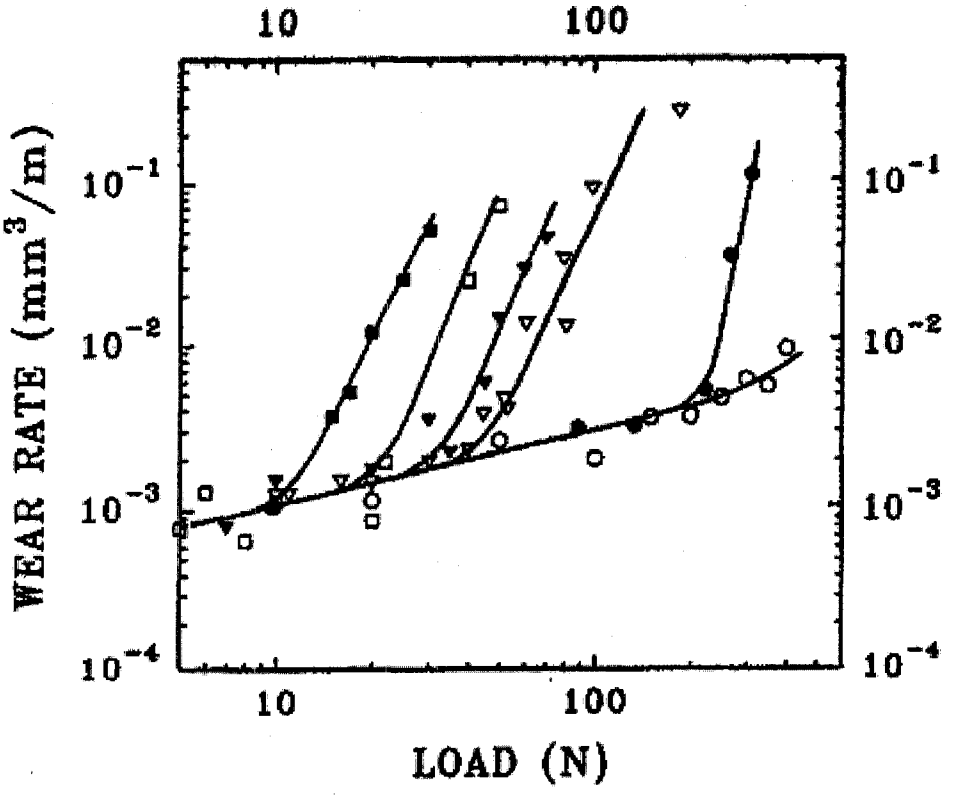

Fig. 2.7. Variation of wear of 6061 aluminum with normal load at different sliding speeds (configuration: ring-on-block, at ambient air) [38].

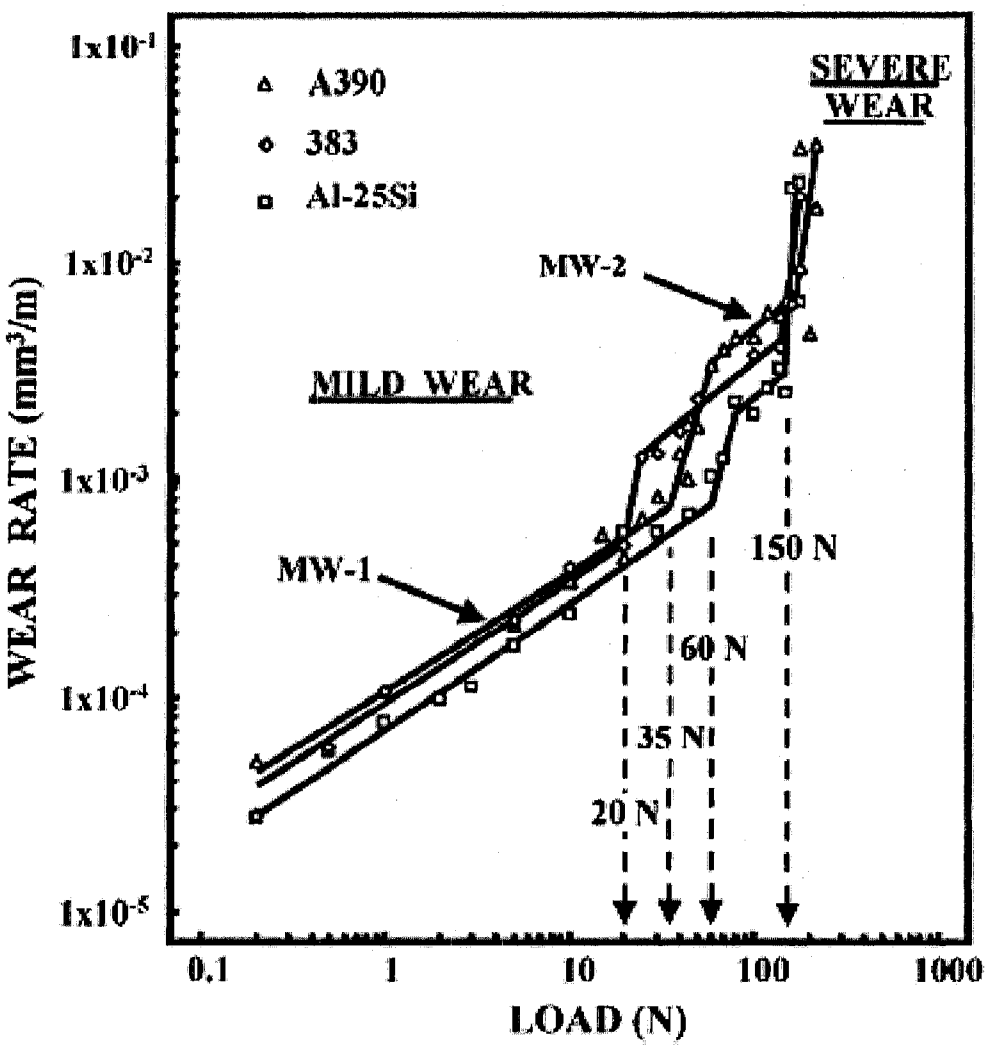

Fig. 2.8. Variation of wear of Al-Si alloys with normal load (configuration: ring-on-block, under controlled dry air environment) [6].

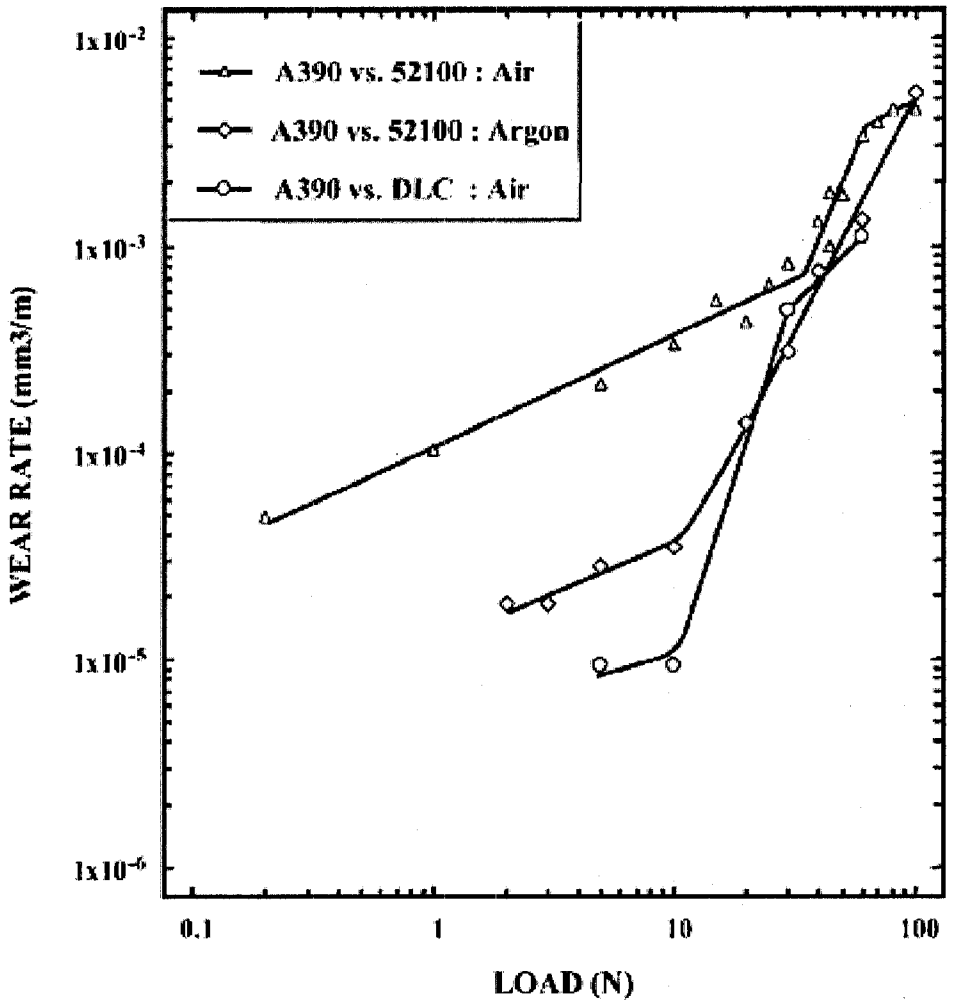

Fig. 2.9. Variation of wear of A390 with normal load showing the effects of environment atmosphere and counterface on wear resistance (Test geometry: ring-on-block, counterface: SAE 52100 steel) [12].

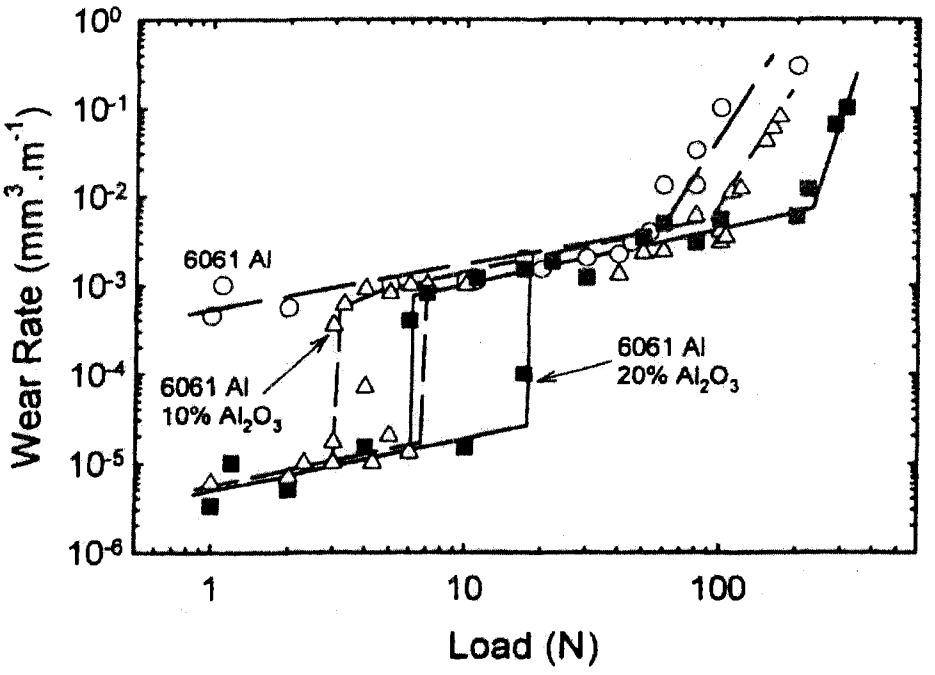

Fig. 2.10. Variations of wear rate with load for Al6061-Al_2O_{3p} MMCs containing 10 and 20 vol.% Al_2O_3 reinforcement, as well as the unreinforced alloy [17].

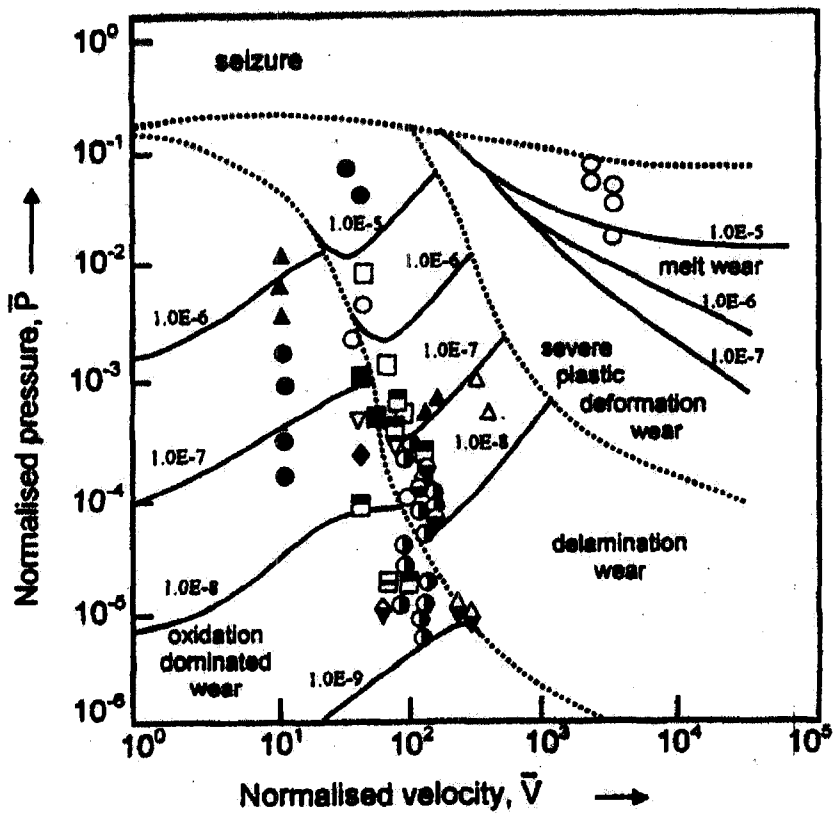

Fig. 2.11. Quantitative wear map for aluminum and aluminum alloys sliding against a steel counterace showing contours of constant wear rates and wear mechanism [46].

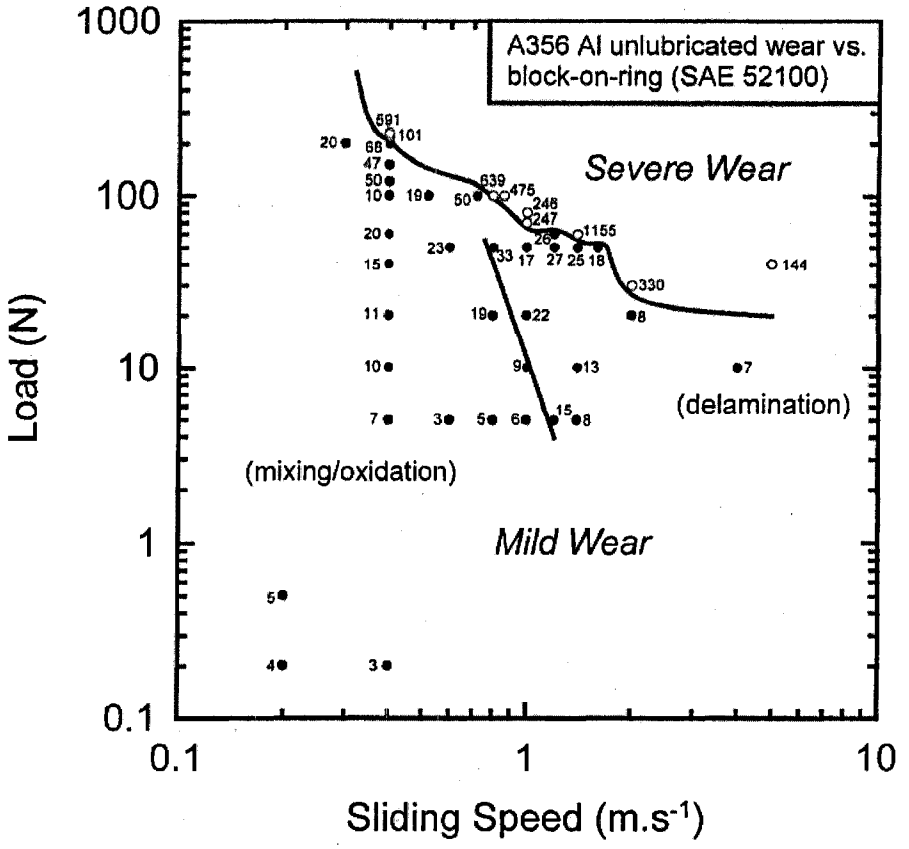

Fig. 2.12. Wear map of A356 worn against SAE 52100 steel (configuration: ring-on-block, in ambient air (Units of the wear rates shown in the map are 10^{-4} mm^3/m) [48].

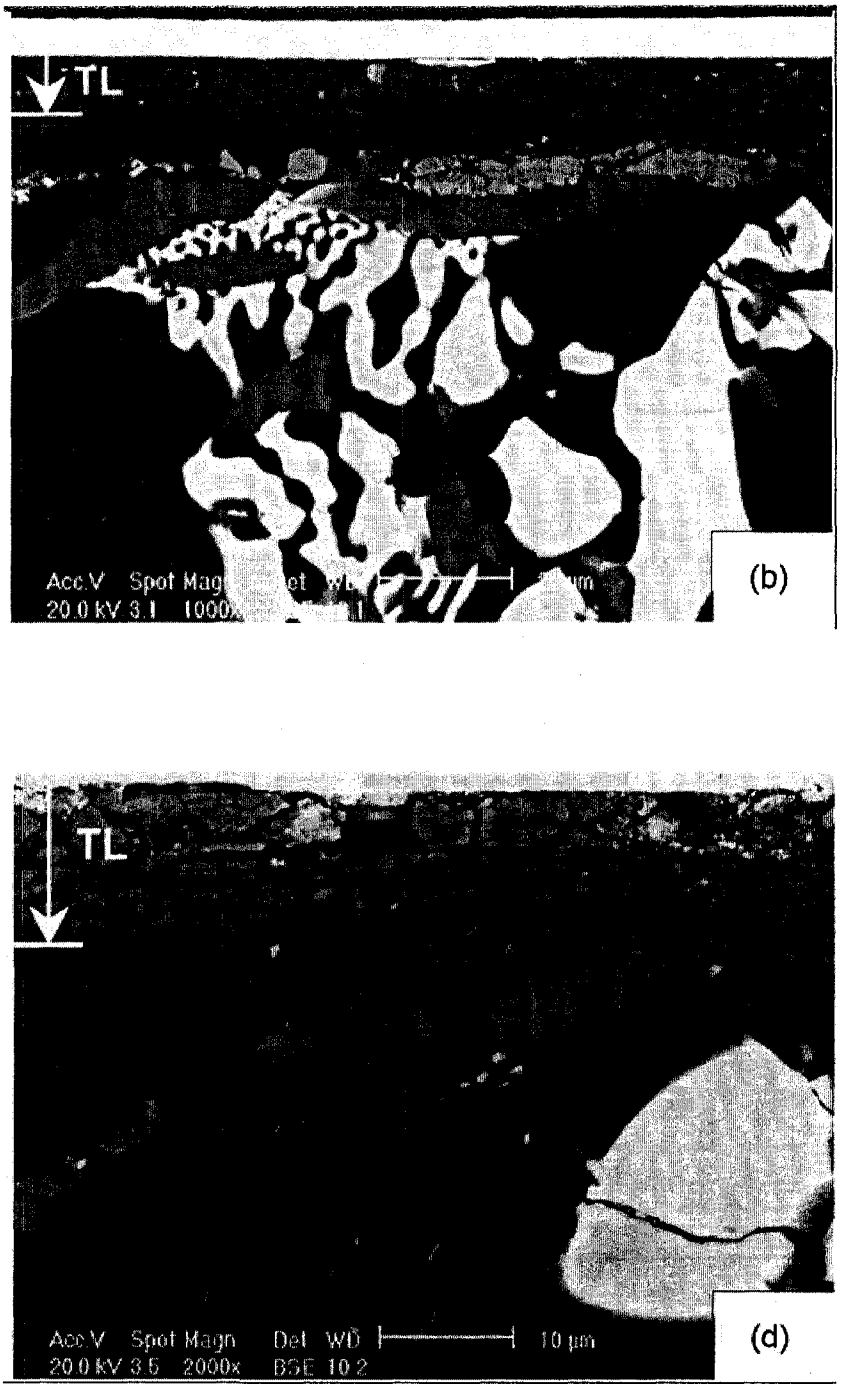

Fig. 2.13. Backscattered SEM images of Tribolayer generated after sliding wear **(a)** in argon atmosphere, and **(b)** in dry air (5% RH) [12].

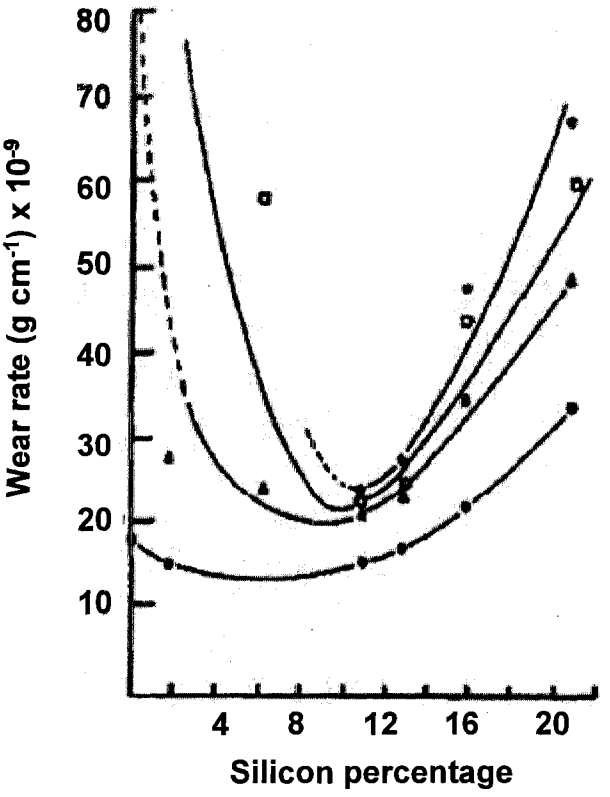

Fig. 2.14. Variation of wear rates of Al-Si alloys sliding against a hard steel bush at a speed of 1.96 m/sec and at a load range of 1 to 2.5 Kg [63].

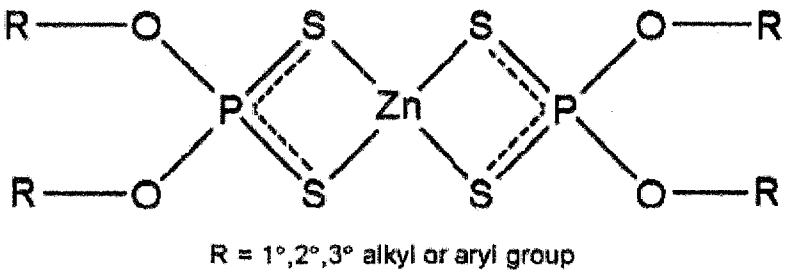

Fig. 2.15. The structure of ZDDP. The R group dictates whether it is an alky- or aryl-dithiophosphate [75].

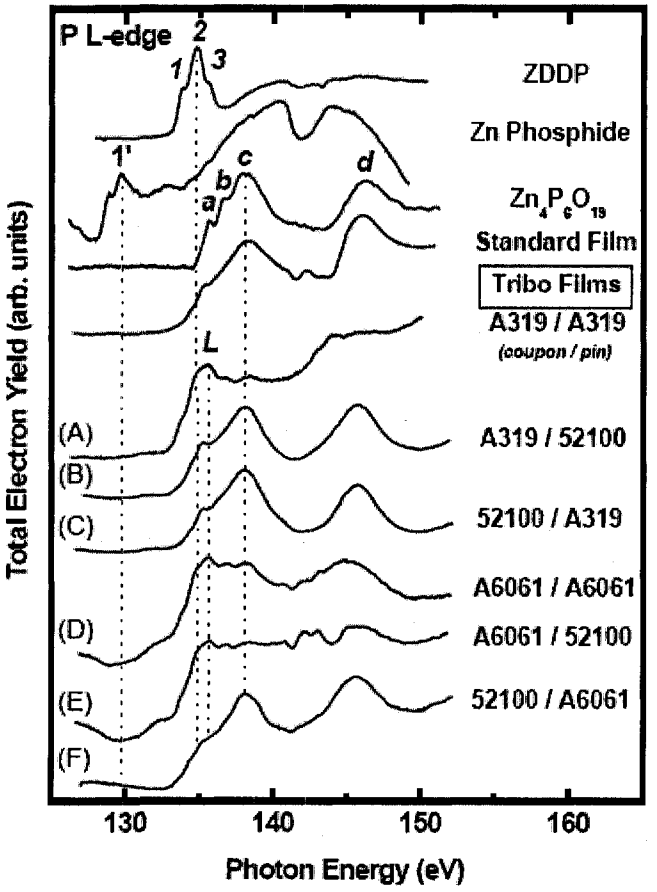

(a)

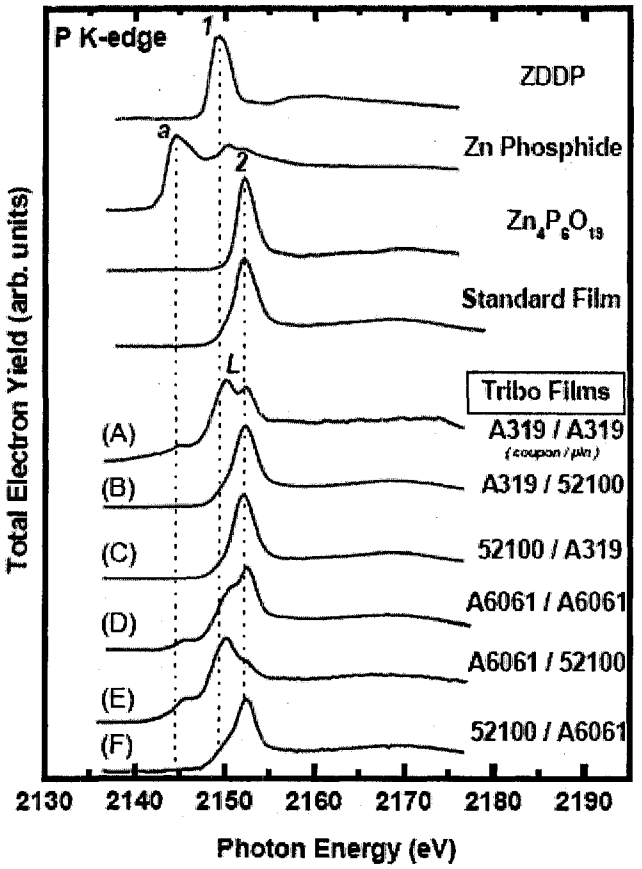

(b)

Fig. 2.16. XANES spectra of model compounds and the ZDDP anti-wear films formed on the coupon of different Al-Si alloy and steel couples. **(a)** P L-edge, and **(b)** P K-edge spectra [89].

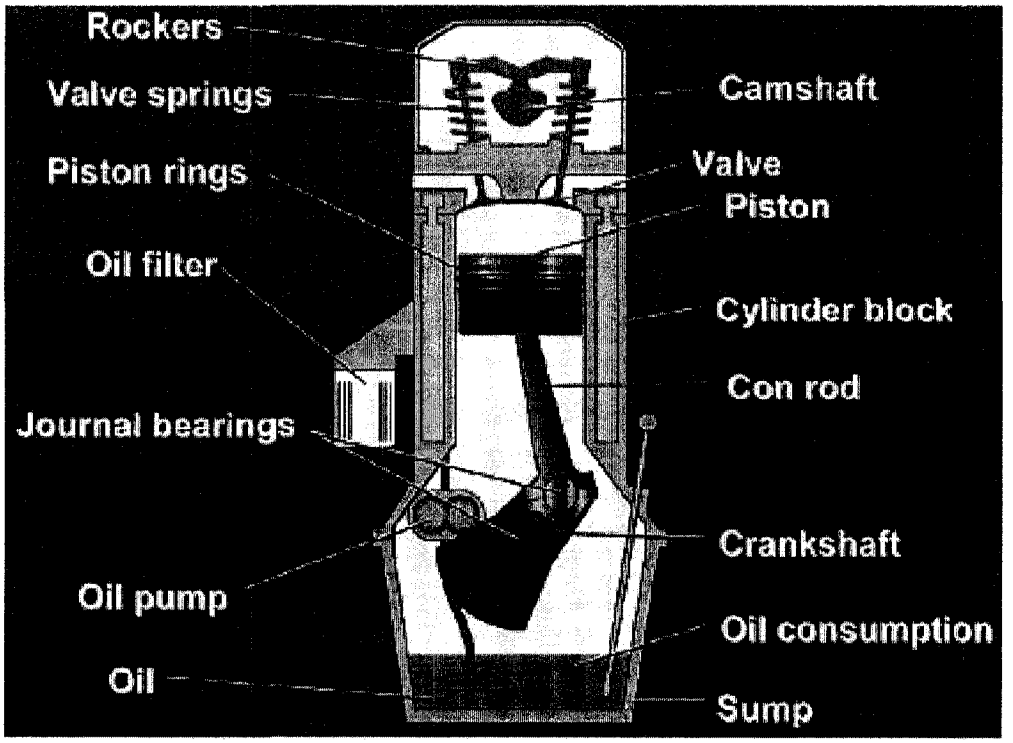

Fig. 2.17. Main engine components in an internal combustion engine [2].

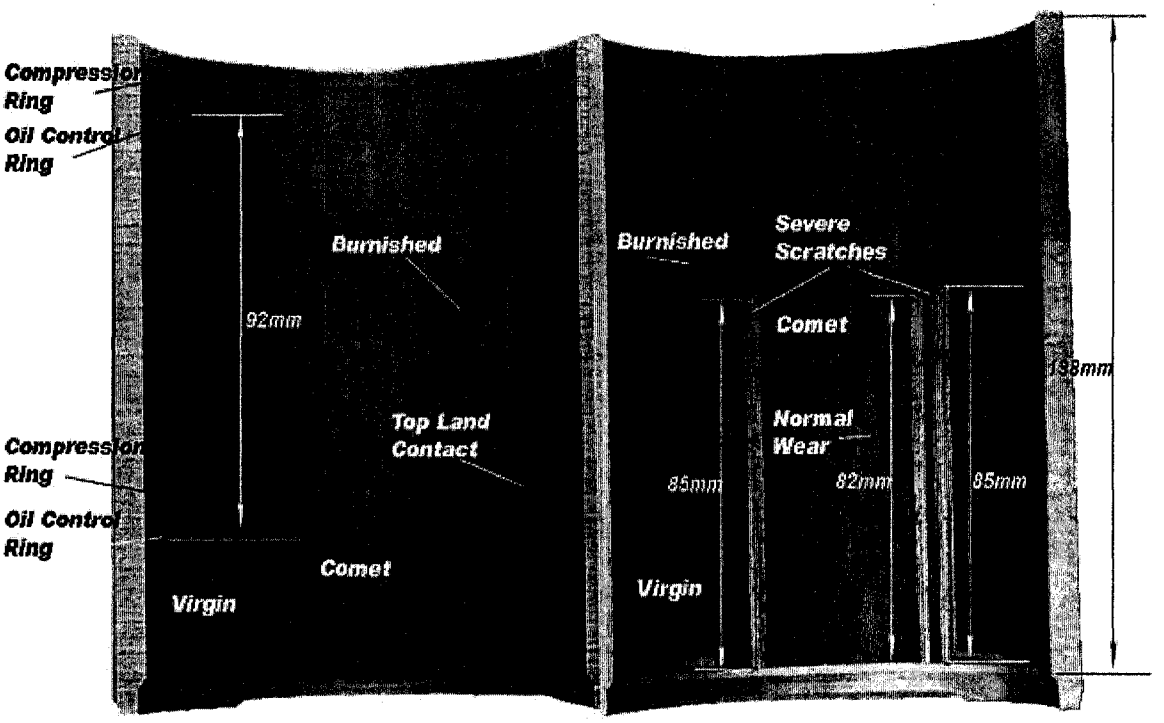

Fig. 2.18. Stereographic photos of the two major and minor surfaces with the indications of different wear zone [11].

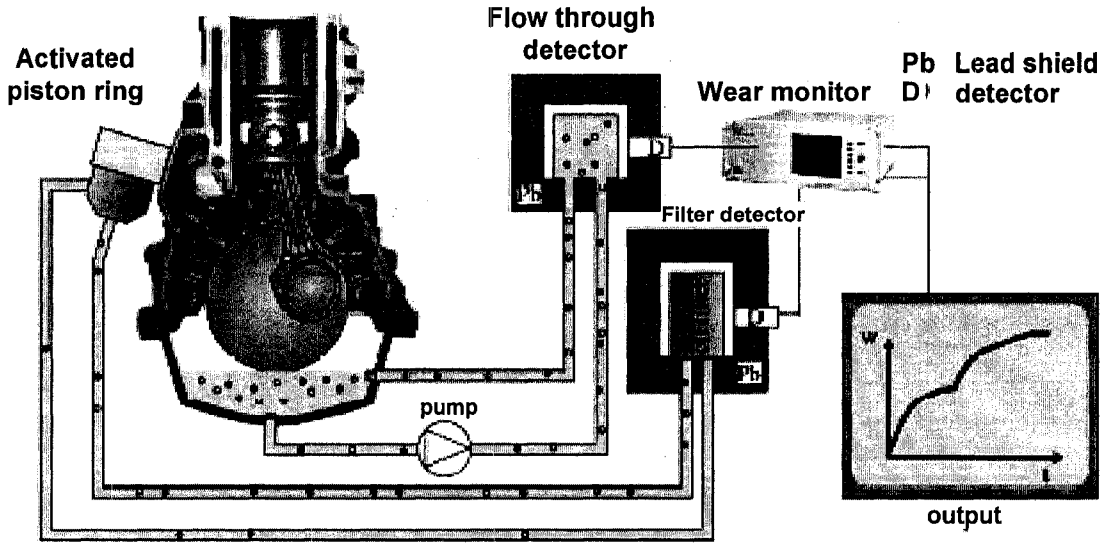

Fig. 2.19. A schematic illustration of RNT technique used to measure engine the wear that occurs to automotive engines [99].

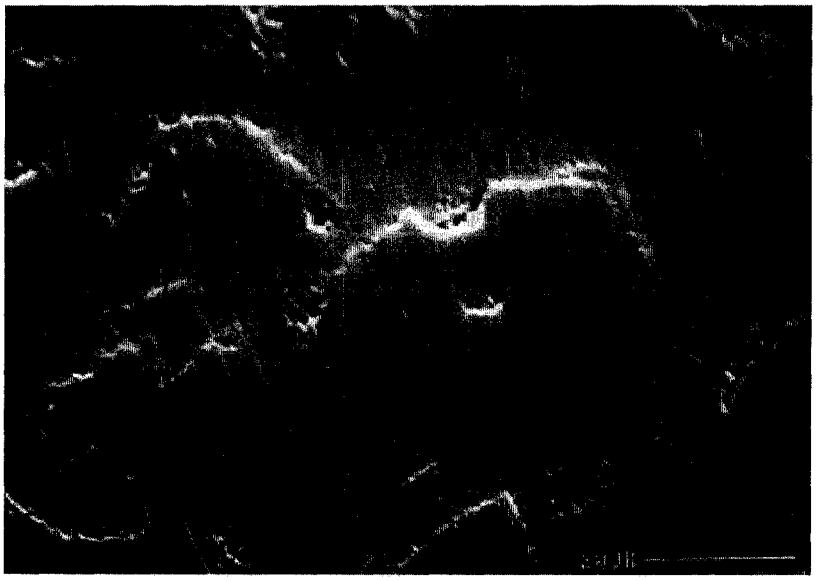

Fig. 2.20. SEM image showing the Si particles stand proud of aluminum matrix on the ALUSIL engine surface [100].

CHAPTER 3 MATERIALS AND EXPERIMENTAL PROCEDURES

3.1. Introduction

In this chapter, the materials tested and the methodology employed in the analysis are described. The sliding wear tests were intended to simulate the surface damage that occurs to engine components under normal running conditions, corresponding to the UMW regime. The micromechanisms leading to UMW damage, as well as the miscrostructual factors controlling the UMW mechanisms, were systematically investigated.

Section 3.2 describes the compositions and hardness of the Al-Si alloys. **Section 3.3** presents the microstructure, the secondary phases identified, and silicon particle sizes and morphology. **Section 3.4** describes all the efforts made to achieve the UMW regime. This section starts with dry sliding tests performed on sand cast eutectic Al-11% Si-C and T6 treated Al-11% Si-C using a ring-on-block machine in ambient air and a humid atmosphere (**Section 3.4.1**). The sliding wear tests conducted using a pin-on-disk tribometer under lubricated conditions, including the test machine, testing procedures, lubrication conditions, and sample preparation, for the wear tests employed to simulate the UMW regime are explained in **Section 3.4.2**.

Section 3.5 describes the procedures developed for the evaluation of the wear test results, including the quantitative determination of the surface damage to silicon particles and aluminum. Finally, **Section 3.6** explains the analytical methods employed in the characterization of the worn surface and subsurface microstructures.

3.2. Al-Si Alloys Tested and Their Properties

The alloys tested in this research included a binary eutectic Al-Si alloy (Al-12% Si, sand cast), two eutectic Al-Si alloys (Al-11% Si, sand cast with different cooling speeds, both are T 7 treated), a hypereutectic alloy (Al-18.5% Si, sand cast), and a spray formed hypereutectic alloy (Al-25% Si). The T 7 heat treatment was a solution treatment at 490°C for 6 hours then a quench in forced air to less than 90°C, cooling at between 80 and 100 degree C /min; followed by aging at 240°C for 4 hours. The alloys were provided by General Motors Research and Development Center in Warren, Michigan, USA (referred as GM R&D Center hereafter in the text) and were used as received. Chemical compositions, in weight %, of the alloys tested are listed in **Table 3.1**. A Brinell hardness tester was used to measure the bulk hardness of the alloys with a 10 mm diameter ball and at a load of 500 kg. A microhardness tester, Buehler Micromet II® (Model 1600-9000) with a square-base diamond pyramid indenter (136 ° tip angle) was used to measure the aluminum matrix hardness. The indentation load applied was 10 g. The bulk and matrix hardnesses of tested alloys are listed in **Table 3.2**. Each value in **Table 3.2** represents an average of at least 10 indentations performed on each sample.

3.3. Microstructures of the Al-Si Alloys Tested

All the samples for the microstructural examination were prepared with conventional grinding and polishing techniques. The samples were wet ground with 180, 240, 400, 600, 1200, and 2400 SiC emery papers successively on a rotating polishing machine. After the final grinding, the samples were polished using 3 and 1 μm diamond suspension, the final polishing was performed using 0.1 μm diamond suspension. The etching for the microstructural observations was performed by immersing the samples

into Graff-Sargent solution, which consisted of 84 ml H_2O, 15 ml HNO_3, 0.5 ml HF, and 3 g CrO_3 for 5 seconds. Quantitative metallographic measurements of the silicon particle size were conducted on an optical microscope, Axiovert 25, equipped with image analysis software. The quantitative microstructual measurements included measurement of the maximum silicon particle length and width. The particle length was determined by measuring the maximum length of each particle parallel to the maximum length, and the particle width was determined by measuring the widest distance across each particle in a direction perpendicular to the direction of the maximum length. About 250 silicon particles were used in these measurements and the results were summarized in the form of a histogram showing the distribution of the silicon particle size. Other measurements of the Si particle morphology included the aspect ratio, sphericity, and area density. The aspect ratio is defined as the average particle length divided by average particle width, and the sphericity is defined by

$$Sphericity = \frac{4 \times \pi \times area}{perimeter^2} \tag{3.1}$$

The sphericity values range between zero and one, in which a value of one corresponds to a perfect circle. The more contours a particle has in its perimeter, the lower the sphericity value it has. The area density of Si particles is defined by the percentage of total area of Si particles divided by the total area analyzed. The average area density was obtained from 8 to 10 measurements from each alloy.

3.3.1. Microstructure of the Al-12% Si Alloy

The optical micrograph shown in **Fig. 3.1** illustrates the morphology and the distribution of the silicon particles as well as the intermetallic phases in Al-12% Si. The

silicon particles in Al-12% Si were plate-like. The histograms in **Figs. 3.2 a** and **b** show the maximum silicon particle length and width. The average value of the maximum silicon particle length in Al-12% Si was 86 ± 50 μm, and the average width was 4 ± 2 μm (**Fig. 3.2**). The silicon aspect ratio was 21 in Al-12% Si. The sphericity measured with the image analysis software was 0.2 ± 0.1. The average areal density of silicon particles was 0.1 ± 0.1. In this alloy, only trace amount of intermetallic phase, $Al_{15}(Fe,Mn)_3Si_2$ was identified, as the EDS spectrum shown in **Fig. 3.3**. The $Al_{15}(Fe,Mn)_3Si_2$ intermetallics appeared to be coarse and script type.

3.3.2. Microstructures of the Two Al-11% Si Alloys

Figure 3.4 presents the morphology and the distribution of the silicon particles, as well as the intermetallic phases in the two alloys. Dramatic differences in the alloy microstructures can be observed, this is due to the differences in the cooling rates of the casting. The alloy with coarse plate-like silicon particles was designated as Al-11% Si-C, and the one with small silicon particles was designated as Al-11% Si-F. The histograms in **Figs. 3.5** and **3.6** show the maximum silicon particle length and width in the two alloys. The average value of the maximum silicon particle length in Al-11% Si-C was 93 ± 46 μm, and the average width was 8 ± 2 μm (**Figs. 3.5 a** and **3.6 a**). The average maximum silicon particle length in Al-11% Si-F was 6 ± 3 μm, and the average particle width was 3.40 ± 1.80 μm (**Figs. 3.5 b** and **3.6 b**). Therefore, the silicon aspect ratio was 12 in Al-11% Si-C and 2 in Al-11% Si-F. The mean sphericity of the silicon particles in Al-11% Si-C was 0.2 ± 0.1 and 0.6 ± 0.2 in Al-11% Si-F. The average areal densities of silicon particles in Al-11% Si-C and Al-11% Si-F were 0.1 ± 0.1 and 0.1 ± 0.1, respectively. The phases in the two alloys, identified using SEM with EDS, were similar,

i.e., eutectic Si, θ-Al_2Cu, and $Al_{15}(Fe, Mn)_3Si_2$. The alloys also had small amounts of $Al_5Cu_2Mg_8Si_6$. The spectra for Al_2Cu, and $Al_5Cu_2Mg_8Si_6$ are presented in **Figs. 3.7 a** and **b**. The $Al_{15}(Fe, Mn)_3Si_2$ intermetallic phase also had a script-type morphology.

3.3.3. Microstructure of the Al-18.5% Si Alloy

The optical micrograph in **Fig. 3.8** shows the microstructure of the Al-18.5% Si, where large (polyhedral) primary silicon particles can be seen. Si particle sizes in terms of maximum length and width are summarized in **Fig. 3.9**. The results indicated that the maximum length = 68 ± 32 μm (**Fig. 3.9 a**), and the average particle width of silicon was 36 ± 16 μm (**Fig. 3.9 b**). The silicon particle aspect ratio was therefore 2 ± 0.4. The sphericity of the Si particles in the alloy measured as 0.5 ± 0.2. The average areal density of silicon particles was 0.2 ± 0.1. The main intermetallic phases were $Al_{15}(Fe,Mn)_3Si_2$ and $CuAl_2$. A small amount of $Al_5Mg_8Cu_2Si_6$ was also detected.

3.3.4. Microstructure of the Al-25% Si Alloy

Al-25%Si samples were cut from the liner insert of a Mercedes engine block. The microstructure of Al-25% Si is shown in **Fig. 3.10 a**, where small silicon particles with an equiaxed shape and a uniform distribution can be seen. The average value of the maximum silicon particle length in the alloy was 8 ± 2 μm, and the average width was 5 ± 2μm (**Fig. 3.11**). Therefore, the aspect ratio of the alloy was 2 ± 0.7. The average value of the sphericity of the alloy was measured as 0.6 ± 0.3. The average areal density of silicon particles was 0.3 ± 0.1. The intermetallic phases identified were $CuAl_2$ and $Al_5Cu_2Mg_8Si_6$, which also appeared to be equiaxed and in the average size of 4.0 μm, as shown in high magnification optical image in **Fig. 3.10 b**.

3.3.5. Summary of the Microstructural and Hardness Analysis of the Tested Alloys

Optical micrographs presented in **Fig. 3.12** show the microstructures of the five Al-Si alloys at the same magnification. The microstructures of the alloys in terms of silicon particle size, morphology, and distribution were different. The results of the matrix hardnesses and quantitative metallographic analysis for the five alloys are summarized in **Table 3.3** for comparison. It can be seen that the silicon particle morphology in Al-12% Si and Al-11% Si-C were similar; they appeared to be plate-like and had similar silicon particle length, and sphericity. But the matrix of Al-11% Si-C was much harder than that of Al-12% Si. The Al-11% Si-C and Al-11% Si-F had similar matrix hardness, but the Si particle size and morphology in the two alloys were dramatically different. Al-25% Si had a similar silicon particle size and morphology with Al-11% Si-F, but the silicon particles in Al-25% Si appeared to be more uniformly distributed, and the average area density (0.25 ± 0.09) was much higher when compared to Al-11% Si-F (0.11 ± 0.1). Al-18.5% Si had block-like large primary Si particles with an aspect ratio of 1.9 and sphericity of 0.48 ± 0.22. Al-18.5% had a harder matrix (85) than the three eutectic Al-Si alloys. Al-25.5 % had the highest average sphericity value (0.52 ± 0.25), area density (0.25 ± 0.09), hardest matrix, and smallest aspect ratio (1.7). Al-12% Si had the softest matrix.

The purpose of selecting the Al-Si alloys with different hardness and microstructure is to examine the effects of matrix hardness and microstructure in terms of Si particle size, morphology, and distribution on the UMW mechanisms and for maintaining UMW-I. Al-12% Si, with the softest matrix, was intended to be tested as the model alloy for the identification of the UMW mechanism, then Al-11% Si-C with a

similar silicon morphology, but harder matrix was tested to examine the effect of matrix hardness on the UMW mechanism. The Al-18.5% Si alloy was tested to examine both effects of matrix hardness and a large block-like primary Si on the UMW mechanism. Al-11% Si-C and Al-11% Si-F, which have comparable hardness and silicon percentage, were tested to investigate the evolution of morphological features with the sliding cycles and applied load. The microstructural factors in terms of Si particle morphology, size, and distribution in the controlling the transition from UMW-I to the UMW-II regime and the propensity of the formation an oil residue layer leading to the attainment of UMW-III , namely, the stabilization of UMW were examined. Al-25% Si was tested to examine the effects of matrix hardness, Si particle distribution, namely, the area density, in delaying the onset of the UMW-II regime, and stabilization of the UMW (facilitating the initiation of UMW-III).

3.4. Achieving UMW

Systematic investigations of the sliding wear of Al-Si alloys performed by Eyre and Shivanath et al. [4, 5] and Elmadagli and Alpas [6] showed that mild wear (MW) involved an over all plastic deformation of Al-Si alloys, and a huge amount of material transfer, or back transfer, at the contact surfaces. Therefore, the wear tracks generated in the MW regime showed gross indentation deformation, and MW generally yielded significant material loss, with a magnitude of $> 10^{-5}$ mm^3/m.

The testing procedures to achieve UMW were, therefore, selected to prevent the contact surfaces from experiencing significant macroscopic plastic deformation, i.e., indentation deformation, material transfer, and measurable material loss.

3.4.1. Dry Sliding Tests

As received sand cast Al-11% Si-C and T6 heat treated Al-11% Si-C intended to increase the matrix hardness were tested using a ring-on-block machine sliding against 52100 steel at a broad range of applied loads from 0.5 to 200 N to obtain a general view of the wear progression in these eutectic Al-Si alloys under dry sliding conditions. The T6 treatment was performed at 480°C solution treated for 8 hours and then aging treated at 193°C for 8 hours. After the T6 treatment, the hardness of the alloy increased to 92 HB. The description of the ring-on-block machine can be found in reference [69].

Fig. 3.13 presents a summary of the wear rate plots of Al-11% Si-C and T6 treated Al-11% Si-C with applied load in ambient air, and also Al-11% Si-C sliding against cast iron tested under a humid air atmosphere of RH 44%. The wear rates in **Fig. 3.13** were measured with a conventional weight loss based method, by measuring the sample weight before and after each wear test. The difference in the weight before and after each wear test was then converted into a volumetric loss using the density of the alloy (2.7 g/cm^3). Like most Al-Si alloys reported so far, a variation of wear rates of Al-11% Si-C and T6 treated Al-11% Si-C with applied load can be divided into two regimes, i.e., 'mild wear' with a wear rate range between 5.29 x 10^{-5} mm^3/m and 6.89 x 10^{-3} mm^3/m, and 'severe wear' with a wear rate range from 6.89 x 10^{-3} mm^3/m to 2.01 x 10^{-2} mm^3/m. Similar to the experimental observations made by Elmadagli et al. [6], the mild wear regime could be further divided into two sub-regimes as shown in **Fig.3.13**. A short transition regime from 20 to 35 N existed for the tested alloys between these two regimes. In comparison with Al-11% Si-C, the T6 treated alloy exhibited better wear resistance in the mild wear regime, the wear rates of T6 treated was about 16% lower than those of Al-

11% Si-C without T6 treatment at each load tested in the mild wear regime. The transition load to the second mild wear sub regime was also delayed by 5 N. The worn surfaces generated from all the sliding tests showed obvious indentation deformation, and material transfer.

The testing condition was changed by increasing atmosphere humidity to 44%, and using cast iron as counterface to further decrease wear rates from the Al-11% Si surfaces to reach the expected UMW regime. The wear rate from the contact surface of Al-11% Si-C sliding against cast iron in humid air in the load range of 0.5 to 2.0 N decreased by 50 % in comparison with that measured in ambient air with a humidity of RH 10% (**Fig. 3.13**). This can be attributed to the graphite in the cast iron counterface, which absorbs water vapor under high relative humidity and has an anti-wear effect. However, the wear rate abruptly increased when the load was greater than 3 N. At 3.0 N, the wear rate was 6.39 $x10^{-4}$ mm^3/m, which was 40 % higher than that the wear rate measured at the same load in dry air. At 7.0 N, the wear rate measured from the alloy surface sliding against cast iron in humid air was 5.25 $x10^{-3}$ mm^3/m, which was close to the wear rates obtained in dry air at 120 N. Similar observations were made by Elmadagli et al. [12] on A 390 (18.5% Si), which was tested in an argon atmosphere and against DLC coated counterfaces. This infers that the maintaining the low wear rate under dry sliding conditions is difficult. This is probably because all the test conditions used do not facilitate the formation of a stable tribolayer, immediate damage to the aluminum matrix starts when the applied load increases.

The material loss rates measured from the Al-11% Si-C alloy sliding against cast iron under a humid atmosphere with RH 44% still belonged to mild wear and severe wear. Therefore, performing laboratory test with different procedures was necessary to

reach the UMW regime. This is given in the **Sections 3.4.2** through **3.4.5.**

3.4.2. Lubricated Sliding Tests

In order to simulate surface damage that occurs to Al-Si engine components under normal running conditions, corresponding to the UMW regime, all the sample surfaces were etched, and the tests were conducted under lubricated conditions, with engine oil as the lubricant. The Al-Si samples had a surface area of 25 mm x 25 mm x 5 mm. The tests were done under constant loads of 0.5, 1.0, and 2.0 N for between 5×10^2 and 6×10^5 sliding cycles. A sliding speed of 50 mm/s was used.

3.4.2.1. Sample Preparation for the Wear Tests

3.4.2.1.1. Etching Treatment

Following the conventional practice for Al-Si alloys in tribological applications, such as engine bores, all samples to be subjected to sliding wear tests in this work were prepared using a chemical etching technique. The purpose of chemical etching is to eliminate direct contact of the aluminum matrix with the counterface by leaving the silicon particle peaks standing proud of the aluminum surface. The polished surfaces were etched in a 10% NaOH solution for 180 s, to expose the top portions of the silicon particles and make them protrude above the aluminum matrix, following the procedure proposed by Riahi et al. [71-72]. They showed that longer etching times (> 420 s) resulted in the easy detachment of particles from the contact surfaces during sliding, and therefore, reduced the scuffing resistance.

3.4.2.1.2. Sample Surface Morphology

An optical surface profilometer (WYKO NT-1100) was used to examine the

silicon particle morphology of the etched surface and to determine a particle height distribution. Typical three dimensional surface profilometer images of a section of the etched five Al-Si alloy surfaces are shown in **Fig. 3.14**. A statistical analysis in the form of a histogram was adopted to determine the average Si particle heights. The histograms were plotted with the software provided with the WYKO NT 1100 profilometer. The elevation profile of the aluminum matrix in areas adjacent to these Si particles was also determined (**Fig. 3.15**). It can be seen that both the aluminum matrix and Si particles on the surfaces to be subjected to sliding wear are not the same height, but varied approximately in the form of Gaussian curves. The separation distance between the aluminum peak and silicon particle peak is the average Si particle height on the surfaces before wear tests. The average silicon particle heights on the initial surfaces were determined from about 100 to 350 silicon particles depending on the silicon particle size, distribution in the tested alloys, and magnification used. **Table 3.4** list the average height of silicon particles on the five etched Al-Si alloys before the sliding tests.

3.4.2.2. Description of Tribometer

All the sliding wear tests were conducted on a pin-on-disc type wear testing machine (CSM tribometer, Switzerland). **Fig. 3.16 a** shows the general view of the experimental set-up. The sample holder, filled with engine oil, is shown in **Fig. 3.16 b**, and the contact geometry, ball-on-disk, is shown in **Fig. 3.16 c**. The tribometer is connected to a computer that controls the sliding speed. The friction force is measured by a built-in strain gauge from the very small deflections of the friction arm. The test duration can be set by the total number of revolutions, sliding distance, or time elapsed. In this research, the test duration was set by the total number of revolutions, i.e., the number

of sliding cycles. The tests were run between 5 x 10^2 and 6 x 10^5 sliding cycles.

A standard test routine was established and followed for each test. First the pin was polished, cleaned with acetone, and installed in corresponding holders attached to the tribometer. The polishing of pins is described in **Section 3.4.2.3**. Then, the diameter of the sliding track was adjusted by turning the knob which moves the friction arm horizontally. The friction arm is built with a position sensing capacity so that the sliding track diameter can be displayed on the computer. Both the friction arm and disc holder were leveled horizontally using a pocket level (Starrett® EDP 50570) for precise loading. The test load was applied on top of the pin holder. After all the test information (load applied, sliding speed, test duration) were keyed into the computer program, the test was started.

3.4.2.3. Counterface Materials

In this research, all the Al-Si alloys were tested against 6 mm diameter AISI 52100 grade steel balls with the following composition (wt%): 0.98 to 1.1 % C, 0.25 to 0.45 % Mn, 0.15 to 0.30 % Si, 1.30 to 1.60 % Cr, and the balance is Fe. All the balls were polished using 0.1 μm diamond suspension on a polishing machine. During the polishing process, the pin was rotated evenly from left to right and back to forth to prevent the tip of the ball from being flattened. The initial r.m.s roughness value after the polishing was measured with an optical surface profilometer as 0.06 μm. The hardness of the steel balls was measured with a microhardness tester as HV25 = 700 at an indentation load of 25 g.

3.4.2.4. Lubrication Condition

Tests were conducted using SAE 5W-30 grade synthetic engine oil (Mobil). As

the following analysis shows, the tests were done under boundary lubricated conditions. The ratio (λ) of minimum lubricant film thickness, $h_{\min}$, to the r.m.s roughness of the two surfaces, σ^*, in contact defines the severity of asperity interactions in lubricated sliding

$$\lambda = \frac{h_{\min}}{\sigma^*} \tag{3.2}$$

$h_{\min}$ can be estimated using [101]

$$h_{\min} = 1.79 R^{0.47} \alpha^{0.49} \eta_0^{0.68} U^{0.68} (E^*)^{-0.12} W^{-0.07} \tag{3.3}$$

Where E^* = 59 GPa, is the composite elastic modulus, calculated using

$$\frac{1}{E^*} = \left[\frac{\left[1-(\nu_{Al-Si})^2\right]}{E_{Al-Si}} + \frac{\left[1-(\nu_{steel})^2\right]}{E_{steel}} \right] \tag{3.4}$$

Al-Si alloys are considered as a two component material with Si particles as reinforcements. The composite elastic modulus, E_{Al-Si}, is, therefore, calculated using

$$E_{Al-Si} = E_{Si} w_{Si} + E_{Al}(1 - w_{Si}) \tag{3.5}$$

where w_{Si} designates the weight fraction of silicon phase. $\nu_{Al-Si} = \nu_{Si} w_{Si} + \nu_{Al}(1 - w_{Si})$ is the Poisson's ratio of Al-Si alloys. U is the sliding speed (50 mm/s), W is the normal load (0.5, 1.0, and 2.0 N), and R is the radius of the counterface ball (3mm), α and η_0 are viscosity constants of the oil and are related to each other by the following relationship [102]

$$\alpha \approx (0.6 + 0.965 \log_{10} \eta_0) \times 10^{-8} \tag{3.6}$$

Table 3.5 lists the parameters used for the calculation of $h_{\min}$. σ^* is calculated using

$$\sigma^{*2} = R_{q1}{}^2 + R_{q2}{}^2 \tag{3.7}$$

where R_{q1} and R_{q2} are the r.m.s roughness values for the Si particle surfaces and steel ball surface measured with a surface profilometer, since for the current system the contact is made between the Si particles and steel ball. h_{min} and the corresponding λ values were calculated using these parameters, and are also listed in **Table 3.5**. Accordingly, calculated λ values for the alloys tested at the applied loads of 0.5 to 2.0 N were smaller than 1, indicating that all sliding tests satisfied boundary lubricated conditions. It follows that direct contact between Si particles and the counterface happens under the current test conditions. Si particles inside the contact area, therefore, carry the applied load.

3.5. Quantitative Measurement of Wear Damage to the Al-Si Alloys

3.5.1. Quantitative Determination of the Damage to Silicon Particles

All the initial surfaces were etched to make the silicon particles stand proud above the aluminum matrix; quantitative analysis of the silicon particle height change was one way to evaluate surface damage in the UMW regime. It was achieved by statistical analyses of the surface profilometer images taken from the wear tracks, which show the variations of height distributions of the silicon particles with respect to the aluminum matrix after stopping the wear tests at various sliding cycles.

To determine the silicon particle height change with the sliding cycles, a sub-region including only the wear track was selected from a surface profilometer image after sliding for various cycles, as shown in **Fig. 3.17**. Then from the selected region, a histogram showing the silicon particle height distribution with respect the aluminum matrix adjacent to these silicon particles was determined. The average silicon particle height at each sliding cycle was determined from four different evenly spaced locations inside the wear track, which totally included about 20 to 30 silicon particles in Al-12% Si,

Al-11% Si-C, and Al-18.5% Si. These alloys had large silicon particles. In Al-11%Si-F and Al-25% Si with fine silicon particles, the average silicon particle heights were determined from about 200 silicon particles inside the wear tracks. The widths of the areas inspected were approximately equal to the wear track widths.

It should be noted that either embedding of Si particles into aluminum or wear of the tops of Si particles changes the Si particle height. The Si particle peak and the aluminum matrix peak merge into a single peak, when Si particles are completely embedded into the aluminum matrix. Each specific location on the contact surface makes contact with the counterface once during each sliding cycle; sinking-in of the Si particles into the aluminum matrix is a cumulative process. Therefore, plastic deformation of the aluminum matrix around the sunken-in particles, as well as working hardening, will affect the Si particle height change data. A sharp decrease followed by a gradual reduction in the Si particle height with increasing sliding cycles is expected.

3.5.2. Measurement of Volumetric Wear from the Aluminum Matrix

Under the loading conditions used in the sliding experiments neither the mass of debris particles nor material loss from the contact surface was large enough to be measured using a high sensitivity electronic balance that can measure weights as small as 10^{-5} g. This is a typical feature of the ultra-mild wear regime of Al-Si alloys tested using a pin-on disc geometry. An alternative method for the estimation of very small quantities of volumetric wear loss was developed and used. This method was based on the measurement of certain wear features using an analytical optical interference microscope. Material loss has been observed to be associated with the formation of long grooves, extending on the contact surfaces in the sliding direction and in particular on bulged out

portions of the aluminum matrix (aluminum pile-ups). Thus, the volume loss of material for a given number of sliding cycles is defined as the cross-sectional area (removed area) that falls below the reference position (indentation) of the elevated aluminum matrix multiplied by the perimeter of the wear track. The Si particles were not distributed evenly in the Al-Si alloys tested, as shown in **Fig. 3.12**, which made the surface damage inside the wear tracks not uniform. Therefore, the cross-sectional area was determined by averaging 24 measurements from different locations along the entire wear track. More specifically, **Fig. 3.18** illustrates the method used to measure the volume loss after a given number of cycles. After removing the sample tested to a given number of cycles, the sample surfaces were cleaned with hexane, then 2-D surface profilometer images were taken from eight different, equally spaced locations in the wear tracks, in the order shown schematically in **Fig. 3.18 a**. As an example, **Fig. 3.18 b** shows half of the wear track taken from an Al-25% Si surface after sliding for 3 x 10^5 cycles, at 2.0 N with the areas where the 2-D cross-sectional profilometer images were taken. One of these sections is marked as AA' in the top view of the wear track **Fig. 3.18 c**. As indicated above, three of these sections one 50 μm above one 50 μm below the line AA' were taken. **Fig. 3.18 d** shows the cross-sectional contour taken along AA' in **Fig. 3.18 b**. Taking the average zero value of the instrument as the reference position at each location. The average cross-sectional area of the wear track at a location, j, was determined by

$$A_j = \frac{1}{3}\left(\sum_{i=1}^{k} A_i + \sum_{i=1}^{k} A_i + \sum_{i=1}^{k} A_i\right) \tag{3.8}$$

where A_i is the area below the 0-0 line, which indicates the initial height of elevated aluminum matrix, as shown in **Fig. 3.18 c**. A_i was measured with the software provided with the optical profilometer. k is the total number of A_i at any given section. The total

average cross-sectional area, A_T, of the whole wear track was determined by

$$A_T = \frac{1}{l}\sum_{j=1}^{l} A_j \tag{3.9}$$

where l = 8 (number of the fields examined). The volumetric material loss, V, was therefore

$$V = 2\pi R_w \times A_T \tag{3.10}$$

where R_w is the radius of the wear track.

As the contact surface is oxidized or covered with a tribo-layer (an oil residue tribo-layer) after longer sliding cycles, some of the scratches formed at low sliding cycles might be filled with oxidized fragments or the layer, the average cross-sectional area will decrease. This will cause the volumetric loss, V, drop accordingly.

3.6. Worn Surface Characterization

Microstructural features of the worn surfaces were examined using a scanning electron microscope (JEOL 5800/EDAX and FEI Nano 200F/EDAX) equipped with an energy dispersive spectroscope (EDS), and a digital optical microscope (Keyence VHK 600K). Surface profilometer images were taken using a non-contact optical interference microscope.

Site-specific cross-sectional microstructural observations of the wear tracks were performed using a focused ion beam microscope (FIB, FEI Nova 200 at the University of Michigan or FEI Nova Nanolab at the University of West Ontario) and a TEM (Philips EM430) located at GM R&D Center. First, a cross-sectional slice of approximately 3 mm thick was cut from the portion of the wear track. Then the cut section was prepared using conventional mechanical pre-thinning for FIB/SEM and TEM investigations. The

preparation of the cross-sectional TEM samples was carried out using the H-bar FIB milling method [103]. First, a pre-thinned cross-sectional slice (approximately 20 μm thick and 20 μm wide) was mounted onto a TEM grid using an epoxy adhesive and allowed sufficient time to cure. The mounted slice was then mechanically polished to less than 100 nm to reduce FIB milling time. A platinum layer was deposited on the top surface of the sample to prevent beam damage during ion milling. Finally, the polished specimen was loaded into a FIB microscope for precise ion beam thinning. During the FIB milling process, some cross-sectional images of the area of interest were taken by controlling the location of the ion beam to reveal the cross-sectional structure of interest.

The chemical compositions of the oil residue layer generated during lubricated sliding contact were characterized with a PHI-5702 multi-functional X-ray photoelectron spectrometer (XPS), using a pass energy of 29.35 eV, an excitation source of Mg-Kα radiation (hv = 1253.6 eV), and a take-off angle of 35°. The chamber pressure was about 3×10^{-8} Torr. The binding energy of contaminated carbon (C1s: 284.8 eV) was used as a basic reference. The morphology of the generated layer was examined using a CSPM4000 atomic force microscope (AFM) in tapping mode.

The mechanical properties of the oil residue layer were evaluated with a MTS Nano indenter XP located at GM R&D. The hardness of the worn surfaces where an oil residue layer was assumed to be formed was measured and compared with the initial surface from recorded load-displacement curves using the analysis methods developed by Oliver and Pharr [104]. The indentation depth was set as 200 nm. Four indentation tests were performed on each selected field of interest at 50 μm apart to obtain an average value of the hardness. The test data was processed with the software provided with MTS Nano indenter XP.

Table 3.1. Chemical compositions in wt % of the Al-Si alloys studied.

Alloy	%Si	%Cu	%Fe	%Mg	%Mn	%Ni	%Sr	%Ti	%Zn	Bal.
Al-11% Si	11.2	2.2	0.5	0.26	0.8	0.01	0.016	0.06	0.02	Al
Al-12% Si	12.1	0.03	0.01	<0.01	0.01	<0.01	<0.005	<0.01	0.01	Al
Al-18.5% Si	18.4	4.0	0.23	0.57	0.07	0.02	<0.002	0.05	0.1	Al
Al-25% Si	25.0	4.0	0.21	1.12	<0.01	<0.01	<0.002	0.01	<0.01	Al

Table 3.2. Bulk Hardness and aluminum matrix hardness of the alloys tested

Alloy	Al-11% Si-C	Al-11% Si-F	Al-12% Si	Al-18.5% Si	Al-25% Si
Bulk Hardness (HB)	79 ± 2	79 ± 2	40 ± 2	97 ± 7	102 ± 4
Matrix hardness (Kgf/mm^2)	68 ± 13	67 ± 12	50 ± 2.50	85 ± 8	110 ± 20

Table 3.3. Summary of the matrix hardness and quantitative metallurgical measurement on Si particle size, morphology, and area density in the five alloys tested

Alloy	Matrix hardness (Kgf/mm^2)	The maximum Si particle length (μm)	Aspect ratio	Sphericity	Area density (%)
Al-12% Si	50 ± 3	86 ± 50	21	0.2 ± 0.1	0.1 ± 0.1
Al-11% Si-C	68 ± 13	93 ± 46	12	0.2 ± 0.1	0.1 ± 0.1
Al-11% Si-F	67 ± 12	6 ± 2	2	0.5 ± 0.2	0.1 ± 0.1
Al-18.5% Si	85 ± 8	70 ± 30	2	0.5 ± 0.2	0.2 ± 0.1
Al-25% Si	108 ± 20	8 ± 2	2	0.5 ± 0.3	0.3 ± 0.1

Table 3.4. Initial silicon particle height on the five etched Al-Si alloys

Alloy	Al-12% Si	Al-11% Si-C	Al-11% Si-F	Al-18.5% Si	Al-25% Si
Initial Height (μm)	1.8 ± 0.3	1.6 ± 0.2	1.7 ± 0.3	1.6 ± 0.2	1.8 ± 0.4

Table 3.5 Parameters used to calculate λ and h_{min} in **Equations 3.2** and **3.3.** (See the text for the definition of the terms.)

Alloy	E_{steel} **(GPa)**	E_{Al} **(GPa)**	E_{Si} **(GPa)**	η_0 **(mPa.s) 20°C**	**α (Pa^{-1})**	R_{q1} **(μm)**	R_{q2} **(μm)**	W **(N)**	h_{min} **(μm)**	**λ**
Al-12% Si	210	70	107	200	2.82×10^{-8}	0.06	0.15	0.5 1.0 2.0	0.088 0.084 0.080	0.54 0.52 0.50
Al-11% Si-C	210	70	107	200	2.82×10^{-8}	0.06	0.16	0.5 1.0 2.0	0.088 0.084 0.080	0.51 0.50 0.49
Al-11% Si-F	210	70	107	200	2.82×10^{-8}	0.06	0.15	0.5 1.0 2.0	0.088 0.084 0.080	0.54 0.52 0.50
Al-18.5% Si	210	70	107	200	2.82×10^{-8}	0.06	0.16	0.5 1.0 2.0	0.088 0.084 0.080	0.51 0.50 0.49
Al-25% Si	210	70	107	200	2.82×10^{-8}	0.06	0.10	0.1 0.1 0.1	0.088 0.084 0.080	0.73 0.70 0.66

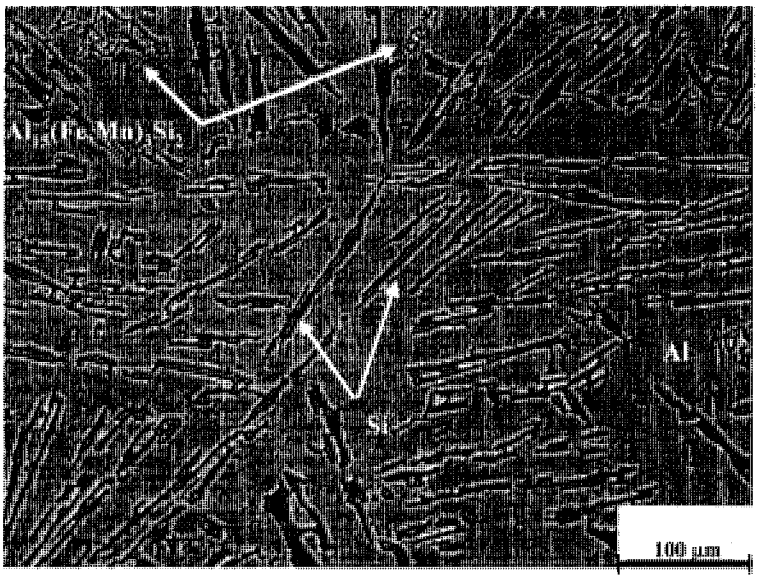

Fig. 3.1. Optical micrograph showing the microstructure in Al-12% Si.

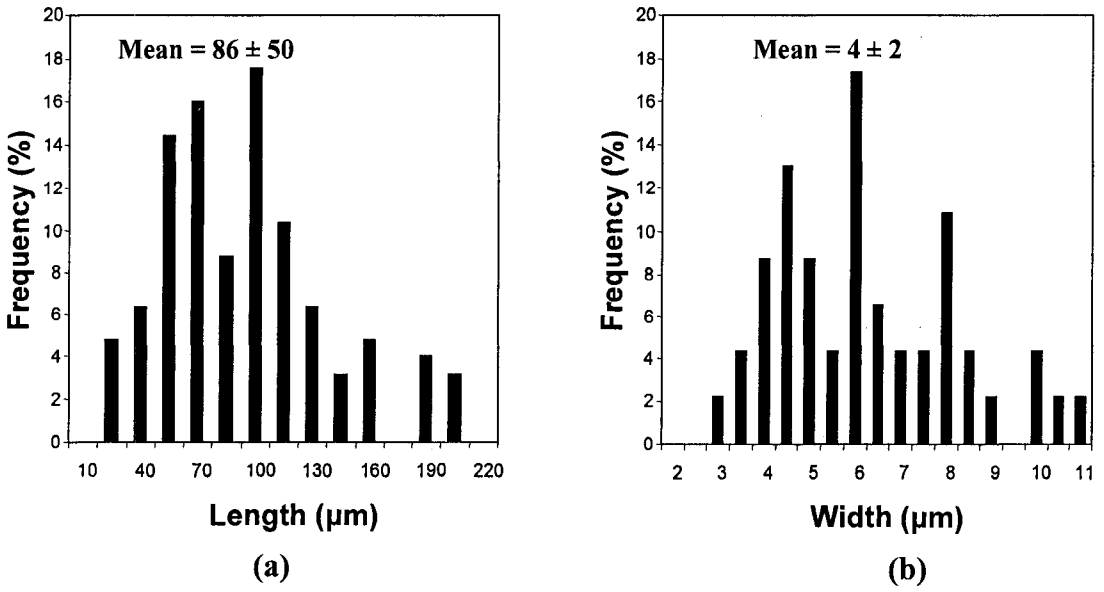

Fig. 3.2. Histograms showing the distribution of silicon particle **(a)** length and **(b)** width in Al-12% Si.

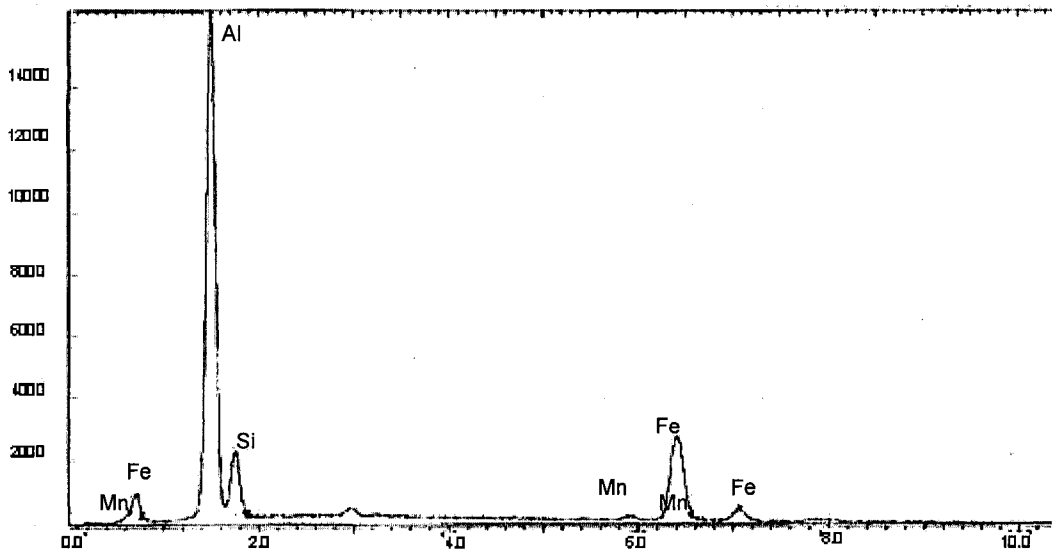

Fig. 3.3. EDS spectrum showing the $Al_{15}(Fe,Mn)_3Si_2$ phase identified in Al-12% Si.

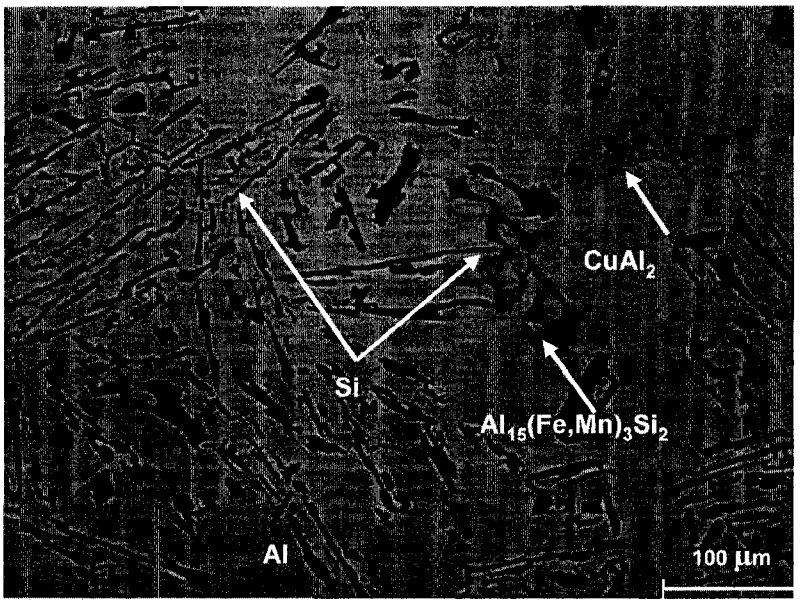

(a)

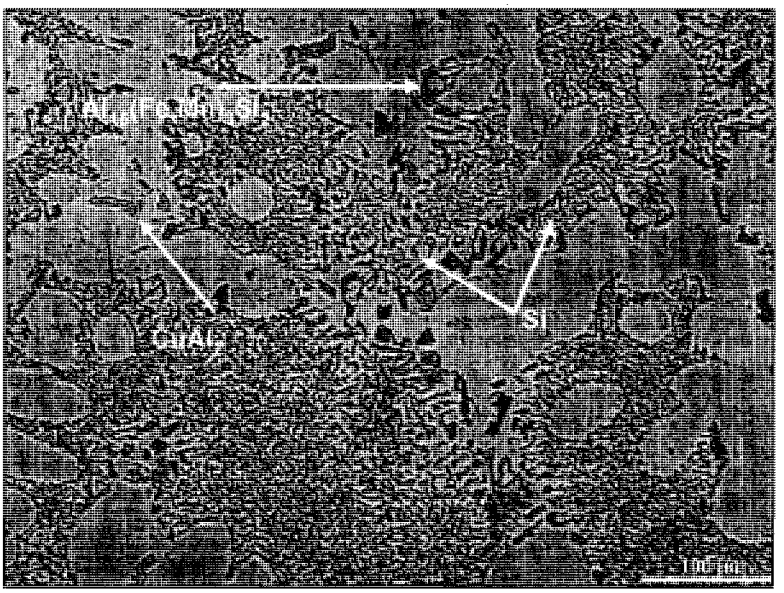

(b)

Fig. 3.4. Optical micrographs showing the microstructures in **(a)** Al-11% Si-C, and **(b)** Al-11% Si-F.

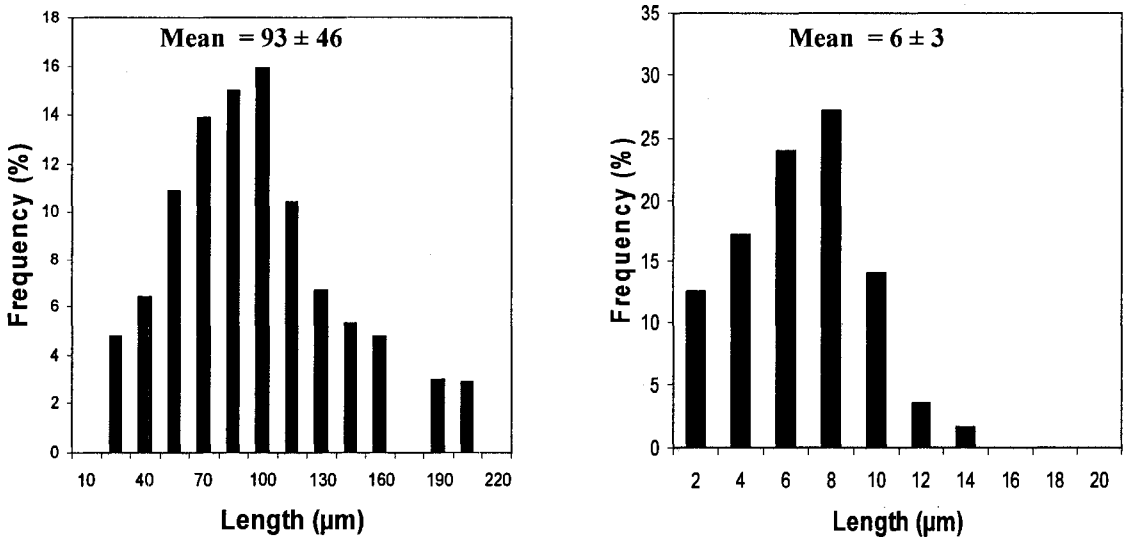

(a) (b)

Fig. 3.5. Histograms showing the Si particle length in **(a)** Al-11% Si-C, and **(b)** in Al-11% Si-F.

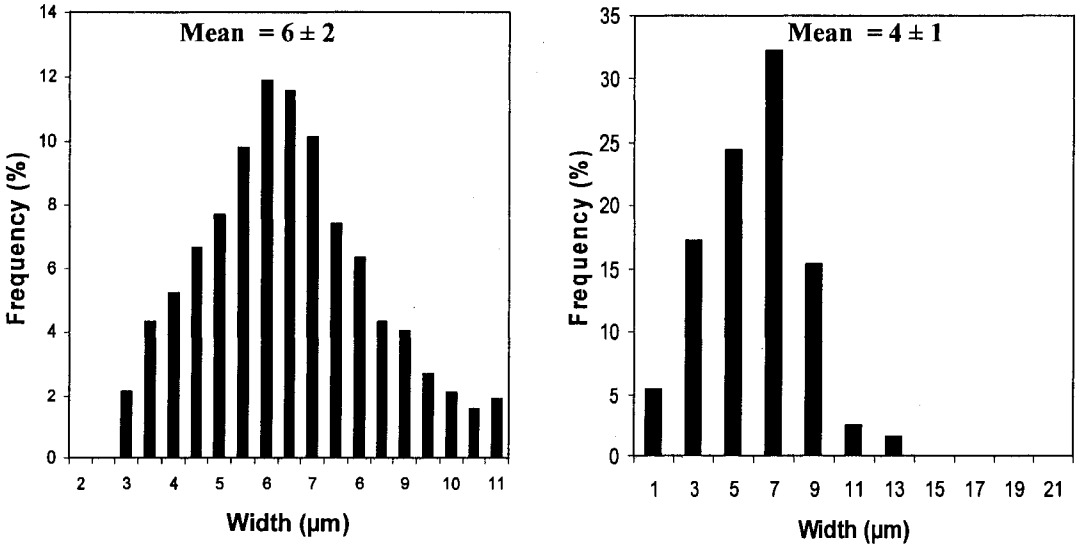

(a) (b)

Fig. 3.6. Histograms showing the Si particle width in **(a)** Al-11% Si-C, and **(b)** in Al-11% Si-F.

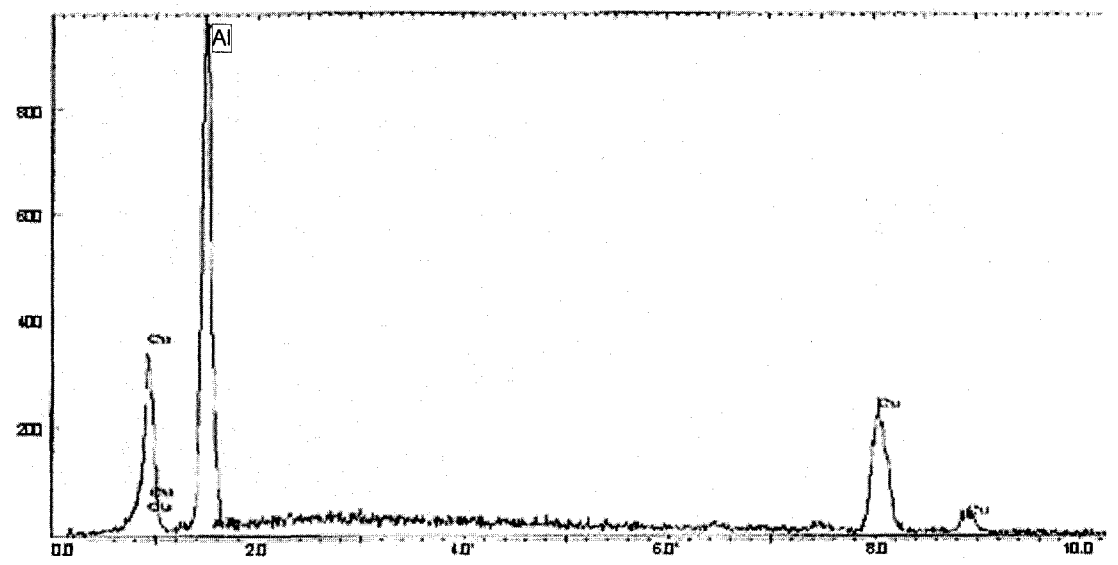

(a)

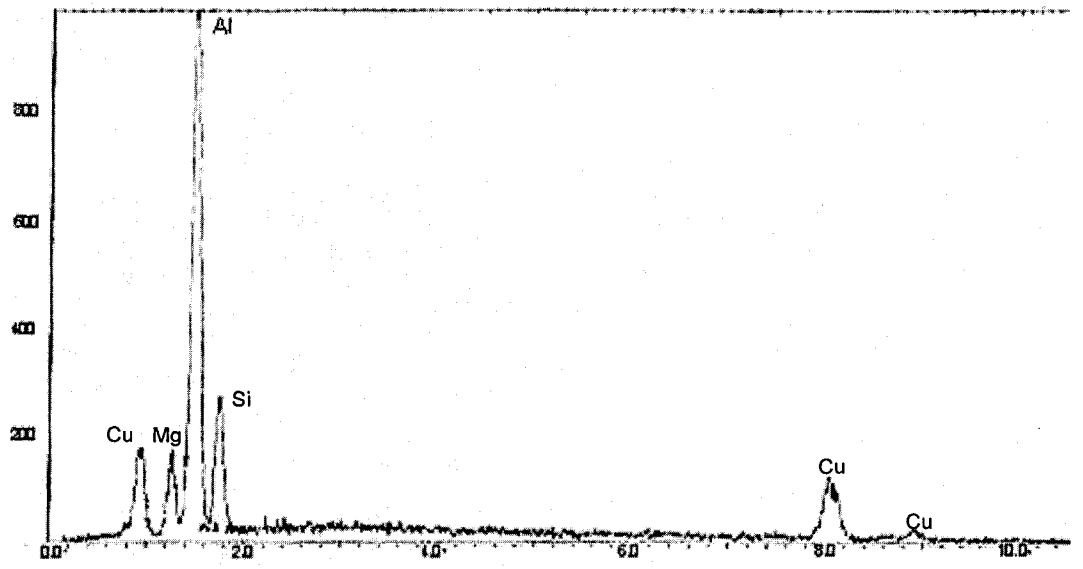

(b)

Fig. 3.7. EDS spectra showing **(a)** Al_2Cu, and **(b)** $Al_5Cu_2Mg_8Si_6$ identified in Al-11% Si-C and Al-11% Si-F.

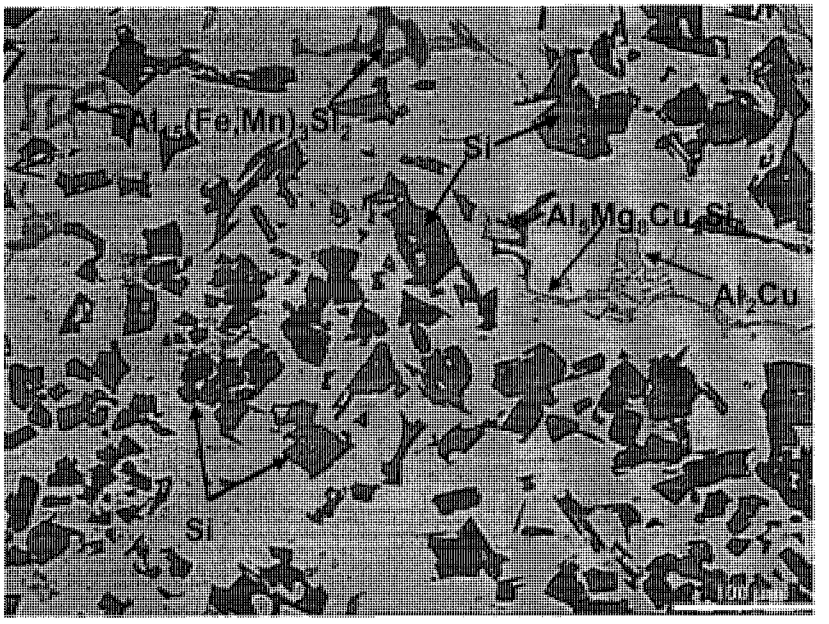

Fig. 3.8. Optical micrograph showing the microstructure in Al-18.5% Si.

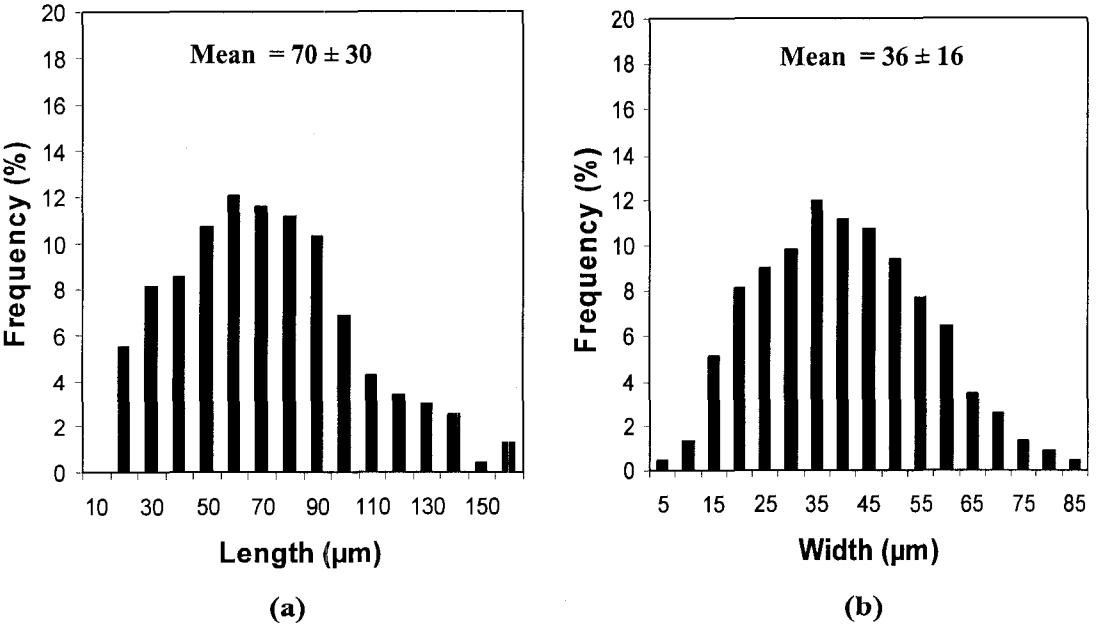

Fig. 3.9. Histograms showing **(a)** silicon particle (maximum) length, and **(b)** silicon particle width in Al-18.5% Si.

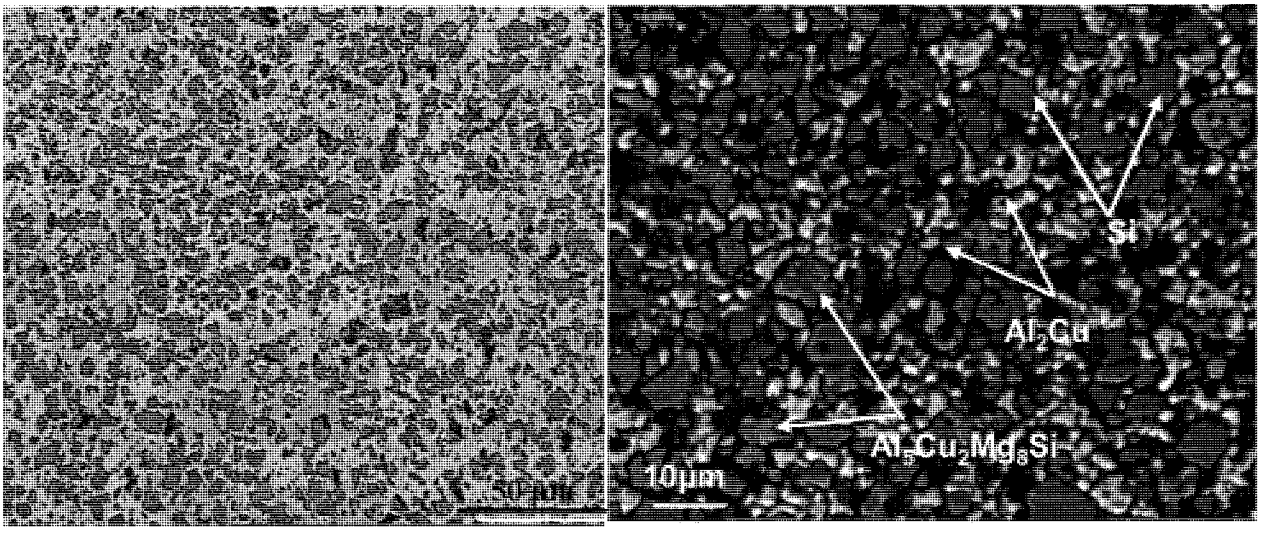

(a) (b)

Fig. 3.10. Microstructure of Al-25% Si **(a)** low magnification optical micrograph, and **(b)** high magnification optical micrograph after etching with 10% NaOH.

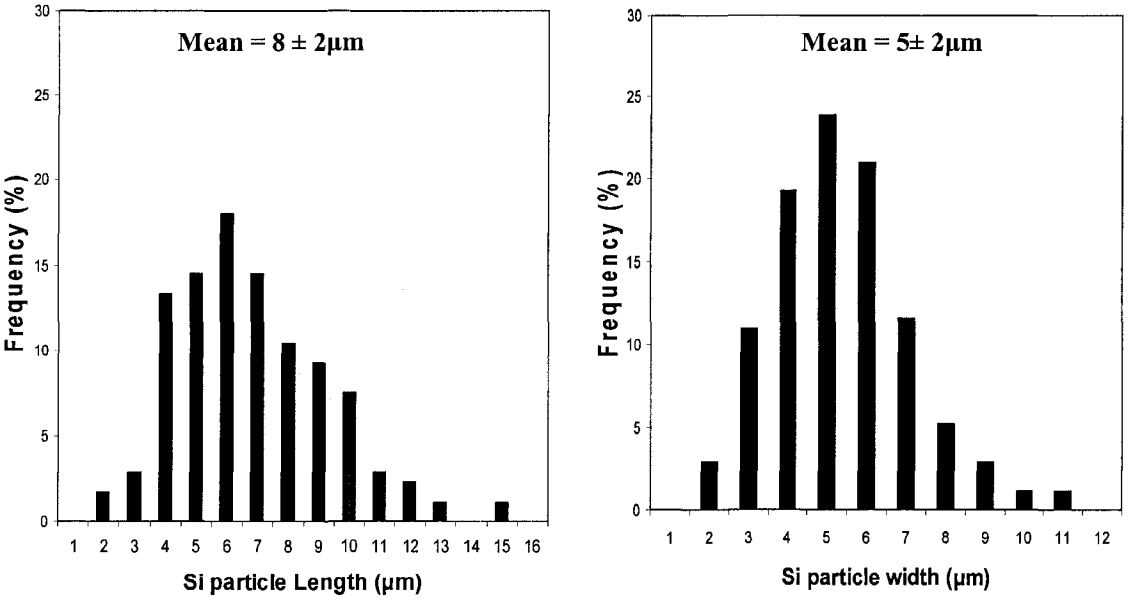

(a) (b)

Fig. 3.11. Histograms showing the Si particle length and width in Al-25% Si.

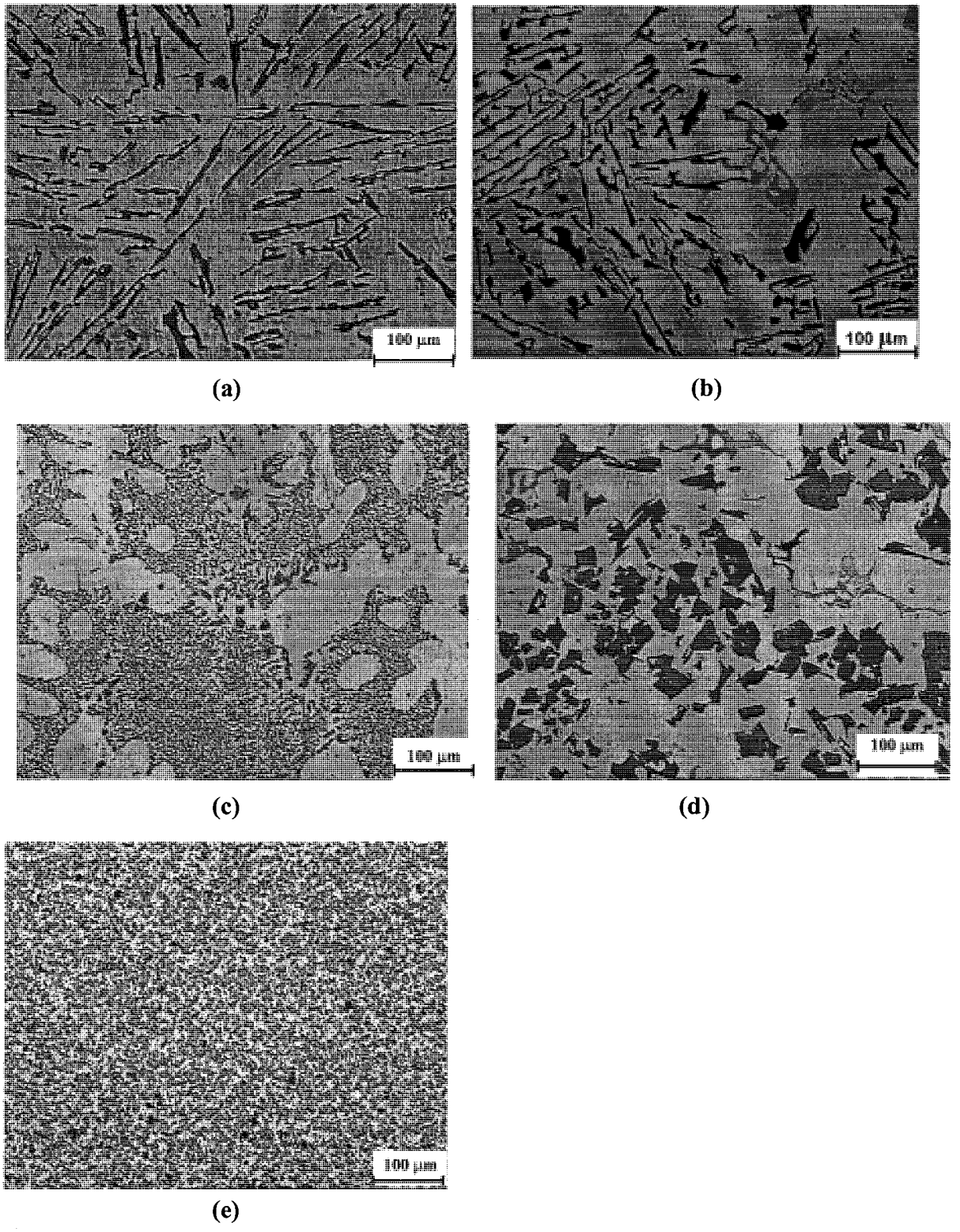

Fig. 3.12. Optical micrographs showing the microstructures of **(a)** Al-12% Si, **(b)** Al-11% Si-C, **(c)** Al-11% Si-F, **(d)** Al-18.5% Si, and **(e)** Al-25% Si at the same magnification.

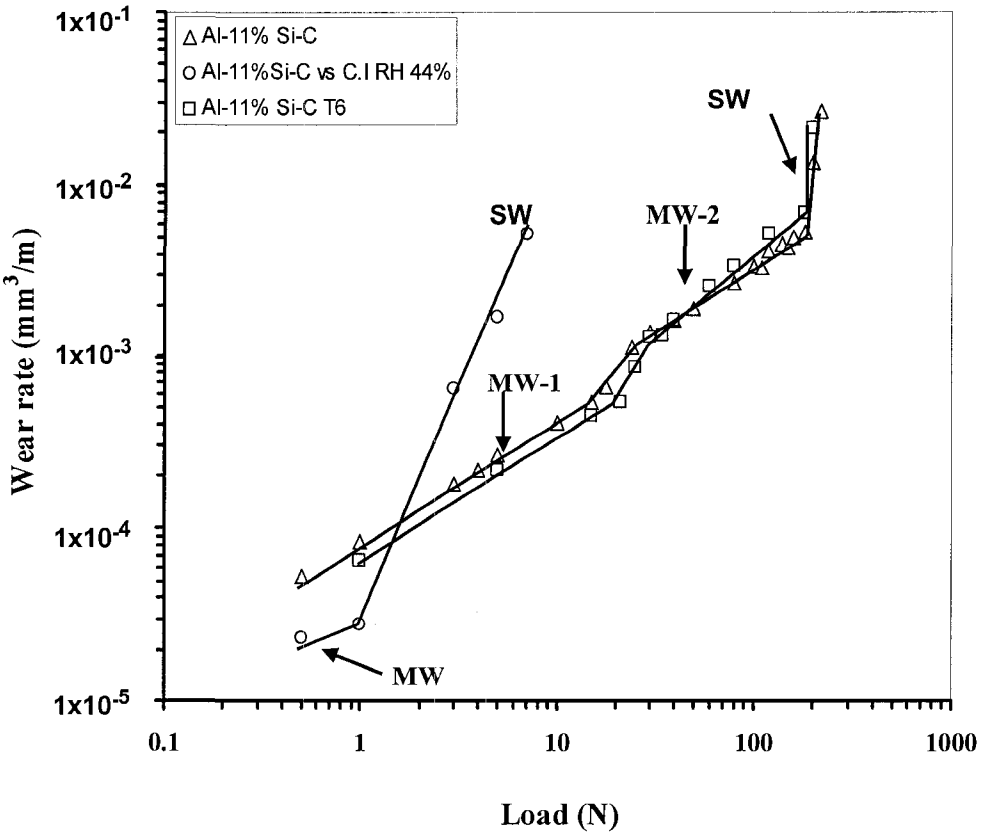

Fig. 3.13. Variation of wear rate with the applied load showing transition of wear regime in Al-11% Si-C under dry sliding conditions. C.I is cast iron, and R.H is relative humidity.

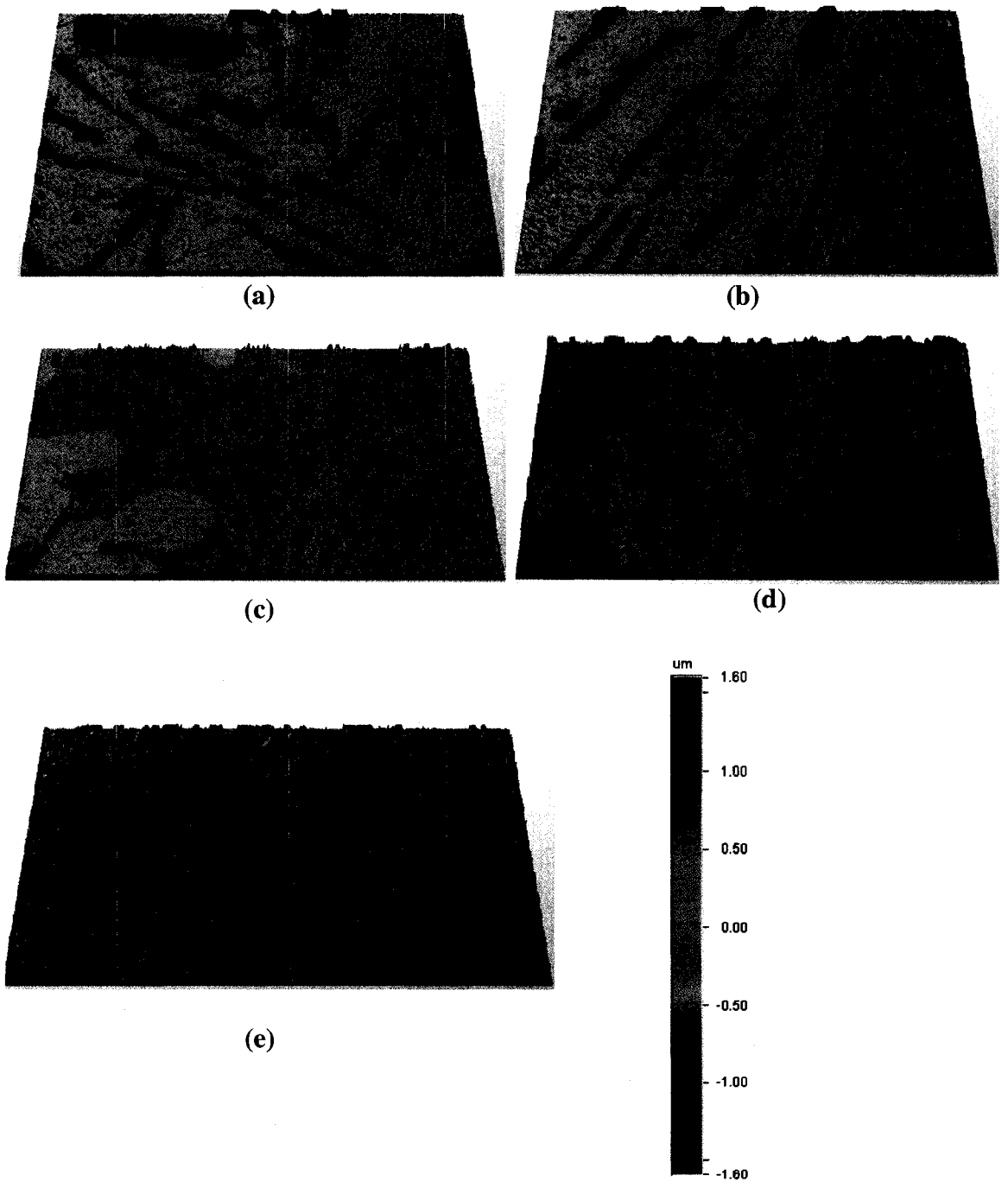

Fig. 3.14. 3-D optical surface profile image showing the etched **(a)** Al-12% Si, **(b)** Al -11% Si-C, **(c)** Al-11% Si-F, **(d)** Al-18.5% Si, and **(e)** Al-25% Si surface. The dimension of the area shown in **(a)** and **(b)** is 436.3 x 311.2 μm, and that shown in **(c)**, **(d)**, and **(e)** is 1,112 μm x 595 μm.

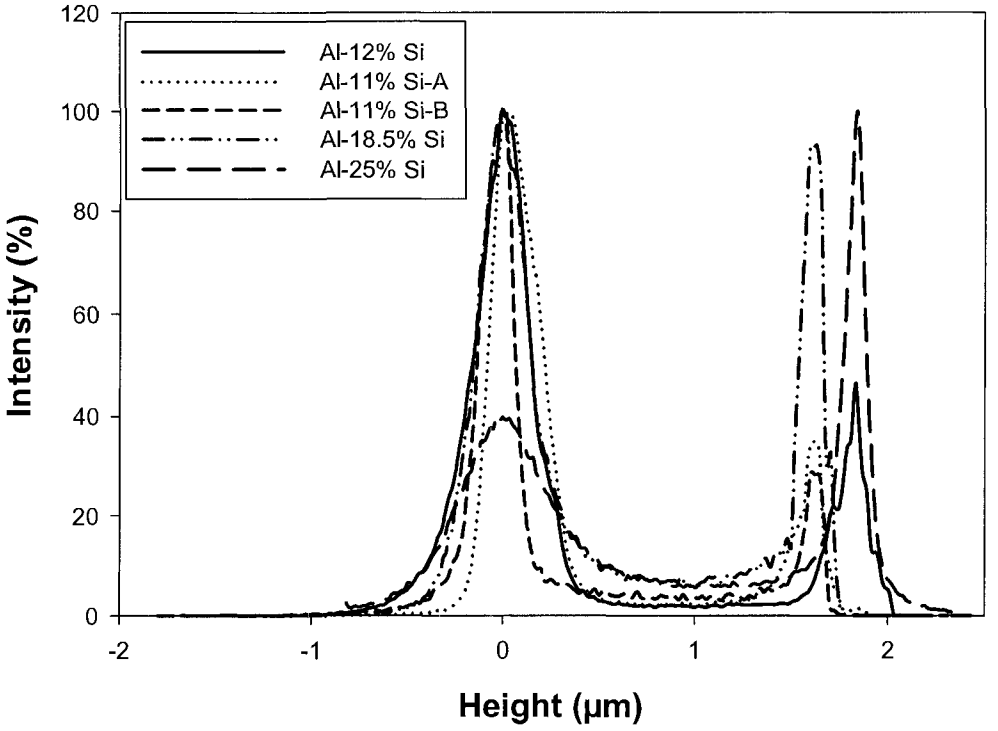

Fig. 3.15. Histograms showing the height distributions of matrix (first peak with lower height (μm)) and particles (second peak with larger height (μm)) of the five etched alloy surfaces (Al-12% Si, Al-11% Si-C, Al-11% Si-F, Al-18.5% Si, and Al-25% Si) prior to wear tests.

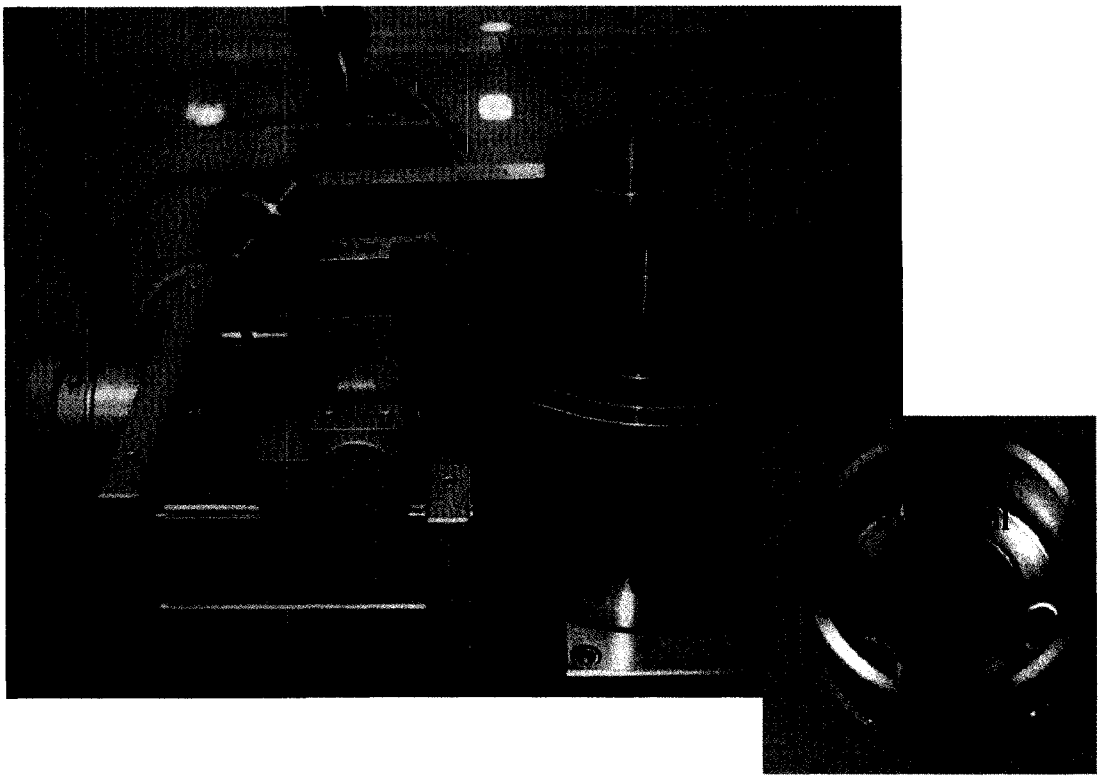

(a) (b)

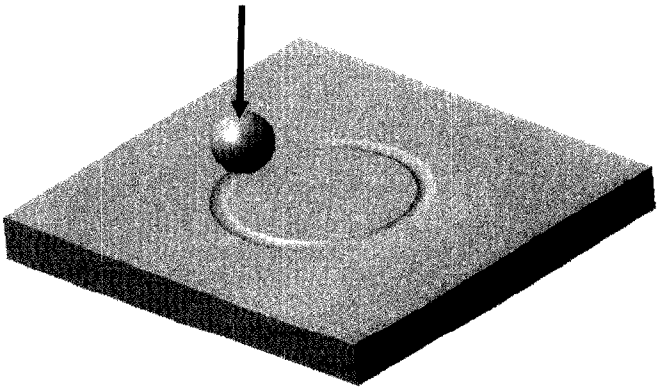

(c)

Fig. 3.16. **(a)** A photograph showing pin-on-disk tribometer (CSM, Switzerland), **(b)** a photograph showing sample holder with lubricant, and **(c)** schematic drawing showing the contact geometry.

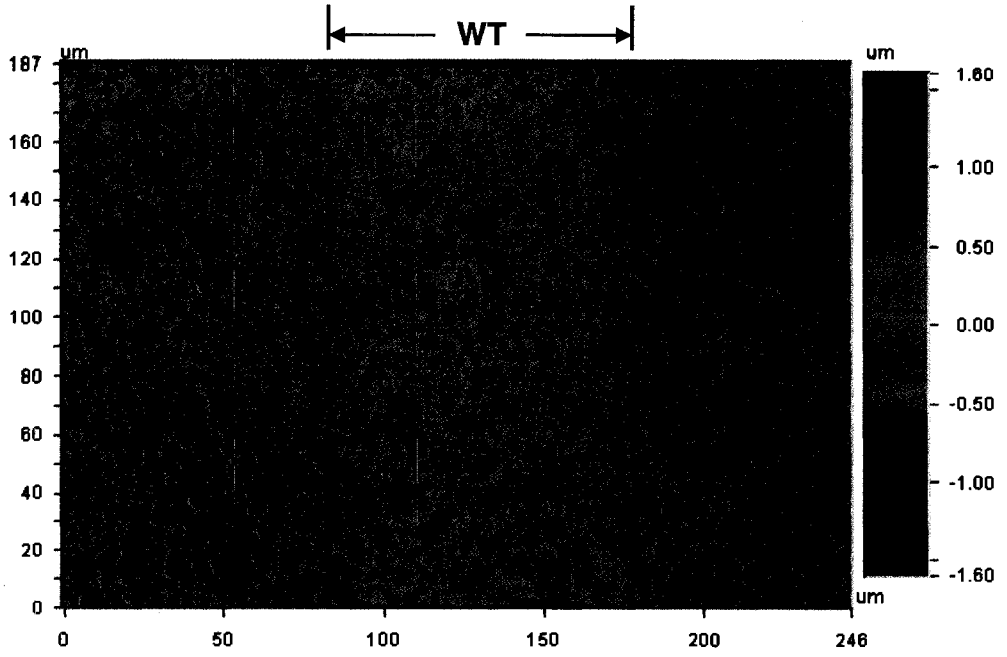

(a)

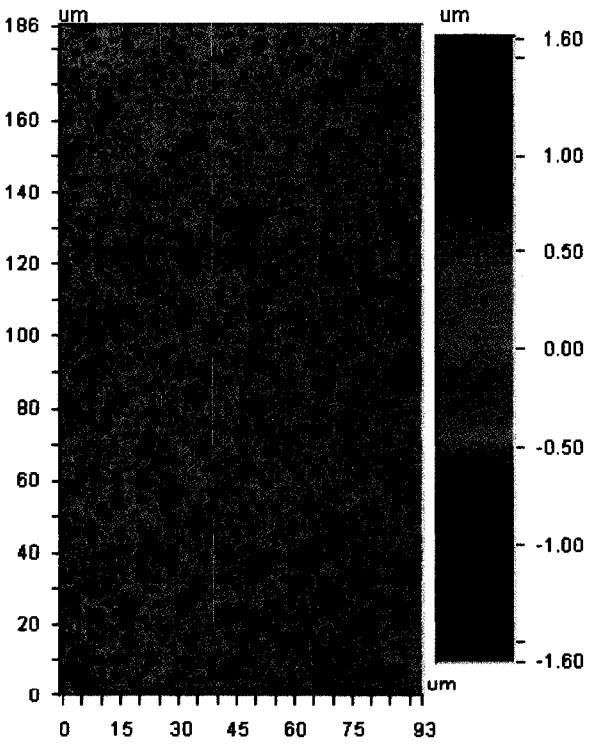

(b)

Fig. 3.17. An illustration of selecting the sub-region from a 2-D surface profilometer image, **(a)** general 2-D surface profile image taken from Al-25% Si surface after sliding to $6x10^5$ cycles at 0.5 N, **(b)** selected sub-region.

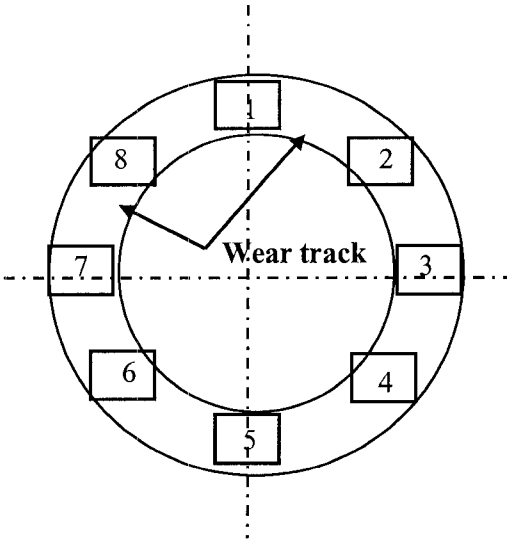

(a)

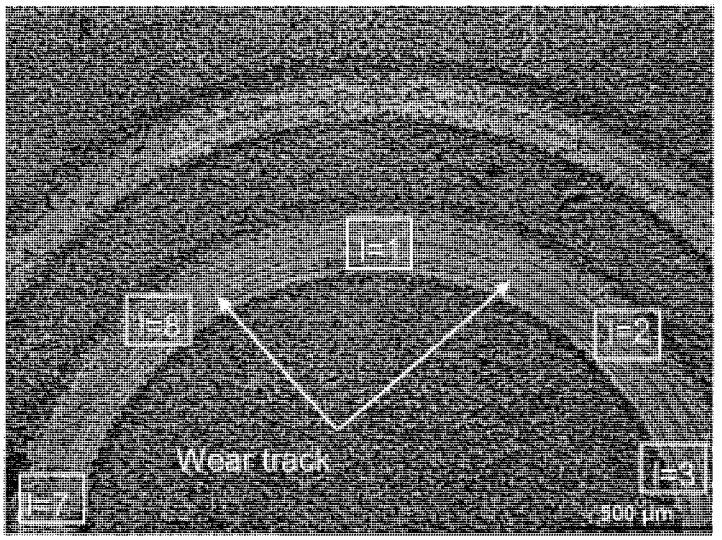

(b)

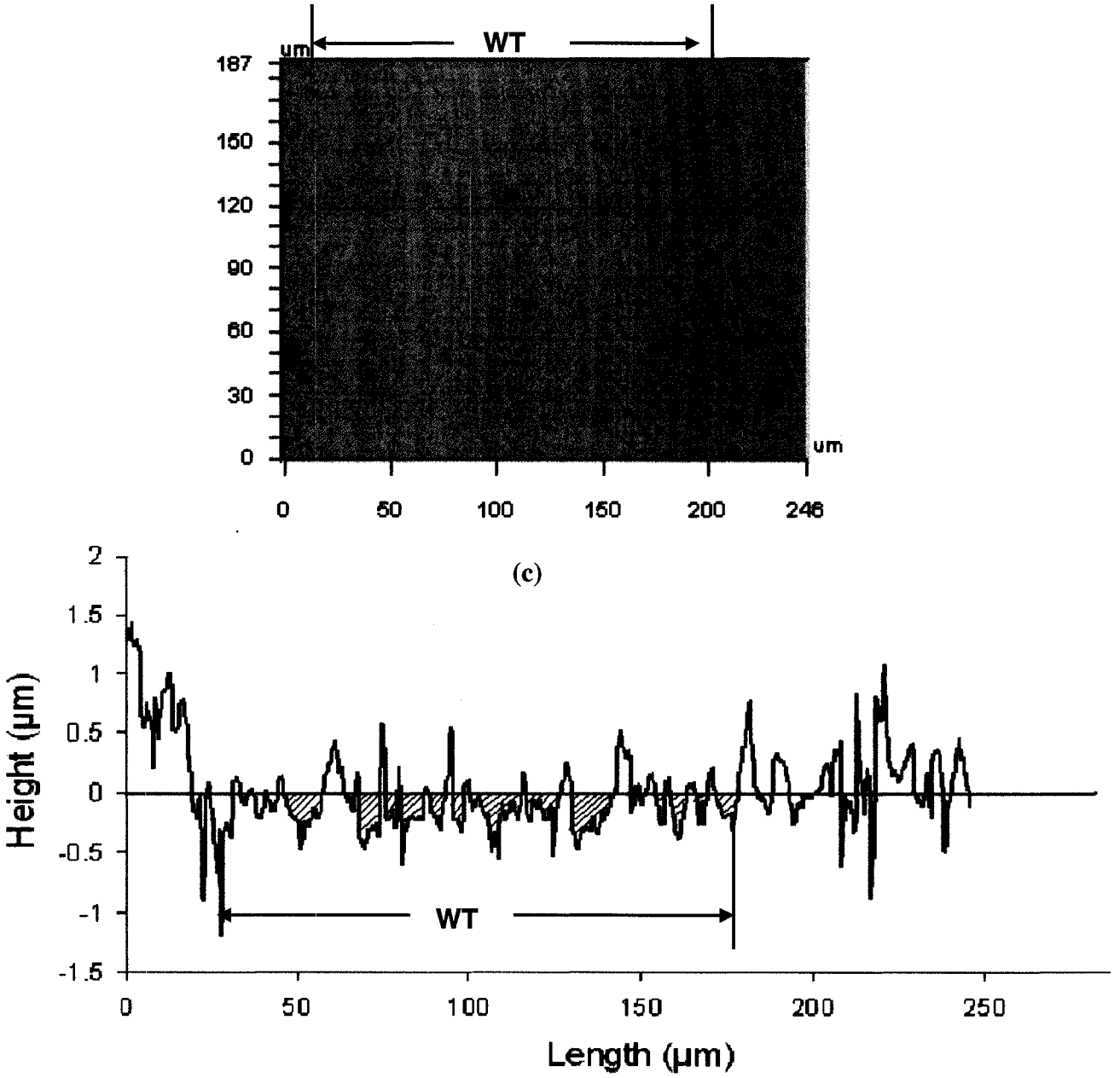

Fig. 3.18. An illustration of the method used to measure volume loss. **(a)** Schematic drawing showing image locations; **(b)** An optical microscopic image of half of the wear track of the contact surface of Al-25% Si; **(c)** A typical 2-D surface profile image taken from a location 'l=8' in **(b)**; **(d)** Cross-sectional profile scanned along AA′in **(c)**. WT is wear track.

CHAPTER 4 CONTACT PRESSURE ANALYSIS

4.1. Introduction

The conventional wisdom for Al-Si alloys used in tribological applications is that silicon particles standing proud of the aluminum matrix carry the load [1, 22]. Accordingly, all the surfaces to be subjected to sliding wear tests were etched using 10% NaOH, which makes silicon particles protrude above the aluminum matrix, and hence carry the applied load. The Greenwood and Tripp numerical contact model was adapted in this dissertation for analyzing the contacts between the etched Al-Si alloys and 52100 steel balls. The maximum apparent contact pressures, the maximum real contact pressures applied on the alloys tested, the effective contact radius, and the real contact radius were estimated. The results are also compared with Hertzian contact theory.

In **Section 4.2** of this chapter, the stress analysis at the contact surface based on Hertzian theory and the Greenwood and Tripp numerical model, is introduced. **Section 4.3** compares the current Al-Si alloy system with the Greenwood and Tripp model. This is followed by an explanation of all the equations and methodology employed in the calculation. Calculation results for the five alloys tested followed by a modification of Tabor's criterion and upper-bound calculation using the slip-line field theory, used for indentation and plastic deformation, are presented in **Section 4.4**.

4.2. Introduction to Stress Analysis at Contact Surfaces

4.2.1. Hertzian Contact

Hertz did the pioneering work on analysis of the deformation and pressure at the

contact of two elastic solids with geometries defined by quadratic surfaces, and such contacts are referred to as Hertzian [105]. Hertzian analysis is based on the following assumptions: i) each solid can be considered as an elastic half-space in the proximity of the contact region, ii) the surfaces are continuous, smooth, and noncomforming; iii) the strains are small; and iv) the surfaces are frictionless. Two solids of general shape (but chosen convex for convenience) loaded together are shown in cross-section after deformation in **Fig. 4.1**. The x-y plane is the contact plane. The first point of the contact is taken as the origin of the Cartesian coordinate system in which the x-y plane is the common tangent plane to the two surfaces, and the z-axis lies along the common normal directed positively into the lower solid. The separation between the two surfaces at radius r before loading is $z_1 + z_2$. Under the compression by a normal force W, distant points in the two bodies T_1 and T_2 move toward O, parallel to the z-axis, by vertical displacement, respectively. If the solids did not deform their profiles would overlap, as shown by the dashed line in **Fig. 4.1**. The elastic deformation results in displacement of the surface outside the footprint, therefore, the contact size is smaller than the overlap length caused by the intersection of the dashed lines. When the contact pressure is applied, the surface of each solid is displaced parallel to Oz by $\bar{u}_{z1}$ and $\bar{u}_{z2}$ (measured positive into each solid), relative to the distant points T_1 and T_2, points S_1 and S_2 become coincident. The total displacement, $=\delta_1 + \delta_2$, is called the total interference or normal approach, which is defined as the distance by which points on the two solids remote from the deformation zone move together under the applied normal load. If the two bodies are solids of revolution, then from polar symmetry the contact area will be circular and centered at O.

For two spheres with radii of R_1 and R_2 and in solid contact with a normal load of

W, the contact area is circular having a radius of a and the contact pressure is elliptical with $p(r)$ at a radius in the contact zone. From Hertzian analysis, the pressure distribution is

$$p(r) = p_0\{1-(r/a)^2\}^{1/2} \tag{4.1}$$

where p_0 is the maximum contact pressure and is given by

$$p_0 = \frac{3}{2}p_m = \frac{3W}{2\pi a^2} = (\frac{6WE^{*2}}{\pi^3 R^2})^{1/3} \tag{4.2}$$

where p_m is the mean pressure, and E^* is composite elastic modulus

$$\frac{1}{E^*} = \frac{1-\nu_1^{\ 2}}{E_1} + \frac{1-\nu_2^{\ 2}}{E_2} \tag{4.3}$$

and R is the effective or composite curvature and given by

$$\frac{1}{R} = \frac{1}{R_1} + \frac{1}{R_2} \tag{4.4}$$

The parameters E and ν are Young's modulus of elasticity and the Poisson's ratio, respectively; subscript 1 and 2 refer to the two bodies.

The contact radius is given by

$$a = \frac{\pi p_0 R}{2E^*} = (\frac{3WR}{4E^*})^{1/3} \tag{4.5}$$

and the contact area is therefore

$$A = \pi a^2 = \pi R\delta \tag{4.6}$$

K. Johnson [105] found the solution for the stresses between two frictionless solids exerted by Hertz pressure. The polar components of the stress field in the surface at z = 0, inside the loaded circle ($r \le a$) are,

$$\sigma_r / p_0 = \frac{1-2\nu}{3}(a^2/r^2)\{1-(1-r^2/a^2)^{3/2}\} - (1-r^2/a^2)^{1/2} \tag{4.7}$$

$$\sigma_\theta / p_0 = -\frac{1-2\nu}{3}(a^2/r^2)\left\{1-(1-r^2/a^2)^{3/2}\right\} - 2\nu(1-r^2/a^2)^{1/2} \qquad (4.8)$$

and outside the circle

$$\sigma_r / p_0 = -\sigma_\theta / p_0 = (1-2\nu)a^2/3r^2 \qquad (4.9)$$

The radial stress is therefore tensile outside the loaded circle, and it reaches its maximum at the edge of the circle at $r = a$. The stress distributions within the two solids with ν= 0.30 are presented in **Fig. 4.2**. In this figure, the stress produced by an uniform pressure acting on a circular area are also shown for comparisons. In the case of axisymmetric contact of two spheres exerted by a Hertzian pressure distribution, along the z-axis, σ_r, σ_θ, and σ_z are the principal stresses. The principal shear stress, $\tau_1 = \frac{1}{2}|\sigma_z - \sigma_r|$; has a maximum value of 0.31 p_0, and lies below the surface at a depth of 0.48 a. Accordingly, based on the Tresca criterion, the value of p_0 for yield is given by

$$(p_0)_y = 3.2\,k = 1.6\,Y \qquad (4.10)$$

Therefore, for the axisymmetric contact of two spheres loaded by a Hertzian pressure distribution, plastic deformation is expected to initiate beneath the surface. As the normal load is applied to the two contacting bodies, they initially elastically deform according to their Young's moduli of elasticity. Plastic deformation may start from one of the two solids with the lower hardness. As the normal load is further increased, the plastic zone grows until the entire material surrounding the contact has gone through plastic deformation.

4.2.2. Contact at Two Rough Surfaces

Contact depicted in **Section 4.1.1**, which is continuous within the nominal contact area and zero outside it, is extremely rare in reality. In general, contact between two solid

surfaces is not continuous and the contact initiates at discrete contact spots, i.e., the asperities on the surfaces, because the real surfaces, irrespective of the method of formation, are rough on a microscopic scale. Therefore, the real area of contact is only a small fraction of the nominal contact area. Unlike Hertzian contact, asperities are the first to come into contact, and hence, deformation initiates in the region of the contact asperities as the two surfaces are brought into contact [105].

Modeling of the contact of rough surfaces is difficult and has been conducted by many researchers [105-107]. Greenwood and Williamson [106] proposed a classical statistical model for a combination of elastic and plastic contacts between a plane and a nominally flat surface covered with a large number of asperities. In the Greenwood and Williamson model, it is assumed that i) surfaces are composed of hemispherically tipped asperities with the same radius of curvature, ii) their heights follow a normal, i.e., Gaussian distribution about a mean plane. Their elastic-plastic model was defined by two topographical parameters: σ, the standard deviation of the asperity height distribution, and β, the mean radius of curvature of the asperities. A parameter, the plastic index, ψ, which combines the material and topographical properties of the solids in contact, was proposed to predict whether contacts are elastic or plastic. It is defined as

$$\psi = (E^* / H)\sqrt{(\sigma / \beta)} \tag{4.11}$$

where E^* is the composite elastic modulus, which is the same as the one used in Hertzain theory, and H is the hardness, σ is the standard deviation of asperity height, and β is the mean curvature radius of asperities . The essential point of Greenwood and Williamson's model is that the behaviour of rough surfaces is determined by the statistical distribution of asperity height, and secondarily by their mode of deformation. Following Greenwood

and Williamson's model, when ψ is less than 0.6, plastic deformation could be caused only if the surfaces were brought in contact under very large nominal pressure. But when ψ exceeds 1.0 plastic flow will occur even at low nominal pressures.

Greenwood and Tripp [107] extended the Greenwood and Williamson model to the contact between a sphere and nominally flat surface covered with a large number of asperities as shown in **Fig. 4.3**. The model was based on the same assumptions as Greenwood and Williamson's model, that is, i) the asperity height distribution obeys a normal, i.e., Gaussian, distribution, ii) the top of the asperities are spherical, all with the same radius of curvature. Following these two assumptions, Greenwood and Tripp derived the relation connecting the separation distance between the mean surfaces with the pressure created by compressing the asperities through elasticity theory, i.e., Hertzian analysis.

The results of Hertzian analysis for the contact between a sphere with a radius of β and a plane was firstly written in terms of the compliance w, the distance, which points away from the deformation zone move together, during deformation, statistic distribution of the asperity height, Gaussian distribution was considered.

The area of contact A_i and the load P_i are

$$A_i = \pi\beta w \tag{4.12}$$

$$P_i = \frac{4}{3} E^* \beta^{1/2} w^{3/2} \tag{4.13}$$

where E^* is the composite elastic modulus and is the same as the one used in Hertzian contact. If the separation of the nominal surfaces at the position of a particular asperity is u, then there will be a contact at that asperity if its height z is greater than u. The probability of this is

$$prob(z > u) = \int_u^\infty \phi(z)dz \tag{4.14}$$

where $\phi(z)$ is the probability density function of the distribution of asperity heights. The first contact occurs at the highest asperity, the compliance w will equal z-u, and the resulting contact area will be $\pi\beta(z-u)$. Therefore, the expected contact area is given by

$$\overline{A_i} = \int_u^\infty \pi\beta(z-u)\phi(z)dz \tag{4.15}$$

Similarly the expected applied load at this contact is

$$\overline{P_i} = \int_u^\infty \frac{4}{3}E^*\beta^{1/2}(z-u)^{3/2}\phi(z)dz \tag{4.16}$$

For an element of area da over which the separation between the nominal surfaces is u, and the density of asperities is η. Then the expected number of contacts dN, the expected real contact area dA, and the expected applied load dP occurring within da will be

$$dN = \eta da \int_u^\infty \phi(z)dz \tag{4.17}$$

$$dA = \pi\eta\beta da \int_u^\infty (z-u)\phi(z)dz \tag{4.18}$$

$$dP = \frac{4}{3}\eta E^*\beta^{1/2} da \int_u^\infty (z-u)^{3/2}\phi(z)dz \tag{4.19}$$

Introducing standardized variables and describing the asperity height in terms of the standard deviation σ of the height distribution, the above equations can be written as

$$dN = \eta da F_0(h) \tag{4.20}$$

$$dA = \pi\eta\beta\sigma da F_1(h) \tag{4.21}$$

$$dP = \frac{4}{3}\eta E^* \beta^{1/2} \sigma^{3/2} da F_{3/2}(h) \equiv \lambda da F_{3/2}(h) \tag{4.22}$$

where $\lambda = \frac{4}{3}\eta E^* \beta^{1/2} \sigma^{3/2}$, and $h = u/\sigma$

$$F_n(h) = \int_u^\infty (s-h)^n \phi^*(s) ds \tag{4.23}$$

and $\phi^*(s)$ is the standardized height distribution, that is, the height distribution scaled to make the standard deviation unity. For a Gaussian distribution of heights,

$$\phi^*(s) = \frac{1}{(2\pi)^{3/2}} \exp(-\frac{1}{2}s^2) \tag{4.24}$$

Taking the force dP on the area da to be equivalent to a uniform pressure p, the pressure distribution is given by

$$p = \lambda F_{3/2}(u/\sigma) \tag{4.25}$$

For the contact between rigid spheres of radii R_1 and R_2, the relation between separation the u and the radial position r is given by

$$u = d + r^2/2B \tag{4.26}$$

where d is the minimum separation and $1/B = 1/R_1 + 1/R_2$. If $w(r)$ is the displacement of the nominal surfaces at r, then

$$u = d + r^2/2B + w(r) + w(0) \tag{4.27}$$

and therefore

$$p(r) = \lambda F_{3/2}(1/\sigma\{d + w(r) - w(0) + r^2/2B\}) \tag{4.28}$$

From elasticity theory, the displacements are related to the pressure distribution by

$$w(r) = \frac{2r}{E^*} \int_0^\infty p(\xi r) L(\xi) d\xi \tag{4.29}$$

where

$$L(\xi) = \frac{2}{\pi}\xi K(\xi) \qquad \text{for } \xi < 1$$

$$= \frac{2}{\pi} K(1/\xi) \qquad \text{for } \xi > 1$$

and $K(\xi)$ is an elliptic integral of variable ξ.

Introducing dimensionless variables,

Displacement $w^* = w/\sigma$

Separation $u^* = u/\sigma$, $d^* = d/\sigma$ (4.30)

Radial distance $\rho = r/\sqrt{2R\sigma}$

Pressure $p/(E^*\sqrt{\sigma/8R})$

The equations then become

$$p^*(\rho) = \mu F_{3/2}(d^* + \rho^2 + w^*(\rho) - w^*(0)) \tag{4.31}$$

$$w^*(\rho) = \int_0^\infty \rho p^*(\rho\xi) L(\zeta) d\zeta \qquad (\rho > 0) \tag{4.32 a}$$

$$w^*(0) = \int_0^\infty p^*(\xi) d\zeta \tag{4.32 b}$$

Where $\mu = \frac{8}{3}\eta\sigma\sqrt{2RR_p}$.

The self-consistent displacements and pressure distributions were computed by a numerical iterative loop using **Equation 4.31** to **4.32** and the results were compared with Hertzian analysis. The singularity (logarithmic) at ξ =1 was removed by a change of variable. Let

$$s(\xi) = \int_0^{\infty} L(\xi')d\xi'$$

so that $ds = L(\xi)d\xi$. Thus

$$w^*(\rho) = \int_0^{\infty} \rho p^*(\rho\xi(s)ds$$

$s(\xi)$ can be shown to be

$$\frac{2}{\pi}\xi^2 B(\xi) \qquad \text{for } \xi \leq 1$$

$$\frac{2}{\pi}\xi E(1/\xi) \qquad \text{for } \xi \geq 1$$

Where $B(\xi)$ and $E(1/\xi)$ are elliptic integrals of variable ξ.

The calculation results reveal that the classical Hertzian analysis is close to the results at high loads for rough surface, and that there is significant difference at low loads as shown in **Fig. 4.4**. Greenwood and Tripp also compared the apparent contact pressure with the real contact pressure. In Greenwood and Tripp's model, the real contact pressure was defined as the pressure occurring locally over each microcontact, namely, the asperities, which really make contact with the counterface. They showed that the maximum real contact pressure is much higher than the maximum apparent contact pressure.

4.3. Stress Analysis at the Contacts between Etched Al-Si Alloys and Steel Ball

4.3.1. Adaptation of Greenwood Tripp's Model to Current Contact System

On the etched surfaces of Al-Si alloys, the summits of silicon particles act as the asperities that come in contact with the steel counterface. The contact geometry between

the etched Al-Si alloy surface and a steel ball is schematically presented in **Fig. 4.5**. It shows a typical etched surface profile of the tested alloys determined using the optical surface profilometer together with a schematic of the counterface tip with radius R contacting the protruding silicon particles. Following the Greenwood and Tripp model, the silicon particles standing proud of the aluminum matrix surface were considered as load carrying asperities in contact with the counterface, and the variations of the silicon particle height were fitted to a Gaussian distribution. The actual silicon height distribution deviates from a true Gaussian because of the etching procedure, but for this analysis, the actual data (as shown in **Fig. 4.5**) was fitted with a single, pure Gaussian curve.

For an element of surface, $d\Psi$, which has a total of n silicon particles, the expected number of contacts, dN, the real area of contact, dA_r and the total load, dP, are given as

$$dN = n\int_u^\infty \phi(z)dz \tag{4.33}$$

$$dA_r = \pi n R_p \int_u^\infty (z-u)\,\phi(z)dz \tag{4.34}$$

$$dP = \frac{4}{3} nE^* R_p^{1/2} \int_u^\infty (z-u)^{3/2}\phi(z)dz \tag{4.35}$$

where z is the silicon particle height, and R_p is the equivalent curvature radius of the silicon particle tips. The heterogeneous nature of asperity contact in etched Al-Si surfaces differs from the original model that treats contacts between the asperities of monolithic materials. Here Si particles in contact with the steel are supported by the aluminum matrix. Thus, E^* is the composite elastic modulus of Al-Si and steel calculated using **Equations 3.4** and **3.5** and $\phi(z)$ is the height distribution function [106]. u is the separation of the nominal contact surfaces at the position of a particular silicon particle.

Switching to dimensionless variables in the above equations gives

$$dN = \eta \, d\Psi F_0(h) \tag{4.36}$$

$$dA = \pi\eta\sigma R_p \, d\Psi F_1(h) \tag{4.37}$$

$$dP = \frac{4}{3}\eta \, E^*(R_p\sigma)^{1/2}\sigma \, d\Psi F_{3/2}(h) \tag{4.38}$$

where η is the density of the silicon particles, *i.e.*, the number of silicon particles per unit area and thus $\eta d\Psi = n$. The term $\eta(R_p\sigma)$ in this dissertation represents the areal density of the silicon particles (measured using quantitative metallography, as described in **Section 3.3**), while σ is the standard deviation of silicon particle height, which was obtained by fitting the initial particle height distribution curve in **Fig. 3.15** to Gauss 1 distribution using MATLAB software. As an example, the initial silicon particle height profile measured from an etched Al-18.5% Si surface profile is used to illustrate the method of obtaining the standard deviation of silicon particles. Firstly, plot the silicon particle height distribution, that is, the second peak in the histogram (**Fig. 3.15**) as shown by the dotted curve in **Fig. 4.6**, then select the fitting type as general Gaussian mode, defined as

$$f(x) = a_1 \exp(-((x-b_1)/c_1)^2 \tag{4.39}$$

where a_1, b_1, and c_1 are coefficients of the general mode Gauss 1. When compared with the general Gaussian distribution function, which is defined as,

$$f(x) = \frac{1}{\sqrt{2\pi\sigma^2}} \exp(-(x-a)^2/2\sigma^2) \tag{4.40}$$

where a is the mean value, and σ is the standard deviation, $a_1 = 1/\sqrt{2\pi\sigma^2}$, b_1 is the mean value, and $c_1 = \sqrt{2}\sigma$. Therefore, $c_1/\sqrt{2}$ is the standard deviation of the silicon particle

height.

The fit is plotted as a solid curve in **Fig. 4.6**. The fitting confidence bound was selected as 95%. After each fitting procedure, all the three coefficients were obtained. **Table 4.1** lists all the coefficients obtained from the curve fitting of the five tested alloys.

4.3.2. Apparent Contact Pressure

The apparent contact pressure describes the combined effect of the force transmitted through the individual silicon particles (micro-contact) averaged over each area element of the surface. The apparent contact pressure can be referred to as the pressure distributed over the contact surface. Thus, the apparent contact pressure distribution *p(r)* is obtained by considering *dP* applied on the area $d\Psi$ to be equivalent to a uniform pressure, and is given by

$$p(r) = dP / d\Psi = \frac{4}{3}\eta E^* R_p^{1/2} \sigma^{3/2} F_{3/2}(h) \tag{4.41}$$

where $h = u / \sigma$, and $u = d + r^2 / 2R + w(r) - w(0)$, d is the minimum separation, $w(r)$ is the displacement of the nominal surfaces at r and given by

$$w(r) = \frac{2r}{E^*} \int_0^\infty p(\xi r) L(\xi) d\xi \tag{4.42}$$

where

$$L(\xi) = \frac{2}{\pi} \xi K(\xi) \qquad \text{for } \xi < 1$$

$$= \frac{2}{\pi} K(1/\xi) \qquad \text{for } \xi > 1$$

and $K(\xi)$ is an elliptic integral of valuable ξ. $F_m(h)$ is the parabolic cylinder function, which for a Gaussian distribution is given by

$$F_m(h) = \left[\frac{1}{(2\pi)^{1/2}}\right]\int_h^\infty (s-h)^m \exp(-s^2/2)ds. \tag{4.43}$$

Introducing dimensionless variables,

Displacement $w^* = w/\sigma$

Separation $u^* = u/\sigma$, $d^* = d/\sigma$ (4.44)

Radial distance $\rho = r/\sqrt{2R\sigma}$

Pressure $p/(E^*\sqrt{\sigma/8R})$

The equations then become

$$p^*(\rho) = \mu F_{3/2}(d^* + \rho^2 + w^*(\rho) - w^*(0)) \tag{4.45}$$

$$w^*(\rho) = \int_0^\infty \rho p^*(\rho\xi)L(\zeta)d\zeta \qquad (\rho > 0) \tag{4.46 a}$$

$$w^*(0) = \int_0^\infty p^*(\xi)d\zeta \tag{4.46 b}$$

Where $\mu = \frac{8}{3}\eta\sigma\sqrt{2RR_p}$.

However, the standard deviation of the silicon particle height, σ, is only included in the expected load dP (**Equation 4.38**). The area used for the estimation of the apparent contact pressure does not consider that the silicon particles in each area of element on the contact surfaces are not at the same height. It is, therefore, not reasonable to assume that all the particles on the contact surface will make contact with the counterface, and hence, carry the applied load uniformly. Practically, the contact only occurs between the

particles with the height greater than the separation distance of the nominal contact surfaces and the counterface. Hence, the height distribution of the silicon particles as well as their size should be taken into account in both the contact area and the expected load to calculate the contact pressure applied on Si particles. That is, the real contact pressure is more realistic to be used to depict the contact between two rough surfaces. This is given in **Section 4.3.3**.

4.3.3. Real Contact Pressure

The real contact pressure, as defined by Greenwood and Tripp [107], describes the pressure occurring locally over each micro contact. On etched surfaces of Al-Si alloys the counterface is in contact with the silicon particles. The magnitude of contact pressure on the silicon asperities is, therefore, determined from the ratio of the total expected load, dP, to the real contact area, dA_r, i.e.,

$$P_r = dP / dA_r \tag{4.47}$$

Substituting dA_r and dP (**Equations 4.37** and **4.38**) into **Equation 4.47**, then

$$p_r = dP / dA_r = (\frac{4}{3\pi}) E^* (\sigma / R_p)^{1/2} F_{3/2}(h) / F_1(h) \tag{4.48}$$

From **Equation 4.48**, it can be seen that the real contact pressure is affected by the elastic modulus E^*, the standard deviation of silicon particle height, σ, the silicon particle sizes, R_p, and the ratio, $F_{3/2}(h)/F_1(h)$. If two alloys have similar values of E^* and σ, the silicon particle size and the ratio, $F_{3/2}(h)/F_1(h)$ would be the major factors that influence the real contact pressure. The ratio, $F_{3/2}(h)/F_1(h)$, decreases with increasing the separation distance, h. Smaller h, that is, greater $F_{3/2}(h)/F_1(h)$ is expected in the alloy with small silicon particles than that with large silicon particles. Accordingly, higher contact

pressure is expected to apply on the silicon particles in the alloy with small silicon particles than that with large silicon particles. When the two alloys have similar silicon particle size but different areal density, according to the curve fitting results listed in **Table 4.1**, the alloy with higher areal density showed smaller σ. The separation distance, h, is greater in the alloy with higher areal density than the one with small areal density. Therefore, smaller contact pressure is expected to apply on the silicon particles in the alloy with high silicon particle areal density than that with small areal density. However, the parameter describing the silicon particle shape, either aspect ratio or sphericity is not included in **Equation 4.48.** This makes comparison of contact stresses in Al-Si alloys with different silicon morphologies difficult.

4.3.4. Numerical Computation Method

The relation between separation distance and pressure was determined by solving **Equations 4.45** to **4.46** numerically by following the iterative procedure illustrated in **Fig. 4.7**. The numerical iterative procedure for finding the final pressure distribution started with a given μ value, specified d^* value, and an initial guess of displacement, $w^*(\rho)$ using **Equation 4.45**. Improved values of the displacement were then calculated from the pressure distribution using **Equation 4.46**. The height distribution function defined in **Equation 4.43** was integrated numerically using a Gauss quadrature. The quadrature integrates a (2m-1)th order polynomial exactly in the form of $Int(p(x)*Fun(x))dx$, where $p(x)$ and $Fun(x)$ are functions, and a and b are integration limits. The calculated values were in agreement with the values listed in the table of the reference [108] by Greenwood and Tripp.

4.4 Calculation Results

4.4.1. Apparent Contact Pressure

In order to compare the Greenwood and Tripp calculation results with Hertzian theory, similar dimensionless variables are introduced, the Hertzian pressure can be given by

$$q^*(\rho) = q^*(0)(1-\rho^2/a^{*2})^{1/2} \tag{4.49}$$

where $q^*(0)$ is the maximum Hertzian contact pressure and is given by

$$q^*(0) = \frac{4}{\pi}\left[\frac{3T}{2}\right]^{1/3} \tag{4.50}$$

a^* is the effective contact radius and is calculated using $a^* = \frac{1}{2}\left[\frac{3T}{2}\right]^{1/3}$, where T is the dimensionless total load, defined by $T = \int_0^\infty 2\pi\rho p^*(\rho)d\rho$. T is related with the actual load, W, by $W = \frac{1}{2}\sigma E^*\sqrt{2R\sigma T}$. The parameters used for the computation are listed in **Table 4.2.**

Figs. 4.8 a - c show the dimensionless plots of the apparent contact pressure distribution with radial distance occurring on the etched surfaces of the five Al-Si alloys at 0.5, 1.0, and 2.0 N calculated by numerically solving **Equations 4.45** to **4.46** and Hertzian Theory (**Equation 4.49**). The corresponding dimensional plots are presented in **Figs. 4.9 a** to **c**, which were obtained by converting both dimensionless apparent pressure and radial distance to dimensional values using **Equation 4.44**. The pressure distributions on the etched surfaces are different from the Hertzian pressure distribution. The Hertzian pressure distribution falls to zero sharply at a particular radius. With the

etched Al-Si surfaces, on the other hand, all the apparent contact pressures became zero at infinity. The peak pressures at each load are smaller than those of Hertzian value, and the contact areas are larger than Hertzian contact area, which is similar to the results obtained by Greenwood and Tripp from the contacts with the composite elastic modulus of 100 GPa (**Fig. 4.4**) [107].

The maximum apparent contact pressures applied on the five alloys tested vary with normal load in the way shown in **Fig. 4.10**, which is similar to the variation of the maximum Hertzian contact pressure with the normal load (**Fig. 4.10**). **Table 4.3** lists the maximum apparent contact pressures and Hertzian pressures under the normal loadings used in the current experiments. The maximum apparent contact pressures applied on the five alloys at each applied load were smaller than those of the maximum Hertzian contact pressure. Although the five tested alloys (see **Section 3.2**) showed different microstructure, the maximum apparent contact pressures applied on the five Al-Si alloys exhibited slight difference at each load tested. The maximum apparent contact pressures applied on the five tested alloys at each applied load decreased in the order of Al-25% Si, Al-11% Si-F, Al-18.5% Si, Al-12% Si, and Al-11% Si-C. It follows that under the conditions tested, the maximum apparent contact pressures and Hertzian contact pressures applied on the five alloys are lower than their matrix hardnesses of 1,060, 660, 830, 670, and 495 MPa, which were converted from the Hv hardness value in **Table 3.2**. Therefore, the apparent contact pressure, which describes the load carried by the silicon particles with a statistical variation in heights within the contact area, might not be suitable for the estimation of stress on the etched Al-Si alloys, since the peak pressures are far too low to suggest fracture of silicon or plastic deformation of the aluminum matrix. An estimation of the real contact pressure, corresponding to the contact pressure applied locally on the

exposed silicon particles, is necessary. This is given in **Section 4.4.3**.

4.4.2. Effective Contact Radius

Following the G&T model, an effective contact radius is defined as

$$a^* = 0.375T / w^*(0) \tag{4.51}$$

where $w^*(0)$ and T are the same terms used in **Equations 4.45** and **4.50**. The variations of the effective contact radius of the five Al-Si alloys with normal load calculated using **Equation 4.51** and $a^* = 0.5[3T/2]^{1/3}$ for the effective Hertzian contact radius are plotted in **Fig. 4.11**. The effective contact radiuses and Hertzian values on the contact surfaces of the five alloys at the tested load of 0.5, 1.0, and 2.0 N are listed in **Table 4.4**. It follows that the effective contact radiuses on the five etched alloy surfaces calculated with G&T model were greater than the Hertzian contact radius and the nominal contact radius is weakly affected by the microstructures in the form of silicon particle size, distribution.

4.4.3. Real Contact Pressure

The variation of the dimensionless separating distance, h, with the radial distance was obtained from an each successful numerical iteration. As an example, **Fig. 4.12** presents the plots of h with radial distance, ρ, in the load range of 0.5 to 3.0 N, obtained from the contact between Al-25% Si alloy and 52100 steel balls. For each h, two parabolic cylinder functions $F_1(h)$ and $F_{3/2}(h)$ were calculated using the method described in **Section 4.3** and then substituted into **Equation 4.48** to calculate the real contact pressure. The variation of the real contact pressure with the dimensionless separating distance, h, presented in **Fig. 4.13** indicates that the real contact pressures decreased sharply when the separation distance was greater than 9. Therefore, the real contact

pressure at the radial distance, ρ, where the separating distance of the two nominal contact surfaces was greater than 10 was set to zero to reduce calculation time. Both dimensionless and dimensional plots of the real contact pressure distribution on the five alloys at the normal loads of 0.5, 1.0 and 2.0 N are presented in **Figs. 4.14** to **4.16**. For the tested alloys, the real contact pressures applied on the exposed silicon particles were the highest at the centre but diminished with the radial distance.

For all the alloys, the peak values of the real contact pressure applied on the exposed silicon particles varied slightly with the normal load, as shown in **Fig. 4.17,** due to the slow increase of the ratio, $F_1(h)/F_{3/2}(h)$ with increasing the normal load. **Table 4.5** lists the maximum real contact pressures under the normal loadings used in the current experiments. The data presented in **Fig. 4.17** and **Table 4.5** indicates that the maximum contact pressures applied to the silicon particles are much higher than the maximum apparent contact pressure (**Table 4.2**) and Hertzian pressure. On the other hand, the real contact pressure was more strongly dependent on the alloy microstructure in terms of silicon particle size and areal density when compared to the apparent contact pressure. The maximum contact pressures applied on the silicon particles in Al-25% Si and Al-11% Si-F, with smaller silicon particle size, at each load were significantly higher than those in Al-18.5% Si, Al-12% Si, and Al-11% Si-C which have larger silicon particle sizes. The three alloys, Al-18.5% Si, Al-12% Si, and Al-11% Si-C, which have similar a magnitude of silicon particle sizes, exhibited little difference in the maximum real contact pressures; the real contact pressures increased with a decrease of the silicon particle size. The Al-25% Si and Al-11% Si-F had similar silicon particle size, but the maximum real contact pressure applied on Al-25% Si was smaller than on Al-11% Si-F. This can be attributed to the difference in the silicon particle areal density. The silicon particles in Al-25% Si were

distributed with much smaller interparticle distance (average areal density of 0.25) than those in Al-11% Si-F (average value of 0.11). It follows that the real contact pressure falls when more silicon particles carry the applied load. In order to confirm this, the contacts between Al-11% Si-F, in which silicon particles were distributed with different interparticle distances, corresponding to areal densities of 0.01, 0.025, and 0.04 /μm^2 and 52100 steel balls at 0.5 N were analyzed. The variations of the dimensionless separation of the nominal contacting surfaces, *h,* used for the calculation of the real contact pressure in **Equation 4.48,** with radial distance at 0.5 N, calculated numerically from the three areas are shown in **Fig. 4.18**. It can be seen that the separation distance, *h,* at $\rho = 0$ increased with increasing area density of silicon particles. The corresponding distributions of the real contact pressure with the radial distance presented in **Fig. 4.19** indicate that the real contact pressures at different areas varied in a similar way with the radial distance. The peak pressures occurred at the center of the contact, and decreased with the radial distance gradually, then sharply to zero. The value of the real contact pressure decreased with increasing the areal density. The maximum real contact pressure applied on Al-11% Si-F at the areas with different silicon particle area density increased slightly with the applied load, as shown in **Fig. 4.20**. At 0.5 N, the maximum real contact pressures applied on the area with the density of 0.04, 0.025, and 0.01/μm^2 were 1,677, 2,492, and 2,631 MPa, respectively.

4.4.4. Real Contact Radius

The real contact radius is defined as the radial distance at which the real contact pressure decreased to zero. **Fig. 4.21** presents the variations of the real contact radius in the five alloys with the applied load. In comparison with the distributions of the apparent

contact pressure applied on the five alloys shown in **Figs. 4.8** to **4.9**, the real contact pressures were distributed over a larger distance than the apparent contact pressures (**Fig. 4.14** to **4.16**). This is attributed to the slow reduction of the ratio, $F_1(h)$ / $F_{3/2}(h)$ with increasing radial distance. The Al-25% Si with high areal density and small silicon particles showed the smallest real contact radius. Increasing the silicon particle size and interparticle distance between small silicon particles, namely, reducing the areal density of small silicon particles, the real contact pressures spread over larger distance. The radial distance at which the real contact pressure decreased to zero at each load is approximately the same magnitude as the widths of the wear tracks of the alloys tested, which were generated after sliding wear tests presented in following chapters. **Table 4.6** lists the estimated real contact radius and the widths of wear tracks of Al-11% Si-F at tested loads of 0.5, 1.0, and 2.0 N. Therefore, the real contact pressures were more useful in terms of understanding the mechanical behaviour of the silicon particles under the tested conditions.

The use of the Greenwood-Tripp model to estimate the contact pressure may be justifiably questioned. The heterogeneous nature of asperity contact in etched Al-Si surfaces differs from the original model, which treats contacts between the asperities of monolithic materials. Here Si particles in contact with the steel are supported by the aluminum matrix. The model also assumes a very specific model for the asperities, i.e., that they are spherical with a single radius, and that they are randomly distributed in height according to a Gaussian distribution. This is very different from our etched surface, which clearly has a bimodal height distribution with acicular random sized particles. These differences will skew the absolute numerical results, but will not change the trends of how contact pressure varies with roughness, and hence the application of the

model is still instructive.

4.4.5. Prediction of Plastic Deformation for the Current Contact Systems

In the original model, the contact is made at the surfaces of homogeneous materials, and the plastic deformation is expected to initiate from the asperities when the real pressure exceeds the yield point of the solid [107]. While for the current contact system, etched Al-Si alloys are considered as a two component system, that is, the heterogeneous nature of the contact between the Al-Si alloy and the steel must be taken into account. The aluminum matrix supported the silicon particles. The hardness or yield point of silicon particles is much greater than that of aluminum matrix. Accordingly, the pressure carried by the silicon particles is transmitted to the aluminum matrix, and hence plastic deformation is expected to start from aluminum matrix adjacent to the load carrying particles.

Tabor [109] proposed that the indentation contact pressure, P = 1.1 Y, is sufficient to initiate plastic deformation of a material with a yield strength, Y, when a (hard) spherical ball pressing on a flat block. Using the slip-line field theory, an upper-bound calculation of a frictionless indentation of a semi-infinite block by a flat punch will require P= 2.89 Y to cause yielding [110]. The silicon sinking-in process can be considered analogous to plain strain deformation of aluminum block with a narrow punch for which the yield pressure for indentation is nearly three times the yield strength of aluminum, $P_m \sim 3$ Y. It is well known that the hardness of the material, H, equals to 3 times of the yield strength, Y [105]. Hence, plastic deformation, in the form of Si particle sinking into the aluminum matrix starts, when P approximately equals to the hardness of the aluminum matrix. The plastic deformation in the aluminum matrix allows silicon

particles to sink into the aluminum, while the aluminum matrix around the sunken-in silicon particle would in turn be pushed out, i.e., the formation of pile up, due to the conservation of material.

Comparison of the maximum real contact pressures applied on the five tested alloys listed in **Table 4.5** with their matrix hardness indicates that the maximum pressures applied on Al-25% Si, Al-11% Si-F, and Al-12% Si at the tested loads of 0.5, 1.0, and 2.0 N exceed theirs matrix hardness of 1,090, 660, and 495 MPa. According to the criterion proposed above, local plastic deformation is inevitable for Al-%25 Si, Al-11% Si-F, and Al-12% Si at all tested loads. Consequently, sinking-in of the silicon particles into the aluminum matrix is expected to happen in these three alloys at 0.5, 1.0 and 2.0 N. While the maximum contact pressures applied on Al-18.5% Si and Al-11% Si-C at 0.5 N were 741, and 654 MPa, which might not be high enough to induce local plastic flow of aluminum around the silicon particles in either alloy. Silicon particles are expected to carry the load and no sinking-in of silicon particles in these two alloys is expected at 0.5 N. But at 1.0, and 2.0 N, the maximum pressures exerted on Al-11% Si-C (690 and 731 MPa) were greater than its matrix hardness of 670 MPa, inferring that local plastic deformation around the silicon particles is inevitable in Al-11% Si-C. While application of 773 MPa at 1.0 N, and 815 MPa at 2.0 N are still not high enough to cause local plastic deformation around silicon particles in Al-18.5% Si. The silicon particles in Al-18.5% Si are not expected to sink into the aluminum matrix at all tested loads. These calculation results will be used to rationalize the surface damage occurred to the tested alloys in UMW regime in the following chapters.

Table 4.1. Curve fitting results from the Si particle height profiles of the five alloys

Alloy	Curve fitting results			
	a_1	b_1	C_1	R-square
Al-12% Si	3903	1.391	0.110	0.97
Al-11% Si-C	3236	1.229	0.106	0.912
Al-18.5% Si	95.64	1.609	0.090	0.979
Al-11% Si-F	961.7	1.544	0.112	0.765
Al-25% Si	2399	1.295	0.067	0.889

Table 4.2. Parameters used to calculate the contact pressure

Alloy	Composite Modulus (E^*, GPa)	Particle length (R_p, μm)	Standard deviation of particle height (σ, μm)	Area density of particles
Al-12% Si	59	86 ± 50	0.08	0.1 ± 0.1
Al-11% Si-C	59	93 ± 46	0.08	0.1 ± 0.1
Al-18.5% Si	61	70 ± 30	0.06	0.2 ± 0.1
Al-11% Si-F	59	6 ± 2	0.08	0.1 ± 0.1
Al-25% Si	62	8 ± 3	0.05	0.3 ± 0.1

Table 4.3. The maximum apparent contact pressure and Hertzian contact pressure

Pressure (MPa)	Load (N) / Alloy	0.5	1.0	2.0
The maximum apparent contact pressure	Al-12% Si	87	138	212
	Al-11% Si-C	90	143	210
	Al-18.5% Si	120	210	280
	Al-11% Si-F	126	185	272
	Al-25% Si	165	247	349
The maximum Hertzian contact pressure		309	403	511

Table 4.4. The effective contact radius and Hertzian contact radius

Radius (μm)	Load (N) / Alloy	0.5	1.0	2.0
The effective contact radius (G&T)	Al-12% Si	23	26	29
	Al-11% Si-C	22	24	28
	Al-18.5% Si	21	23	27
	Al-11% Si-F	21	24	28
	Al-25% Si	18	21	24
The Hertzian contact radius		7	11	15

Table 4.5. The maximum real contact pressure and Hertzian contact pressure

Pressure (MPa)	Load (N) / Alloy	0.5	1.0	2.0
The maximum real contact pressure	Al-12% Si	730	770	810
	Al-11% Si-C	650	690	731
	Al-18.5% Si	740	773	815
	Al-11% Si-F	2493	2580	2682
	Al-25% Si	1570	1620	1672
The maximum Hertzian contact pressure		310	403	511

Table 4.6. Comparison of estimated real contact radius with the width of wear track of Al-11% Si-F

Load (N)	0.5	1.0	2.0
Real contact radius (μm)	136	141	147
Width of the wear track	146 ± 6	152 ± 20	160 ± 16

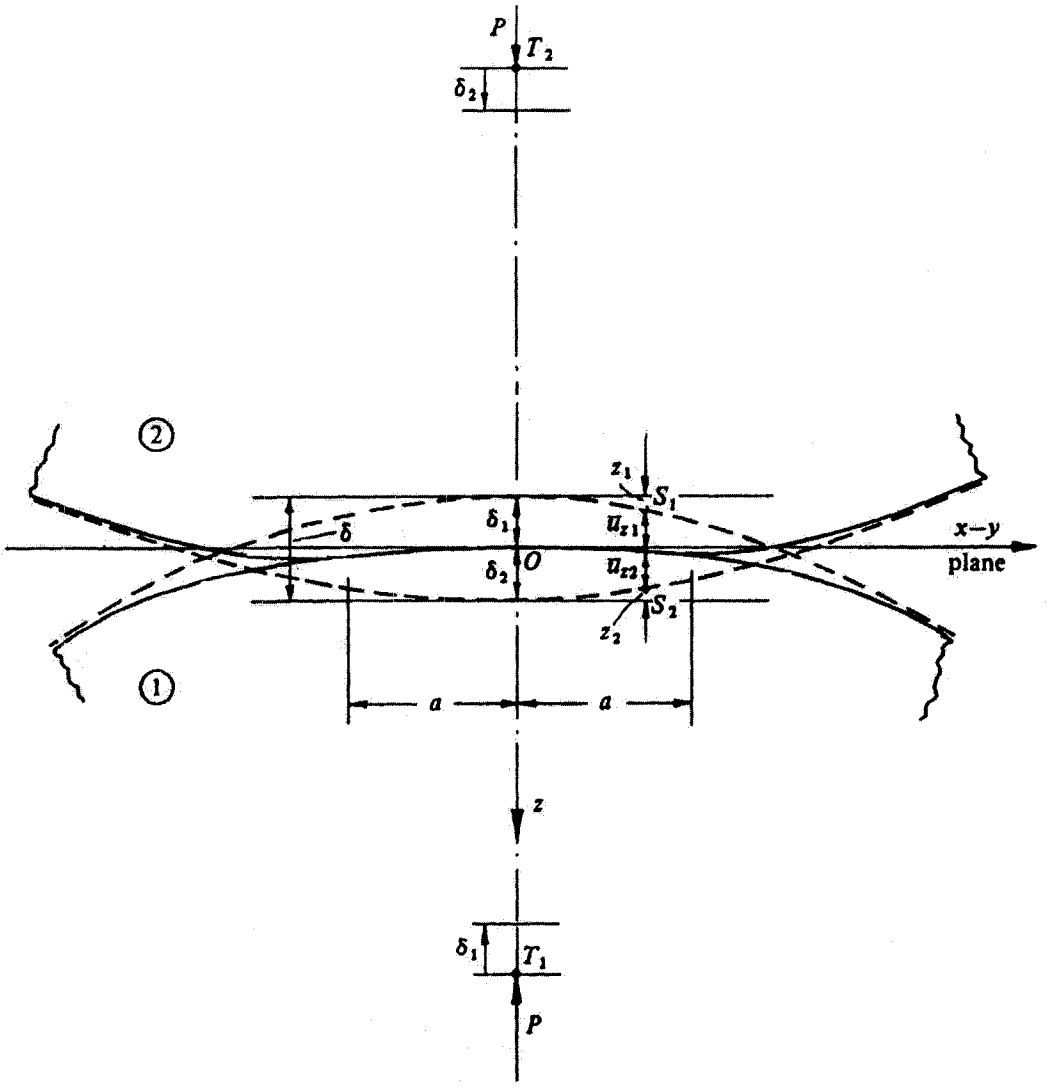

Fig. 4.1. Schematic of two frictionless solids of general shape in static contact [105].

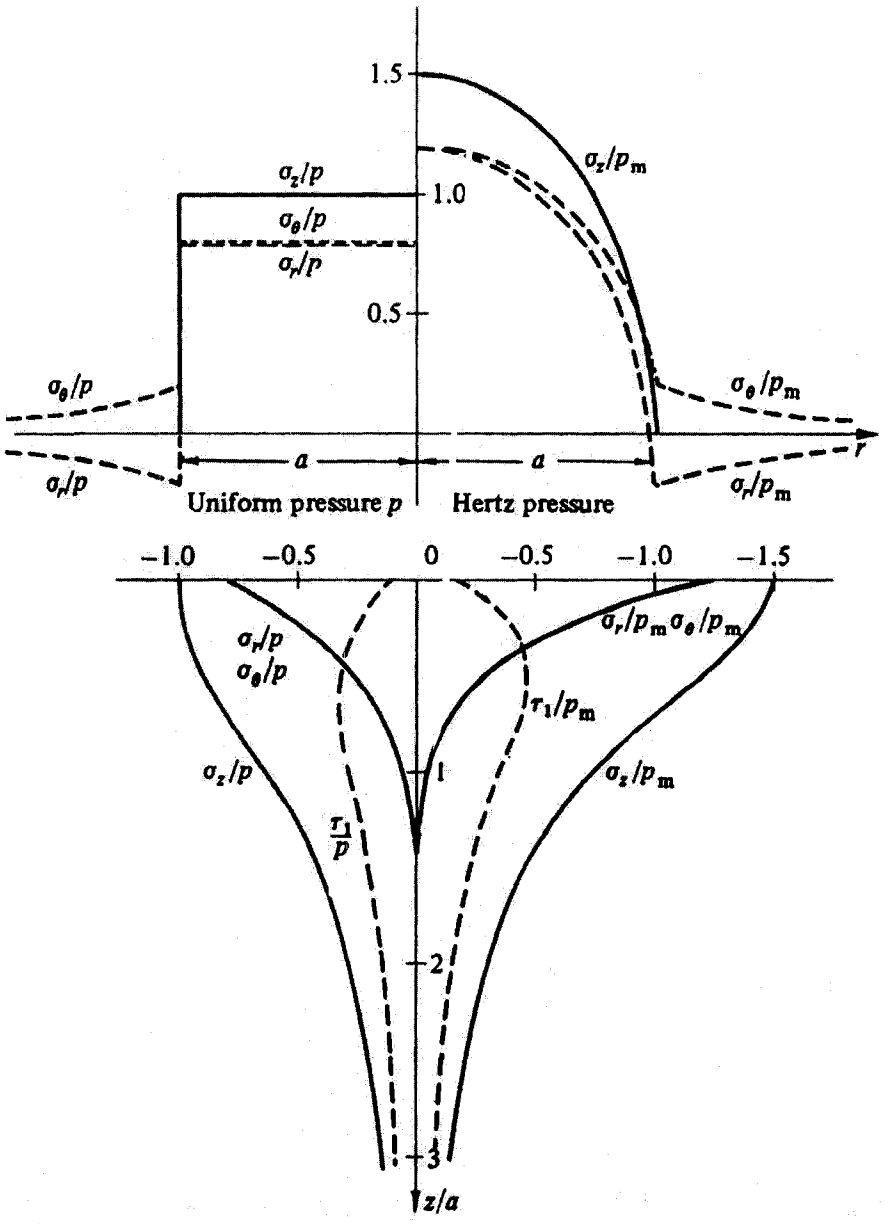

Fig. 4.2. Stress distributions at the surface and along the z-axis of symmetry caused by uniform pressure (left) and Hertzian pressure acting on a circular area of radius a [105].

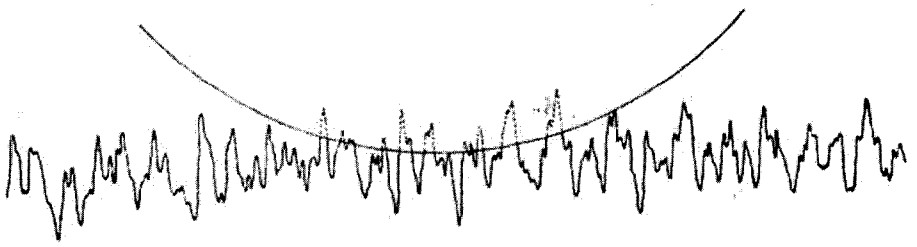

Fig. 4.3. Schematic illustration of the contacts between a nominally flat surface and a smooth sphere used in Greenwood and Tripp contact model [107].

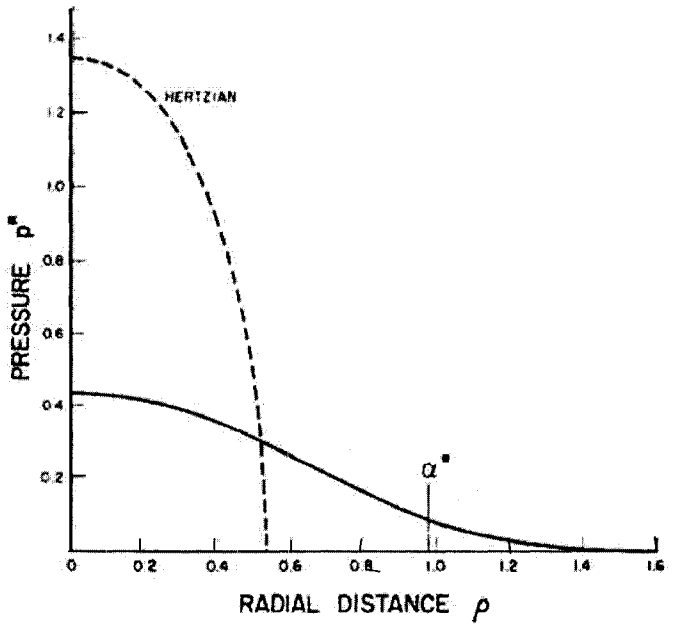

(a)

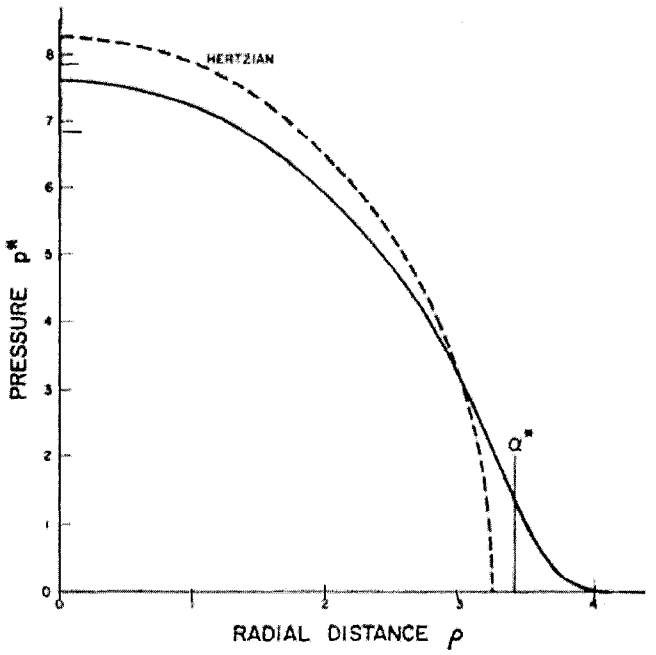

(b)

Fig. 4.4. Comparison of pressure distributions with Hertzian theory. **(a)** At low loads pressures are much lower than Hertzian and spread over much larger area; **(b)** At high loads calculated and Hertzian agrees well [107].

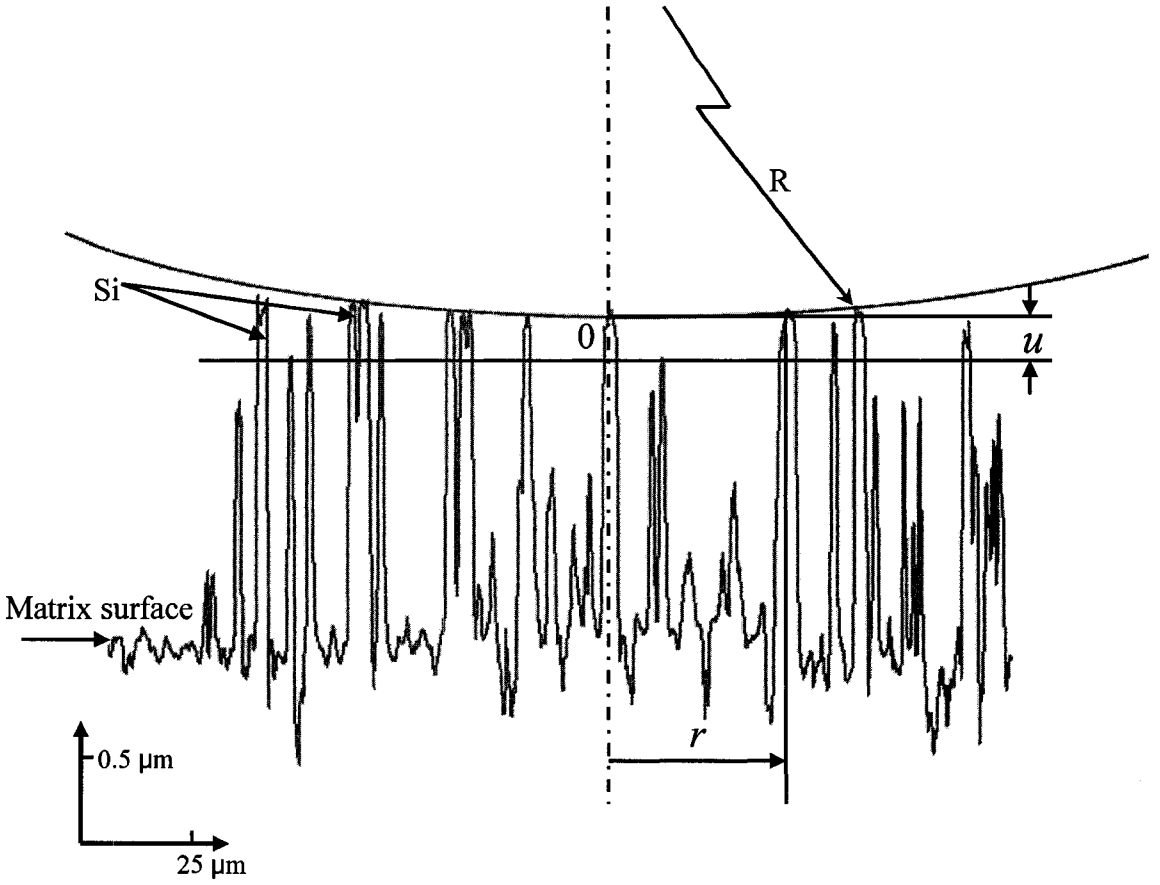

Fig. 4.5. Typical surface profile of the etched Al-Si alloys showing the reference matrix surface with particles (Optical surface profilometry trace) including a schematic of the counterface.

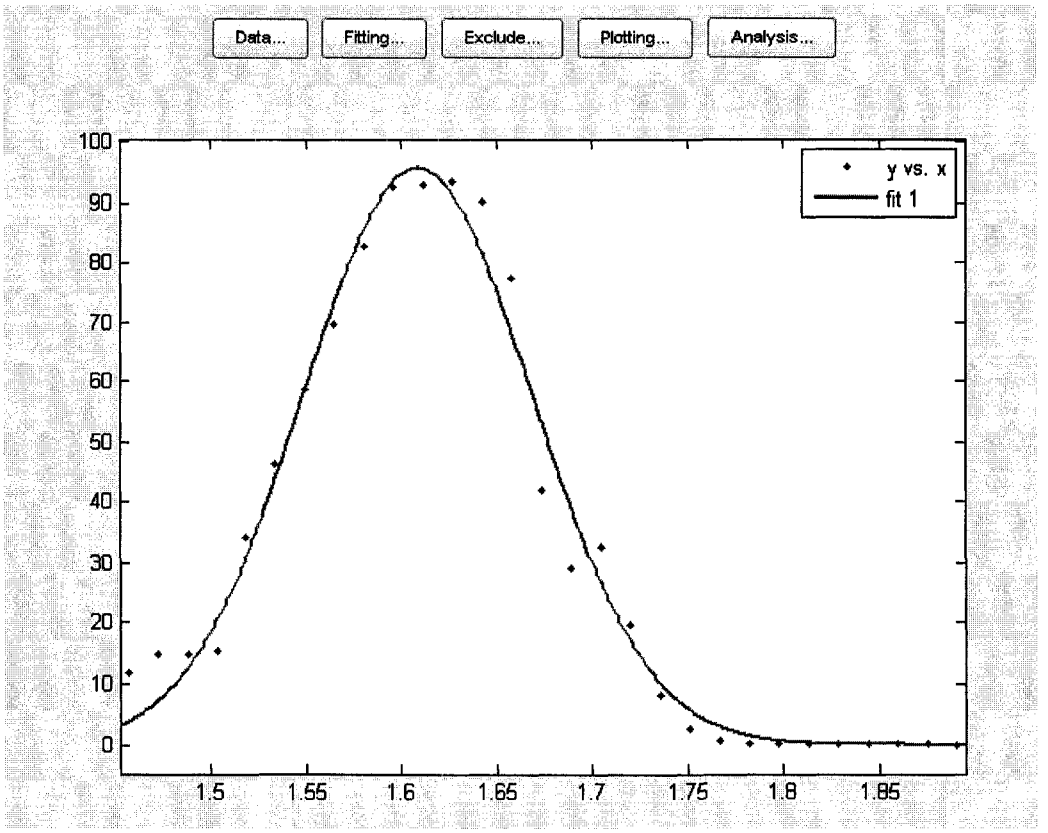

Fig. 4.6. An illustration of the fitting of the silicon particle height profile on the etched Al-18.5% Si surface to general Gaussian curve. The dotted curve is the initial Si particle height distribution on the etched Al-18.5% Si surface, and the Solid one shows the fitting curve.

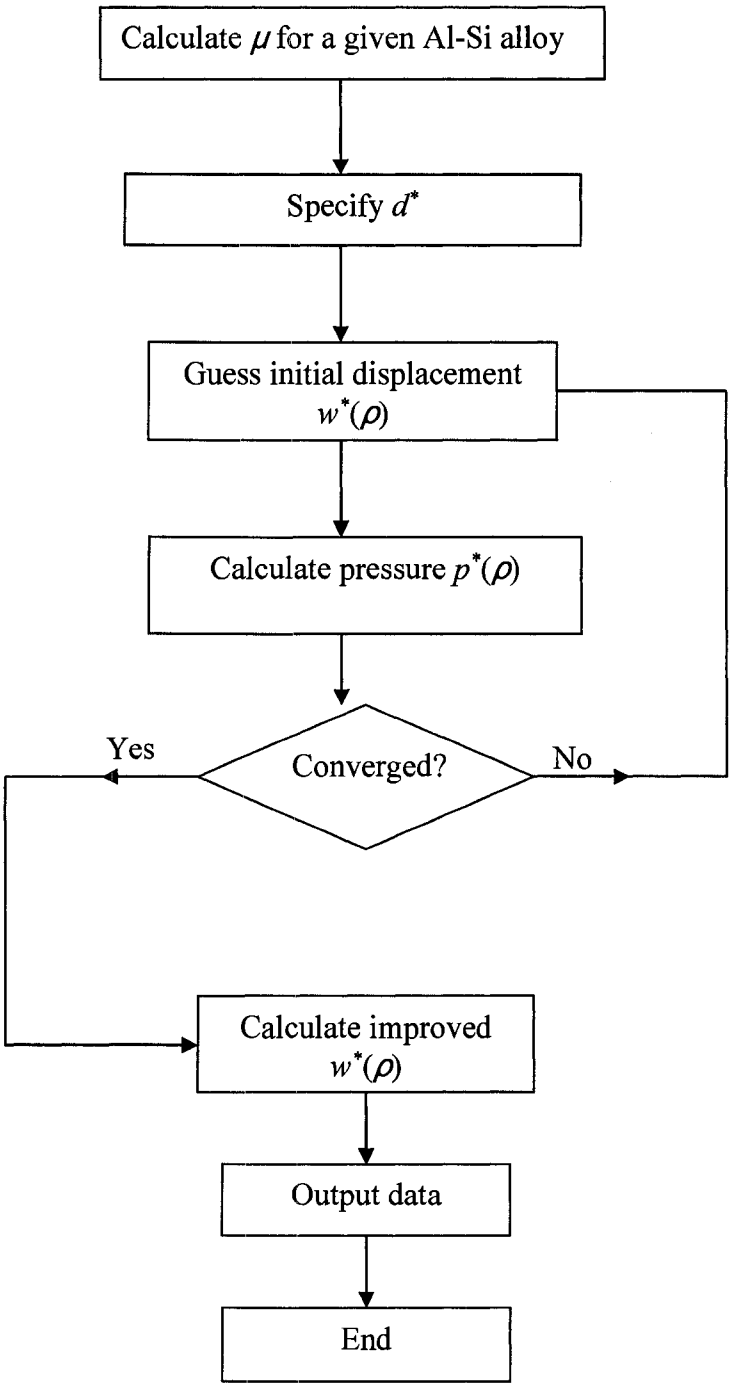

Fig. 4.7. Flow chart showing the numerical iterative procedure for the contact analysis.

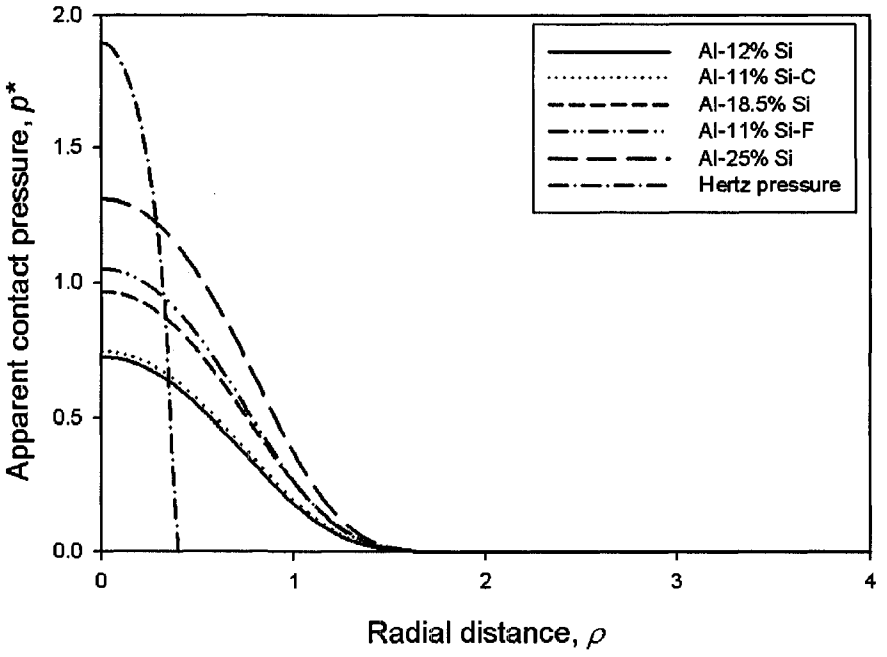
Apparent contact pressure, p*
Radial distance, ρ
Al-12% Si
Al-11% Si-C
Al-18.5% Si
Al-11% Si-F
Al-25% Si
Hertz pressure
0.0
0.5
1.0
1.5
2.0
0
1
2
3
4

(a)

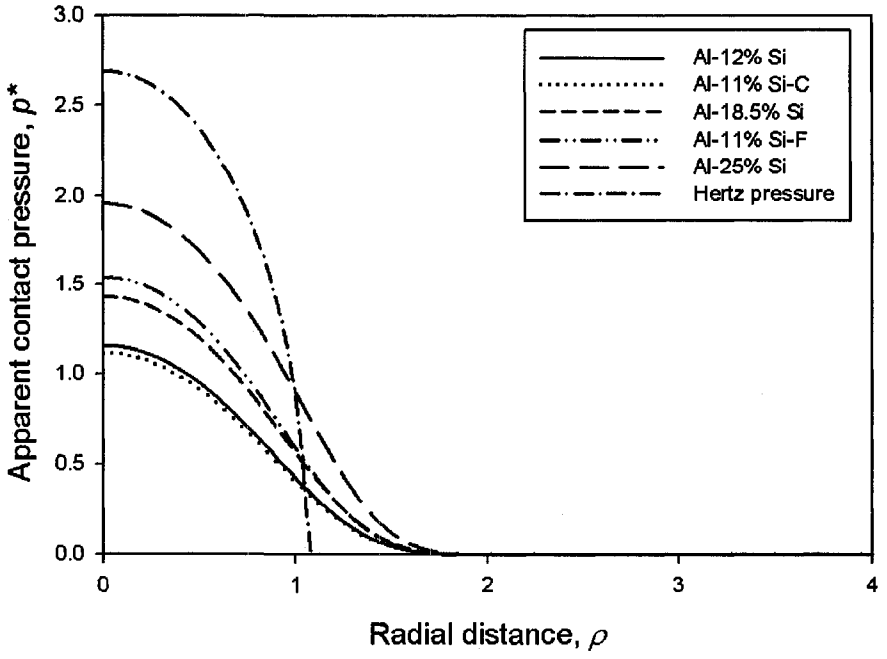
Apparent contact pressure, p*
Radial distance, ρ
Al-12% Si
Al-11% Si-C
Al-18.5% Si
Al-11% Si-F
Al-25% Si
Hertz pressure
0.0
0.5
1.0
1.5
2.0
2.5
3.0
0
1
2
3
4

(b)

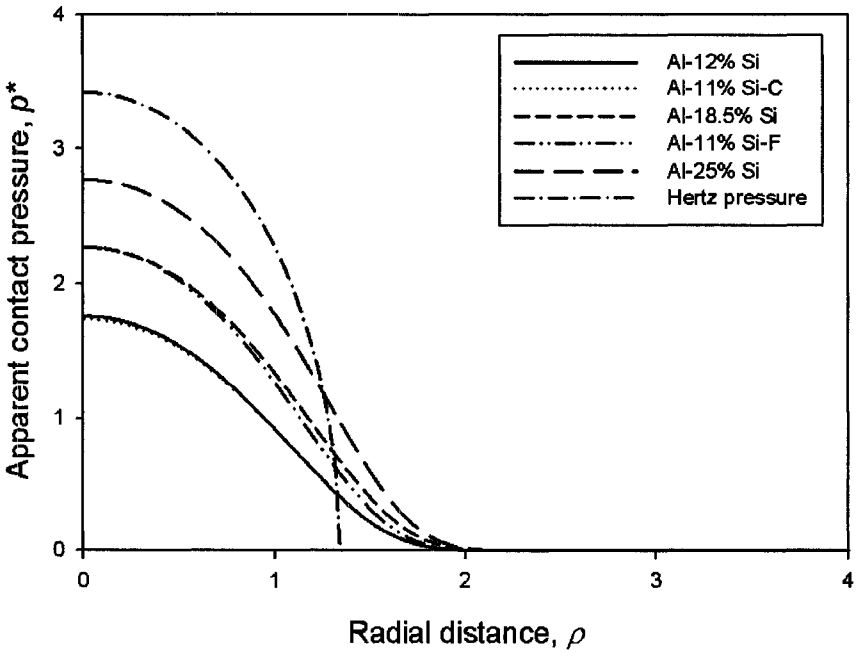

(c)

Fig. 4.8. Plot of dimensionless apparent contact pressure and Hertzian contact pressure applied to the five alloys with dimensionless radial distance at **(a)** 0.5 N, **(b)** 1.0 N, and **(c)** 2.0 N.

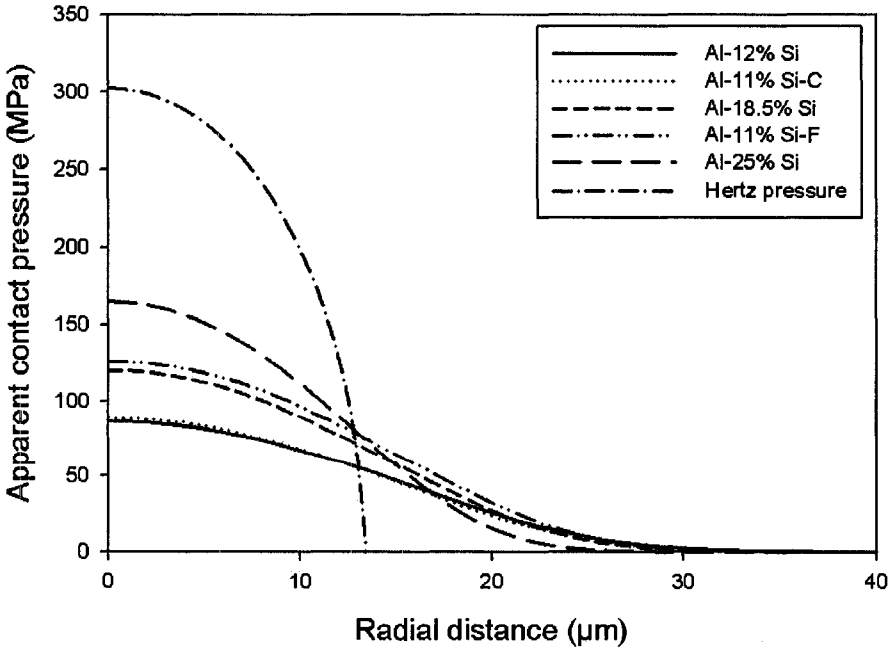

(a)

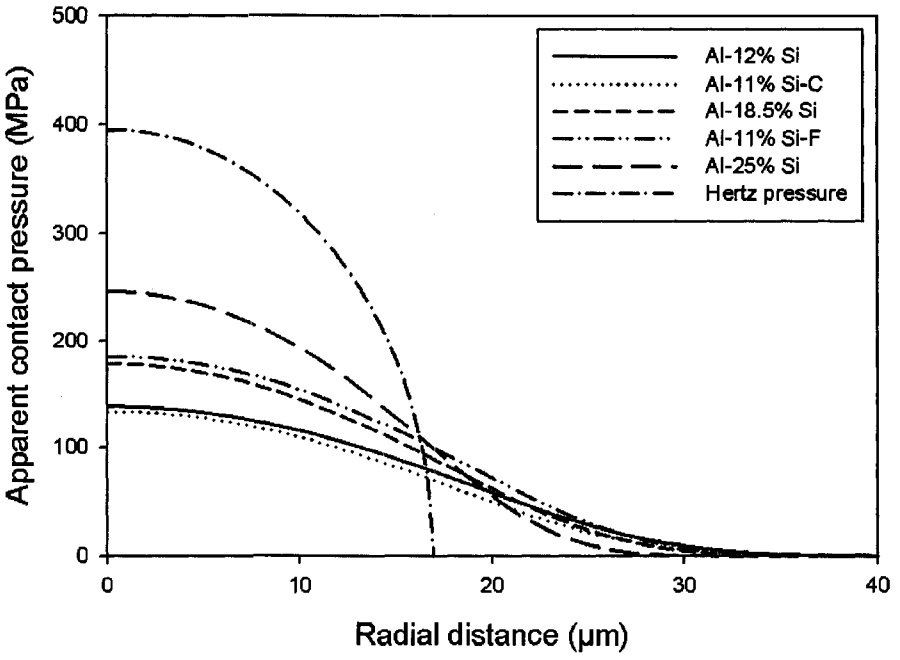

(b)

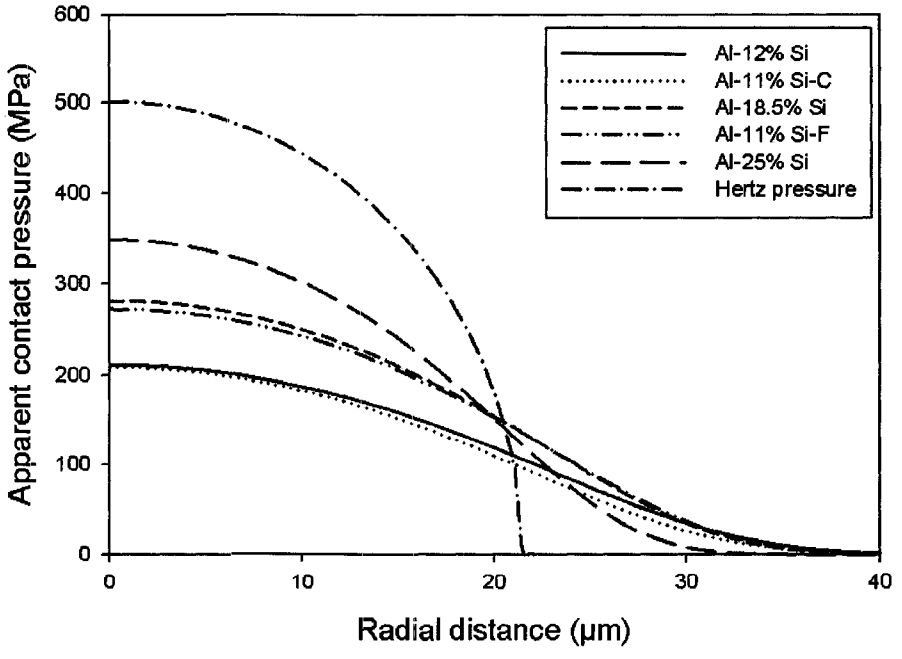

(c)

Fig. 4.9. Plot of dimensional apparent contact pressure and Hertzian contact pressure applied to the five alloys with dimensional radial distance at **(a)** 0.5 N, **(b)** 1.0 N, and **(c)** 2.0 N.

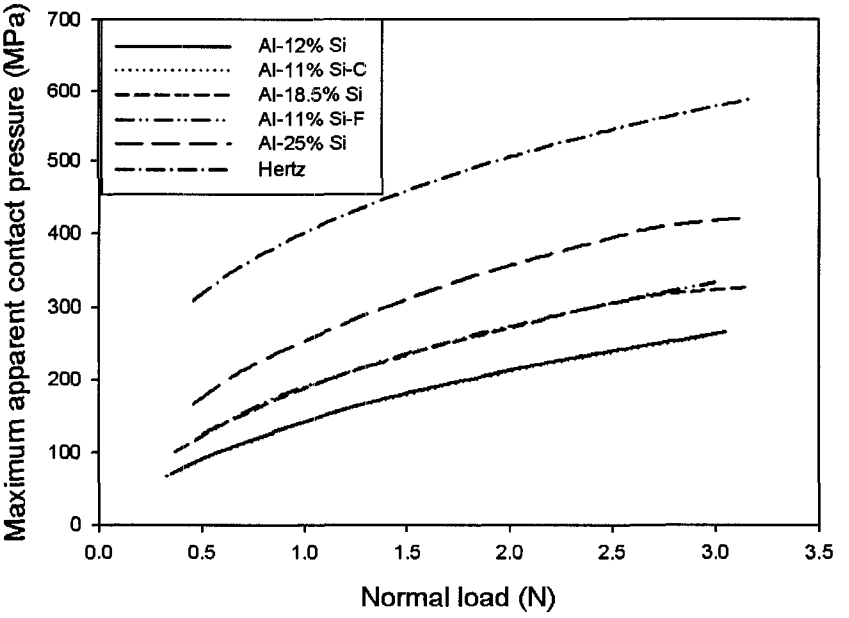

Fig. 4.10. Variation of the maximum apparent contact pressure and Hertzian pressure with normal load applied to the alloys tested.

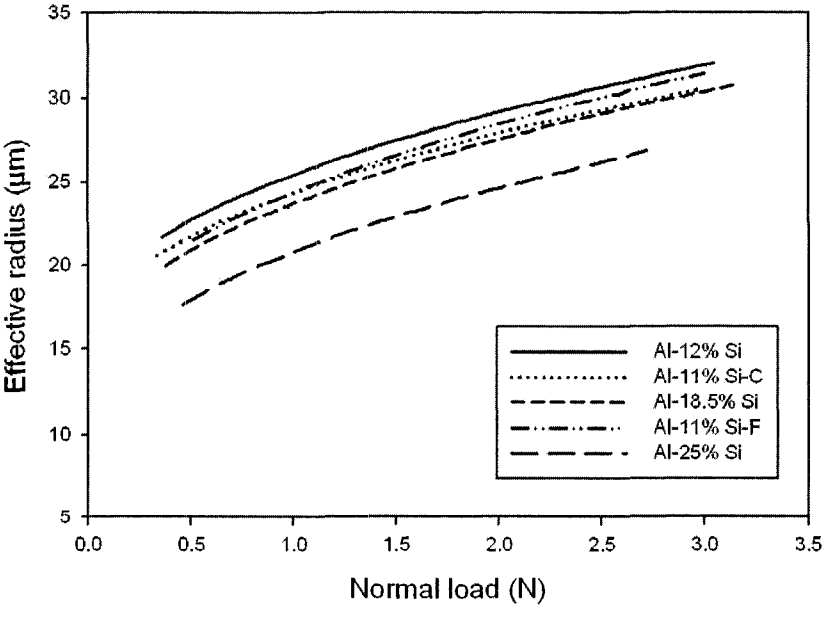

Fig. 4.11. Variation of effective contact radius in the five alloys tested with normal load.

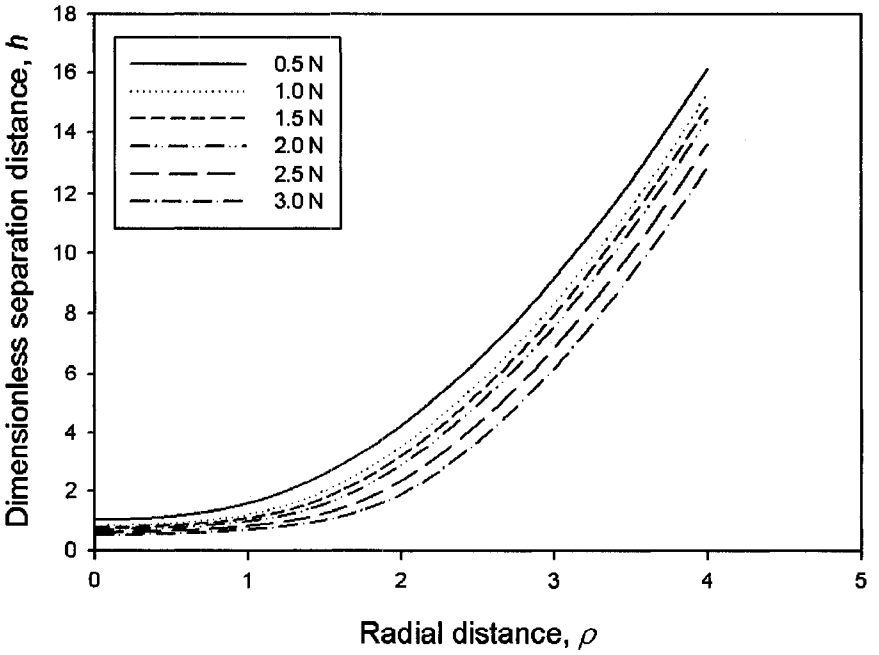

Fig. 4.12. Plot of the dimensionless separation distance with radial distance at each load indicated in the legend box, which was calculated from the contact between Al-25% Si and steel ball.

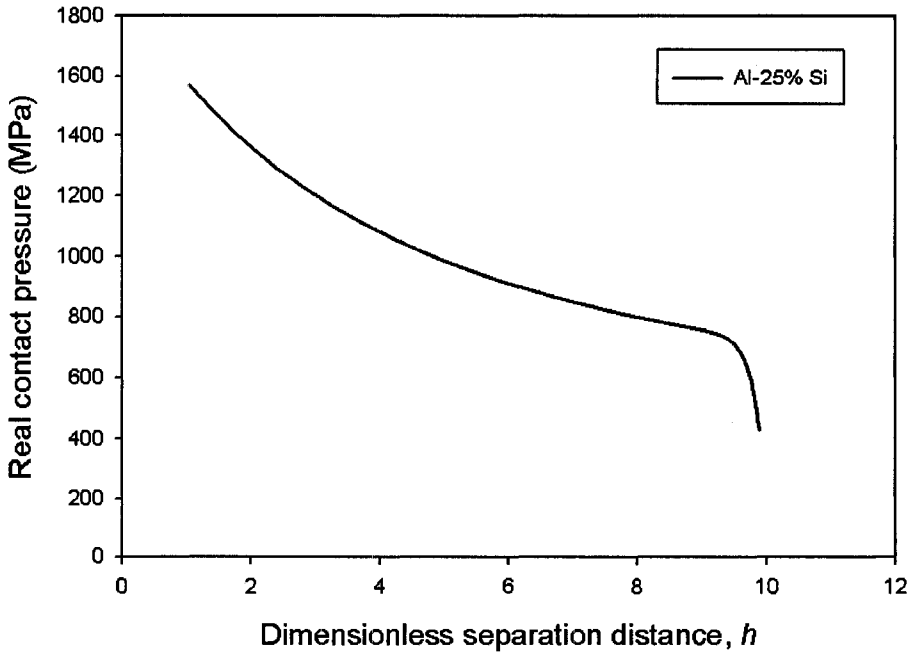

Fig. 4.13. Variation of the real contact pressure with the dimensionless separating distance, h, obtained from the calculation of the contact between Al-25% Si and steel ball at 0.5 N.

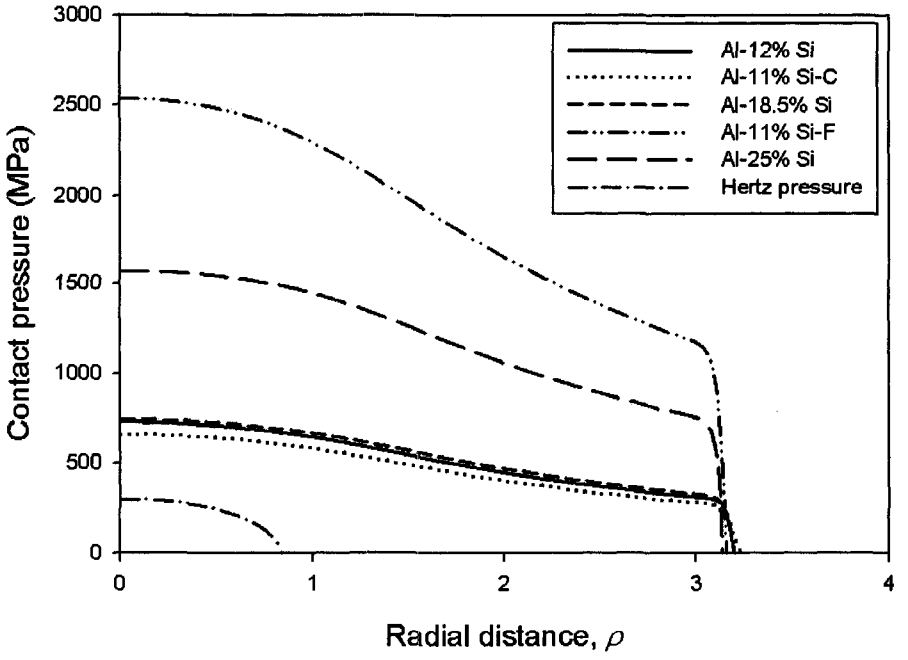

(a)

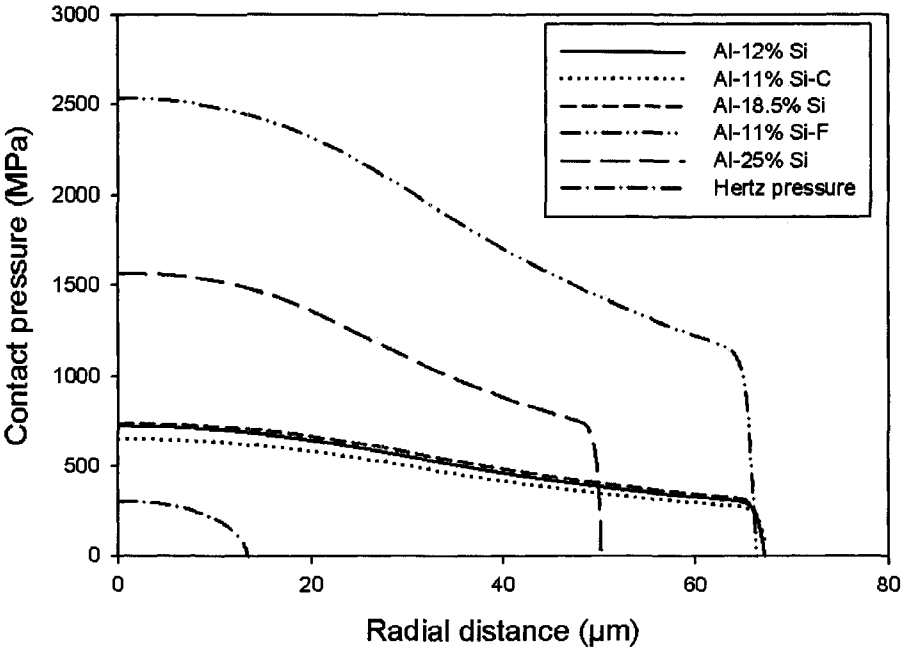

(b)

Fig. 4.14. Comparison of real contact pressure with Hertzian pressure distributions applied on the five tested alloys at 0.5 N. **(a)** Dimensionless plot, and **(b)** dimensional plot.

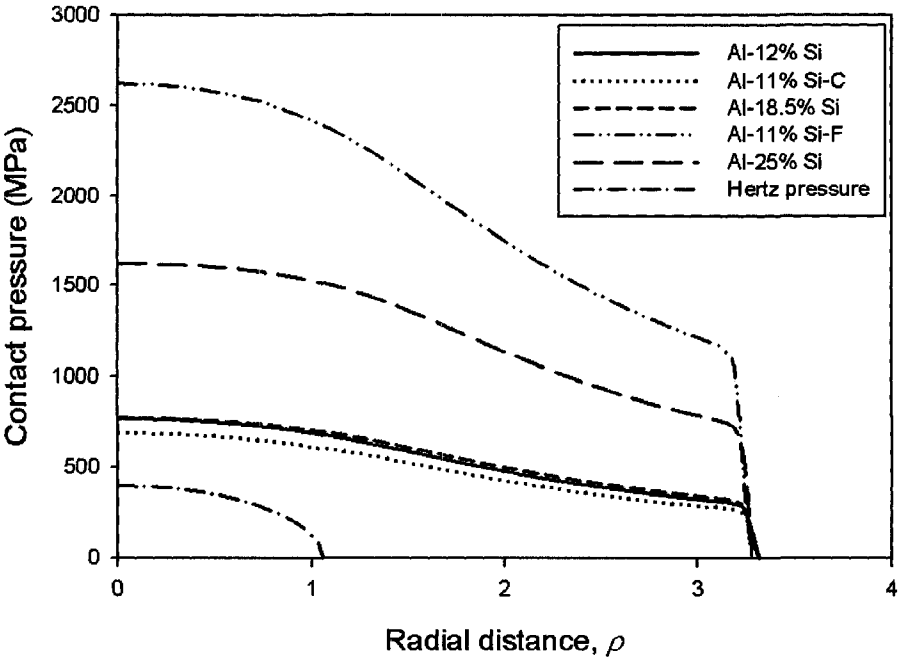

(a)

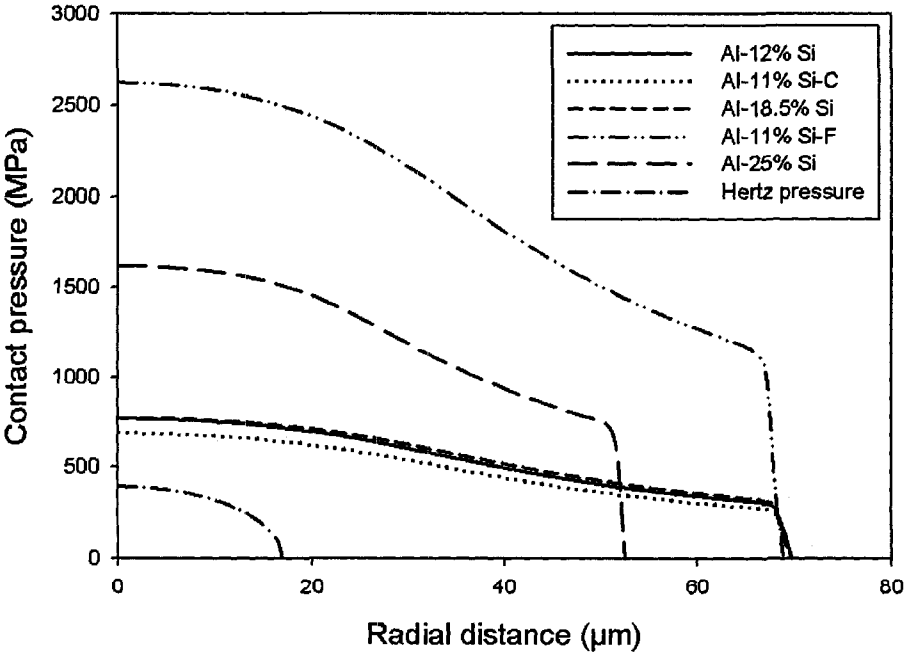

(b)

Fig. 4.15. Comparison of real contact pressure with Hertzian pressure distributions applied on the five tested alloys at 1.0 N. **(a)** Dimensionless plot, and **(b)** dimensional plot.

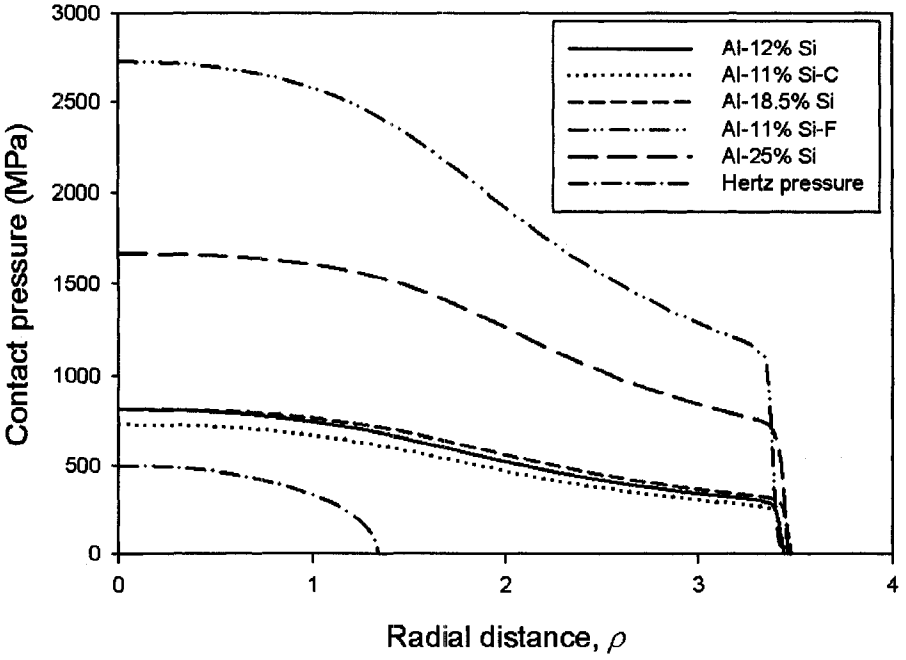

(a)

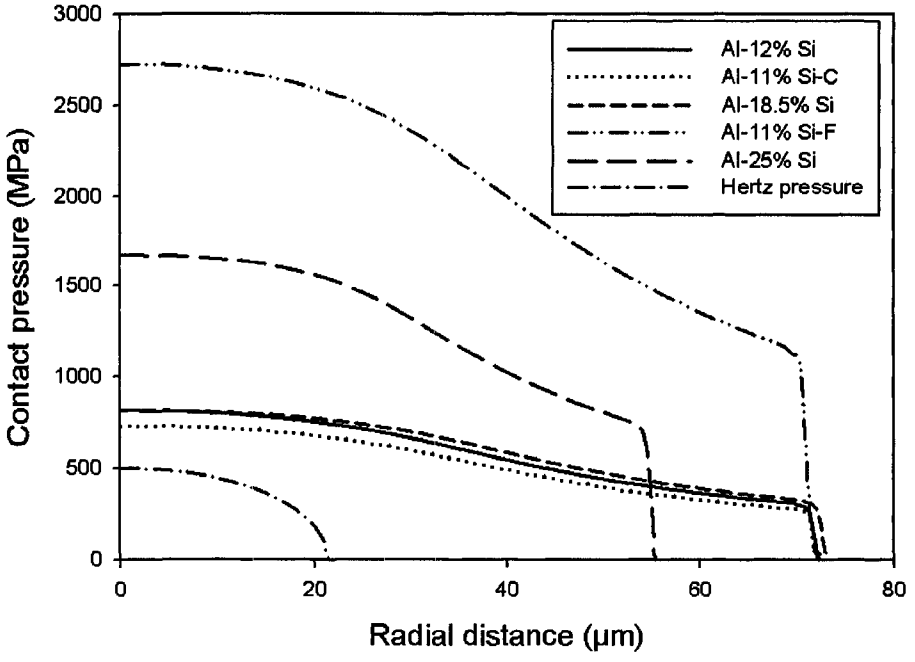

(b)

Fig. 4.16. Comparison of real contact pressure with Hertzian pressure distributions applied on the five tested alloys at 2.0 N. **(a)** Dimensionless plot, and **(b)** dimensional plot.

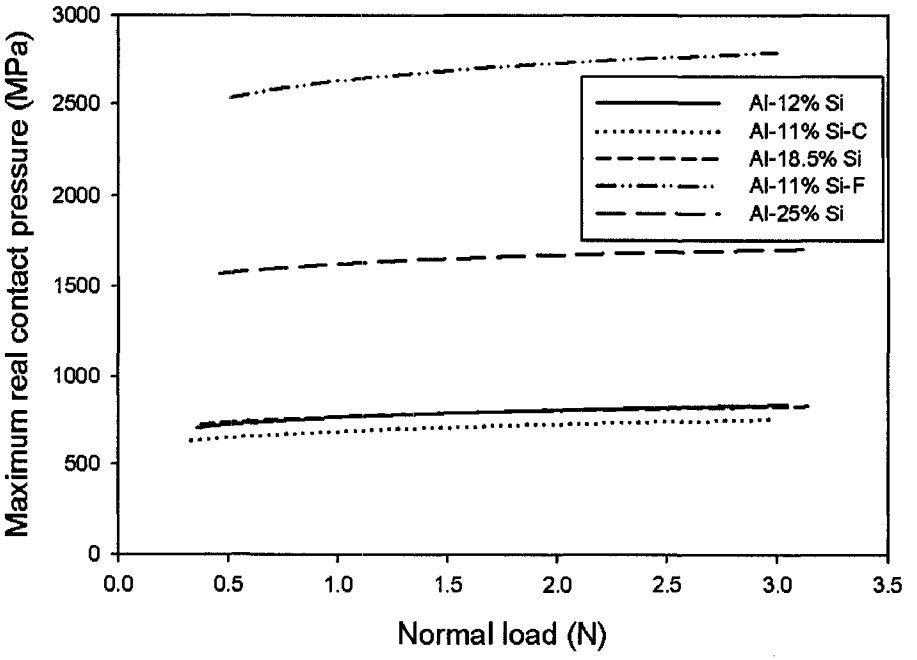

Fig. 4.17. Variations of the maximum real contact pressure applied on the five tested alloys with normal load.

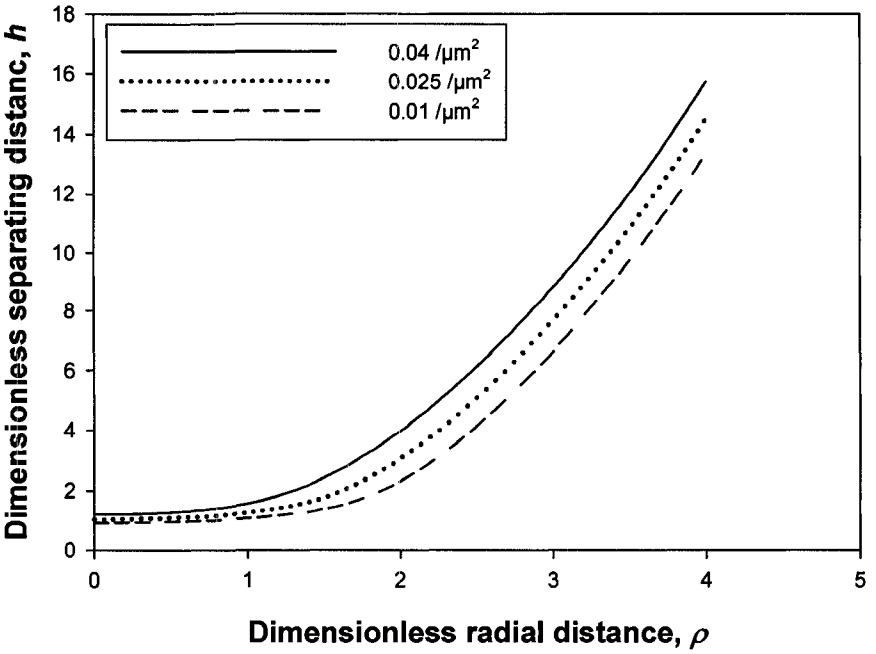

Fig. 4.18. Plot of the dimensionless separation distance with radial distance showing the effect of area density of silicon particles on the separation distance in Al-11% Si -F.

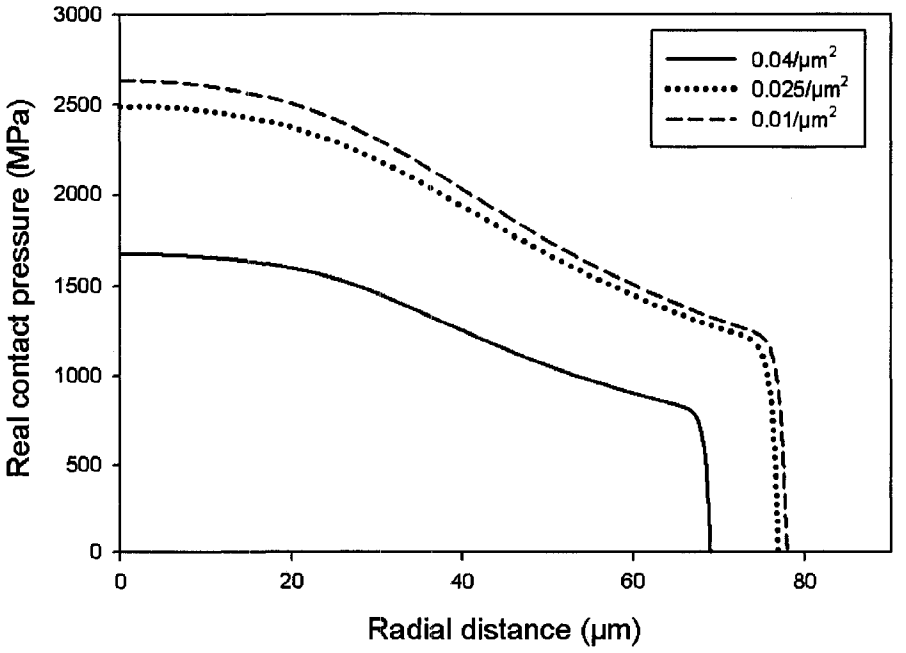

Fig. 4.19. Comparison of real contact pressure distributions applied on the Al-11% Si-F alloys with different Si particle area density at 0.5 N.

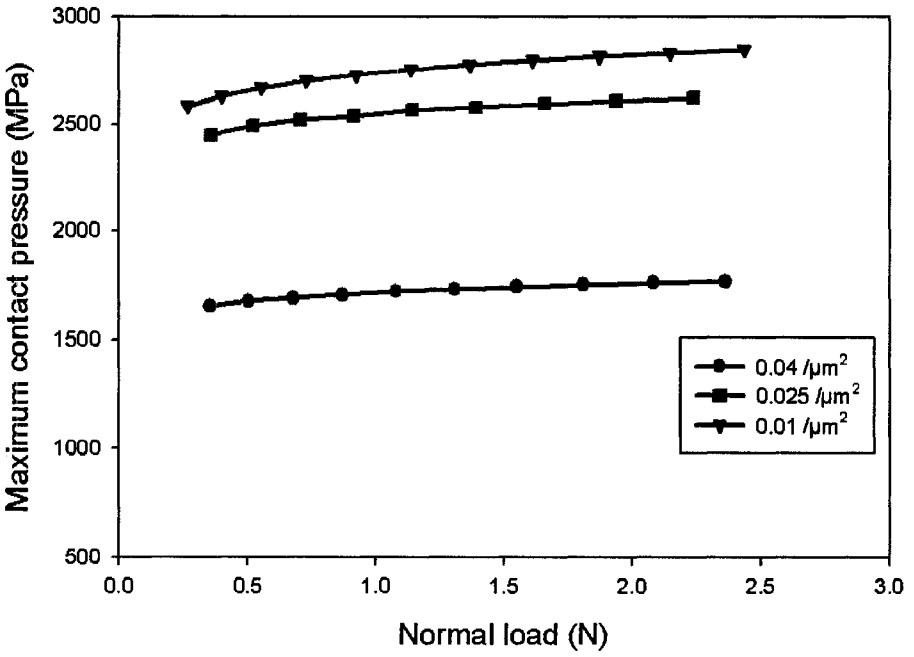

Fig. 4.20. Variation of the maximum real contact pressure with normal load applied to the Al-11% Si-F alloy with different Si particle area density.

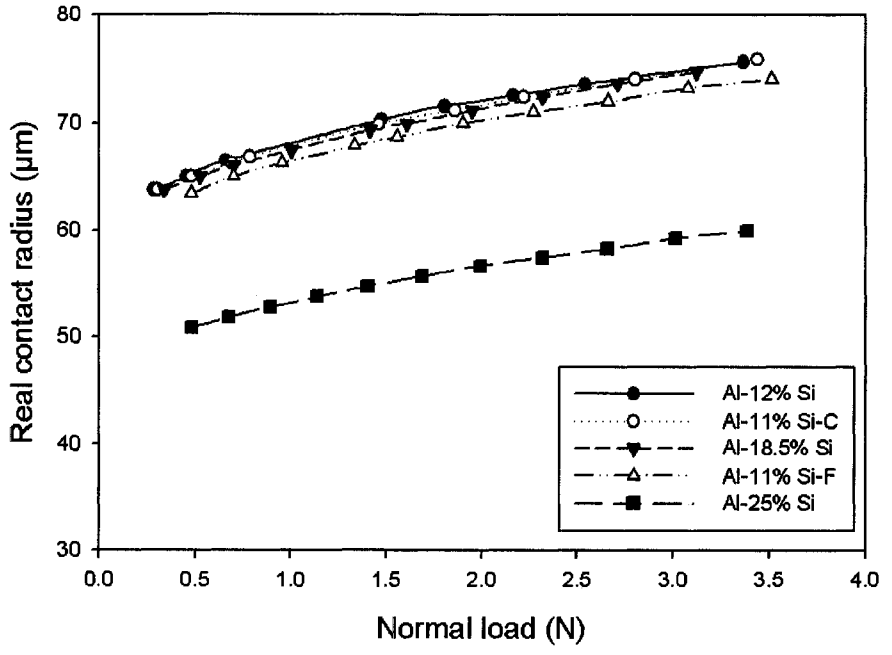

Fig. 4.21. Variation of real contact radius with normal load on the five alloys tested.

CHPATER 5 ULTRA-MILD WEAR MECHANISMS IN Al-Si ALLOYS

5.1. Introduction

In this chapter, UMW wear mechanisms are identified using a combination of optical profilometry and scanning electron microscopy. The surface damage characteristics of Al-Si alloys in the UMW regime, which was achieved by conducting the sliding wear tests at light load of 0.5 N, and under boundary lubricated conditions with synthetic engine oil as lubricant, is presented. The propensity of plastic deformation for the loaded Si particles in Al-12% Si and Al-11% Si-C, with similar silicon particle aspect ratio and size, are compared in **Section 5.2**. **Section 5.3** presents the identification of wear mechanisms operating in the UMW regime using Al-12% Si as a model alloy. In **Section 5.4**, the effect of matrix hardness on the UMW mechanism is examined by performing sliding wear tests on Al-11% Si-C with similar silicon particle morphology and size but harder matrix under the same test conditions. Ultra-mild wear damage happened to Al-18.5% Si under the same test conditions is presented in **Section 5.5**, aiming to examine the effect of microstructure on UMW mechanism.

5.2. Propensity for Plastic Deformation in Al-12% Si and Al-11% Si-C

The maximum contact pressures applied to Al-12% Si, and Al-11% Si-C varies with the applied load in the way shown in **Fig. 5.1**. The maximum contact pressure on the silicon particles in Al-12% Si at the applied test load of 0.5 N used in the current experiments is 730 MPa. In the alloy with higher matrix hardness (Al-11% Si-C) the

maximum contact pressure applied to the particles is 654 MPa. The maximum contact pressures on the two alloys are similar because the silicon particle size, aspect ratio, and exposed height are comparable. It follows that the contact pressure applied to Al-12% Si exceeded the matrix hardness of 495 MPa, while the contact pressure on Al-11% Si-C was slightly lower than its matrix hardness of 670 MPa. Thus, in the Al-12% Si alloy there is a higher propensity for the loaded silicon particles to induce plastic flow of aluminum in their vicinity as a result of the penetration of the silicon particles into the matrix when compared to Al-11% Si-C. Consequently, the silicon particles in Al-12% Si are expected to sink into the Al matrix under the load conditions used in the current experiments. Experimental evidence for particle sinking-in and aluminum piling-up mechanisms is given in **Section 5.3**.

5.3. Ultra-mild Wear in Al-12% Si

5.3.1. Characteristic Features of Damage in Ultra-Mild Wear

Surface damage in the ultra-mild regime occurred in two ways i) via the reduction of silicon particle height, primarily by sinking-in of the hard particles into the soft aluminum, and ii) via plastic deformation and the flowing-out of the adjacent aluminum matrix in the form of pile-ups at the vicinity of sunken-in silicon particles. These mechanisms are described in **Sections 5.3.2** and **5.3.3**.

5.3.2. Statistical Evaluation of the Particle Height Reduction Process

An important aspect of the surface damage process in the Al-Si alloy studied was the reduction in the heights of the silicon particles located within the wear tracks. Evidence for particle height reduction during ultra-mild wear is given in **Figs. 5.2**. The

initial average silicon particle height of 1.80 μm in Al-12% Si rapidly decreased to 0.28 after sliding for 10^3 cycles (**Fig. 5.2**). After sliding for 5 x 10^3 cycles, the average height of the silicon particles projecting above the aluminum matrix was only 0.08 μm. After sliding for 10^4 cycles it was no longer possible to differentiate the locations of silicon peak heights from the aluminum surface profile. The reduction in the average silicon particle height with the sliding distance is plotted in **Fig. 5.3**.

5.3.3. Metallographic Evidence for Particle Sinking-in and Aluminum Pile-up Formation

Metallographic evidence for the particle sinking-in mechanism responsible for particle height reduction during sliding wear of Al-12 % Si is given in **Figs. 5.4** to **5.7**. These figures show the back-scattered SEM images taken within the wear tracks of Al-12% Si, as well as the corresponding 3-D surface profiles constructed from the optical profilometer data of the same wear tracks shown in the SEM micrographs. They collectively illustrate the evolution of the surface morphology during wear at 0.5 N at different stages for the soft eutectic Al-Si alloy after testing to sliding cycles that varied between 10^3 cycles and 5 x 10^4 cycles.

The optical profilometer image shown in **Fig. 5.4 a** obtained after sliding for 10^3 cycles indicates that the damage inside the wear track consisted of a reduction in the heights of the particles in comparison to those outside the track. The matrix material adjacent to the particles became elevated compared to the parts that lay away from the particles. The corresponding SEM image in **Fig. 5.4 b** shows that there was no evidence of particle fracture. The particle contact surfaces did not appear to exhibit signs of wear; no evidence for particle abrasion can be seen on the contact surfaces of the particles. In

fact, the SEM image in **Fig. 5.4 b** confirms that top surfaces of silicon are smooth and free of abrasive scratches. Thus, the particle height decrease was the result of the sinking-in of silicon particles into the aluminum matrix. To accommodate the downward motion of the silicon particles, soft aluminum adjacent to these particles flowed out of the matrix to accommodate the indentation made by the particles penetrating into the matrix. Consequently, at these locations the matrix became raised above its initial level -i.e. aluminum pile-ups were formed around the sunken-in silicon particles. The formation of aluminum pile-ups adjacent to most silicon particles can be seen in **Fig. 5.4 b**. **Fig. 5.4 c** is a 3-D optical surface profilometer image of the same section of the wear track, where the same aluminum pile-ups next to the matching silicon particles can be seen. In addition, it becomes clear that silicon particles within the wear track have become embedded in the aluminum matrix. These particles with reduced elevation within the wear track are also indicated in **Fig. 5.4 c.** The EDS analyses confirmed that the material piling-up around the sunken-in silicon particles had the same composition as the surrounding matrix material (**Fig. 5.5**).

At 5 x 10^3 cycles, the wear track became wider, and the average height of the particles inside the wear track continued to decrease (Fig. **5.6 a**). The areas covered by aluminum pile-ups adjacent to the particles became larger. The pile-ups in the vicinity of the particles, as seen in **Fig. 5.6 b**, also suggests that the size of the pile-ups is not symmetrical, but generally more material tends to accumulate in front of the silicon particles along the sliding direction. This can be attributed to the bending of the Si particles by the shear stress toward the sliding direction, which results in the matrix ahead of the silicon particles being pushed forward in the direction of sliding. The initiation of direct contact between the top portion of the aluminum pile-ups and the couterface now

leads to the surface damage to these elevated plateaus. Consequently, surface damage in the form of longitudinal scratch marks within the wear track started to appear.

Figs. 5.7 a and **b** show the evolution of damage within the wear track at 10^4 cycles, where the silicon particles became almost totally embedded into the aluminum matrix. The longitudinal surface scratches on the pile-ups are continuous. At 5 x 10^4 cycles (**Figs. 5.8 a** to **c**) the same damage mechanisms continued to operate. An additional feature of the damage progress, however, becomes apparent in **Fig. 5.8 b,** where the silicon particles show evidence of fracture and fragmentation. In fact, the silicon fracture process began earlier (fractured particles can be seen at 10^4 cycles in **Fig. 5.8 b**. It is conceivable that work-hardening of the aluminum matrix during sliding made particle sinking more difficult and thus facilitated particle fracture. The effect of matrix hardness on ultra-mild wear can be better understood when the behaviour of the harder of the eutectic alloys -the Al-11% Si-C- is investigated in detail (**Section 5.4**).

5.3.4. Microstructural Features of the Subsurface Adjacent to the Contact Surface

Additional evidence for the damage mechanisms in ultra-mild wear explained above is provided by the investigation of a cross-section of the wear track prepared using a focused ion beam milling (lift-out) technique. A cross-sectional secondary electron FIB image of the wear track at 5 x 10^4 cycles is given in **Fig. 5.9**. This image shows the morphology of a silicon particle embedded within the wear track, and the formation of aluminum pile-up around it. Microstructural features around the sunken-in silicon particle are presented in the cross-sectional TEM image (**Fig. 5.10**), which was taken from the same area as the FIB image in **Fig. 5.9**. The silicon particle in the TEM image was pulled out during TEM sample preparation. It is noted that aluminum grains in the piled up

plateau and the aluminum matrix adjacent to the sunken-in silicon particle are refined to the nano-crystalline size. The grain sizes are smaller in the top section (around 120-200 nm) than those in a deeper area (300-400 nm). Dislocation networks are also observed in the aluminum matrix around sunken-in silicon particles, which indicates a plastic deformation zone. This infers that the silicon particle sinking-in leads to extensive plastic deformation to the aluminum matrix adjacent to the sunken-in silicon particles, even at 0.5 N.

5.4. Ultra-mild Wear in Al-11% Si-C

5.4.1. Silicon Particle Height Reduction in Al-11% Si-C

The matrix hardness (670 MPa) of the Al-11% Si-C alloy was 70% higher than that of Al-12% Si (495 MPa). Because of this high matrix hardness, the particles in Al-11% Si-C are not expected to sink-in as readily as those located in the wear tracks of Al-12% Si. The stress analysis presented in **(Sections 5.2 and 4.4)** suggests that, at the test load of 0.5 N, the contact pressure applied to the silicon particles in Al-11% Si-C- 654 MPa (**Fig. 5.1**) -might not be high enough to press these particles into the matrix.

Fig. 5.11 presents the histograms showing the variation of silicon particle height with respect to the aluminum matrix height with the sliding cycles. The reduction in the average silicon particle height with the sliding cycles is plotted in **Fig. 5.12**. According to **Figs. 5.11** and **5.12**, only a slight decrease in the silicon particle height could be observed within the wear tracks of the Al-11% Si-C after sliding for 5 x 10^3 cycles. The initial average silicon particle height of 1.60 μm in the Al-11% Si decreased to 1.53 after 10^3 cycles (**Fig. 5.12**). After sliding for 5 x 10^3 cycles, the average height of the silicon particles projecting above the aluminum matrix was 1.42 μm. After 10^5 cycles, silicon

particles still protruded above the aluminum matrix by 0.81 μm.

5.4.2. Evolution of the Worn Surfaces in Al-11% Si-C

Figs. 5.13 a to **c** show the surface damage within the wear tracks of Al-11% Si-C after sliding for 10^4 cycles. A 3-D surface profilometer image shown in **Fig. 5.13 a** illustrates that after sliding for 10^4 cycles a small number of silicon particles exhibited a height decrease. No obvious matrix piling-up could be observed around these silicon particles (**Fig. 5.13 b**). The contact surfaces of the silicon particles within the wear track shown in **Fig. 5.13 c** exhibited microscopic scratches in the sliding direction suggesting that they had been subjected to wear. The initial particle sinking-in in this alloy was not as prominent as in the Al-12% Si; the particles did show a height reduction in Al-11% Si due to wear of the silicon plateaus rather than their sinking into the matrix.

Pile-ups started to form after 5 x 10^4 cycles, as shown in **Figs. 5.14 a** to **c**. The Si particle surfaces within the wear track appeared to be rougher and did not have the polished appearance of those outside the wear track. The silicon particles around which pile-ups were observed were also found to be fractured and fragmented into smaller sections (**Fig. 5.14 b**). This observation infers that the pile-up process and, in turn the silicon particle sinking-in, was likely assisted by the fragmentation of large aspect ratio particles to shorter segments. Thus, as the sliding process progressed, the particle sinking-in mechanism has become prominent even in the alloy with high matrix hardness. Eventually, after sliding for 10^5 cycles, silicon particle sinking-in and piling-up of aluminum around the sunken-in silicon particles became obvious (**Fig. 5.15 a** and **b**).

5.4.3. Summary and Discussion

From the experimental observations made on the worn surfaces of eutectic Al-Si alloys, which were presented in previous sections in this chapter, the progression of surface damage events in UMW regime was identified to generally consist of the following steps:

i) Wear of the top surfaces of silicon particles by the counterface,

ii) Embedding of silicon particles into aluminum matrix (or particle sinking-in),

iii) Plastic deformation of aluminum causing the formation of aluminum pile-ups adjacent to the sunken-in silicon particles,

iv) Wear of the elevated portions of aluminum plateaus by the counterface.

The main stages of the surface damage process during ultra-mild wear are schematically illustrated in **Fig. 5.16**. However, the alloy with the harder matrix, Al-11% Si-C, exhibited less damage in UMW than the softer Al-12% Si. The silicon particles in both alloys had a similar aspect ratio and size (**Figs. 3.2** to **3.5**), indicating that the matrix hardness played a key role in the ultra-mild wear resistance. The silicon particle height in the Al-12% Si decreased rapidly at the beginning of the sliding process. No wear features were observed on the silicon particle plateaus located inside the wear tracks. It was difficult to identify step i in Al-12% Si. Aluminum pile-up occurred around the sunken-in silicon particles after just sliding for 10^3 cycles, in order to accommodate the sinking-in process and to conserve the plastically deformed volume. After sliding for 5×10^3 cycles, scratch marks caused by the counterface appeared on the raised portions of the aluminum pile-ups around the sunken-in silicon particles. After sliding for 5×10^4 cycles, silicon particles were almost completely embedded in the aluminum matrix.

On the other hand, silicon particles in the Al-11% Si-C showed signs of wear at the early stages of sliding. There was neither a comparable reduction in silicon particle

exposure, nor aluminum pile-up formation after sliding for 10^4 cycles. However, silicon particles with large aspect ratio located on the contact surface exhibited evidence of fracture, indicating the high propensity of fragmentation for the large aspect ratio silicon particles. Based on **Equation 4.48**, which was used to estimate the real contact pressure applied on the Si particles in **Chapter 4**, the real contact pressure increases with decreasing the particle size if other parameters, E^*, σ, are kept constant. **Fig. 5.17** shows the variation of the maximum contact pressure on the silicon particles with the silicon particle size calculated for Al-11% Si-C at the applied load of 0.5 N using **Equation 4.48** in **Section 4.3**. When silicon particle fracture occurred during the course of sliding, the particle size decreased and the maximum contact pressure exerted to the particles increased. According to **Fig. 5.17**, the pressure exerted by the counterface on the exposed silicon particles should increase with a decrease in the silicon particle size, exceeding the aluminum matrix hardness and prompting local plastic flow around the fractured silicon particles in the Al-11%-C Si. The associated matrix pile-up was then observed around the fractured silicon particles (**Figs. 5.14 – 5.15**). Therefore, modifying the silicon particle morphology, that is, decreasing silicon particle aspect ratio, is important to prevent silicon particles in Al-Si alloys from fracture, leading to the formation of Si particle sinking- in and aluminum pile–up.

The formation of aluminum pile-ups around the sunken-in silicon particles is a critical step of the wear mechanism in the ultra-mild wear regime. This is because the elevated portions of the soft aluminum matrix became susceptible to permanent sliding contact damage inflicted by the counterface, leading to material loss, that is, more severe surface damage. Following the definition in **Chapter 1**, step i to iii belong to UMW-I. Hence, this process is the precursor to the wear transition from UMW-I to UMW-II -with

wear in the form of mass loss.

In summary, Step iii is the precursor to the onset of UMW-II, namely, a more severe ultra mild wear regime, which accompanied by materials loss in the form of abrasive scratches. Capturing the onset of the UMW-II regime in Al-Si alloys will be presented in **Chapter 6**. Therefore, preventing the sinking-in of the load carrying hard particles (Step ii) is the critical step in holding up the transition to UMW-II. This is expected to be achieved through increasing the matrix hardness and size of the load-carrying hard particles, and by reducing the aspect ratio of the silicon particles to reduce possibility of particle fracture. Therefore, it is conceivable that the use of Al-Si alloys with harder matrix and small aspect ratio Si particles, namely Si particles appear to be block-like or spherical. The hypereutectic Al-Si alloy, Al-18.5%, with large primary silicon particles and harder matrix would be advantageous in reducing wear damage under UMW conditions. This premise was tested by performing sliding wear tests on a hypereutectic Al-18.5% Si alloy under similar testing conditions that corresponded to under UMW regime. This is presented in **Section 5.5**.

5.5. Ultra-mild Wear in Al-18.5% Si

5.5.1. Characteristic Features of UMW Damage in Al-18.5 % Si

The worn surfaces were periodically observed by SEM and optical surface profilometry. Worn surface damage features that developed after sliding for 3 x 10^6 cycles are shown in **Figs. 5. 18 a-c**, and those observed after 6 x10^6 cycles are shown in **Figs. 5. 19 a-c.** Although there was no measurable weight loss in the UMW regime, microscopic damage was evident on the alloy's contact surface as described below.

The SEM image taken from the contact surface of Al-18.5% Si after stopping the

test at 3 x 10^6 cycles **(Fig. 5.18 a)** shows that the top surfaces of the silicon particles inside the wear track are worn. **Fig. 5.18 b** is the corresponding 3-D optical surface profilometer image **of** the same portion of the wear track. In **Fig. 5.18 b** wear on silicon particles is also evident from the longitudinal surface scratches that are elongated in the sliding direction. The cross-sectional profilometer image taken across the wear track **(Fig. 5.18 c)** indicates that scratches were rather shallow and did not penetrate more than a very small fraction of the total height of the protruded sections of the silicon particles. At the longest sliding distance of 6 x 10^6 cycles, SEM **(Fig. 5.19 a)** and surface profilometer images **(Fig. 5.19 b** and **c)** reveal that the wear mechanism did not change. Still merely the contact surfaces of the silicon particles suffered superficial wear damage. The original aluminum and silicon morphology remained virtually unchanged i.e., no particle fracture or fragmentation or damage to the aluminum matrix was observed. Therefore, throughout the course of the sliding process silicon particles in Al-18.5% Si remained intact and effectively protected the aluminum surface from wear.

5.5.2. Quantitative Determination of UMW Damage in the Al-18.5% Si Alloy

The distributions of the topographical features on the contact surfaces in the Al-18.5% Si alloy obtained by analyzing surface profilometer data are given in **Fig. 5.20**. The change in the elevation of silicon particles with respect to the aluminum surface can be estimated from the peaks of the histograms. As stated before in **Section 3.4.2** , the average initial height of the silicon particles protruding from the aluminum surface in Al-18.5% Si was 1.60 μm. Measurements made inside the wear track after sliding for 6 x10^5 cycles showed a very small reduction of 0.14 μm in the protruded silicon particle height occurred as a result of sliding wear. Accordingly, the UMW damage in Al-18.5 %Si

remained confined to superficial scratch damage on the tops of the particles. The reductions in silicon particle elevations in Al-18.5 %Si after various sliding distances are plotted in **Fig. 5.21**. The hypereutectic Al-18.5% Si alloy offers effective wear resistance and a minimal amount of surface damage under the UMW conditions. Silicon particles in this alloy do not sink into the matrix and are successful in shielding etched aluminum surface from plastic deformation and permanent damage.

5.5.3. Discussion

Experimental observations presented in **Section 5.3** showed that the formation of aluminum pile-ups around the embedded silicon particle led to more severe damage to the aluminum matrix. As a result, the elevated portions of the aluminum matrix become susceptible to permanent contact damage inflicted by the counterface leading to material loss. **Fig.5.22** summarizes the silicon particle height reduction with the sliding cycles in the three alloys tested for comparison. It is noted that the silicon particle sinking-in is dependent on matrix hardness and silicon particle morphology. Increasing the matrix hardness, and using particles with low aspect ratio would improve the load carrying ability of the alloys, and thus would prevent surface damage to the aluminum matrix. This can be rationalized with the mechanical response of silicon particles to the applied load.

The variation of the maximum contact pressure applied to the particles in Al-18.5% Si with normal load is shown in **Fig 5.23 (Section 4.4)**. Under the load used in the current experiment (0.5 N) the maximum contact pressure on the silicon particles in Al-18.5% Si is estimated as 741 MPa, which is smaller than its matrix hardness of 834 MPa (85 HV). Based on the criterion for the prediction of plastic deformation presented in

Section 4.4.5, application of a (maximum) contact pressure of 741 MPa is not likely to induce local plastic flow of aluminum around the silicon particles in Al-18.5 % Si. Therefore, silicon particles in Al-18.5% Si are expected to carry the applied load at the tested load, no plastic deformation in the form of aluminum pile-up induced by the silicon particle sinking-in is expected in this alloy. In Al-18.5% Si, neither silicon particle sinking-in nor damage to aluminum matrix in the form of plastic deformation and wear was observed even after sliding the longest cycle of 6 x 10^5. Only top surfaces of Si particles suffered from abrasive wear, that is, only the first step (Step i) identified in the two eutectic Al-Si alloys (**Section 5.4**) is maintained throughout the UMW regime in Al-18.5% Si.

On the other hand, no obvious fracture was observed to the large block-like primary Si particles in Al-18.5% Si (**Fig. 5.18** and **5.19**), indicating that block-like primary Si particles with aspect ratio of 1.6, which is about 10 times smaller than plate-like Si particles in Al-12% Si and Al-11% Si-C, exhibit lower propensity for fracture. Therefore, the real contact pressure applied on the Si particles in Al-18.5% Si remains virtually unchanged throughout the course of sliding. Accordingly, the hypereutectic Al-18.5% Si alloy offers effective wear resistance and a minimal amount of surface damage under the UMW conditions. Silicon particles in this alloy do not sink into the matrix and are successful in shielding etched aluminum surface from plastic deformation and permanent damage.

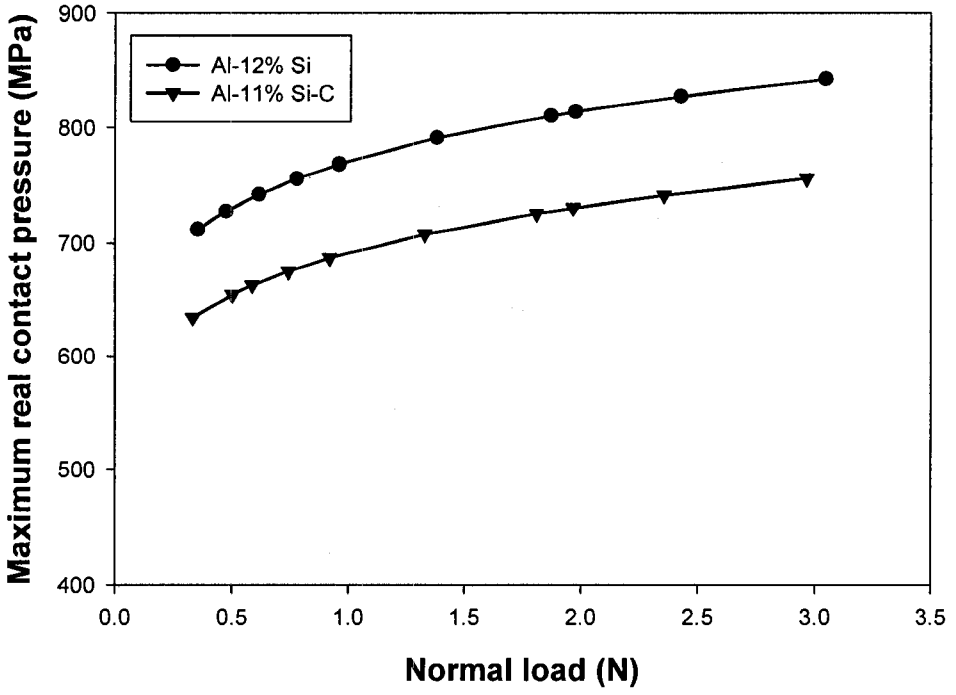

Fig. 5.1. Variations of the maximum contact pressure exerted on the particles with the normal load.

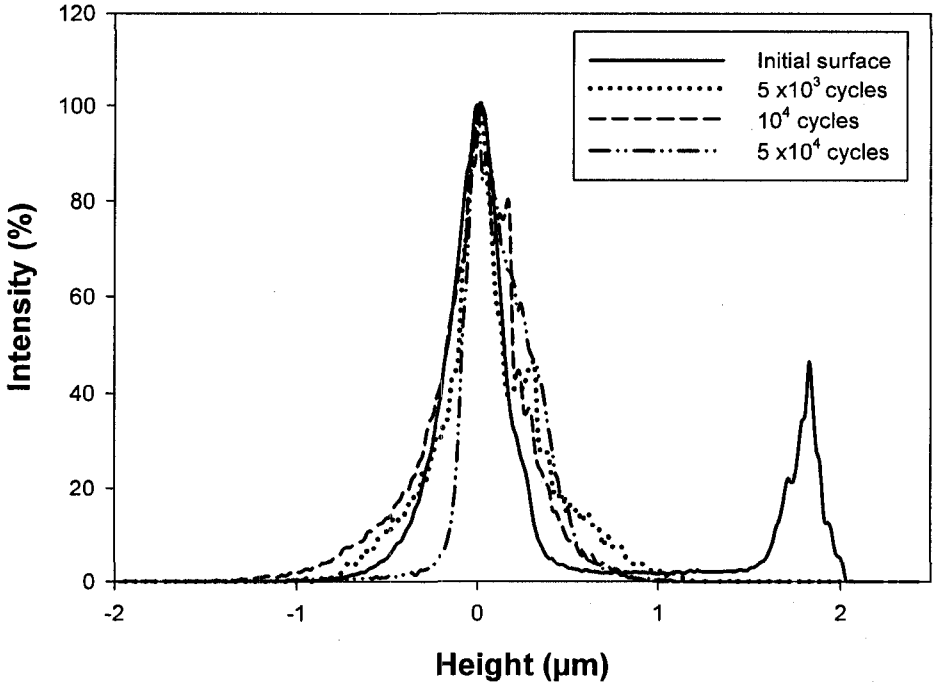

Fig. 5.2. The distribution (frequency) of surface topography of Al-12% Si at various sliding cycles. At each sliding cycle, the first peak (with lower height (μm)) represents the Al surface and the second peak (with larger height (μm) is particle elevation.

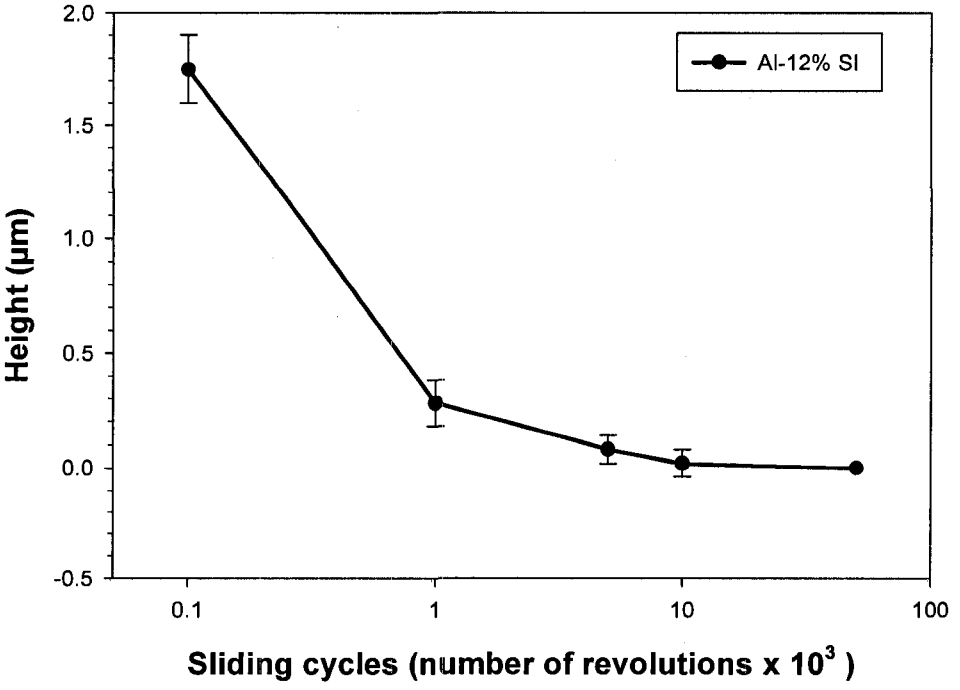

Fig. 5.3. Change in the Si particle height projected above the Al matrix in Al-12% Si with the sliding cycles.

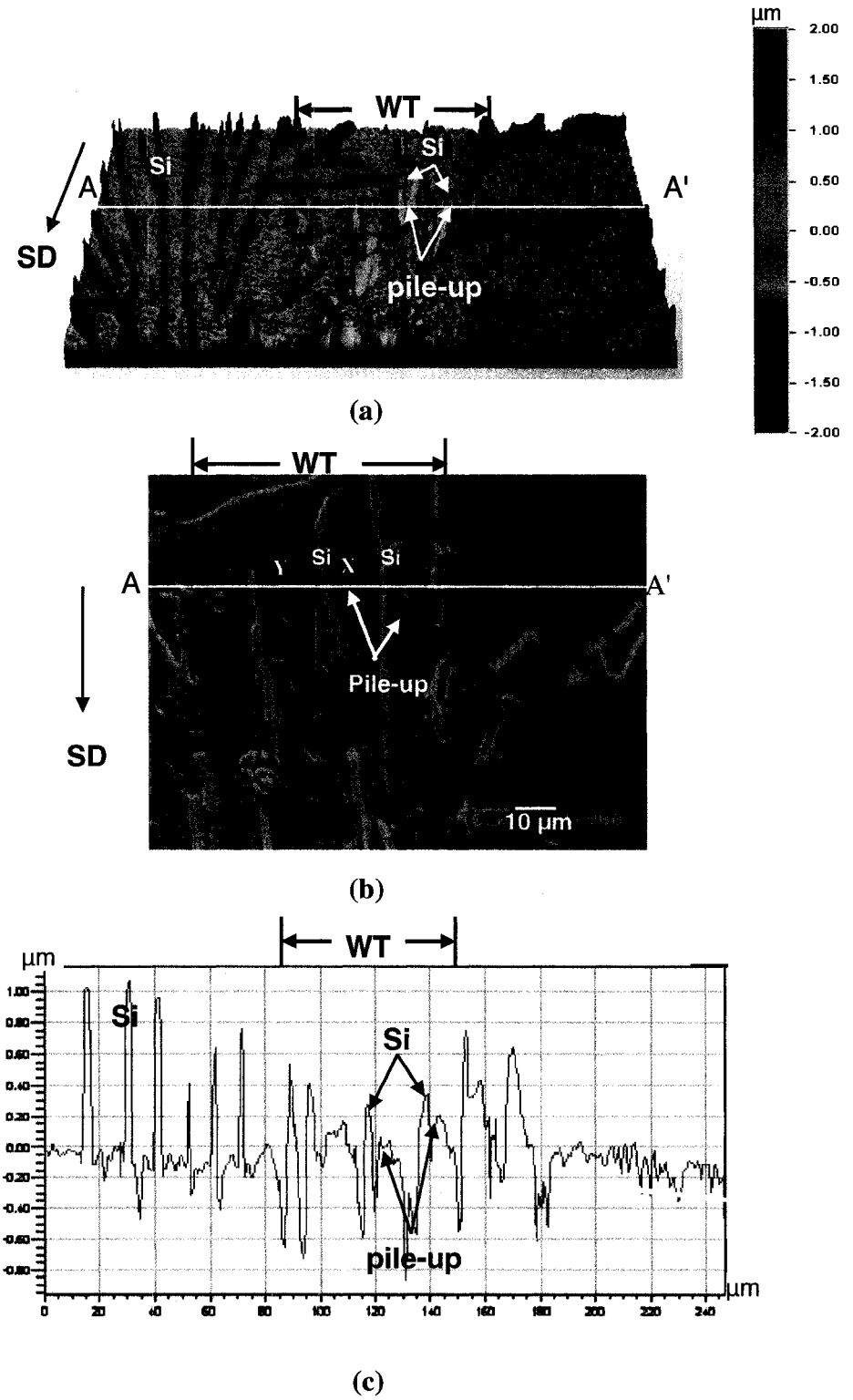

Fig. 5.4. Surface damage in Al-12% Si after sliding for 10^3 cycles: **(a)** 3-D surface profile image; **(b)** Backscattered SEM image of the same area as **(a)**; **(c)** Surface profile scanned along the horizontal line (AA') indicated in **(a)** and **(b)**. The dimension of the area shown is 246 μm x 187 μm;

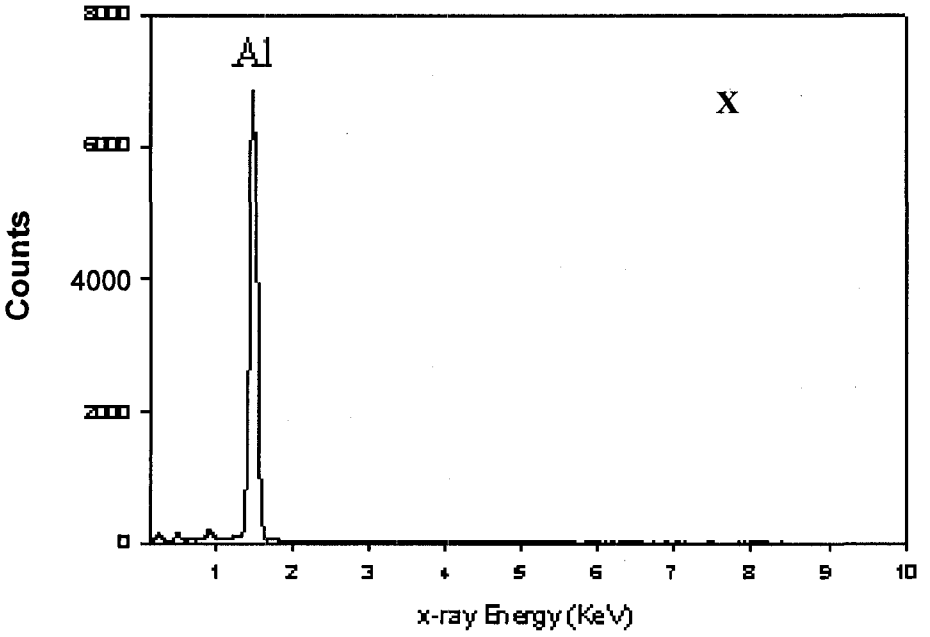

(a)

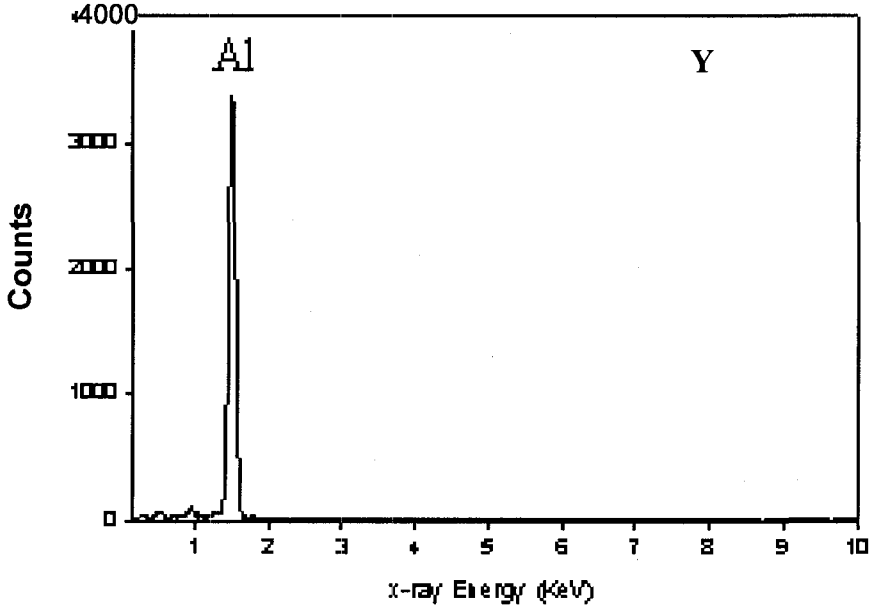

(b)

Fig. 5.5. EDS spectrum showing the composition of **(a)** the material around the sunken-in silicon particles taken form the indicated area, X and **(b)** the matrix aluminum taken from the area of Y.

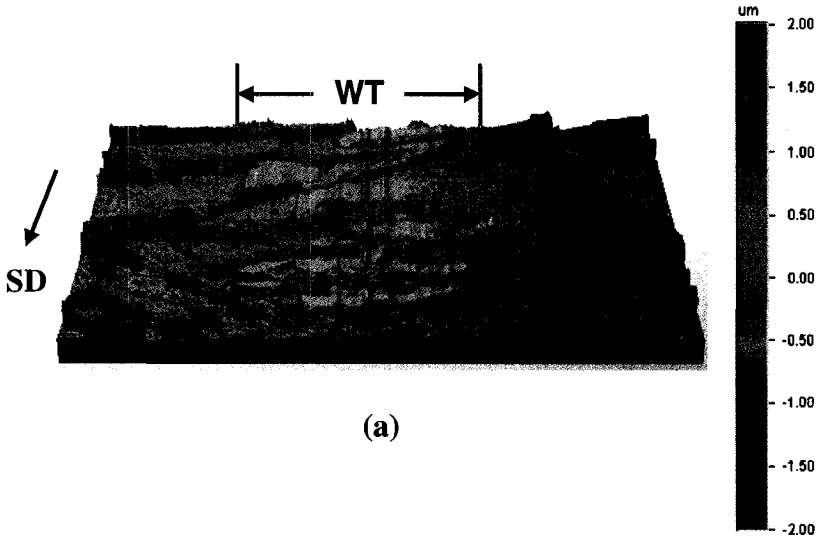

(a)

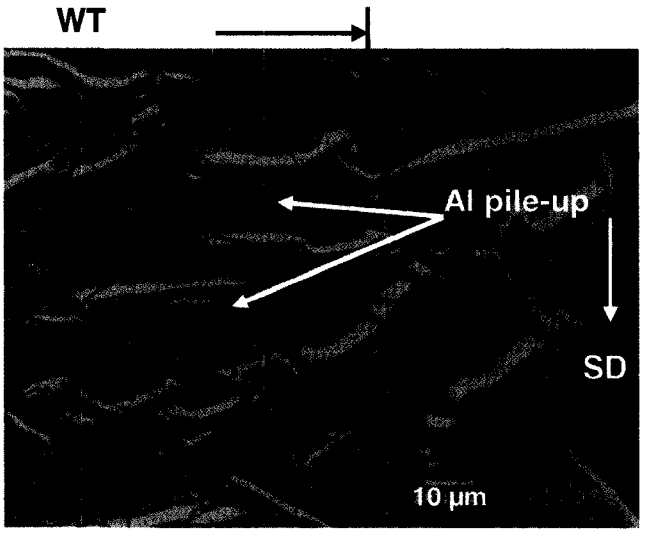

(b)

Fig. 5.6. Surface damage in Al-12% Si after sliding for 5 x 10^3 cycles: **(a)** 3-D surface profile image; **(b)** Backscattered SEM image of the same area as **(a)**. The dimension of the area shown is 246 µm x 187 µm.

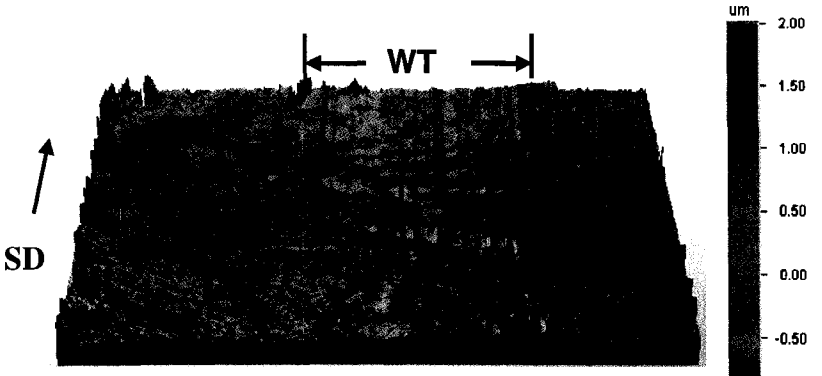

(a)

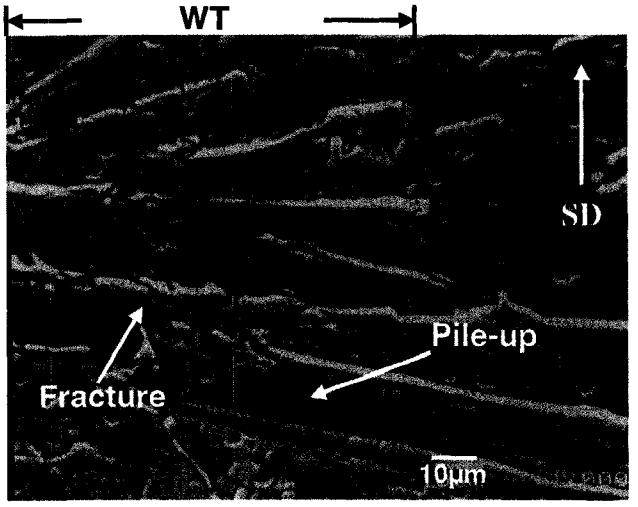

(b)

Fig. 5.7. Surface damage in Al-12% Si after sliding for 10^4 cycles: **(a)** 3-D surface profile image; **(b)** Backscattered SEM image of the same area as **(a)**.The dimension of the area shown is 246 μm x 187 μm.

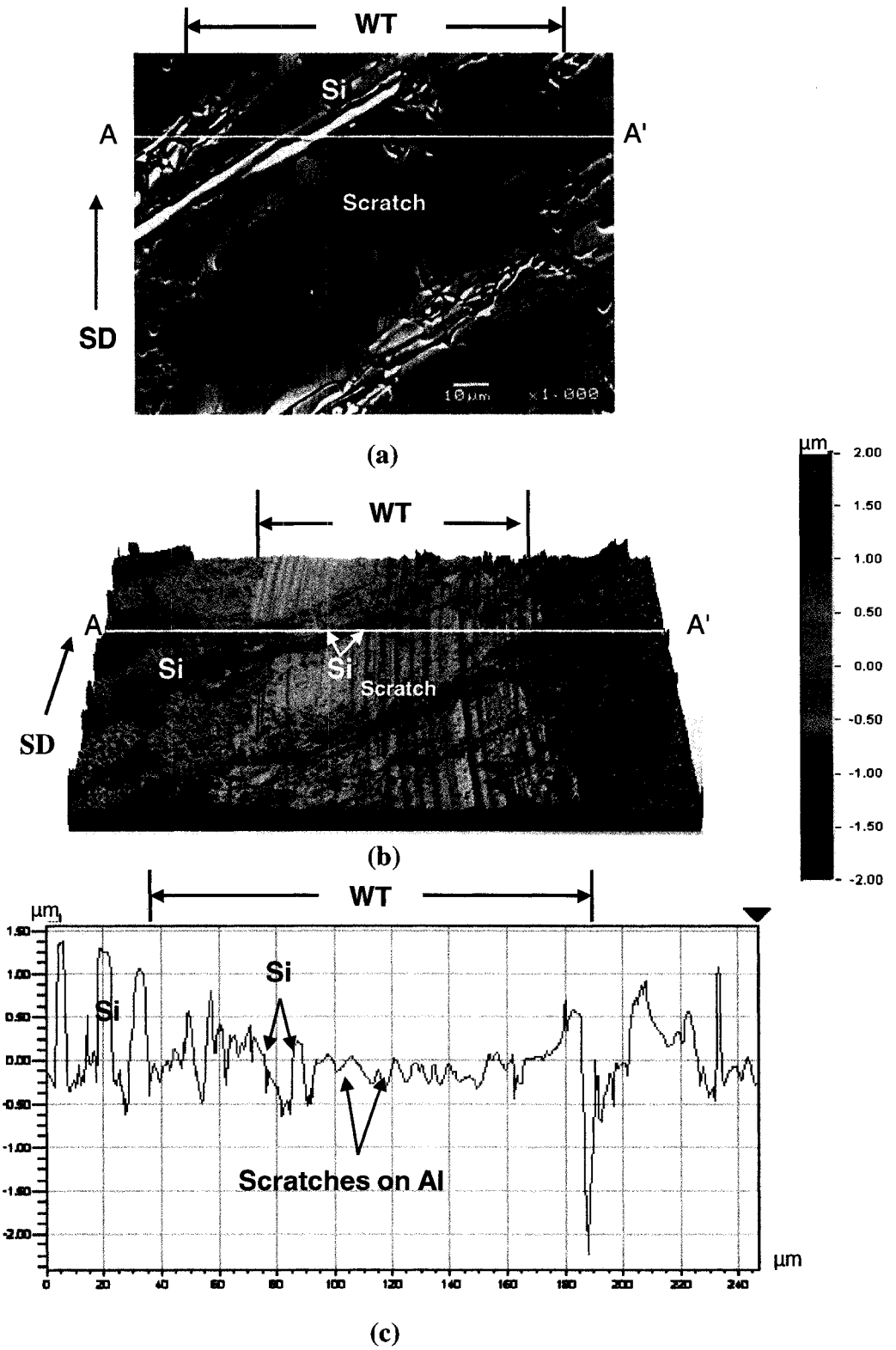

Fig. 5.8. Surface damage in Al-12% Si after sliding for 5 x 10^4 cycles: **(a)** Backscattered SEM image; **(b)** 3-D surface profile image of the same area as **(a)**; and **(c)** Surface profile scanned along the horizontal line (AA') indicated in **(a)** and **(b)**. The dimension of the area shown is 246 µm x 187 µm.

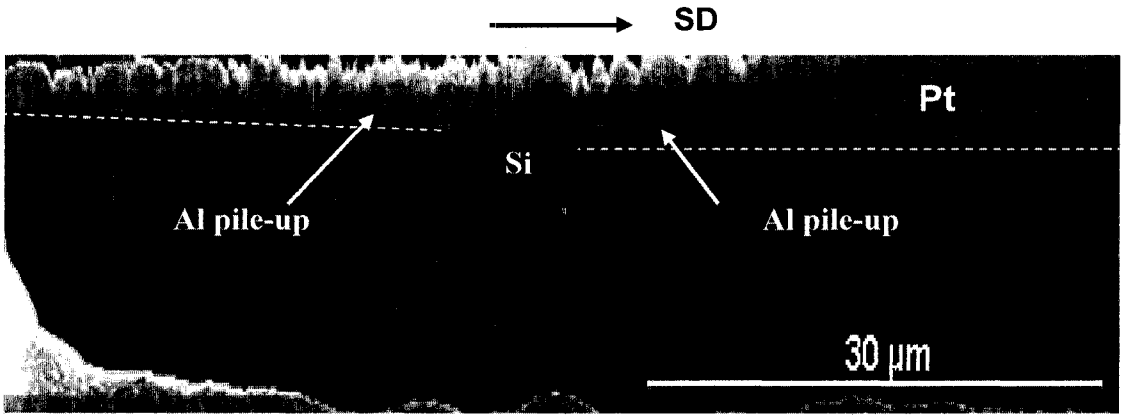

Fig. 5.9. Cross-sectional FIB secondary image (taken by Dr. Meng-Burany) of the wear track showing Al matrix pile up around the Si particle.

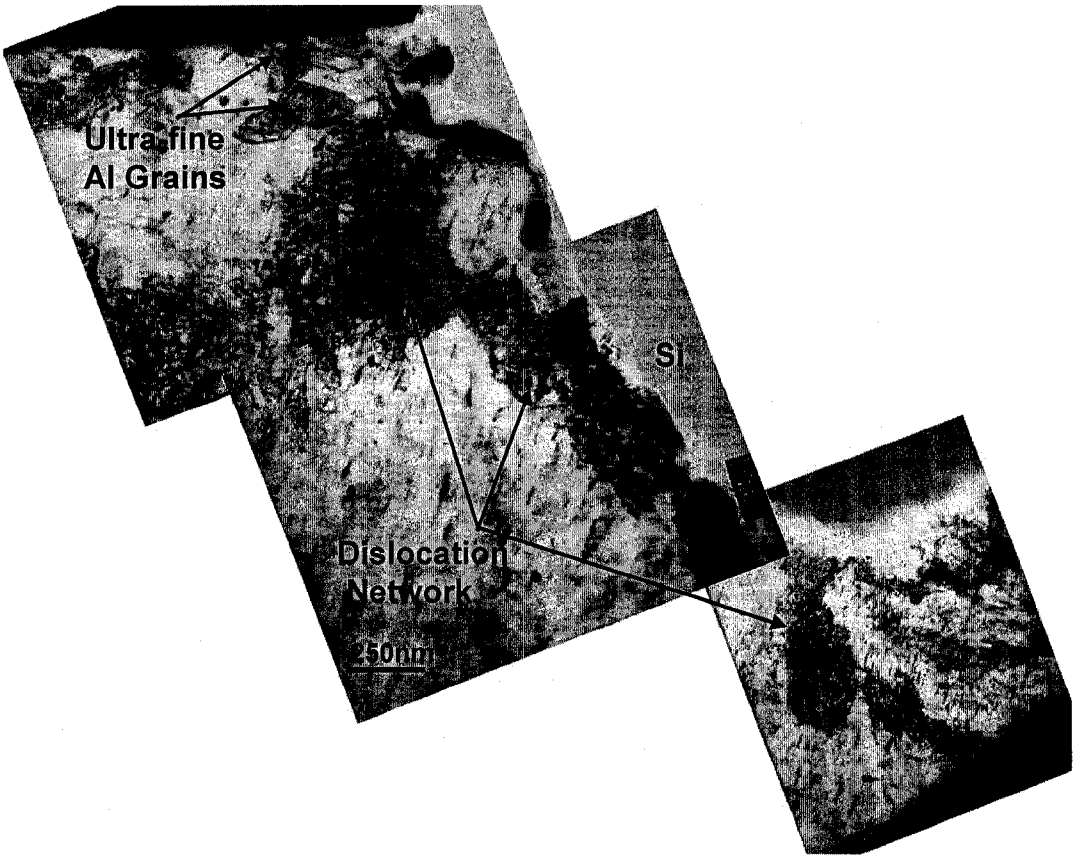

Fig. 5.10. Cross-sectional TEM image (taken by Dr. Meng-Burany) of the wear track showing dislocation networks in the aluminum around the sunken-in Si particle.

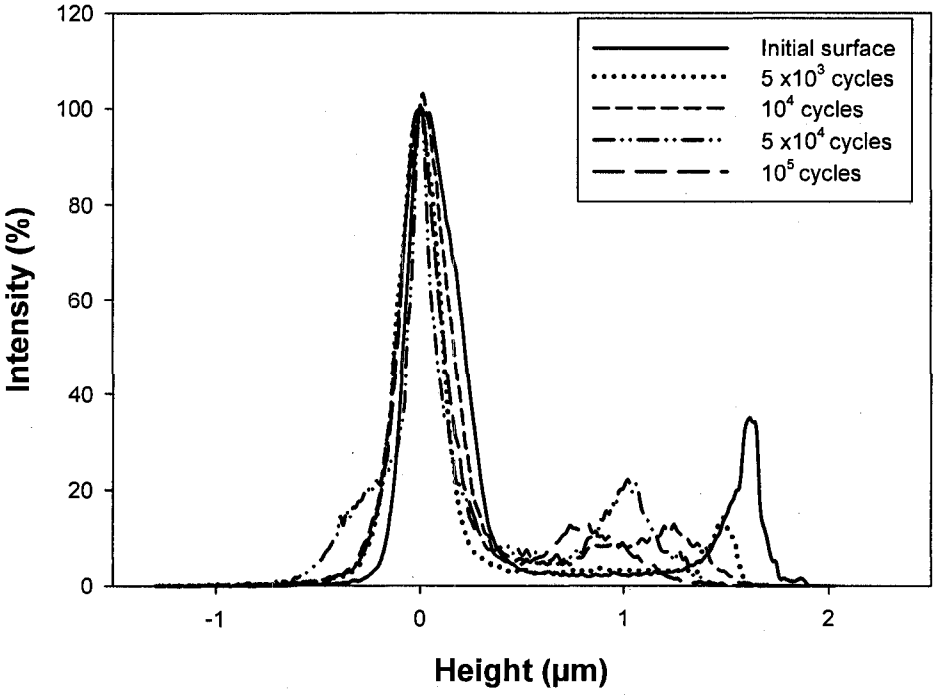

Fig. 5.11. The distribution (frequency) of surface topography of Al -11% Si-C at various sliding cycles. At each sliding cycle, the first peak (with lower height (μm)) represents the Al surface and the second peak (with larger height (μm) is particle elevation.

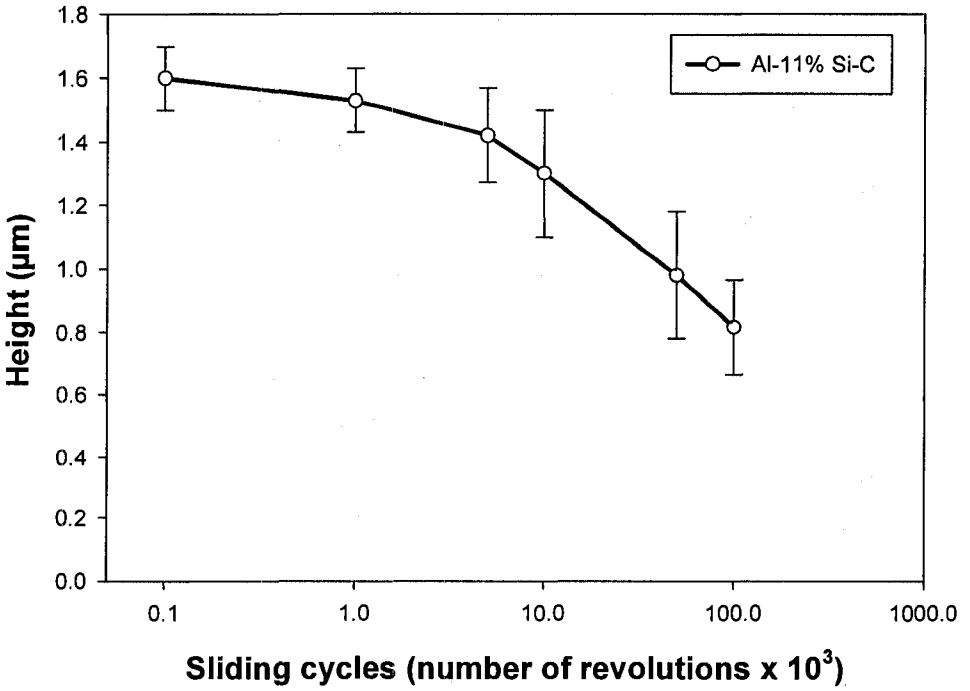

Fig. 5.12. Change in the Si particle height projected above the Al matrix in Al-11% Si-C with the sliding cycles.

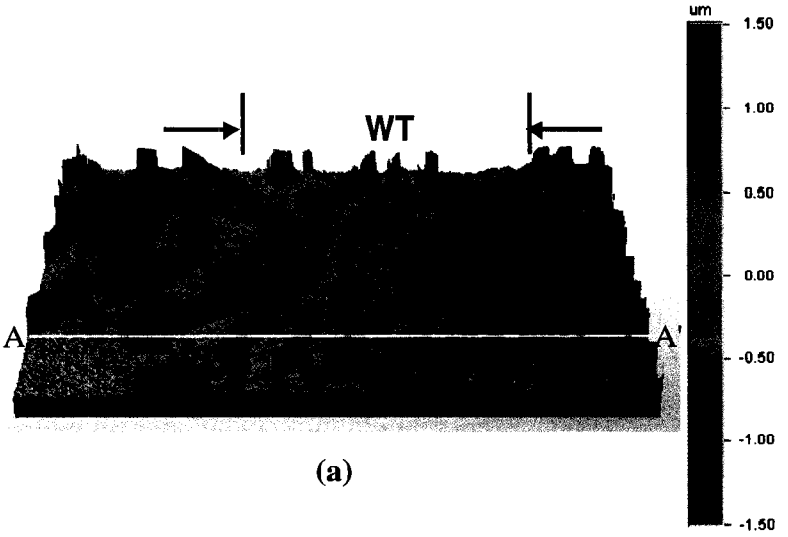

(a)

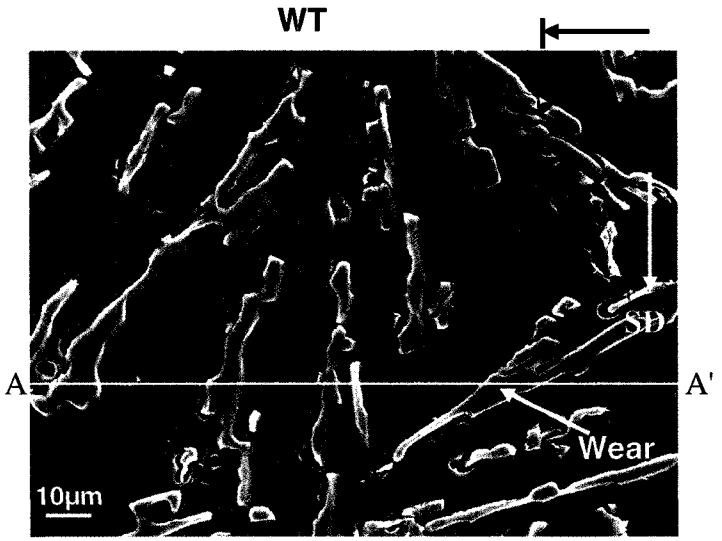

(b)

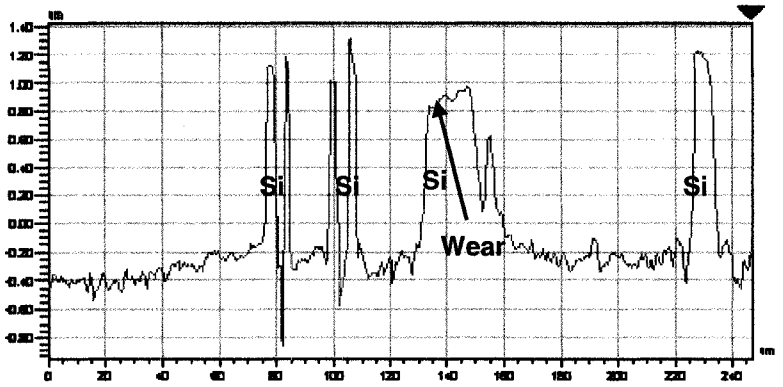

(c)

Fig. 5.13. Surface damage in Al-11% Si-C after sliding for 10^4 cycles: **(a)** 3-D surface profile image; **(b)** Backscattered SEM image of the same area as **(a)**; **(c)** Surface profile scanned along the horizontal line (AA') indicated in **(a)** and **(b)**. The dimension of the area shown is 246 μm x 187 μm.

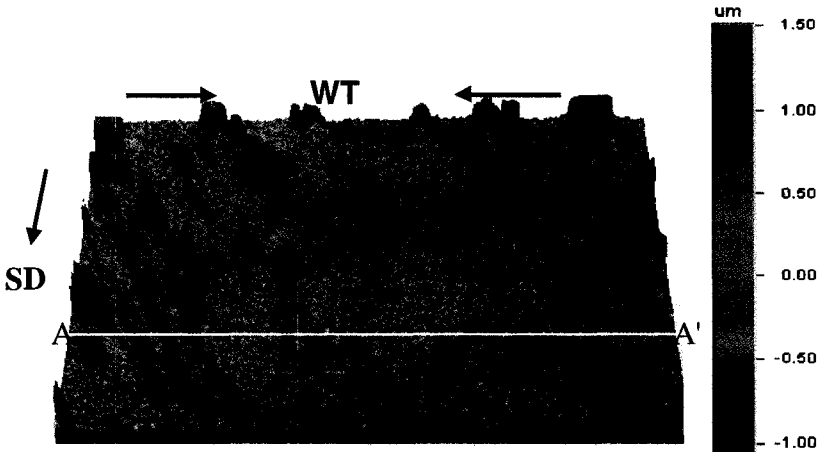

(a)

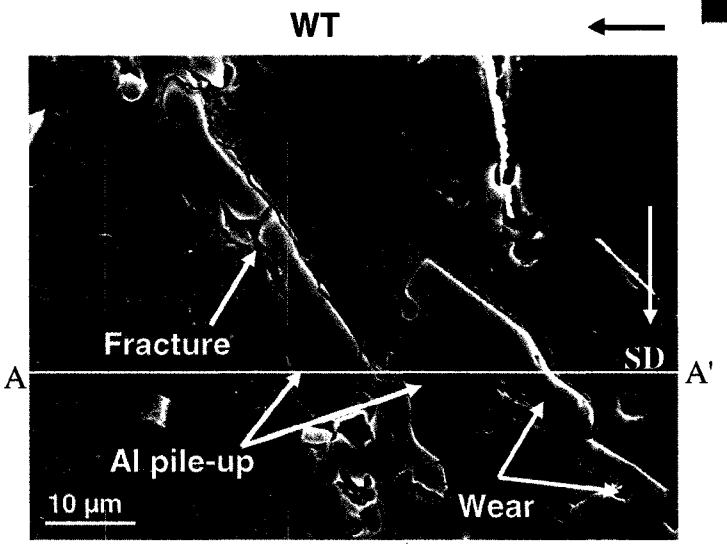

(b)

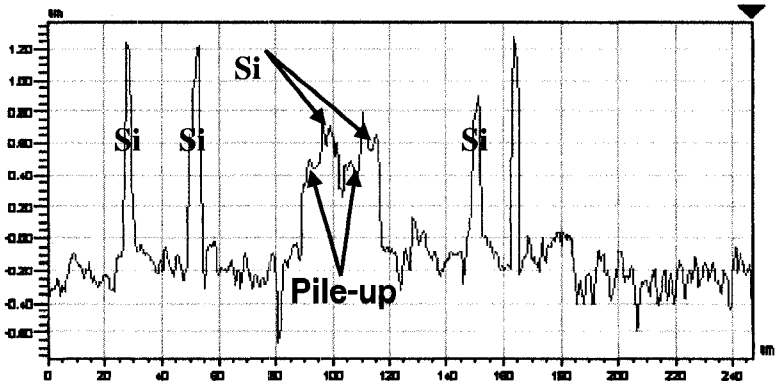

(c)

Fig. 5.14. Surface damage in Al-11% Si-C after sliding for 5 x10 ^{4} cycles: **(a)** 3-D surface profile image; **(b)** Backscattered SEM image of the same area as **(a)**. The dimension of the area shown is 246 µm x 187 µm.

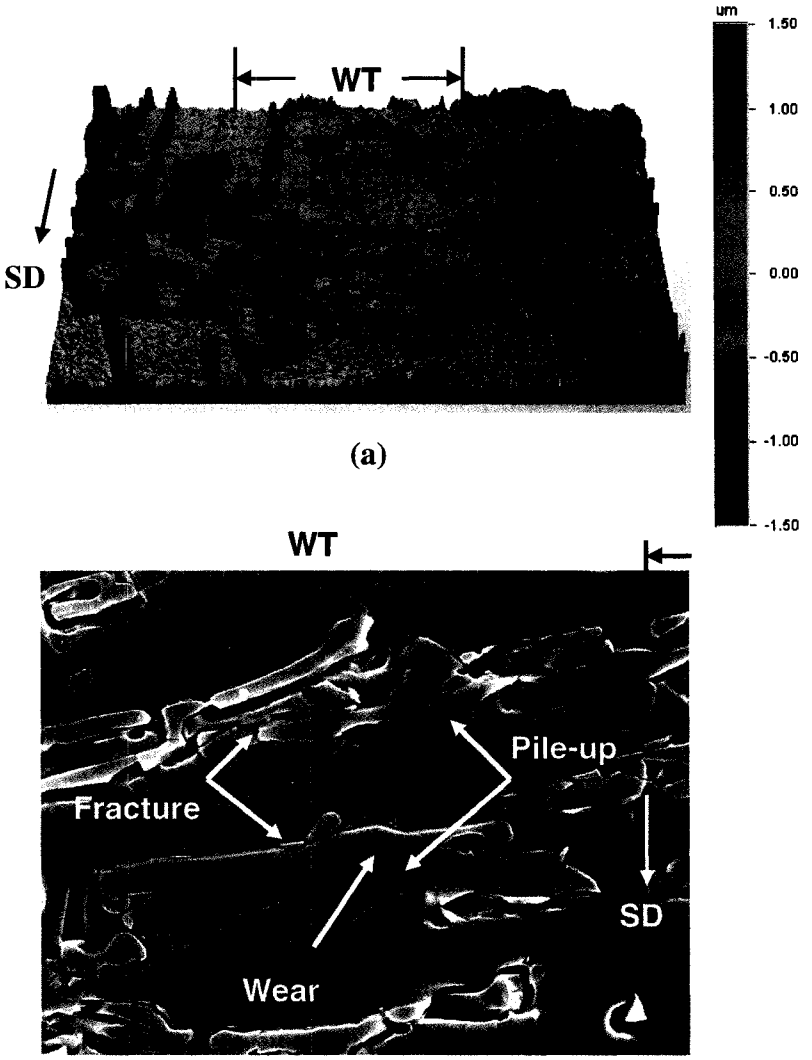

Fig. 5.15. Surface damage in Al-11% Si-C after sliding for 10^5 cycles: **(a)** 3-D surface profile image; **(b)** Backscattered SEM image of the same area as **(a)**. The dimension of the area shown is 246 μm x 187 μm.

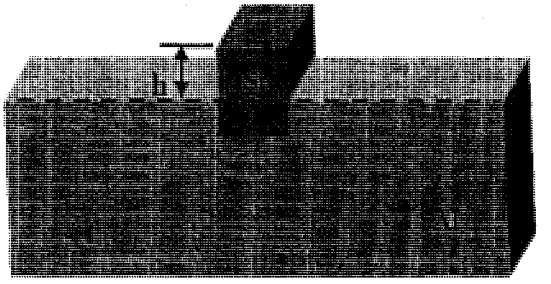

(a) Cross-sectional view of a Si particle with height h on an etched surface prior to wear.

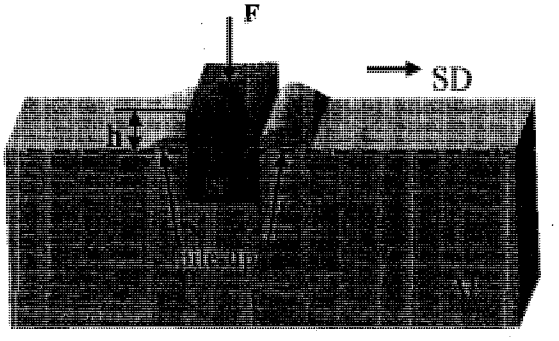

(b) Particle sinking-in and Al matrix piling up during sliding.

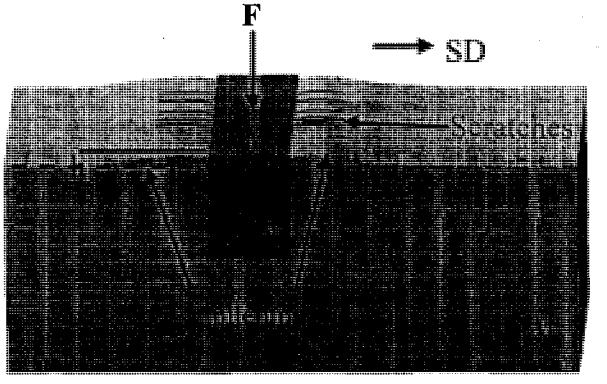

(c) Micro-scratching of piled-up aluminum.

Fig. 5.16 Schematic representation of ultra mild wear mechanisms in eutectic Al-Si alloys (with soft matrix).

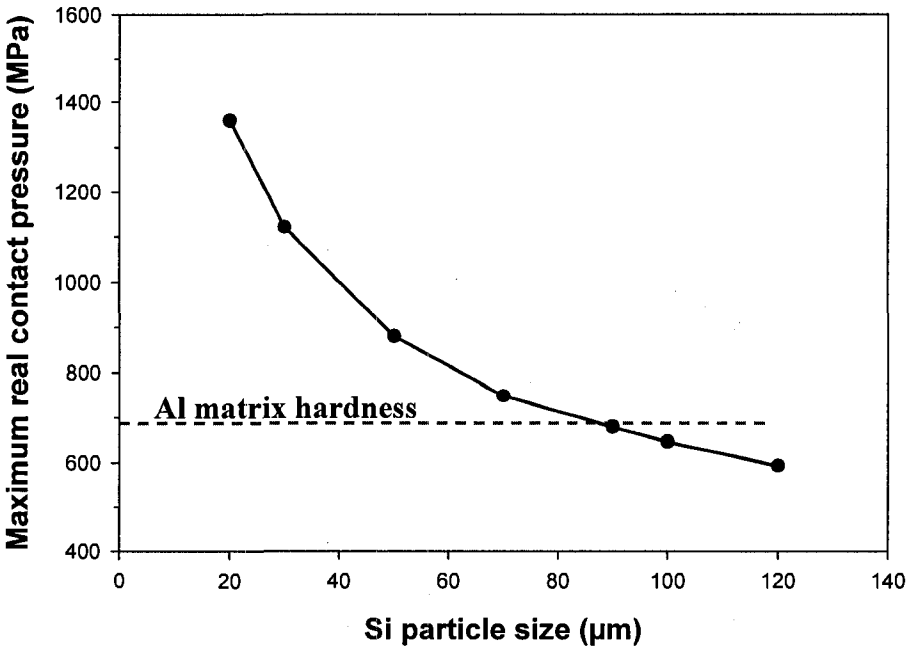

Fig. 5.17. Variation of the maximum contact pressure with Si particle size in the range of 20 to 120 μm at 0.5 N. Matrix hardness (667 MPa) of the alloy was assumed equivalent to that of Al-11% Si-C.

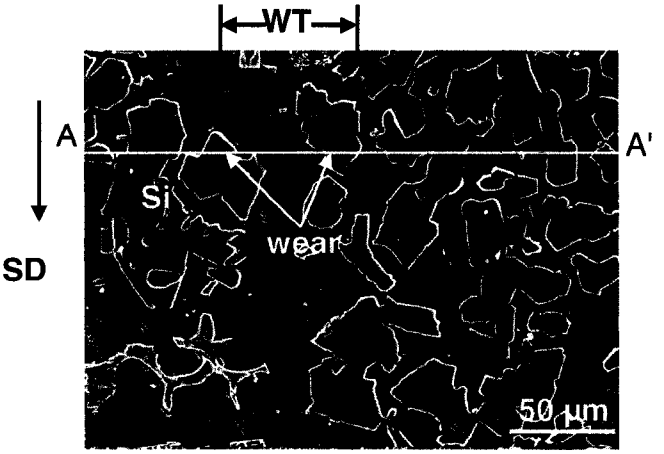

(a)

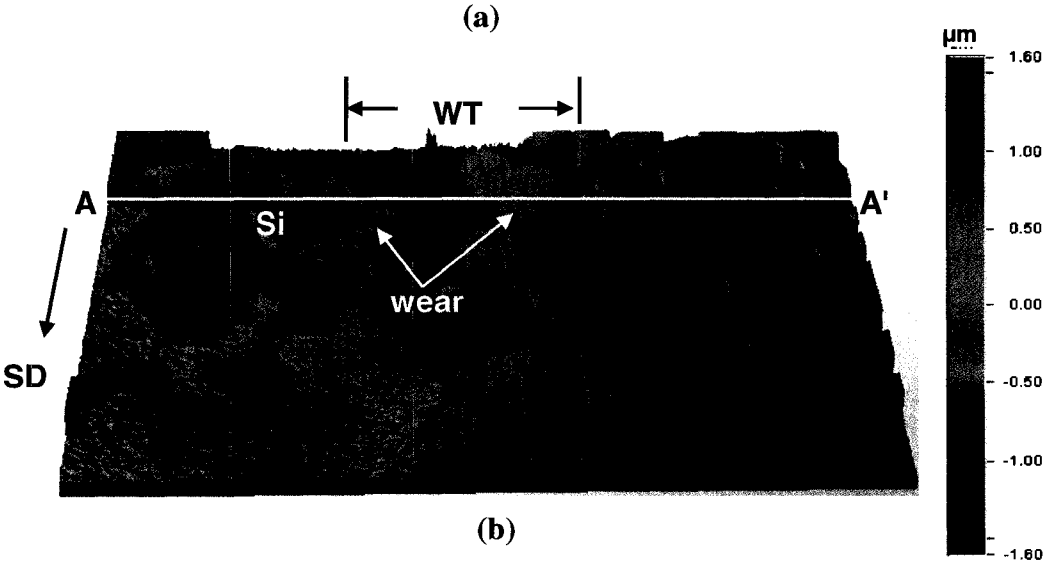

(b)

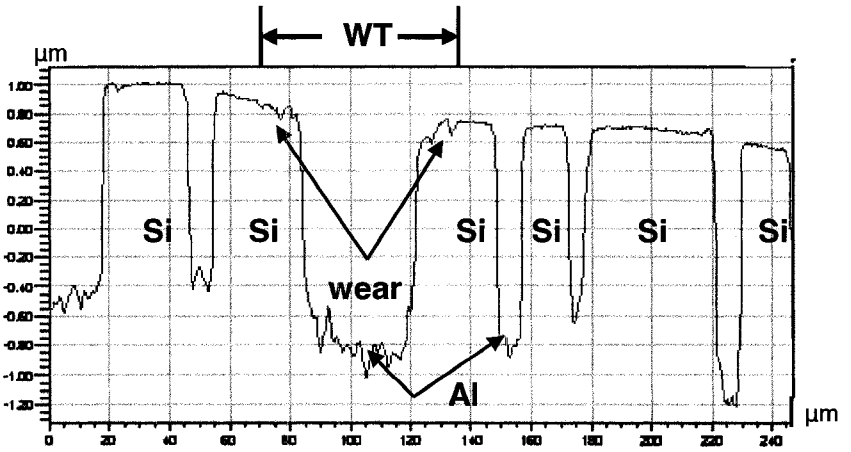

(c)

Fig. 5.18. Surface damage in Al-18.5% Si after sliding for 3 x 10^5 cycles: **(a)** Secondary SEM image; **(b)** 3-D surface profile image of the same area as in **(a)**; and **(c)** Surface profile scanned along the horizontal line (AA') indicated in **(a)** and **(b)**. WT is the wear track, SD is the sliding direction.

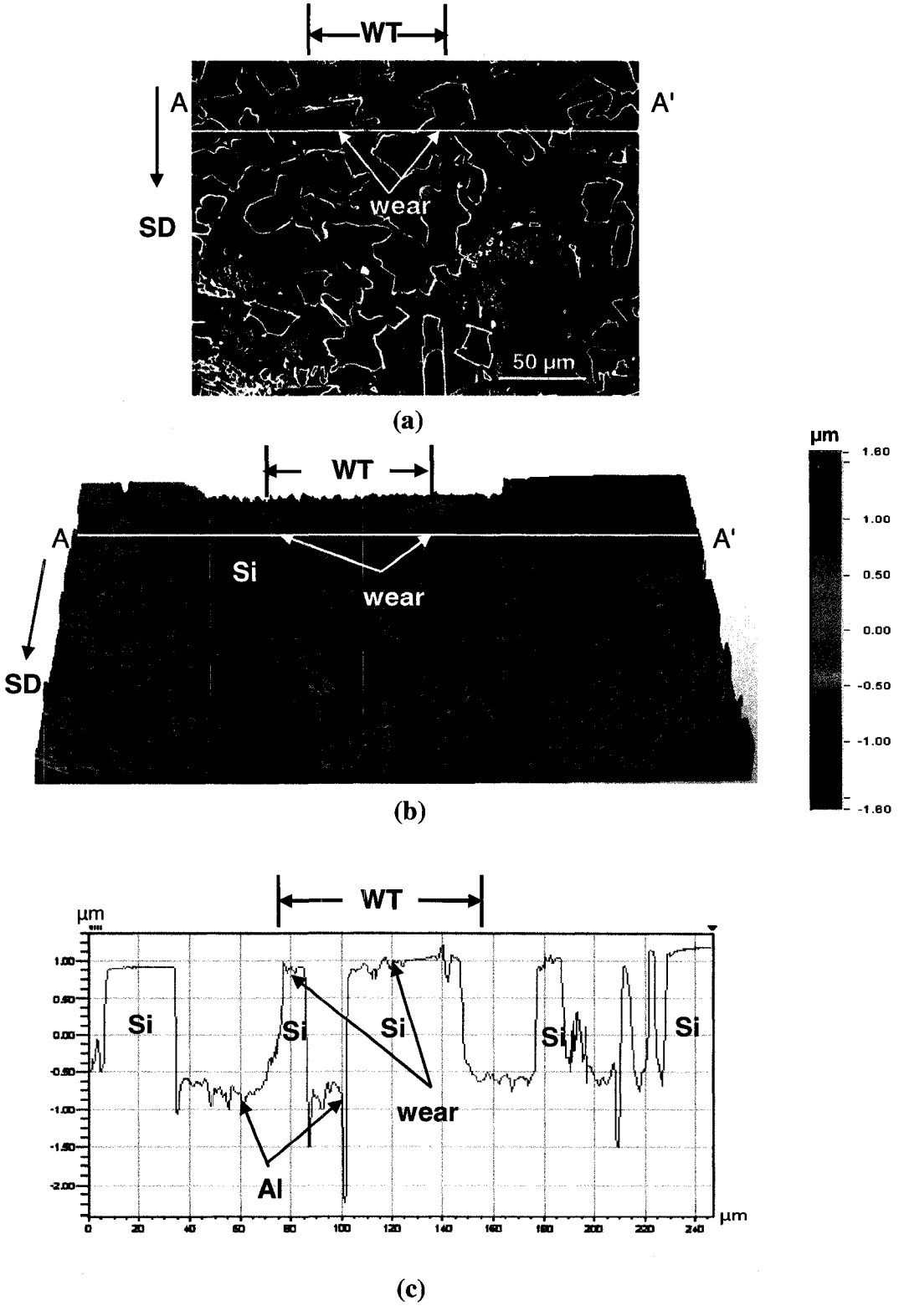

Fig. 5.19. Surface damage in Al-18.5% Si after sliding for 6 x 10^5 cycles: **(a)** Secondary SEM image; **(b)** 3-D surface profile image of the same area as **(a)**; and **(c)** Surface profile scanned along the horizontal line (AA') indicated in **(a)** and **(b)**.

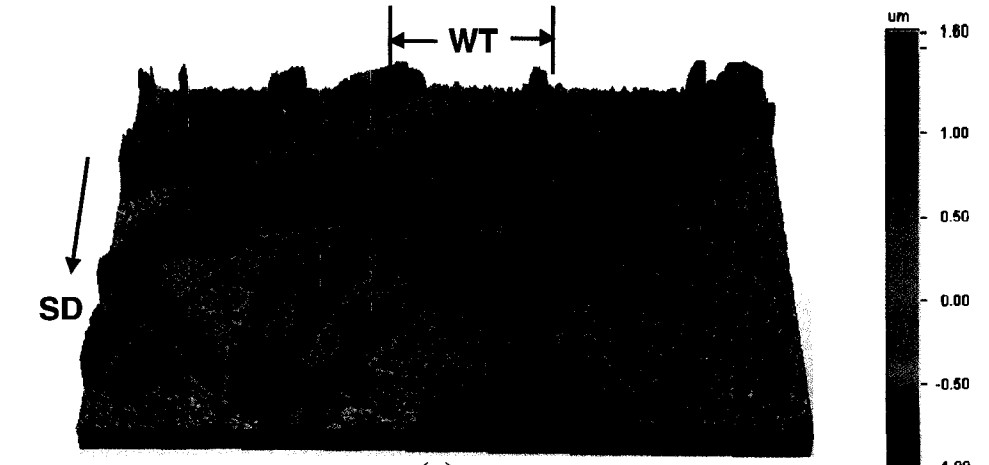
WT
SD
um
1.60
1.00
0.50
0.00
-0.50
-1.00
-1.60

(a)

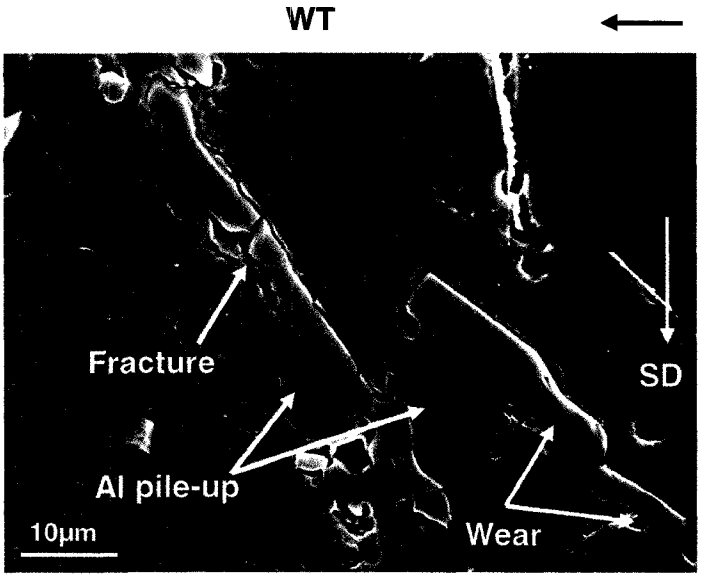
WT
Fracture
SD
Al pile-up
10μm
Wear

(b)

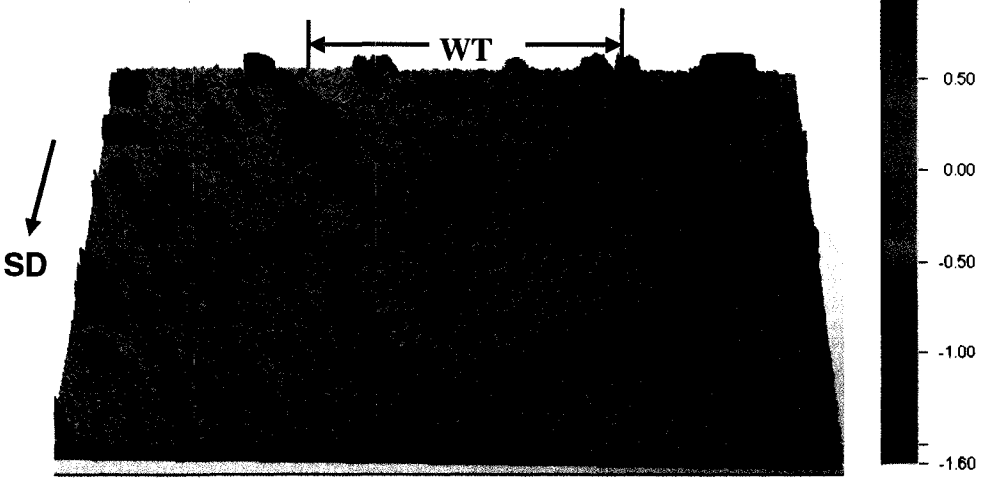
WT
SD
um
1.60
1.00
0.50
0.00
-0.50
-1.00
-1.60

(c)

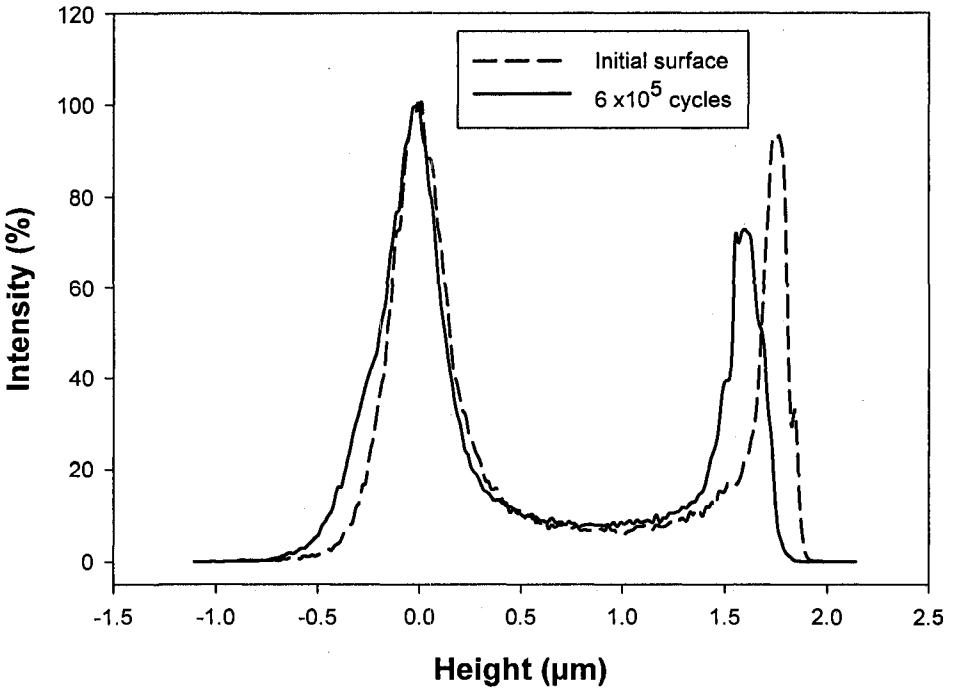

Fig. 5.20. The distribution (frequency) of topographical features on the contact surface of Al-18.5% Si with the sliding cycles.

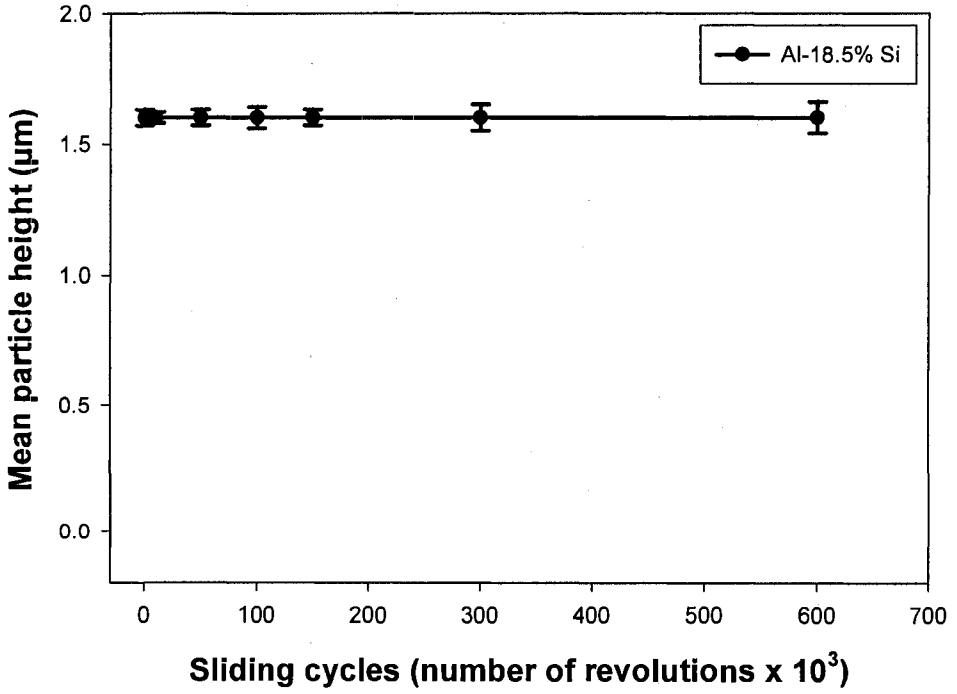

Fig. 5.21. Variation of the mean silicon particle height with sliding cycles, showing that silicon particle elevation does not change with sliding distance in Al-18.5% Si.

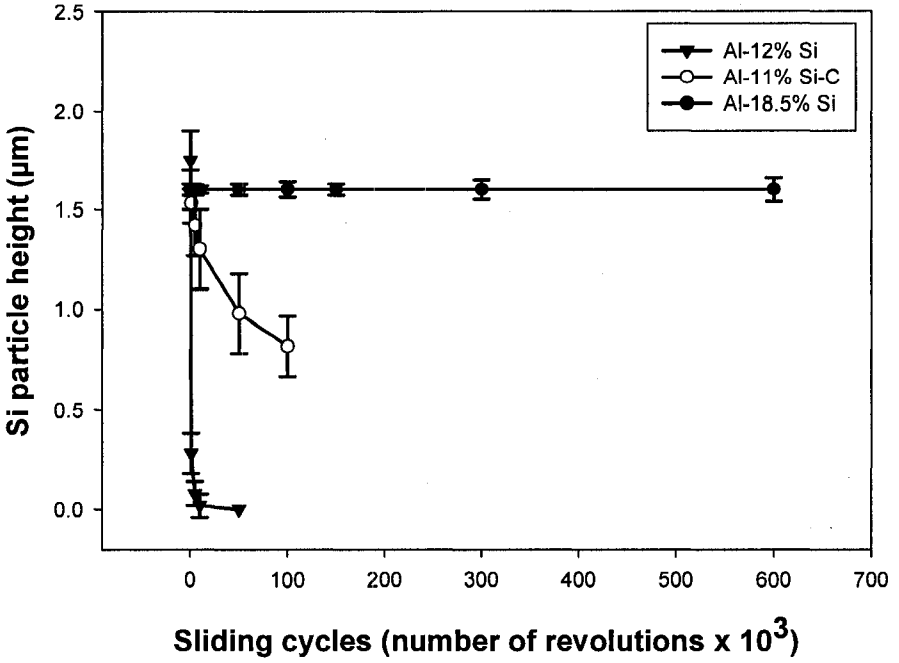

Fig. 5.22. Variations of the mean silicon particle height with sliding cycles in Al-12% Si, Al-11% Si-C, and Al-18.5% Si.

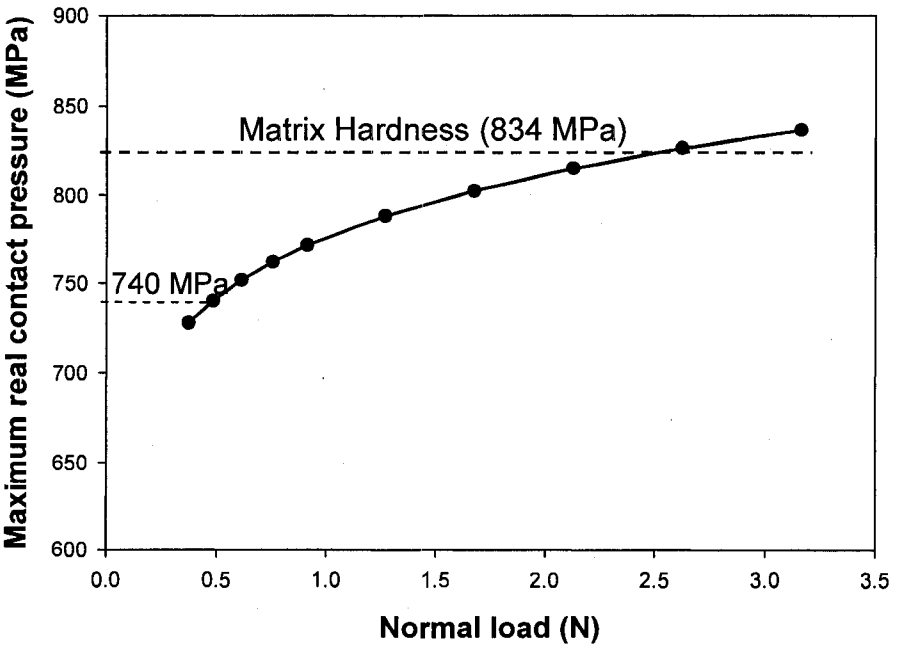

Fig. 5.23. Variation of the maximum contact pressure on the particles in Al-18.5% Si with the normal load.

CHAPTER 6 TRANSITIONS FROM UMW-I TO UMW-II AND UMW-III

6.1. Introduction

Measurable volumetric wear loss does not occur on contact surfaces in the UMW-I regime. Surface damage is limited to the microscopic level. The deviation of volume loss from zero, that is, detectable material loss, indicates the transition from UMW-I to UMW-II. The purpose of this chapter is to capture the transition point when the damage inflicted by the counterface started leading to material loss from the deformed aluminum matrix, namely, the onset of UMW-II, and subsequently the onset of UMW-III, with reduced wear rate after long sliding cycles. The mechanisms triggering these transitions and the microstructural factors in terms of silicon particle morphology, size, distribution, and matrix hardness responsible for these transitions are examined. The worn surfaces of the two eutectic alloys, Al-11% Si-C, Al-11% Si-F, containing a similar percentage of silicon and with comparable hardness of matrix, but different silicon morphologies and sizes were periodically observed by a SEM and an optical surface profilometer after completing a test to a given number of cycles at tested loads of 0.5 to 2.0 N. Similar observations were made on a spray formed Al-25% Si, which has similar silicon particle size and morphology but with a much higher silicon particle areal density and harder matrix in comparison with Al-11% Si-F.

In the first section of this chapter (**Section 6.2**), the evolution of the surface damage that occurred under UMW conditions in Al-11% Si-C and Al-11% Si-F with applied load and sliding cycles is presented. This section starts with a comparison of the

maximum contact pressures applied on the exposed silicon particles in the two eutectic alloys (**Section 6.2.1**). The experimental results from the wear tests are presented in **Section 6.2.2** for the Al-11% Si-C alloy, then the Al-11% Si-F in **Section 6.2.3**. This is followed by summaries of observations of oil layer deposits in **Section 6.2.4** and an analysis of changes in Si particle heights for both alloys in **Section 6.2.5**.

The sliding wear mechanisms of Al-11% Si-C and Al-11% Si-F in the UMW regime and the mechanism of triggering the onset of UMW-II and UMW-III in the two eutectic Al-Si alloys are discussed in **Section 6.2.6,** based on the mechanical response of silicon particles to the applied load, and the propensity of the formation of the oil residue layer.

The evolution of microstructural events and surface damage of Al-25% Si are delineated in **Section 6.3**. The observed wear mechanisms are compared with those in Al-11% Si with similar Si particle morphology and size, interesting differences and similarities are noted, to shed light on the effect of microstructure on damage mechanisms in the UMW regime.

Sections 6.3.1 to **6.3.3** present the worn surface evolution with applied load and sliding cycles in the order they were detected in Al-25% Si, starting from the lowest load applied. Quantitative determination of damage to silicon particles and the aluminum matrix in Al-25% Si is presented in **Section 6.3.4**. The mechanisms leading to the surface damage in Al-25% Si, and the effect and silicon particle distribution on the sliding wear behaviour are discussed in **Section 6.3.5**. The difference in the micromechanisms responsible for the surface damage in the two alloys is rationalized with the mechanical response of the silicon particles to the applied load, the propensity to form an oil residue layer, the coefficient of friction, and wear to the counterface.

6.2. Evolution of the Surface Damage with Sliding Cycles and Applied Load in Eutectic Al-Si Alloys

6.2.1. The Maximum Real Contact Pressures Applied on the Two Eutectic Al-Si Alloys

The contact pressure analysis conducted in **Section 4.4** suggested that the maximum contact pressure is strongly dependent on silicon particle size and distribution. **Fig. 6.1** shows the variation of the maximum real contact pressure applied on Al-11% Si-C and Al-11% Si-F with the normal load. The maximum contact pressures applied on the two alloys under the normal loadings used in the current experiments are listed in **Table 6.1**. The data listed for Al-11% Si-F was calculated with a density of $0.04/\mu m^2$. The maximum contact pressures applied on the silicon particles in Al-11% Si-F are about 2 times higher than those in Al-11% Si-C. It follows that at the load of 0.5 N, the maximum real contact pressure applied on Al-11% Si-C was slightly smaller than its matrix hardness (670 MPa), while that applied to Al-11% Si-F exceeds its matrix hardness of 660 MPa. Therefore, local plastic deformation is more likely to occur in Al-11% Si-F in comparison with Al-11% Si-C at 0.5 N. The maximum pressures applied on the contact surfaces of the two alloys at 1.0 and 2.0 N are greater than their matrix hardness. Consequently, sinking-in of the silicon particles into the aluminum matrix is expected to happen in both alloys at 1.0 and 2.0 N. These calculation results will be used to explain the contact surface evolution and UMW behaviour of the two alloys in the following sections.

6.2.2. Surface Damage Evolution in Al-11% Si-C

6.2.2.1. Variation of Volume Loss with Sliding Cycles

Fig. 6.2 shows the volume losses of Al-11% Si-C with sliding cycles at applied loads of 0.5, 1.0, and 2.0 N. It indicates that the transition from UMW-I to UMW-II happens to the alloy at all applied loads. At 0.5 N, volumetric loss started to be measurable after sliding to 3 x 10^5 cycles, indicating that the UMW-I regime was maintained in the alloy up to this point. At this sliding cycle the volume loss was 4.2 x 10^{-5} mm^3. At an applied load of 1.0 N, the transition from UMW-I to UMW-II started after sliding to 5 x 10^4 cycles; the measured material loss was 1.58 x 10^{-4} mm^3. At 2.0 N, UMW-I lasted only to 1 x 10^4 cycles; the volume loss was 1.0 x 10^{-4} mm^3.

Immediately after the transition point, the volume loss increased with increasing sliding distance and normal load. The initial increase at 2.0 N corresponded to a wear rate of 9.79 x 10^{-10} mm^3/cycle (8.67 x 10^{-8} mm^3/m). An important aspect of the plots shown in **Fig. 6.2** is that they indicate a decrease in the wear after certain number of cycles, inferring that the alloy enters UMW-III. In fact, the volume loss of the alloy tested at 2.0 N showed a drop off after 6 x 10^5 cycles. The volumetric wear loss after sliding for 6 x 10^5 cycles was 3.58 x 10^{-4} mm^3, which corresponded to an 18% reduction compared to wear at 3 x 10^5 cycles (w= 4.4 x 10^{-4} mm^3). Examination of the worn surfaces with sliding distance is instructive to better understand the transition from UMW-I to UMW-II. Metallurgical evidence is provided in **Section 6.2.2.2**.

6.2.2.2. Contact Surface Evolution with Sliding Cycles

The contact pressure listed in **Table 6.1** suggests that at an applied load of 0.5 N, the maximum contact pressure applied to the silicon particles (654 MPa) in Al-11% Si-C was slightly less than its matrix hardness (670 MPa), indicating that the silicon particles were not expected to be pushed into the aluminum matrix. Accordingly, the silicon

particles should carry the applied load and no surface damage should be inflicted on the aluminum matrix.

Figs. 6.3 a to **e** illustrate the evolution of the worn surface morphologies in Al-11% Si-C at 0.5 N. After sliding for 5 x 10^2 cycles (**Fig. 6.3 a**), the silicon particle surfaces inside the wear tracks show slight wear on their contact surfaces in the form of longitudinal scratches along the sliding direction, but no obvious particle height reduction or damage to the aluminum matrix were observed. It is observed that silicon particles with high aspect ratio started to fracture at 5 x 10^4 cycles (**Fig. 6.3 b**). This is consistent with observations made by Riahi et al. [71-72]. Fragmentation of the silicon particles facilitated silicon particle sinking-in, due to the increase in the pressure applied on the small fractured sections (**Fig. 5.17**). The stress intensification on fragmented particles was discussed in **Section 5.4.3**. The aluminum matrix around the sunken-in particles bulged out to accommodate the displacement caused by the particle indentation (**Fig. 6.3 c**). It is notable that damage that occurred so far was still at the microscopic level, no material loss was detectable within the detection limits for the sensitivity of the test machine, therefore, UMW-I was maintained with minimal surface damage.

The elevated aluminum plateaus are susceptible to permanent contact damage by the counterface. According to **Fig. 6.2**, volumetric wear loss started to deviate from 0 after 3 x 10^5 cycles; hence the alloy entered UMW-II. **Fig. 6.3 d** presents the corresponding contact surface morphologies. Significant surface damage, in the form of continuous scratches parallel to the sliding direction was observed on the aluminum surface, and material loss became obvious and measurable. In addition, most of the silicon particles inside the wear tracks appeared to be fractured into smaller sections, which became embedded into the aluminum matrix. At the longest sliding distance, *i.e.*,

at 6 x10^5 cycles, the SEM image in **Fig. 6.3 e** reveals a similar wear mechanism. The abrasive scratches on the wear track are continuous and deeper, inferring an increase in material loss. The silicon particles inside the wear track are fully embedded into the aluminum matrix. These observations suggest that the onset of the running-in period is inevitable when the silicon particles became embedded in the aluminum matrix leading to a loss of their load carrying ability.

Evaluation of the microstructure at 1.0 and 2.0 N applied loads showed that damage to the silicon particles and the aluminum matrix around the particles occurred at shorter sliding distances due to the higher contact pressure (**Section 6.2.1**). Fundamentally the images offer no new information from those presented in **Fig 6.3**. **Figs. 6.4 a** to **d** present the evolution of the worn surfaces at 2.0 N after stopping the sliding tests between 5 x 10^2 and 6 x 10^5 cycles. The back scattered SEM image in **Fig. 6.4 a**, taken after 5 x 10^2 cycles illustrates that silicon particle fracture and sinking-in started to happen in the very beginning of surface damage process. **Fig. 6.4 b** presents the image taken after 1.5 x 10^3 cycles, where asymmetrical aluminum pile-ups around the fractured and sunken-in silicon particles were observed. With increasing sliding cycles, the continuous abrasive scratches became deeper and wider, inferring a transition to the UMW-II regime. Damage and material loss on the contact surface is shown in **Fig. 6.4 c** after sliding for 6 x 10^5 cycles. In addition, the SEM image in **Fig. 6.4 c** shows that the elevated aluminum surface in some areas, such as indicated by the arrows marked ORL, became dark in color compared to the area outside the wear track. Further analysis showed that this is an oil residue layer (ORL). The layer is only formed after the contact had evolved by sliding; *i.e*, after Si fragmentation and damage to deformed aluminum. More analysis of the layer is presented in **Section 6.2.4**. The enlarged backscattered SEM

image in **Fig. 6.4 d** reveals details of fractured Si particles inside the wear track that are embedded into the aluminum matrix. The arrow in **Fig. 6.4 d** indicates displacement of fractured parts of the fractured particles leading to opening of gaps on the aluminum surface through which oil residues can diffuse inside the matrix and to the matrix particle interfaces.

6.2.3. Surface Damage Evolution in Al-11% Si-F

6.2.3.1. Variation of Volume Loss with Sliding Cycles in Al-11% Si-F

The tribological behaviour of the alloy with the finer microstructure, Al-11% Si-F was not identical to Al-11% Si-C. **Fig. 6.5** shows the variation of volumetric wear loss of Al-11% Si-F at the applied loads of 0.5, 1.0, and 2.0 N. According to **Fig. 6.5**, the UMW-I regime was maintained at 0.5 N even after sliding to 6 x 10^5 cycles, i.e., no material loss could be detected to Al-11% Si-F. At 1.0 N, the transition from UMW-I to UMW-II started at 5 x 10^4 cycles, the measured material loss was 7.53 x 10^{-5} mm^3. At an applied load of 2.0 N, the deviation of volumetric wear loss from zero started after just 5 x10^3 cycles, the corresponding volume loss was 1.40 x 10^{-4} mm^3.

Similar to Al-11% Si-C, the volume loss increased with increasing sliding distance and normal load. However, the plots shown in **Fig. 6.5** indicate that the volume loss decreased after sliding for 3 x10^5 cycles at 1.0 N, and 10^4 cycles at 2.0 N, the alloy entered the UMW-III regime. This is again similar to the decreasing wear trend seen in **Fig. 6.2** for Al-11% Si-C. The mechanisms responsible for delaying the transition to UMW-II at all sliding cycles at 0.5 N and the attainment of the UMW-III accompanied by a decrease in volume loss after sliding long cycles will be understood through the metallurgical evidence provided in **Section 6.2.3.2.**

6.2.3.1.1. Microstructural Features of the Worn Surfaces of Al-11% Si-F

The contact pressure analysis presented in **Section 4.4** suggests that the maximum real contact pressure applied on the silicon particles in Al-11% Si-F was dependent on the silicon particle distribution. The maximum contact pressure decreased with a reduction in the separating distance between the silicon particles (**Fig. 4. 20**). At all the applied loads used, the maximum contact pressures applied to the silicon particles exceeded the matrix hardness (660 MPa). This infers that Si sinking-in is expected, and more plastic deformation is expected to the areas with small silicon particle areal density. Consequently, the transition to the UMW-II regime should occur at a lower number of cycles, and more material loss is expected compared to Al-11% Si-C.

Figs. 6.6 to **6.8** illustrate the evolution of the worn surface morphologies of Al-11% Si-F at 0.5 N. **Figs. 6.6 a** and **b** show the 3D surface profilometer images taken after interrupting the sliding tests at 5×10^2 and 1.5×10^3 cycles. They show that the damage mechanism operating in Al-11% Si-F differed from that of Al-11% Si-C: Silicon particle sinking-in started in the very beginning. At 5×10^4 cycles the particle height continued to decrease (**Fig. 6.7**). To accommodate the indentation made by the silicon particles, aluminum pile-ups were formed around the sunken-in silicon particles, as in the case of Al-11% Si-C. However, as shown in **Fig. 6.7 a** and the magnified SEM image shown in **Fig. 6.7 b**, the aluminum pile-up in Al-11% Si-F depended on the Si inter-particle spacing. Aluminum pile-up was generally observed around those sunken-in silicon particles which had a larger separation between the silicon particles, that is, around sparsely distributed sunken-in silicon particles, *i.e.*, where the area density of silicon particles is $< 4 \times 10^{-2}$ μm^{-2}. The arrows in **Fig. 6.7 b** indicate a location of pile-ups. When

the inter-particle distance between silicon particles was small, corresponding to a particle density > $4x10^{-2}$ μm^{-2}, little or no aluminum pile-up was observed. The bulging out of the aluminum matrix around the sunken-in silicon particles can also be observed in the 2-D surface profilometer image (**Fig. 6.7 c**). Compared with the aluminum pile-up adjacent to the plate-like silicon particles in Al-11% Si-C, the aluminum bulging-out around the small spherodized silicon particles appears to be more symmetrical, as the arrows indicate in **Figs. 6.7 a** and **b**. While the asymmetry in pile-up formation in high aspect ratio Si particles is noted in **Figs. 6.3** and **6.4 b** where more aluminum accumulation was observed ahead of the plate-like silicon particles in Al-11% Si-C.

Figs. 6.8 a – c show the evolution of surface damage within the wear track after sliding for 6 $x10^5$ cycles at 0.5 N. The silicon particle height continued to decrease, however, no significant damage, *i.e.*, surface scratches parallel to the sliding direction, were observed (**Fig. 6.8 a**). The surface damage appeared to be a function of the area density of silicon particles. At location 'X' in **Fig. 6.8 a**, where silicon particles were closely distributed (area density of silicon particles $\geq 0.04/\mu m^2$), silicon particle sinking-in was the main damage process. A high magnification view of the inset X is given in **Fig. 6.8 b** to show the sunken-in particles. The top parts of most particles are still visible above the aluminum matrix. While at location 'Y', where silicon particles were distributed with larger spacing and the area density was about $0.01/\mu m^2$, the aluminum matrix around those silicon particles rose above the initial surface and more particles were embedded into the aluminum matrix. In the magnified backscattered SEM image of **Fig. 6.8 c** bulging-out of the aluminum matrix that covered almost all particles is evident. It can be seen that local plastic deformation is extensive, but no scratches could be observed, hence no material loss occurred. The top surfaces of the elevated aluminum

plateaus remained smooth, but assumed a dark color, due to the formation of an oil residue layer, which will be further discussed in **Section 6.2.4**. In summary, UMW-I maintained in Al-11% Si-F at 0.5 N even after the longest sliding cycle used.

At 1.0 N, the transition to the UMW-I regime in Al-11% Si-F was first noted at a sliding distance of 5 x 10^4 cycles. At this point in sliding, the silicon particles became totally embedded in the aluminum matrix. Additionally, longitudinal surface scratches on the elevated aluminum became apparent with continuous tracks. This resulted in measurable quantities of material loss (*i.e.*, 7.5 x 10^{-5} mm^3). At 2.0 N, the degree of silicon particle height reduction was greater in comparison with that at 0.5 N after sliding for any cycle. Obvious silicon particle sinking-in was observed after sliding just 5 x 10^2 cycles. Aluminum bulging out started to form locally after just sliding for 5 x 10^2 cycles as shown in **Fig. 6.9**. Longitudinal scratches were visible after sliding for 5 x 10^3 cycles.

6.2.4. Characterization of the Oil Residue Layer

After sliding for 6 x 10^5 revolutions at 2.0 N, virtually the whole wear track was covered by a dark colored layer, as shown in the optical image **(Fig. 6.10 a)**. This is the oil residue layer. The wear track morphology after sliding for 5 x 10^4 cycles in **Fig. 6.10 a** indicates that the contact surface was first subjected to wear damage; the wear track was not covered with the dark layers, but surface scratches and severe deformation. At 2.0 N (as well as 1.0 N) an oil residue layer was formed after the transition to UMW-II and surfaces evolved for sliding long cycles. Once formed, this layer served to reduce the wear as seen in **Fig 6.5,** that is, the alloy entered UMW-III regime. **Fig. 6.10 b** presents the SEM image taken from the location 'X' in **Fig. 6.10 a** showing the morphology of the

oil residue layer. The oil residue layer spreads over the surfaces of silicon as well as aluminum. The nanometer size morphological features of the layer are seen in the corresponding AFM image shown in **Fig. 6.10 c**. Similar features were observed on the Al-Si cylinder bore surfaces by M. Dienwiebel et al [13]. To identify the microstructural changes in the layers adjacent to the worn surface in UMW-II, FIB and TEM investigations were required.

Fig. 6.11 a shows a cross-section of the wear track prepared using a FIB milling technique. **Fig 6.11 b** is a secondary FIB image giving details of the inset in **Fig. 6.11 a**. In this section the thickness of the oil residue layer is about 0.6 μm. Embedded silicon particles are clearly seen. An oil residue appears to spread under some particles. **Fig. 6.12** presents the cross-sectional TEM image taken from the same section of this FIB image: The layer is visible on the top surface. It exhibits nanocrystalline aluminum grains (note the layer above the silicon particle) with sizes less than 100 nm, consistent with the size of features seen in the AFM image. The aluminum grains immediately below that have an equi-axed shape and nano-crystalline size in the range of 400- 600 nm.

The mechanical properties of the worn surfaces covered with the oil residue layers were evaluated using a nano-indentation tester. Using a maximum load of 2.3 mN the indenter penetrated to a depth of 200 nm and hardness values ranging between 1.5 to 2.5 x 10^3 MPa were obtained. At the same penetration depth the bulk aluminum matrix had a hardness of 750 to 850 MPa, indicating that the hardness of the oil residue layers and the aluminum layers adjacent to them were more than three times higher than that of the aluminum matrix.

Chemical analysis of the composition of the oil residue layer by XPS, as shown in the survey spectrum in **Fig. 6.13**, reveals that engine oil elements were found in the layer:

S, Ca, Zn, C, and O, and aluminum and silicon. This layer has been formed during the course of sliding wear and, therefore, is named an oil residue layer. A closer examination of the chemical state of aluminum in the oil residue layer (**Fig. 6.14 a**) indicated that the uppermost few nanometers (depth sensitivity of XPS is 6-7 nm) of the aluminum layer was composed of aluminum oxide (binding energy 73.7 eV). This contrasts with the XPS spectra of the initial surface where metallic aluminum (binding energy 72 eV) and aluminum oxide (74.8 eV) were observed. When the (dry) sliding wear tests were done in ambient air (45% RH) at 2.0 N, again these two peaks were observed (**Fig. 6.14 a**), thus providing additional evidence that the Al 2p peak at 73.7 eV obtained after the lubricated tests might be attributed to the presence of elements from the oil. A similar Al 2p peak shift was found by Hu et al. [82] from an Al-Si alloy surface sliding against itself, lubricated with amines. Similarly, Timmermans *et al.* [81] detected oil elements on a worn surface generated after fretting wear of hypereutectic P/M Al-Si alloys in an oil environment. The Si 2p spectra presented in **Fig. 6.14 b** show that the silicon in the near surface appeared to be both in the form of silicon oxide and elemental silicon, and that the spectrum remained virtually unchanged from the initial surface or after dry sliding tests.

6.2.5. Evolution of Silicon Particle Height with the Sliding Cycles in the Two Eutectic Al-Si Alloys

Complete sinking-in of silicon particles causing the loss of their load carrying ability, is a precursor to transition from UMW-I to UMW-II, if no oil residue layer is formed. Accordingly, a statistically analysis of the silicon particle height distributions is necessary to quantify damage in the UMW regime. Quantitative analysis of the worn surface morphology is presented for Al-11% Si-C in **Section 6.2.5.1**, and then for Al-11%

Si-F in **Section 6.2.5.2.**

6.2.5.1. Silicon Particle Height Reduction in Al-11% Si-C

Histograms showing the reduction of silicon particle heights in Al-11% Si-C at the applied loads of 0.5, 1.0 and 2.0 N after various sliding distances are plotted in **Fig. 6.15**. The average initial height of silicon particles standing proud of the aluminum matrix in Al-11% Si-C is 1.60 μm. At an applied load of 0.5 N, the average silicon particle height cumulatively decreased to 1.50 μm after sliding for 5 x 10^3 cycles, and to 0.87 μm after sliding for 10^5 cycles. **Fig. 6.15** indicates that after sliding for 3 x 10^5 cycles the height difference between silicon and aluminum peaks disappeared and all the surface profiles merges into a single peak. The reduction in the average silicon particle height on the contact surfaces of Al-11% Si-C with the sliding distance at each applied load is summarized in **Fig. 6.16**.

Figures 6.15 b and **c** show that, the silicon particle height was reduced by a greater amount at 1.0 and 2.0 N than at 0.5 N. The initial silicon particle average height of 1.60 μm in at 1.0 N decreased to 1.40 μm after sliding for just 3 x 10^2 cycles. After sliding for 10^4 cycles, the average height of a silicon particle protruding above the aluminum matrix was only 0.38 μm. After sliding for 5 x 10^4 cycles, it was no longer possible to differentiate the silicon height from the aluminum. At 2.0 N, after sliding for 10^4 cycles, the two peaks merged into a single peak (**Fig. 6.15 c**), inferring that silicon particles were completely embedded in to aluminum matrix.

6.2.5.2. Silicon Particle Height Reduction in Al-11% Si-F

Figs. 6.17 a to **c** present the histograms showing the reduction of silicon particle

heights in the Al-11% Si-F at the applied loads of 0.5, 1.0 and 2.0 N after various sliding cycles. A summary of the analysis of the height histograms after various sliding distances is plotted in **Fig. 6.18**. It indicates that the silicon particle height in Al-11% Si-F also decreased with increasing sliding cycles and normal load. But Al-11% Si-F exhibited a larger degree of silicon particle sinking-in at low sliding cycles at each load when compared to Al-11% Si-C with large plate-like silicon particles (**Fig. 6.15**). On the other hand, the worn surface morphologies presented in **Section 6.2.3** indicates that the embedding of the silicon particles into the aluminum matrix was also affected by the silicon particle distribution. The data for Al-11% Si-F shown in **Fig. 6.17** was constructed by analyzing surface profilometry data measured from locations where silicon particles were distributed with smaller separation distance, the area density was $\geq 0.04/\mu m^2$. At 0.5 N, the initial silicon particle height of 1.74 above the aluminum matrix decreased to 1.45 μm after sliding for 5×10^2 cycles, after sliding for 10^5 cycles, the silicon particle height protruding above the aluminum matrix was just 0.40 μm, while for the large plate-like silicon particles in Al-11% Si-C at 0.5 N, the average particle heights decreased by 0.70 μm after sliding for 10^5 cycles. However, after sliding for 3×10^5 cycles, the average height of the silicon particles projecting above the aluminum matrix in Al-11% Si-F was still 0.26 μm (**Fig. 6.17 b**).

Like the large plate-like silicon particles in Al-11% Si-C, the average heights of the small spherorized silicon particles in Al-11% Si-F decreased by a greater amount by increasing the applied load to 1.0 and 2.0 N (**Figs. 6.17 b** and **c**). At 1.0 N, the initial silicon particle height of 1.74 μm in Al-11% Si-F rapidly decreased to 0.22 μm after sliding for 10^4 cycles (**Fig. 6.17 b**). After sliding for 5×10^4 cycles, it was no longer possible to differentiate the locations of silicon peak heights from the aluminum surface

profile (**Fig. 6.17 b**). At 2.0 N, the initial average heights of the silicon particles in Al-11% Si-F sharply decreased by 1.50 μm after a sliding distance of only 10^3 cycles (**Fig. 6.18**). After sliding for 5 x 10^3 cycles, the height difference between silicon particle and aluminum matrix vanished, and surface profiles of the silicon particle and matrix become merged into a single peak (**Fig. 6.17 c**).

In addition, the number of sliding cycles at which the silicon particle peak height diminishes to zero almost always corresponded to the number of sliding cycles where the running-in period started. Therefore, complete sinking-in of silicon particles, causing the loss of their load carrying ability, is the precursor to the transition from UMW-I to UMW-II provided that an oil residue layer is not formed (**Sections 6.2.2,** and **6.2.3**).

6.2.6. Summary and Discussion

The wear test results show that the transition from UMW-I to UMW-II depends on two factors, one is the mechanical response of the hard phases to the applied load, and the other is the possible formation of an oil residue layer.

Both eutectic Al-Si alloys tested had comparable compositions, and bulk and matrix hardnesses, but different microstructures: the average silicon particle length in Al-11% Si-C was 15 times larger, and the particle aspect ratio was 7 times larger than in Al-11% Si-F. The silicon particle distribution in the alloys was different too (**Fig. 3.4**); the silicon particles in Al-11% Si-C had a larger interparticle spacing when compared to the particles in Al-11% Si-F. Examination of the worn surfaces generated during sliding tests versus sliding cycles revealed that the surface damage mechanism in Al-11% Si-C differed from that of Al-11% Si-F at 0.5 N, while at 1.0 and 2.0 N, the two alloys exhibited a similar wear damage mechanisms. The propensity of the alloys to form an oil

residue layer was different. The contact pressures applied on Al-11% Si-F, where the area density was ≥ 0.04 /μm^2, were about 2.5 times higher at each load than those applied on Al-11% Si-C. At 0.5 N, an initial contact stress exerted on Al-11% Si-C was less than its matrix hardness. The surface damage mechanism evolved with sliding distance in Al-11% Si-C at this load in the following sequence:

i) Abrasive wear on the top surfaces of silicon particles by the counterface,

ii) Fracture of silicon particles,

iii) Sinking-in of fractured silicon particles into the aluminum matrix,

iv) Bulging out of the aluminum matrix adjacent to the sunken-in silicon particles,

v) Wear to the elevated aluminum portions by the counterface, causing material loss.

The experiments at 0.5 N clearly observed fractured silicon in Al-11% Si-C, and not in Al-11% Si-F. This is due to the fact that the size and shape of the silicon particles control their ability to resist the applied contact pressure. Although the estimations of contact pressure provided in **Section 6.2.1** are helpful in rationalizing the response of the silicon particles to the applied load, these calculations do not exactly simulate the experiment. The pin - on- disc experiments have an additional shear stress on the silicon particles. The calculations suggest that larger particles will have a reduced stress level, and hence should perform better. However, the data shows that large particles with a large aspect ratio failed by fracture, and are no better than small spherical particles in resisting the transition to the UMW-II regime. As shown in **Fig. 5.17**, the maximum contact pressure exerted on the fractured silicon particles will increase due to the size reduction. Therefore, fragmentation of the plate-like particles into small pieces assists silicon particle sinking-in. This was in fact experimentally observed. The calculations in **Section 4.4** do not predict the behaviour of the fractured particles; these fragments can be lost

altogether, or easily pushed into the matrix, both of which reduce their ability to carry load in a way that is not predicted by the calculations.

The small spheroidized silicon particles in Al-11% Si-F exhibited a greater decrease in silicon particle height at a low number of cycles in comparison with Al-11% Si-F, due to the much higher contact pressure (**Table 6.1**). The height reduction of particles in Al-11% Si-F was not due to particle abrasion but rather to rapid silicon particle sinking-in, which started at the very early stages of sliding. As stated before, silicon particle sinking-in induced plastic deformation of the aluminum matrix, which led to the formation of aluminum pile-ups around the sunken-in particles. The backscattered SEM images in **Fig. 6.7** indicate that the silicon particle sinking-in and aluminum bulging-out around the sunken-in silicon particles were affected by the particle distribution at 0.5 N. Silicon particles with a smaller separation distance from one another were pushed into the aluminum matrix to a lesser extent than those with a wider spacing. At locations where the local silicon particle density was high, there was little or no pile-up formation. This infers that in these locations where particles were more closely spaced they constrain the matrix and hence induce local hardening at levels higher than where the particles are sparsely distributed – The increased matrix strength makes sinking-in of the closely spaced particles more difficult (**Fig. 6.7**). Unlike Al-11% Si-C, in this alloy no conspicuous wear damage in the form of longitudinal abrasive scratches was observed on the elevated aluminum plateaus. A dark colored layer covered most of the elevated aluminum surfaces after 6 x 10^5 cycles (**Fig. 6.11 a**). Hence, in Al-11% Si-F tested at 0.5 N, the transition to UMW-II was prevented throughout. The evolution of damage in Al-11% Si-F with sliding at 0.5 N can be summarized as:

i) Rapid sinking-in of silicon particles into the aluminum matrix (no abrasion on the

top surfaces was evident), but particle sinking-in depended on interparticle spacing, silicon particles in areas with large interparticle distance sink-in more readily than those with small interparticle spacing,

ii) Development of aluminum pile-ups adjacent to the sunken-in silicon particles,

iii) Formation of an oil residue layer on the elevated aluminum surface.

The formation of the oil residue layer with a higher hardness than the aluminum matrix material has quite significant consequences; it appears that it was effective in inhibiting the transition to UMW-II. This layer prevented direct contact between the nascent aluminum and the counterface (**Fig. 6.8**). The important point is that at 0.5 N applied load, the layer depended on the microstructure and the number of sliding cycles, and that for the Al-11% Si-C microstructure, the layer never formed.

At applied loads of 1.0 and 2.0 N, sinking-in of the silicon particles in the eutectic Al-Si alloys was inevitable due to the high contact pressure, exceeding their matrix hardness (**Table. 6.1**). In spite of the fact that there was some fracture of large silicon particles in Al-11% Si-C, the results indicate that the alloy behaved as though yielding of the aluminum matrix was based on the initial particle size (stress). The wear mechanisms in both alloys appeared to be similar and consisted of the following distinct stages:

- In the UMW-I regime, sinking-in of silicon particles into the aluminum matrix and bulging-out of the aluminum matrix adjacent to the sunken-in silicon particles were observed.
- In the UMW-II regime, wear to the elevated aluminum portions by the counterface, causing material loss started to be measurable.
- In the UMW-III regime, an oil residue layer supported by ultra-fine aluminum

grains was formed, leading to a decrease in the volumetric loss.

At these loads, silicon particles with a smaller size were more rapidly embedded into the aluminum in comparison with large silicon particles. But, ultimately all particles became completely embedded in either alloy. As the particles were pushed in, deformation of the surrounding aluminum occurred in order to conserve volume. The deformed aluminum became exposed to the counterface at low sliding cycles. Hence, the transition to the UMW-II regime occurred earlier. The surface damage process evolved with the sliding cycles during the UMW regime is schematically summarized in **Fig. 6.19**.

The key difference between the alloys at the tested loads was the generation of a black colored oil layer on the elevated aluminum plateaus around the sunken-in silicon particles after sliding for a large number of cycles. Aktary et al. [111] found that the formation of the ZDDP anti-wear film is a function of rubbing time. As with the 0.5 N tests, the details of formation of this layer depended on the microstructure, load, and number of sliding cycles: A greater area of the wear track was covered with this layer at a lower number of sliding cycles for the Al-11% Si-F alloy. This suggests that a competition exists between the kinetics of formation of these deposits, and removal of the layer by wear processes.

The material loss decreased on the contact surfaces in Al-11% Si-C at 2.0 N after 3×10^5 cycles and after approximately 10^5 cycles for Al-11% Si-F at 1.0 N and 2.0 N, these conditions correspond to observations of the oil residue layer nearly completely covering the wear track. The decrease in material loss is possibly attributed to the formation of the oil residue layer with engine oil elements in it. The material loss reduction may also be caused by refinement of aluminum grain size during sliding process. The formation of ultrafine grains adjacent to contact surface increased the local

hardness and possibly provided support to the oil residue layer. Some nano-crystalline aluminum grains were mixed with oil residue in this layer. The surface plastic deformation accompanying formation of the oil residue layers has been noted in **Figs. 6.4**, **6.8**, and **6.11**.

The reduction in the grain size of aluminum during sliding results from severe plastic deformation, inferring that the contact surface was subjected to large plastic strains. During sliding wear, in addition to the shear stress applied to the material layers adjacent to the contact surface, a superimposed hydrostatic pressure field exists. Consequently, aluminum layers can be constrained to very large strains without fracture. The principles of processing of ductile materials with ultra-fine grain sizes using high strain deformation processes are well known [112]. It was estimated that application of a large hydrostatic pressure of about 5 GPa and equivalent plastic strains of the order of 5.0-10.0 were typically induced using torsional deformation carried out under hydrostatic pressure, and in this way ultra-fine grain sizes of the order of 100-200 nm could be obtained [113]. An estimate of the severity of local shear strains generated during sliding contact conditions can be made using the grain size data provided by the cross-sectional TEM micrographs (**Fig. 6.12**). The original aluminum grain size of the two eutectic Al-Si alloys is 10-30 micrometers. During deformation the grain size in the material immediately below the oil residue layers has been reduced to about 500 nm. The size of the aluminum grains within the oil residue layer is even smaller (less than 100 nm). Hence hydrostatic pressures and plastic strains in aluminum that are at the same order of magnitude as noted above are likely to occur during the pin-on-disc tests in the UMW regime and at the beginning of the UMW-II regime. The nanocrystalline aluminum layers are harder than the rest of the bulk alloys (750 – 850 MPa), as the composite hardness of

the oil residue layer and nano-crystalline aluminum surfaces was 1.5- 2.5 GPa. Thus they serve to support the oil residue layer, and help to maintain low wear rates.

It is important to emphasize that the silicon particle height in Al-11% Si-F at 0.5 N, and also for Al-11% Si-C at 1.0 reduced abruptly from the beginning to after some short sliding cycles, for example 5 x 10^4 cycles for Al-11% Si-F at 0.5 N, it then decreased gradually with sliding cycles. This can also be attributed to work hardening of the aluminum matrix due to grain size reduction; the increased strength of the matrix makes the further sinking-in of silicon particles more difficult.

In closing, it should be noted that all tests reported here were conducted at a relatively low sliding speed in order to insure that the lubrication state stayed in the boundary lubricated regime. This use of low speed limited the total number of cycles that any single test could be run, for practical reasons: The longest tests took 4 full days to complete. The trend in the data shows that once the oil layer is formed, the material loss rate tends to decrease with the sliding cycles. The experimental observation made on the two alloys indicates that the UMW finally tends to be stabilized after sliding for long cycles. This makes one wonder whether a new stable condition lies further out in the data, where after even greater number of sliding cycles the tests may return to a stable condition equivalent to the UMW-I regime, which is not accompanied by material loss. To test this premise, the two eutectic Al-Si alloys were tested to 2 x 10^6 cycles at 2.0 N. **Figs. 6.20** and **6.21** present the optical images taken from the wear tracks of Al-11% Si-C and Al-11% Si-F after stopping the sliding tests at 2 x 10^6 cycles. It can be seen that virtually the whole wear tracks of both alloys were covered by a dark-colored layer (**Fig. 6.20 a** and **6.21 a**). But the oil residue layer formed on the Al-11% Si-F surface was more uniform compared with that on Al-11% Si-F (**Fig. 6.20 b** and **6.21 b**,), inferring that the

microstructure in Al-11% Si-F is optimal for the formation of the oil residue layer. For both alloys, the volumetric wear loss continued to decrease compared to the data obtained after shorter sliding cycles of 6×10^5. For example, the volume loss measured from the Al-11% Si-F surface decreased from 1.58×10^{-4} mm^3 to 8.07×10^{-5} mm^3 when the sliding cycles increased from 6×10^5 to 2×10^6 cycles.

The results obtained from Al-11% Si-F with small spheroidized silicon particles suggested that surface damage in the form of silicon particle sinking-in and aluminum pile up was affected by the silicon particle distribution. Accordingly, it is conceivable that the use of an Al-Si alloy with a high areal density of small spheroidized silicon particles, which are evenly distributed with small inter-particle distance, would be advantageous in reducing the wear damage under the UMW conditions. In order to test this premise, a spray formed hypereutectic alloy (Al-25% Si) with a harder matrix (1,090 MPa), high areal density (about 0.3 ± 0.1), and uniformly distributed small silicon particles was tested under the conditions that corresponded to the UMW regime. The experimental results from the wear tests are presented for the Al-25% Si alloy in **Section 6.3.**

6.3. UMW Behaviour of the Al-25% Si Alloy

Microstructural events controlling the wear behaviour of Al-25% Si were complex and depended on the applied load. Also morphological features of the wear tracks evolved with the number of contact cycles. These features are described in the following sections in the order they were detected, starting from the lowest load applied.

6.3.1. Worn Surface Morphologies at 0.5 N

At 0.5 N hardly any visible damage was apparent on the wear tack. **Figs. 6.22 a** and **b** show characteristic features of the wear tracks after sliding for 5 x 10^4 cycles. It was difficult to distinguish the impression of the wear track on the contact surface in the low magnification SEM micrograph of **Fig. 6.22 a**. A small number of fractured silicon particles were observed within the wear track, as marked in the higher magnification SEM image of **Fig 6.22 b**. No wear or damage due to plastic deformation on the aluminum matrix was evident. Examination of the 3-D optical surface profilometer image in **Fig. 6.22 c** of the same portion of the wear track shown in **Fig. 6.22 a** indicates that generally there was a some decrease in the heights of the silicon particles standing out of the wear track.

After sliding for 6 x 10^5 cycles, which is the longest number of cycles used at 0.5N, an assessment of the SEM images of the wear track (**Fig. 6.23 a**) revealed that the main features of the wear remained essentially the same as those from a lower number of cycles. There was an increase in the number of fractured silicon particles, some of which can be seen in **Fig. 6.23 b**. As seen here, larger particles were more prone to fracture. The silicon particle elevation inside the wear track continued to decrease, compared to outside the wear track. However, the silicon peaks still rose above the aluminum surface (**Fig. 6.23 c**). Quantitative evaluation of the silicon particle height distribution within the wear track will be given in **Section 6.3.4**, but it is helpful to note here that the silicon particle height reduction can occur either as a result of the embedding of rigid particles into aluminum or by wear of the tops of particles, depending on the magnitude of the contact stress on and the hardness of the aluminum (**Section 6.2**). In the case of the Al - 25% Si alloy, which has high hardness, wear of silicon peaks is the likely reason for the particle height reduction. Evidence for abrasion on silicon particles can be seen in the high

magnification image in **Fig. 6.23 b**. Embedding of rigid particles into the softer aluminum (silicon sinking-in) is normally accompanied by the formation of aluminum pile-ups in the vicinity of the sunken-in particles (**Sections 5.3.1** , and **6.2.2.3**). At 0.5 N, no clear evidence for matrix deformation could be observed. The salient observation is that the particle elevation is still above the matrix at the end of test, and thus, aluminum did not come in direct contact with the counterface.

A period of high wear, mainly through the loss of aluminum followed. The observations pertaining to the Al- 25% Si alloy therefore, suggest that the high hardness and high silicon content, and hence smaller contact pressure per particle, made this alloy more wear resistant compared to eutectic Al-11%Si-C at this low load. In this respect the wear performance of Al- 25% Si can be considered equivalent to that of cast 390 (Al-18.5% Si) alloys (**Section 5.5**) with similar hardness (97 ± 7 HB), in which the damage was also confined to the silicon particle peaks.

6.3.2. Worn Surface Morphologies at 1.0 N

At 1.0 N local damage to aluminum adjacent to silicon particles became apparent, but otherwise metallurgical features of the worn surfaces of Al-25% Si were in general agreement with those at the lower load. **Figures 6.24 a-d** present images showing the worn surface morphology examined after running to 5 x 10^4 cycles at 1.0 N. The secondary SEM image (**Fig. 6.24 a**) and the high magnification back-scattered SEM image in **Fig. 6.24 b** both indicate that silicon particles became partially embedded into the aluminum matrix. As stated above, silicon sinking-in was accompanied by formation of aluminum pile-ups around these particles. The pile-ups form in order to accommodate the displacement caused by the rigid particle indentation into the plastically deforming

matrix (**Figs. 6.24 c** and **d**). The rise in the average elevation of aluminum within the wear track is seen in **Fig. 6.24 c**. Pile-up formation was not uniform but depended on the location of the silicon particles inside the wear track. Namely, the elevation of aluminum in the vicinity of the particles at the centre of the wear track is higher according to **Fig. 6.24 c**. This correlates well with the higher contact stress distribution at the center of the wear track (see **Section 6.3.5.1**). Another factor that influences the propensity of pile-up formation is the local particle density (i.e., the number of particles per unit surface area). Examination of a large number of optical surface profilometer and SEM images from various locations of the wear tracks indicated that aluminum pile-ups were preferentially formed around silicon particles in regions where the particle density was lower than the average, i.e., $< 4 \times 10^{-2}$ μm^{-2}. In regions where the local silicon density was high, corresponding to a particle density $> 4 \times 10^{-2}$ μm^{-2}, a lower amount of aluminum pile-up development was found. The contact stress depends on the details of the surface roughness, which in this case is dependant on the particle density. It is also likely that the aluminum matrix became more constrained when closely spaced particles were pushed in. This would cause an increase in the local yield strength making initiation of sinking in more difficult.

At 1.0 N, a larger percentage of silicon particles were fractured compared to 0.5 N (**Fig. 6.25**). For example, after 5×10^4 cycles, 8 % of particles were fractured at 0.5 N, while at 1.0 N, 22 % of the particles in the wear track were fractured. Some fractured silicon particles exhibited crack openings as indicated in **Fig. 6.24 b**. Fracture between particles and the matrix was also observed.

The same wear mechanisms continued to operate at higher sliding cycles, and the surface damage accumulated as shown for the tests performed to 6×10^5 cycles. The SEM

images in **Figs. 6.26 a** and **b** clearly show that most of the particles were embedded into the aluminum matrix inside the wear track after 6 $x10^5$ cycles. The average silicon particle size was reduced as a result of particle fracture and fragmentation. Formation of aluminum pile-ups resulted in an increase in the relative height of the matrix as shown in the 3-D surface profilometer image of **Fig. 6.26 c**. An important consequence of the these damage accumulation processes is that the aluminum matrix was left with fewer options to defend itself from contact damage and some direct contact between aluminum and counterface materialized. Scratch marks initiated on the aluminum are shown in **Fig. 6.26 c**, but no mass loss from the sample could be detected using a high sensitivity (10^{-5} g) electronic balance. A method was developed (see **Section 3.5**) to estimate very small quantities of damage for pin on disk tests. Using this method, 2.03 x 10^{-7} g of material was removed during wear from the Al-11% Si-F after 5 $x10^4$ cycles at 1.0 N. No evidence for material loss could be detected for the Al-25% Si alloy using the same method. The first evidence for material removal in Al-25% Si was found at the higher load of 2.0 N, as will be described in the next section.

6.3.3. Worn Surface Morphologies at 2.0 N

At 2.0 N, damage to both silicon and aluminum was more extensive and additional wear mechanisms become operative at longer sliding distances. Metallurgical and compositional data illustrating the wear mechanisms at 2.0 N are presented in **Figs. 6.27 – 6.29**, and described in the following paragraphs.

Figures 6.27 a – c show the evolution of surface damage within the wear track after sliding for 10^4 cycles. Silicon particles inside the wear track were already fractured and became embedded into the aluminum matrix (**Figs. 6.27 a** and **b**). Particle height

reduction and pile-up formation both occurred at this short sliding distance (**Fig. 6.27 c**), and to a larger extent compared with tests at lower loads (i.e., compare **Fig. 6.27 c** with **Figs. 6.24 c** and **6.26 c**). According to **Fig. 6.27 b** the top parts of most particles are still above the aluminum matrix, so that they are not totally implanted in the matrix. The pile-up formations around these particles are marked by the arrows in **Fig. 6.27 b**. Aluminum pile-ups were preferentially formed around the embedded silicon particles in regions where the silicon interparticle spacing was larger than average. This observation once more underlines the earlier point that plastic deformation occurs with more difficulty in regions with high particle density.

A low magnification SEM image of the sample subjected to 5 x 10^4 cycles is given in Fig. **6.28 a**, it shows that the wear track was transformed into an apparently smoother surface, where it is difficult to distinguish individual particles. Silicon particles appear to be fully embedded into the aluminum matrix (**Fig. 6.28 b**). Almost all silicon particles fractured. Small cavities are seen in **Fig. 6.28 b**, and were probably caused by fractured particles that were washed away during sliding. Scratch marks on the aluminum and silicon are an important feature of wear. These marks, which extend in the sliding direction, are clearly seen on **Fig. 6.28 c**. A profilometer trace taken across the continuous scratch marks of the wear track (**Fig. 6.28 d**) shows the profile of the wear. Accordingly, the material loss was 2.2 x 10^{-4} mm^3.

Increasing to 6 x 10^4 cycles, the volume of material loss increased to 3.34 x 10^{-4} mm^3, the wear track became wider, and continuous scratches inside the wear track can be seen in **Fig. 6.29 a**. **Figure 6.29 b** provides additional evidence for other aspects of wear damage, including silicon particle fracture and fragmentation. The tops of the silicon particles are no longer standing out of the wear track, as previously shown, and they are at

the same elevation as the top surface of the aluminum matrix. Parts of the surface were covered with a tribolayer that had a glaze-like appearance (**Fig. 6.29 b**). This layer did not come off after washing with hexane. Details of the layer are better seen in a cross-sectional view of the wear track. To expose the cross-sectional view of the features on, and immediately below the wear track, the wear track was sectioned using a site-specific ion beam milling technique in a focused ion beam (FIB) system, as shown in **Fig.6.29 c**. There are several wear-induced damage features of interest in the cross-sectional SEM image. Of foremost interest is the presence of a tribolayer on the contact surface. This layer is very thin with thickness of the order of 0.1 μm. With the use of XPS analysis, the presence of elements including C, Ca, S, and Zn, which belonged originally to the synthetic oil used to create the boundary lubrication condition, were detected in this layer. The XPS spectrum also indicates oxygen, silicon, and aluminum. Similar layers were also formed on the surfaces of other Al-Si alloys including Al-11% Si-C and Al-11% Si-F (**Figs. 6.4**, and **6.10**). Electron energy loss spectroscopy analyses indicated that the carbon in the oil-residue layer is amorphous, and aluminum oxide was also detected. **Figure 6.29 c** provides an example of a separated interface between silicon adjacent to the contact surface and the aluminum matrix. It shows that oil layers have diffused to the channel formed between the separated interface between silicon and aluminum. Finally, similar to Al-11% Si-F, the size of aluminum grains immediately below the contact surface is much smaller than the original grain size of 3-5 μm. The aluminum grains indicated by the arrows in **Fig. 6.29 c** have an average size of 0.5 μm or less. The grain size reduction can be attributed to the generation of large strains near the contact surfaces [114]. It is proposed that an increase in the matrix hardness afforded as a result of grain refinement would help to strengthen the contact surface. **Fig. 6.30** shows the plots of load versus

displacement measured from the black layer and the aluminum matrix using a maximum load of 2.5 mN the indenter penetrated to a depth of 200 nm and hardness values ranging between 1.5 to 2.5 GPa were obtained. At the same penetration depth the bulk aluminum matrix had a hardness of 750 to 850 MPa, indicating that the hardness of the oil residue layers and the aluminum layers adjacent to them were more than three times higher than that of the aluminum matrix. This would also support the oil-residue layer on the contact surface, thus, acting together with the oil-residue layer to increase wear resistance of the contact surface. However, it is important to note that the layer formed on Al-25% Si surface (0.1 μm) was about 5 times thinner that that formed on Al-11% Si-F (0.6 μm). This will be discussed in **Section 6.3.4.2**.

Damage occurred first on silicon particles and then to the aluminum matrix. Quantitative evaluation of damage inflicted to the constituents of the alloys is presented in **Section 6.3.4**.

6.3.4. Quantitative Evaluation of Damage to Silicon Particles and Aluminum

Metallurgical evidence presented in **Section 3.3.2.1** indicates that the height of silicon particles standing 1.8 ± 0.4 μm above the etched aluminum surfaces decreased during the wear process - either due to wear of silicon summits or sinking-in of particles into aluminum. When the average silicon height decreased, their effectiveness as load carrying constituents diminished, and aluminum became susceptible to wear. These histograms are given in **Figs. 6.31 a-c** for the applied loads of 0.5, 1.0 and 2.0 N after various sliding cycles. It is seen that the silicon summit elevations decrease very gradually with increasing the sliding cycles at 0.5 N to 1.4 after 10^5 cycles and 1.0 μm after 6 x10^5 cycles (**Fig. 6.31 a**). At 1.0 N (**Fig. 6.31 b**), the particle height after 10^5

cycles is 0.9 μm, and 0.4 μm after $6x10^5$ cycles. At 2.0 N (**Fig. 6.31 c**) the decrease in the silicon height is much faster. **Fig.6.32** summarizes the particle height changes relative to aluminum matrix. While after the longest sliding cycles, the average silicon particle height is still above the average elevation of aluminum matrix at 0.5 and 1.0 N, at 2.0 N there is no difference between peaks representing silicon and aluminum after sliding only to 5×10^4 cycles. As stated above, this situation coincides with the initiation of wear and consequently material loss.

Fig. 6.33 shows the volume of material loss from the wear tracks on Al-25% Si at applied loads of 0.5, 1.0, and 2.0 N. As expected at low loads, no material loss was detected. At 2.0 N, however this was not the case as after sliding for 5×10^4 cycles a volume loss of 2.24×10^{-4} mm^3 was measured. This corresponds to the number of sliding cycles where silicon became entirely embedded in the aluminum matrix. The material loss is not a linear function of sliding cycles: The volumetric wear rate loss between $5 \times 10^4 - 10^5$ cycles at 2.0 N corresponded to a wear rate of 2.0×10^{-10} mm^3/cycle (or 1.63×10^{-8} mm^3/m). This is the UMW-II regime. As seen in **Fig.6.33** after sliding for 3×10^5 cycles, the slope of volume loss vs. sliding cycles curve started to decline, namely, entering UMW-III regime. This was attributed to the formation of an oil-residue layer and to hardening of the aluminum subsurface as a result of microstructural refinement under large strains.

6.3.5. Discussion

6.3.5.1. Wear Mechanisms in Al-25% Si

At low loads wear of Al-25% Si was initiated on the summits of silicon particles standing above the contact surfaces and these particles were fractured, some becoming

dislodged. The peaks of silicon particles within the wear track remained above the aluminum surface and continued to carry the applied load, thus protecting aluminum from damage. The damage mechanisms that occurred at 0.5 N can be summarized as:

i) Wear of the top surfaces of silicon particles,

ii) Fracture of silicon particles,

iii) Reduction of particle height but no visible damage to aluminum.

At 1.0 N, evidence for particle sinking-in into the matrix (in addition to fracture and abrasion) was found; this was accompanied by the formation of aluminum pile-ups. These pile-ups were more readily seen around the particles located in contact areas where the average silicon density was low. It was also seen that in general more pile-ups were formed at the centre of the wear track. At this load, evidence for some damage initiation to the aluminum matrix was found in the form of longitudinal grooves, after long sliding cycles. But the wear to aluminum was not large enough to be measured by an electronic balance or quantitative interferometry. Hence, at 1.0 N the surface damage events consisted of the following steps:

i) Wear of the top surfaces of silicon particles, particle fracture and fragmentation,

ii) Particle sinking-in in the aluminum matrix,

iii) Development of aluminum pile-ups adjacent to the sunken-in silicon particles, more prominent at the centre of the wear track and in locations with low particle density.

iv) Initiation of slight wear damage on the aluminum surface in the form of scratches.

At 2.0 N, silicon particle sinking-in and aluminum pile-up formation events were more discernible. Even after sliding for a short number of cycles, it was not possible to distinguish between the silicon peak and the aluminum surface profile. Aluminum wear

became visible at this point, and a period of high wear (UMW-II) ensued. This period was not persistent, and eventually the rate of damage decreased as an oil-residue layer was formed. Wear of Al-25% Si at 2.0 N involved the damage mechanisms summarized below:

i) Wear of silicon particle peaks, particle fracture, fragmentation, and particle/matrix decohesion,

ii) Sinking-in of silicon particles completely into the aluminum matrix ad formation of aluminum pile-ups,

iii) Wear of aluminum, causing measurable quantities of material loss, leading to the transition to the UMW-III regime,

iv) Development of an oil-residue layer on the surfaces of aluminum and silicon particles and strengthening of the aluminum layers by grain refinement, leading to the attainment of the UMW-III regime.

The variations of contact pressure applied on the silicon particle asperities with the radial distance at each of the normal loads of 0.5, 1.0 and 2.0 N are plotted in **Fig.6.34**. The contact pressure applied on the exposed silicon particles is the highest at the centre of the wear track but diminishes with increasing the radial distance. The radial distance at which the contact pressure decreased to zero at each load is approximately the same as the width of the wear track. The applied pressure was distributed over a larger distance at higher loads. On the particles at the centre of the wear track the contact pressure was as high as 1.57 GPa at 0.5 N; 1.62 GPa at 1.0N; and 1.68 GPa at 2.0 N. The contact pressures calculated using the Hertz theory [105], assuming smooth surfaces, are also plotted in **Fig.6.34**. The maximum real contact pressure values calculated following the Greenwood-Tripp analysis were 60% greater than the Hertzian pressures. The

apparent contact pressure calculated using the Greenwood-Tripp's model, at each load spread over an area with greater radius compared with the Hertzian pressure. The maximum apparent contact pressure estimated with Greenwood-Tripp are 164 MPa at 0.5 N, 246 MPa at 1.0 N, and 349 MPa at 2.0 N, which were 40 % lower than the Hertzian pressures.

Examination of the contact pressure distribution curves in **Fig. 6.34** help to rationalize several aspects of particle sinking-in and deformation mechanisms accompanying sliding wear of Al-25% Si. It is seen that the peak values of contact pressures exerted on the silicon particles in locations near the centre of the wear track are higher than the hardness of Al-25% Si alloy and also exceed the hardness of the aluminum matrix (1,090 MPa). Following the criterion proposed in **Section 4.4**, particle sinking-in and aluminum plastic deformation are expected to occur at all loads. According to SEM observations and optical surface profilometry data summarized in **Fig 6.32** the smallest amount of sinking-in is observed at 0.5 N, for which the contact pressure is the smallest. Particle sinking-in was clear at higher loads. The SEM and optical profilometry observations (e.g. see **Figs. 6.26** and **27**) indicated that the particle sinking-in and aluminum yielding preferentially occurred at the centre of the wear tracks. This location is in qualitative agreement with the distribution profile of the contact stresses. Contact stresses exceed the alloy hardness near the centerline of the wear tracks, i.e., at distances smaller than 30 μm according to **Fig. 6.34**. But it should be noted that the contact stress model is static and can not be used in explaining particle height reduction with the sliding cycles.

6.3.5.2. Effect of Areal Density of Silicon Particles and Matrix Hardness on the Transition to UMW-II and the Attainment of UMW-III

When compared the experimental observations made on sand cast eutectic Al-Si alloys (**Section 6.2.3**) with those on the spray formed Al-25% Si (In **Section 6.3),** it is noted that the damage to silicon and aluminum are less severe in the spray deposited Al-25% Si than in the eutectic sand cast Al-Si alloys under similar loading conditions. It is useful to compare the wear performance of Al-25% Si with those of eutectic alloys and draw conclusions on the role of microstructure on the wear mechanisms. Hence, the alloy subjected to fast cooling after casting has been selected for comparison with Al-25% Si. As **Table 6.2** shows, the Al -11%Si-F alloy had small, spherical silicon particles that are comparable to the silicon particles in Al-25% Si (**Table 6.2**), with similar aspect ratio. Yet, the matrix hardness of Al -11%Si-F (67 ± 12 Hv) was about 38 % less than that of the Al-25% Si. The area fraction of silicon on the contact surfaces of Al-11% Si-F was 0.1, which was about 60% smaller than on Al-25% Si (0.3).

The difference in UMW behaviour between the two alloys due to their difference in silicon particle areal density and matrix hardness was rationalized firstly from the contact pressure applied on the silicon particles and then the propensity in the formation of the oil residue layer.

Fig. 6.35 presents the plots of the maximum values of the contact pressures reached at the centre of wear tracks of Al-11% Si-F and Al-25% Si in the load range of 0.5 -3.0 N. The peak value of the pressure at 0.5 N was estimated as 2.49 GPa and as 2.68 GPa at 2.0 N. It is seen that the contact pressure applied on particles in Al-11% Si-F was about 1.6 times larger compared to Al-25% Si at each test load. As stated above, the

silicon particle size for each alloy is comparable, but the particle area density in Al-11% Si-F was about 56% lower, thus increasing the pressure exerted, as a smaller number of particles have to carry the same applied load.

Because of the larger pressure exerted at a given load, and the fact that the Al-11% Si-F alloy has a lower matrix hardness, the particles in this alloy exhibited a greater decrease in height at all sliding cycles compared with Al-25% Si (**Fig. 6.36 a**). The reduction in silicon height in Al-11% Si-F was primarily due to particles sinking into the matrix and formation of aluminum-pile ups; consequently, material loss from the aluminum matrix in Al-11% Si-F occurred earlier (**Fig.6. 36 b**). While no material loss was detected from the contact surfaces of Al-25% Si at 1.0 N, the Al-11% Si-F alloy showed mass loss and wear after 10^4 cycles. At 2.0 N, the transition to UMW-II in Al-11% Si-F initiated 10^3 cycles earlier than the onset in Al-25% Si. The UMW-II regimes were followed by a drop in wear rates at larger sliding cycles.

As noted in **Section 3.5.2** the volumetric wear is derived from the surface profile of the wear track; specifically, from scars in the aluminum. This profile is a function of abrasive wear, but it is also influenced by other processes that alter the surface morphology. Chemical processes, such as surface oxidation or formation of an oil residue layer, or a mechanical process like polishing can lead to a roughening to smoothening transition. These processes can reduce the depth of the wear scars and reduce the volumetric wear seen in **Fig. 6.36 b**. Oil deposits with similar composition, i.e., a mixture of engine oil elements and nano-crystalline aluminum, were observed in the wear tracks of both Al-25% Si and Al-11% Si-F when the wear rate (slope of the curve) of Al-25% Si is slowing, and when the wear rate of Al-11% Si-F is decreasing. The deposits vary in thickness and coverage, and their volume is too small to be measured

directly, hence it is impossible to quantitatively link them to the observed wear behavior, however, qualitatively it appears that these deposits can be correlated with the wear performance. At 2.0 N, after sliding for approximately $6x10^5$ cycles (**Figs. 6. 11 a** and **b**) the wear track on Al-11% Si-F was covered by an oil residue layer. The cross-sectional TEM image of the worn surface of Al-11% Si-F at 2.0 N shown in **Fig. 6.11 b** reveals that the aluminum grains immediately below the oil residue layer had a nano-crystalline size in the range of 400- 600 nm, similar to the Al-25 % Si (**Fig. 6. 29 c**). The ultrafine grains adjacent to the contact surface increased the local hardness, and possibly provided support to the oil residue layer (**Figs. 6.12** and **6.29 c**). Unlike Al-11% Si-F, which was virtually covered with a dark colored oil residue layer (about 0.6 μm), after sliding 6 $x10^5$ cycles at 2.0 N. The wear track of Al-25% Si, on the other hand, was occasionally covered by the oil residue layer (only about 0.1 μm) after sliding 6 $x10^5$ cycles at 2.0 N. At 2.0 N and 10^5 cycles the oil residue for the Al-25% Si alloy was not qualitatively as extensive as in the Al-11% Si-F experiment, and the drop in wear rates in the Al-25% Si alloy is less when compared to Al-11% Si-F. This infers that, for the Al-25% Si, the formation of the oil residue layer might take longer duration. The evolution of the counterface and the coefficient of friction (COF) with the sliding cycles provides more evidence for this premise.

Figures 6.37 and **6.38** present the 3-D surface profilometer images and corresponding cross-sectional profile taken across the center of the wear scars of the counterface balls after sliding against the two alloys for 2 $x10^6$ cycles at 2.0 N. It is interesting to note that a mechanical polishing-like process occurs on the worn surface of Al-11% Si-F; some area of the worn surface of the counterface ball sliding against Al-11% Si-F, as indicated by arrows in **Fig. 6.37 a**, tends to be smooth. While the worn

surface of the counterface ball sliding against Al-25% Si still showed lots of severe scratches, only a very small area became smooth. The variations of the COFs of the two alloys with the sliding cycles, as shown in **Fig. 6.39,** indicates that the COF in Al-11% Si-F was about 16% smaller than that in Al-25% Si at the sliding cycle of 6 $x10^5$. The COF of Al-11% Si-F evolved with an abrupt drop, a gradual increase, and then decrease to the final stable value. The point at which the final stable value of a COF was reached was consistent with the sliding cycles when the whole wear track was covered by an oil residue layer; it was 3 x 10^5 cycles for Al-11% Si-F at 2.0 N. While for Al-25% Si, the COF was not stable even after sliding for 6 $x10^5$ cycles. Also, the slope of the COF drop in the Al-25% was smaller and lasted much longer (about 3 times longer), and the COF exhibited greater fluctuation in comparison with that of Al-11% Si-F. This is highly suggested that the drop of the COF in the beginning is related to the silicon particle sinking-in. The evolution of the COF and counterface morphology provides evidence that the UMW tends to stabilize after the surface evolves with long sliding cycles due to the formation of the oil residue layer. It also infers that the plastic deformation is the precursor to the interaction between materials adjacent to the sliding interface, leading to the tribo-chemical reaction or physical adsorption between the engine oil and materials at the contact surface, and hence, to the modification of the chemical composition of the near-surface material. Accordingly, the oil residue layer is more likely to be formed on Al-11% Si-F, in which the aluminum exhibited a lager degree of plastic deformation compared to Al-25% Si.

In summary, the Al-25% alloy was more successful in delaying the transition to the UMW-II regime compared to the sand cast eutectic Al-11% Si-F alloy with lower matrix hardness and lower silicon content (11 wt. % Si). Although the Al-25% Si alloy is

superior at low loads, this alloy loses its advantage once the Si particles loose their ability to support the counterface. There are differences in the details of the two curves, but the volumetric wear of both alloys is comparable at 2.0 N. Other mechanisms associated with running-in of the Al-11% Si-F surface become dominant in controlling wear, and lead to a stable running surface, very different from the as-prepared surface, that account for the long term wear behavior. The Al-11% Si-F alloy may actually be preferable to Al-25% Si since formation of this stable surface appears relatively quicker in the Al-11% Si-F alloy. Overall, considering the damage to the counterface, and the tendency to the stabilization of the UMW, Al-11% Si-F with small spheroidized silicon particles distributed with larger interparticle spacing, and relatively soft matrix was expected to provide optimal resistance to UMW damage.

Table 6.1. The maximum real contact pressures applied on two eutectic Al-Si alloys

Pressure (MPa)	**Alloy** \ **Load (N)**	**0.5**	**1.0**	**2.0**
The maximum contact pressure	Al-11% Si-C	654	687	731
	Al-11% Si-F	1653	1722	1762

Table 6.2. Properties of spray cast and sand cast Al-11% Si-F alloys.

Alloy	**Matrix hardness (kgf/mm^2)**	**Alloy hardness (HB)**	**Si particle size**		**Si aspect ratio**
			Length (μm)	**Width (μm)**	
Al - 25% Si	110 ± 20	102 ± 4	8 ± 2	5 ± 2	2
Al -11% Si-F	67 ± 11	79 ± 2	6 ± 3	3 ± 2	2

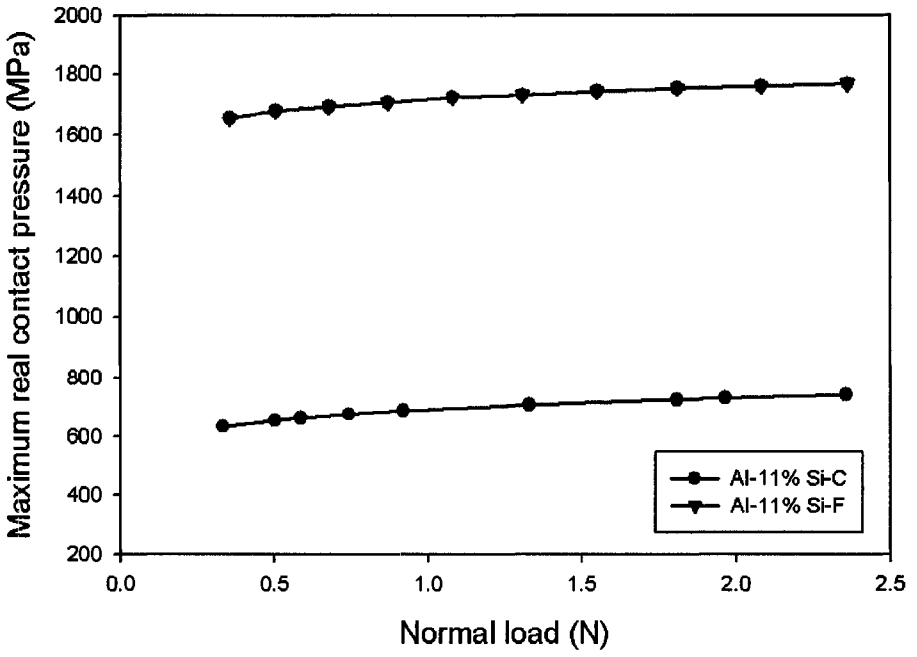

Fig. 6.1. Variation of the maximum real contact pressures applied on Al-11% Si-C and Al-11% Si-F with the normal load.

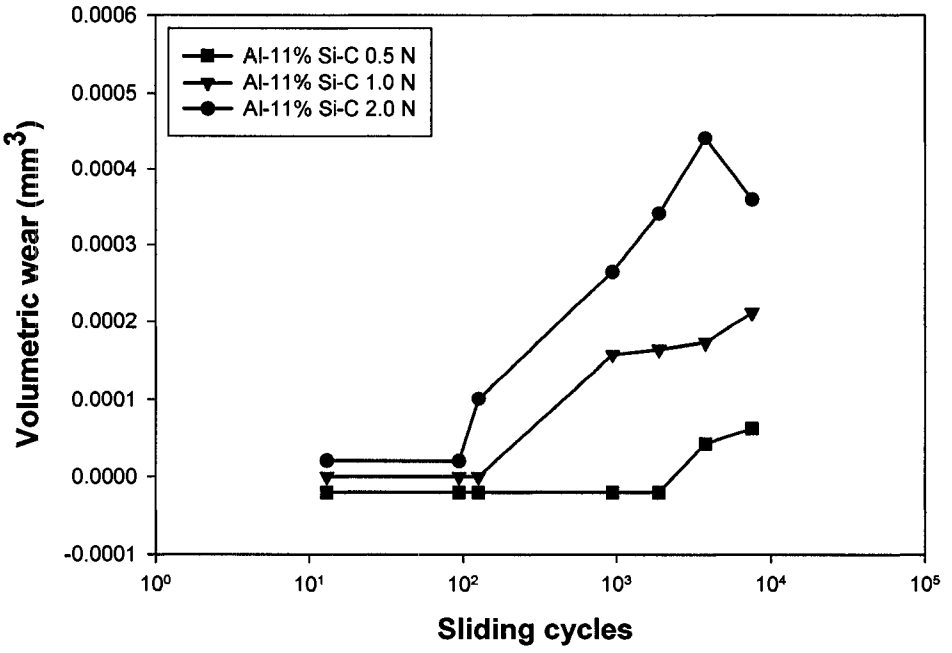

Fig. 6.2. Plot of volume loss with the sliding cycles for Al-11% Si-C. The plots at 0.5, 1.0, and 2.0 N with zero volume loss were shifted vertically for clarity.

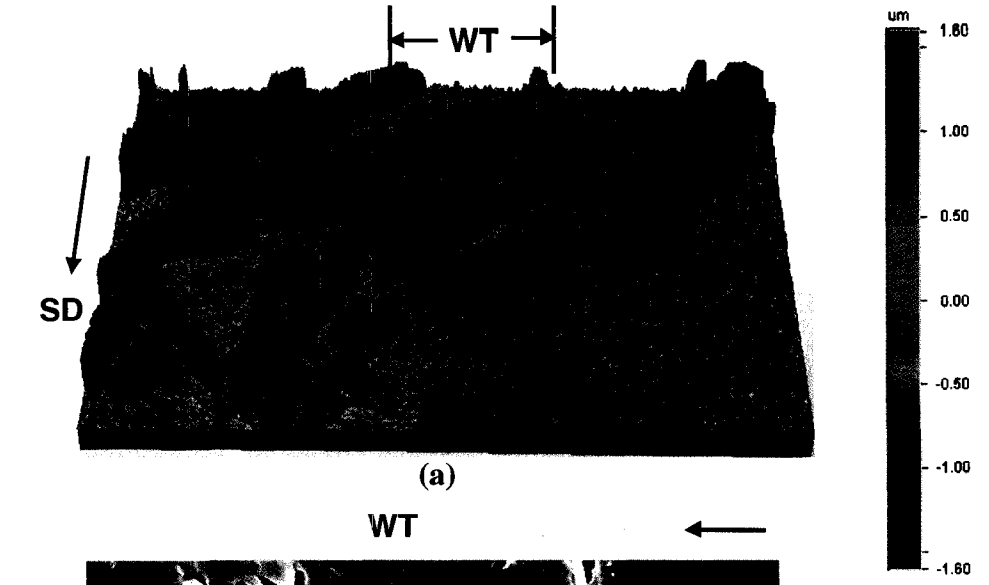
WT
SD
um
1.60
1.00
0.50
0.00
-0.50
-1.00
-1.60

(a)

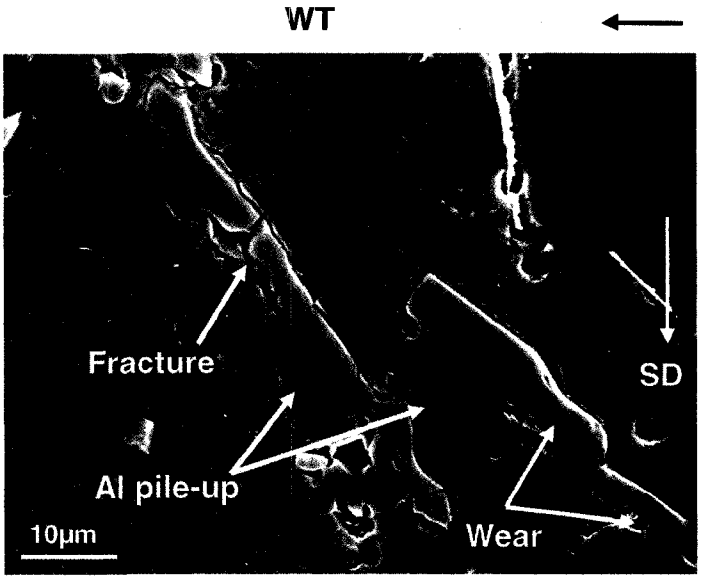
WT
Fracture
SD
Al pile-up
10μm
Wear

(b)

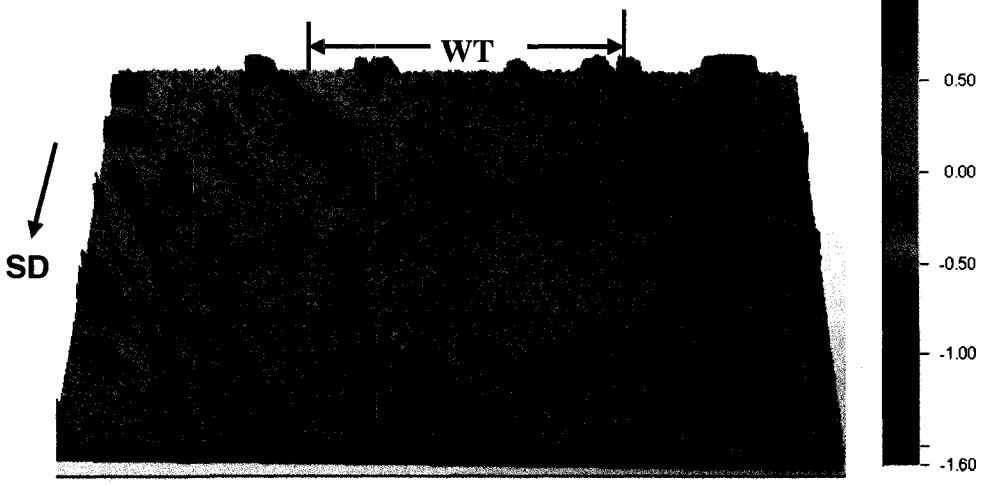
WT
SD
um
1.60
1.00
0.50
0.00
-0.50
-1.00
-1.60

(c)

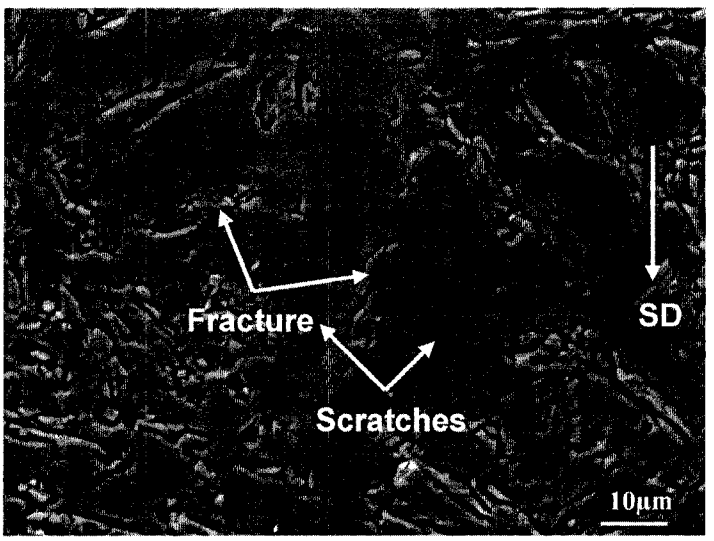

(d)

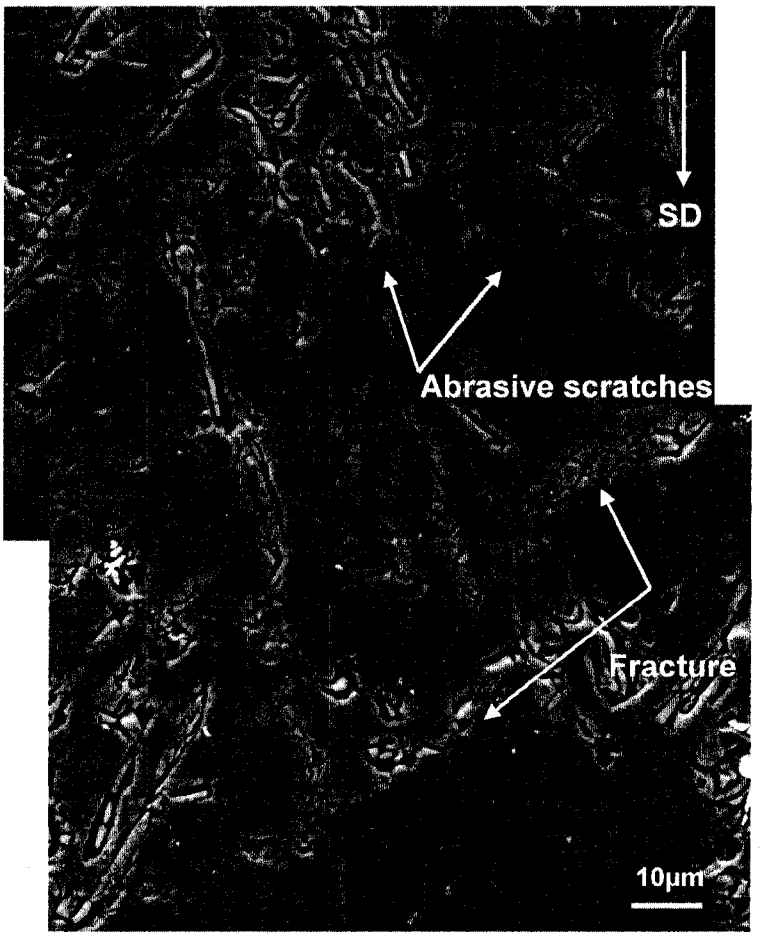

(e)

Fig. 6.3. Evolution of surface damage in Al-11% Si-C with sliding cycles at 0.5 N. **(a)** 3 D surface profilometer image after at 5 x 10^2 cycles; **(b)** Secondary SEM image at 5 x 10^4 cycles showing Si particle fracture; **(c)** 3-D surface profilometer image at 5 x 10^4 cycles showing aluminum pile-up. The view in inset 'X' is the same with the SEM image in **(b)**; **(d)** Backscattered SEM image after sliding for sliding for 3 x10^5 cycles; **(e)** Backscattered SEM image after sliding for 6 x 10^5 cycles. WT is the wear track, SD is the sliding direction.

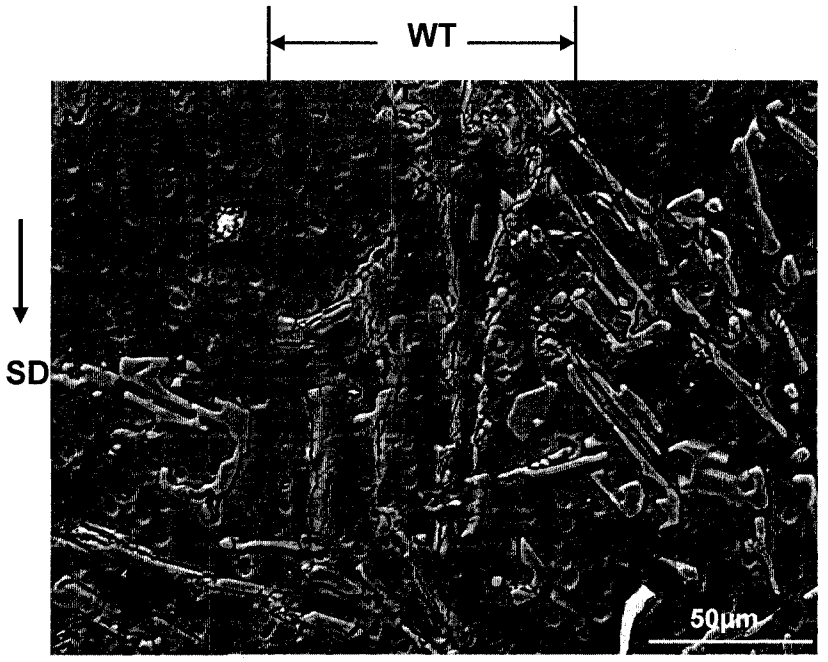

(a)

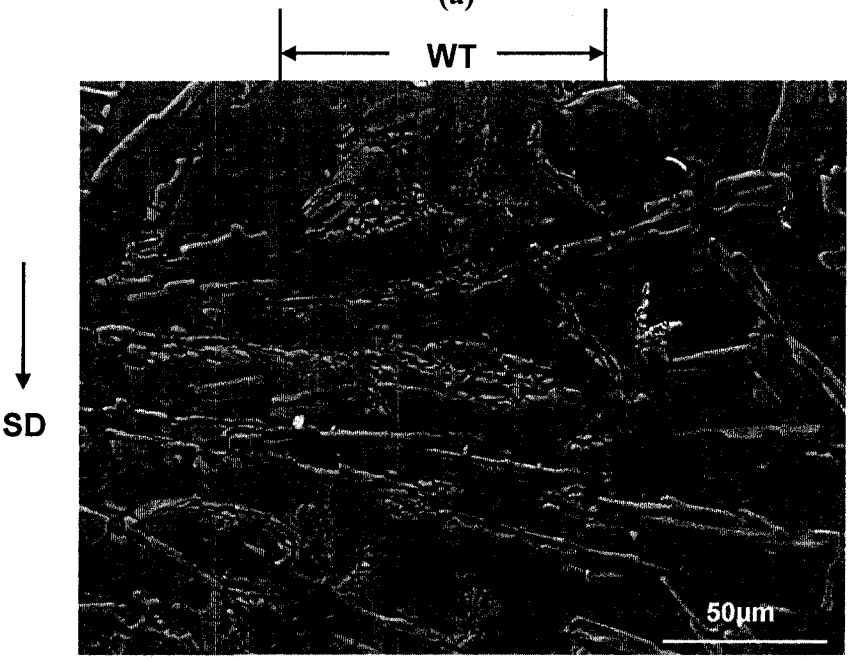

(b)

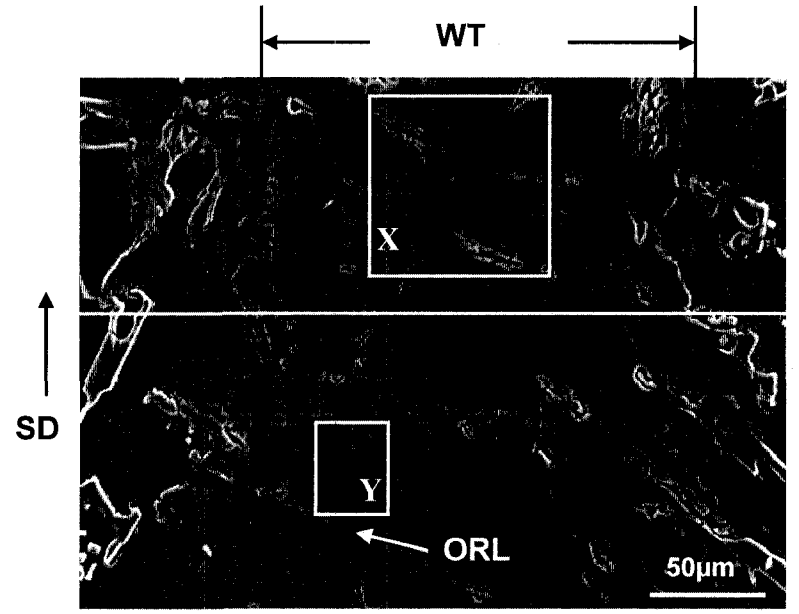

(c)

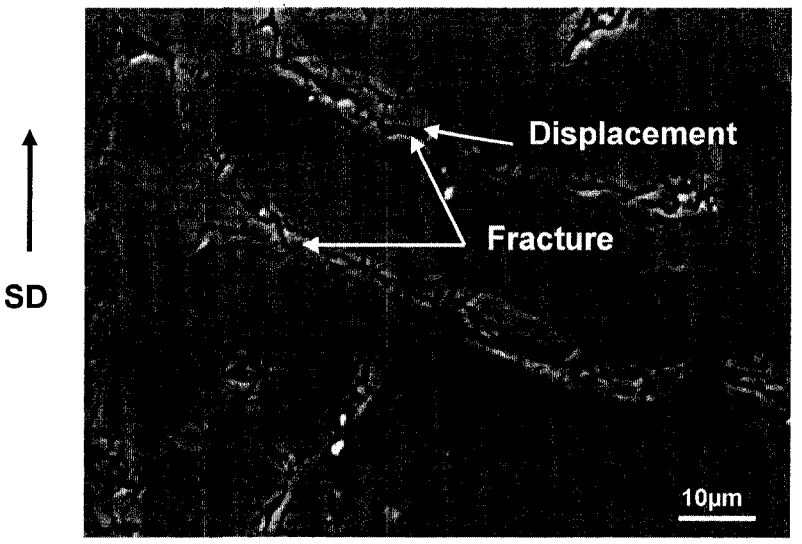

(d)

Fig. 6.4. Surface damage in Al-11% Si-C at 2.0 N: **(a)** Backscattered SEM image after sliding for 5 x 10^2 cycles, **(b)** Backscattered SEM image after sliding for 1.5 x 10^3cycles, **(c)** Backscattered SEM image after sliding for 10^4 cycles, **(d)** Secondary SEM image after sliding for 6 x 10^5 cycles, and **(e)** High magnification backscattered SEM image taken from the inset 'X' in **(d).**

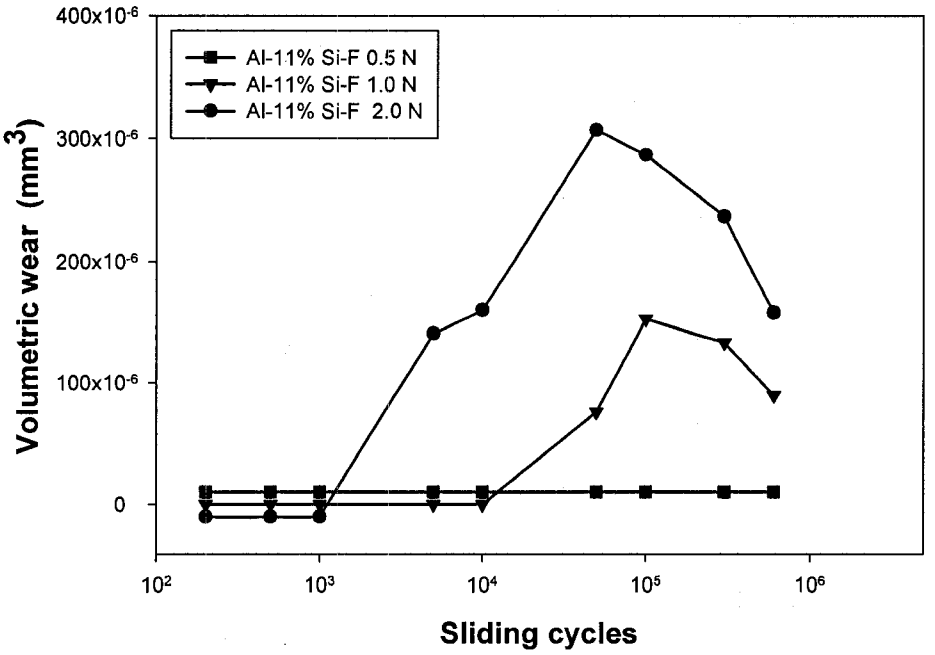

Fig. 6.5. Plot of volumetric loss with the sliding cycles for Al-11% Si-F. The plots at 0.5, 1.0, and 2.0 N with zero volume loss were shifted vertically for clarity.

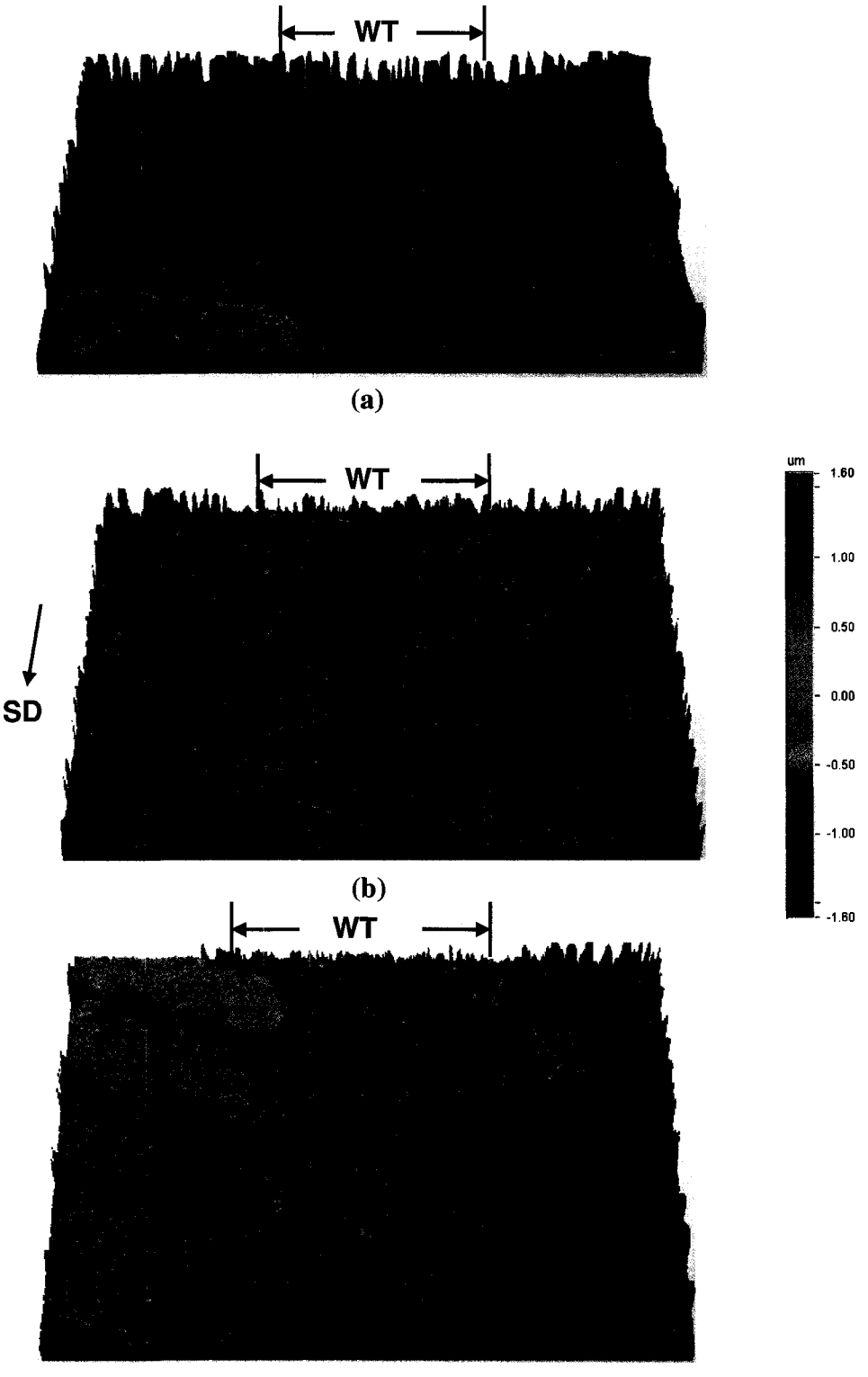

Fig. 6.6. 3 D surface profile images taken from the contact surface of Al-11% Si-F after stopping the sliding tests at **(a)** 5 x 10^2, **(b)** 1.5 x 10^3 and **(c)** 5 x10^3 cycles at 0.5 N.

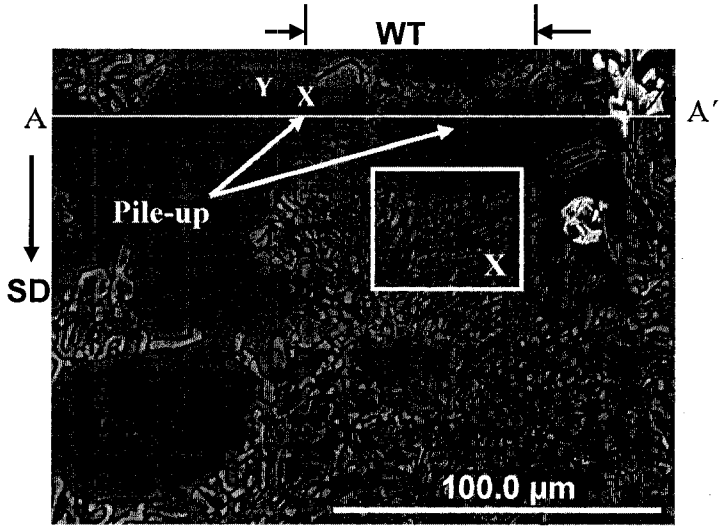

(a)

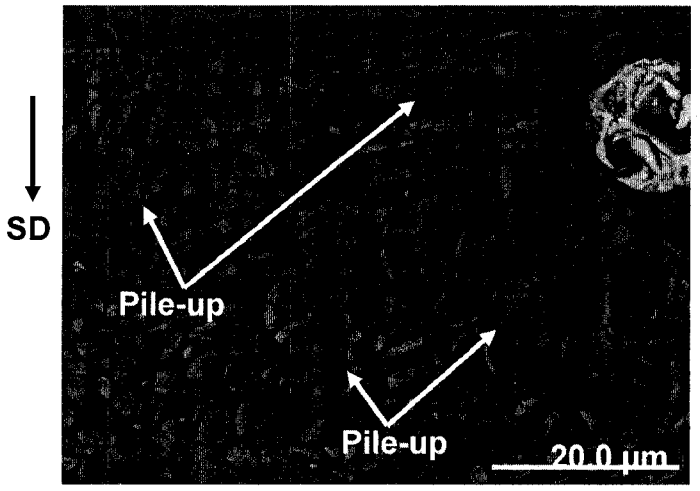

(b)

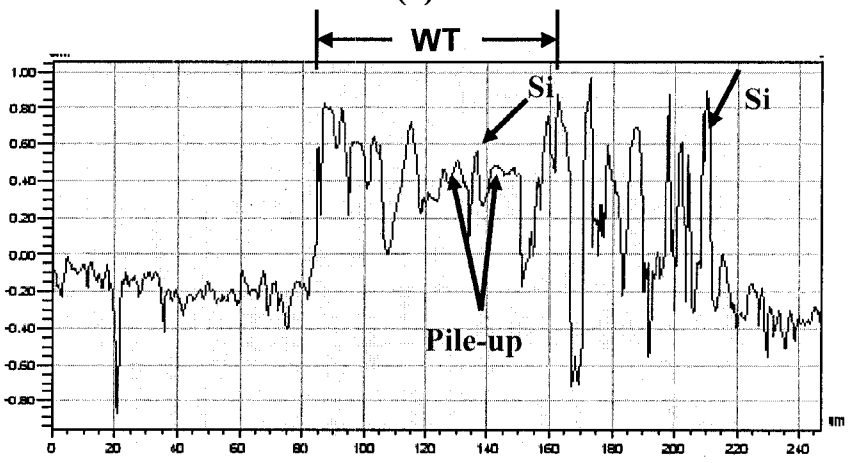

(c)

Fig. 6.7. Surface damage in Al-11% Si-F after sliding for 5 x 10^4 cycles at 0.5 N: **(a)** Backscattered SEM image; **(b)** High magnification backscattered SEM taken form the inset 'X' in **(a)**, **(c)** 2-D surface profilometer scanned along the horizontal line (AA') indicated in **(a)**.

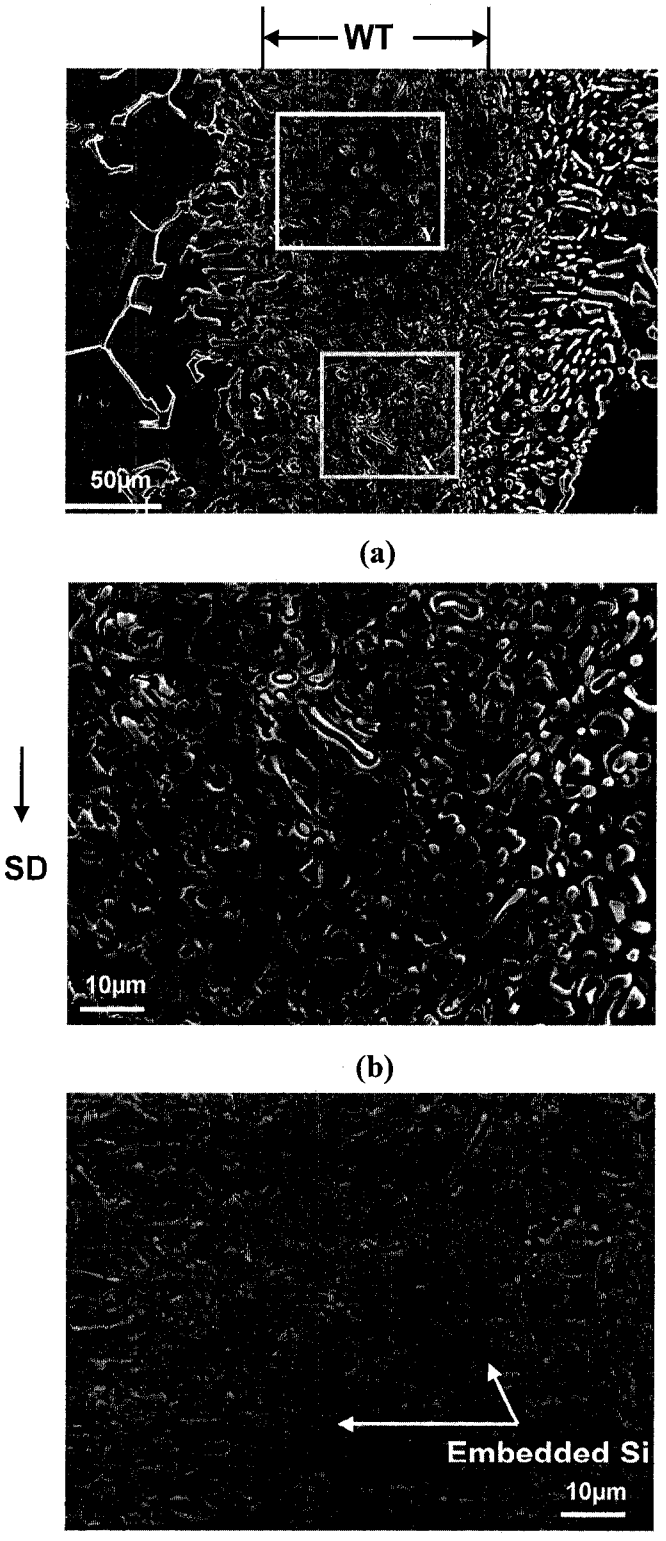

Fig. 6.8. Surface damage of Al-11% Si-F after sliding for 6 x 10^5 cycles at 0.5 N: **(a)** Secondary SEM image; **(b)** High magnification secondary SEM image taken from the inset 'X' in **(a),** and **(c)** High magnification backscattered SEM image taken from the inset 'Y' in **(a).**

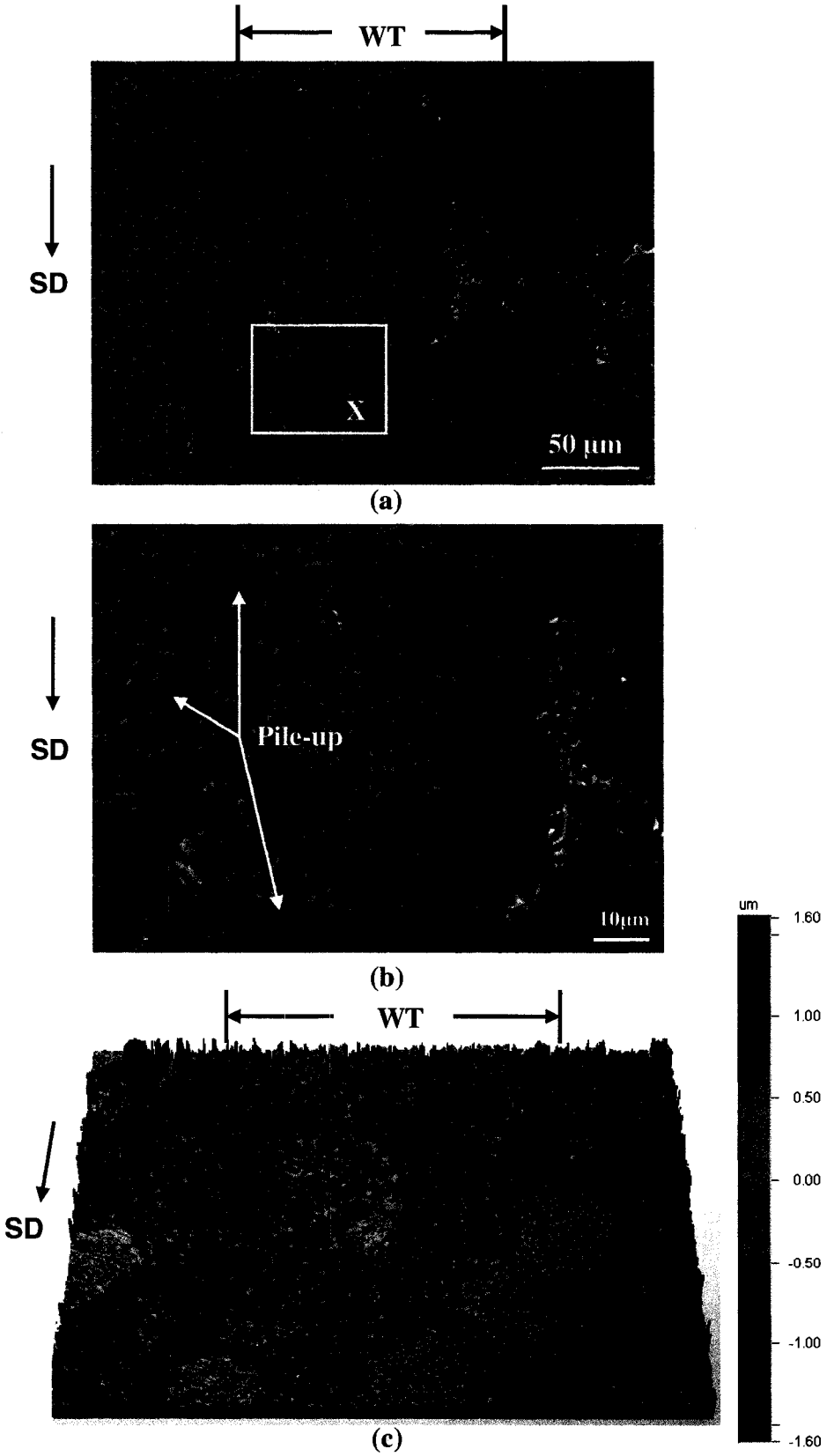

Fig. 6.9. Surface damage in Al-11% Si-F after sliding for 10^3 cycles at 2.0 N: **(a)** Backscattered SEM image; **(b)** Magnified backscattered SEM image taken from the inset X in **(a)**; **(c)** 3-D surface profile image.

(a)

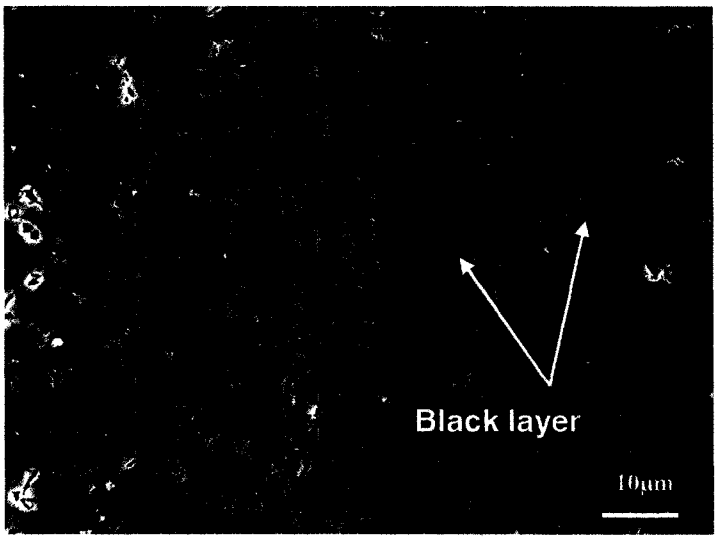

(b)

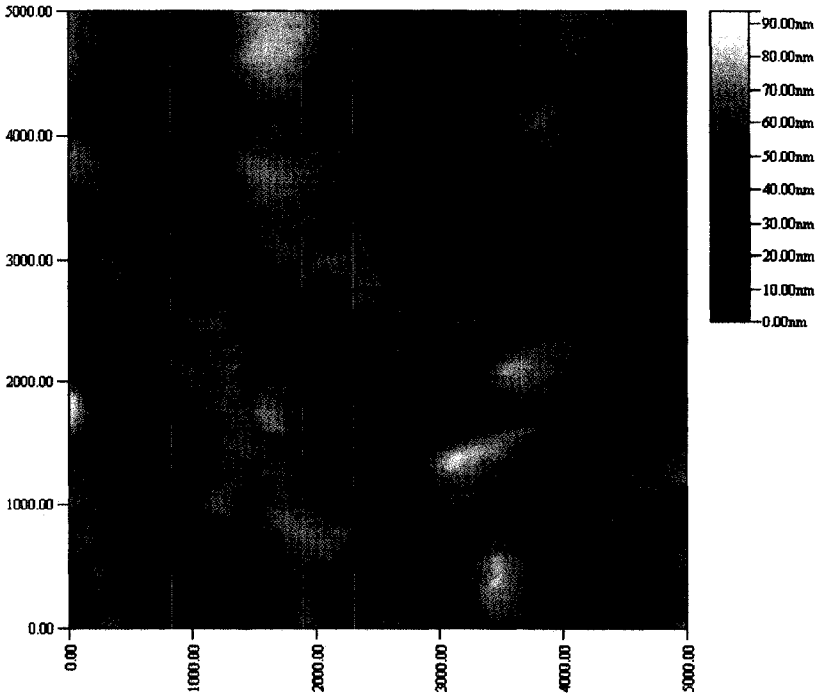

(c)

Fig. 6.10. Surface damage in Al-11% Si-F after sliding for 6 x 10^5 cycles at 2.0 N: **(a)** Optical image showing the wear track covered by dark coloured layer; **(b)** Secondary SEM image taken from the inset 'X' in **(a)**; **(c)** AFM image taken from the inset 'X' in **(a)**.

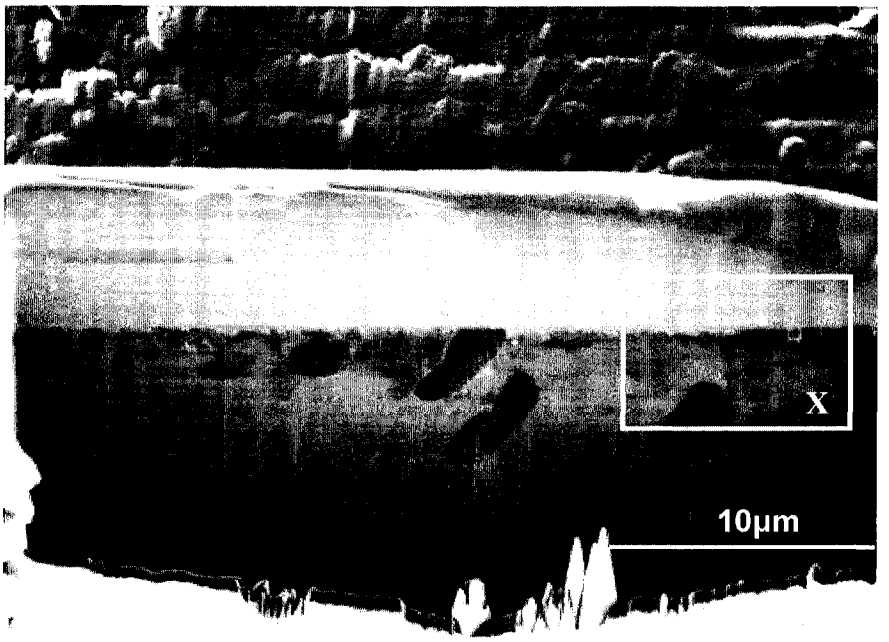

(a)

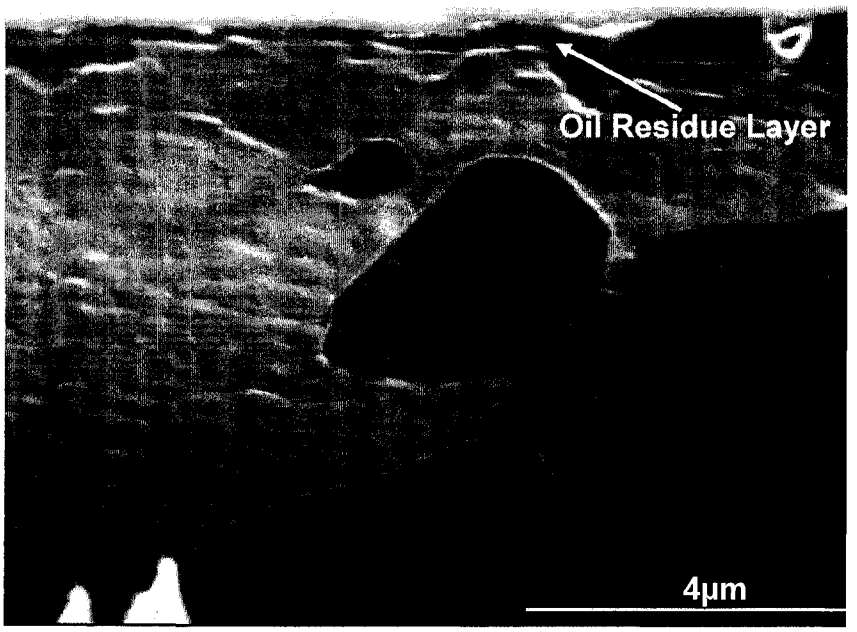

(b)

Fig. 6.11. Cross-sectional FIB secondary image (taken by Dr. Meng-Burany) of the wear track **(a)** general view, and **(b)** detail of inset 'X' in **(a)** showing the oil residue layer generated on the contact surface.

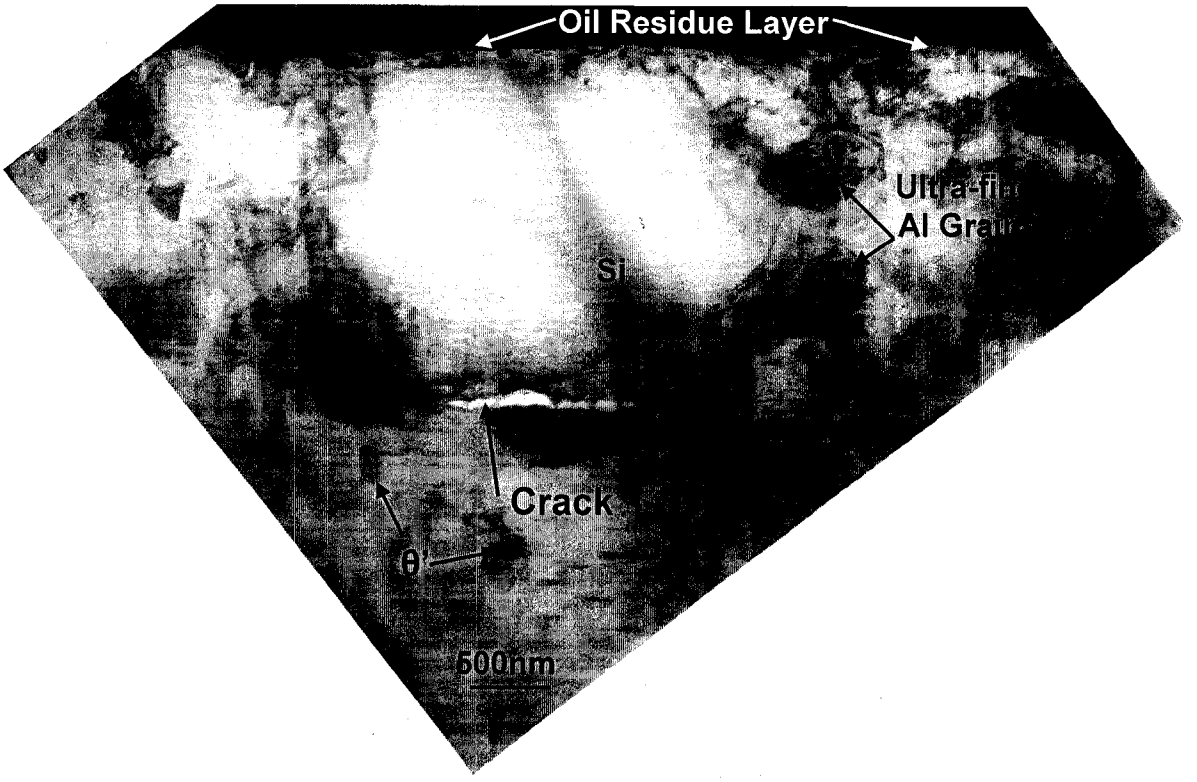

Fig. 6.12. Cross-sectional TEM image (taken by Dr. Meng-Burany) of the wear track showing ultra-fine aluminum grains around the particles.

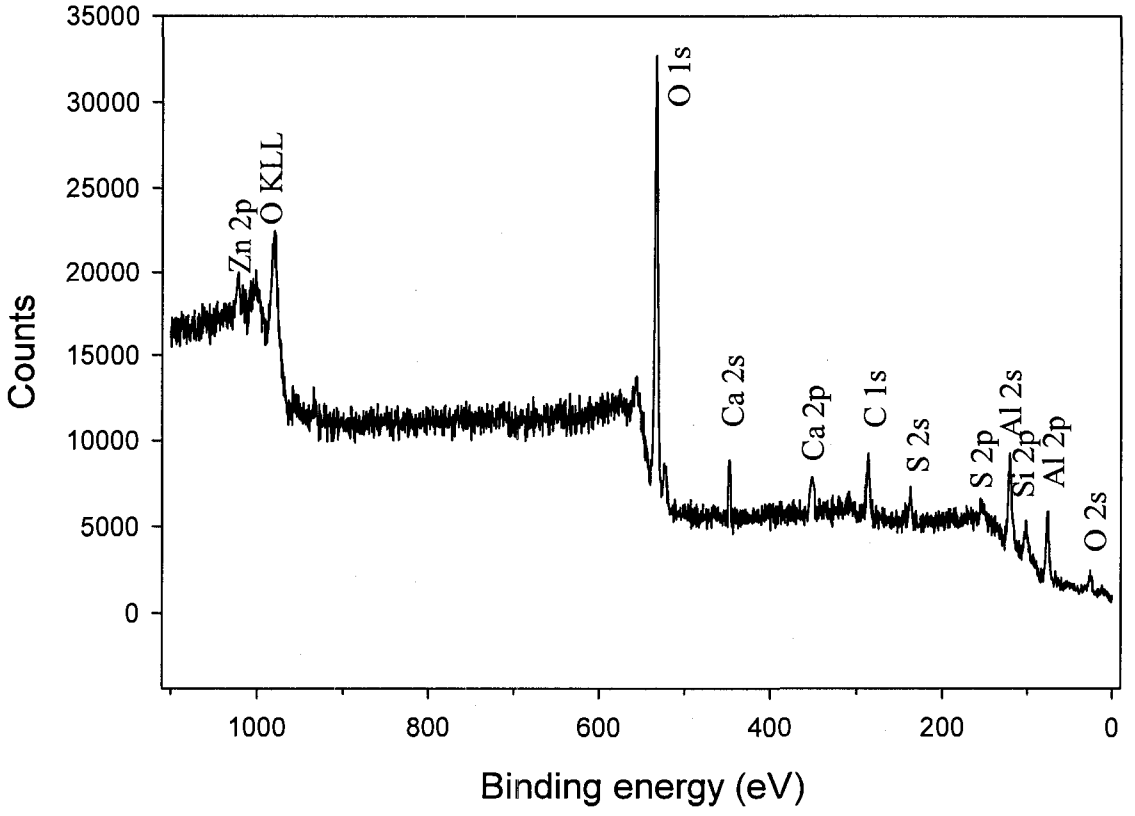

Fig. 6.13. Survey XPS spectrum taken from the black colored layer on the contact surface of Al-11% Si-F after sliding for 6 x 10^5 cycles at 2.0 N.

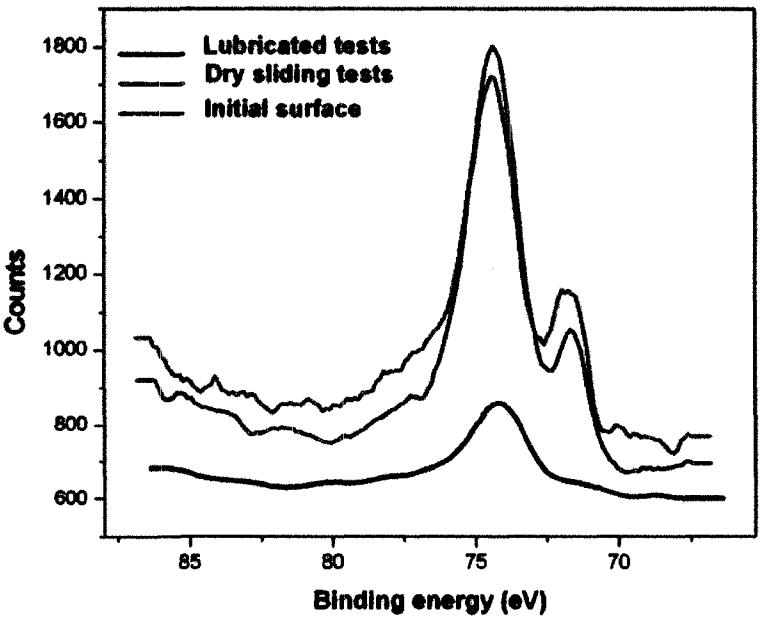

(a)

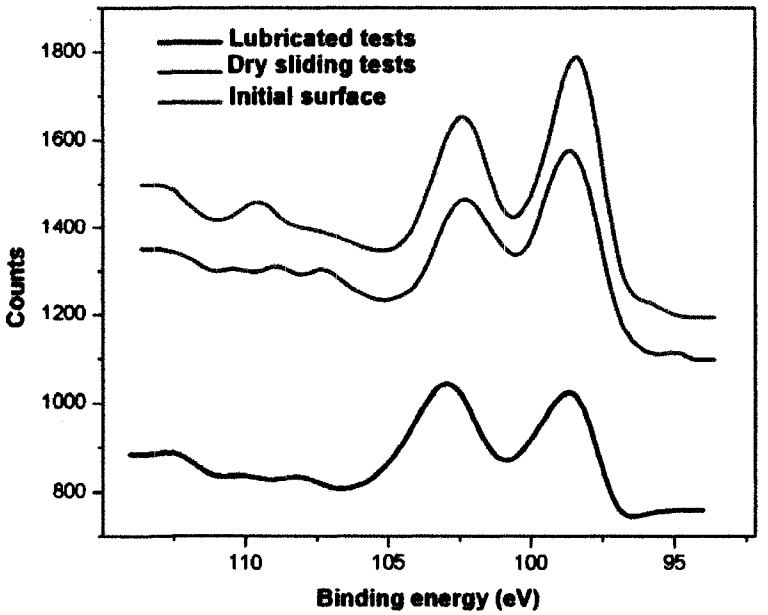

(b)

Fig. 6.14. XPS spectra of **(a)** Al_{2p}, and **(b)**, Si_{2p} taken from the black coloured layer on the contact surface of Al-11% Si-F after sliding for 6 x 10^5 cycles at 2.0 N.

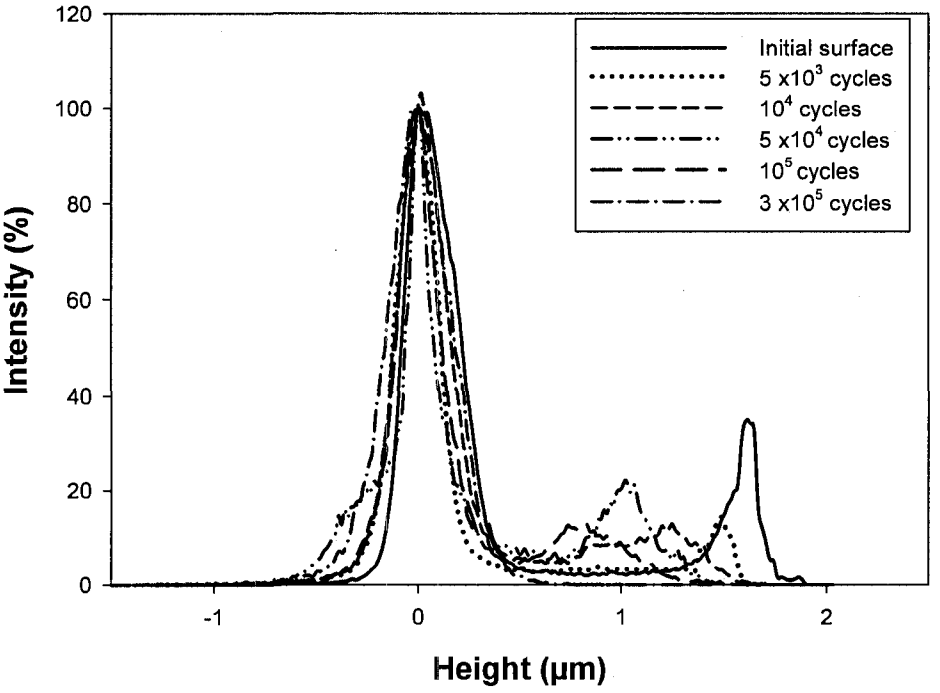
Initial surface
5 x10^3 cycles
10^4 cycles
5 x10^4 cycles
10^5 cycles
3 x10^5 cycles
Intensity (%)
Height (µm)
120
100
80
60
40
20
0
-1
0
1
2

(a)

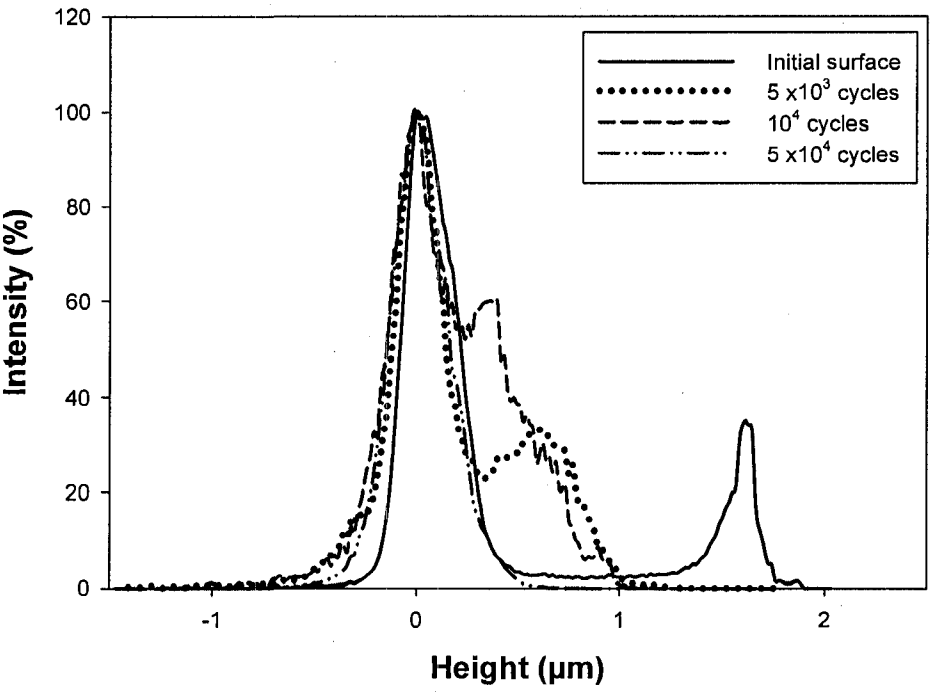
Initial surface
5 x10^3 cycles
10^4 cycles
5 x10^4 cycles
Intensity (%)
Height (µm)
120
100
80
60
40
20
0
-1
0
1
2

(b)

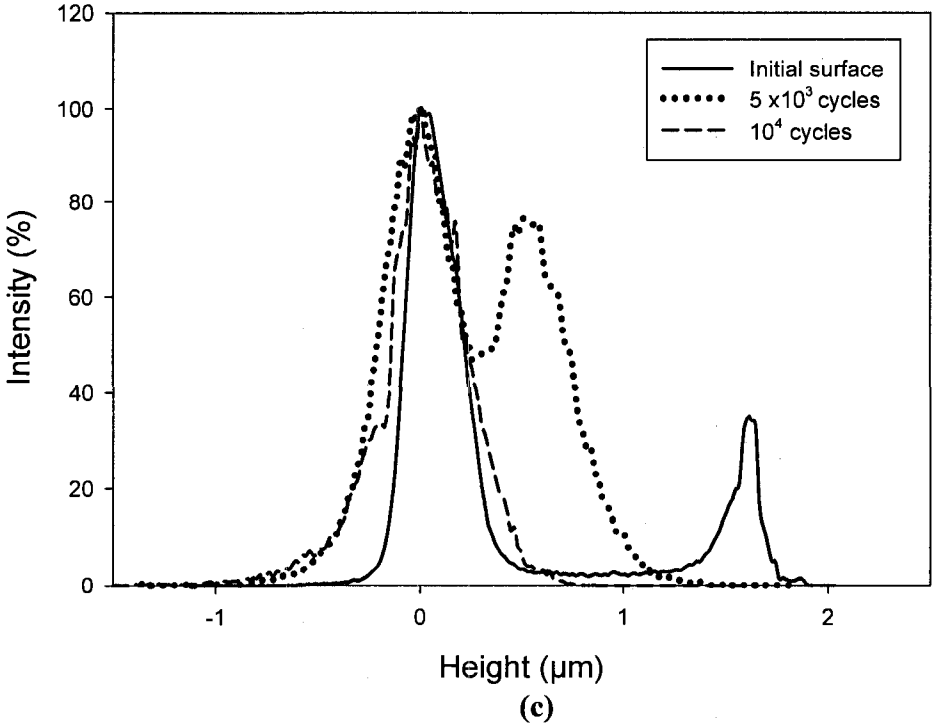

(c)

Fig. 6.15. The distribution frequency of surface topography on the Al-11% Si-C

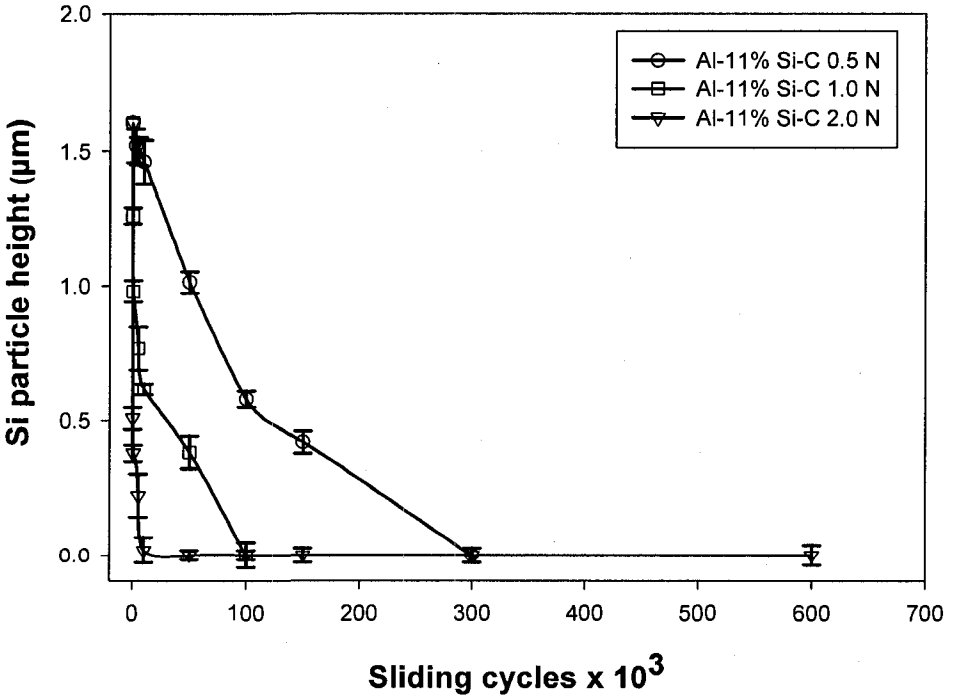

Fig. 6.16. Change in the silicon particle height projected above the aluminum matrix with the sliding cycles in Al-11% Si-C at applied loads of 0.5, 1.0, and 2.0 N.

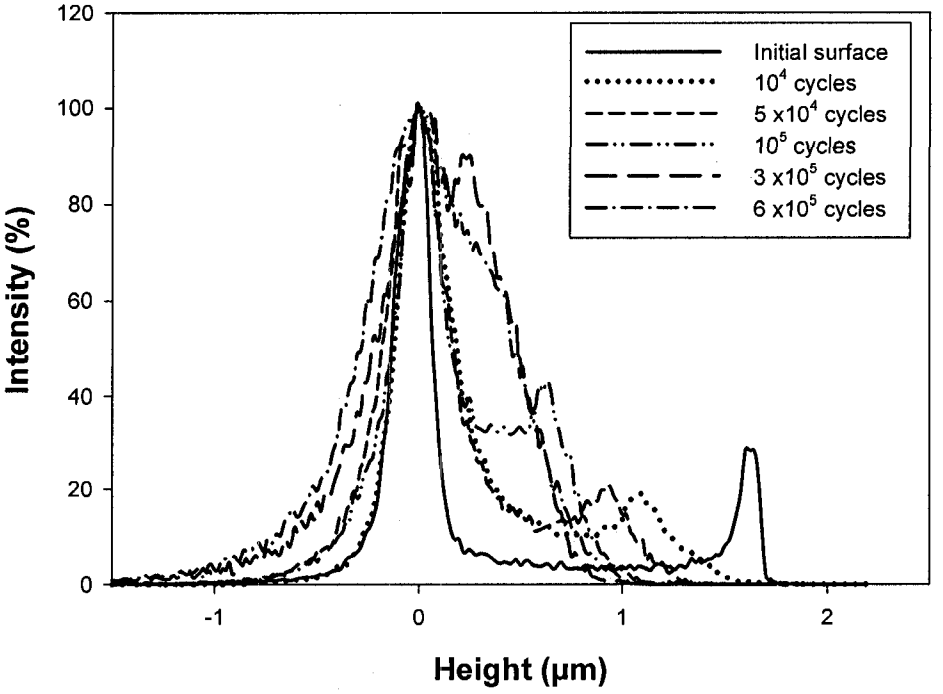
Initial surface
10^4 cycles
5 x10^4 cycles
10^5 cycles
3 x10^5 cycles
6 x10^5 cycles
Intensity (%)
Height (μm)
120
100
80
60
40
20
0
-1
0
1
2

(a)

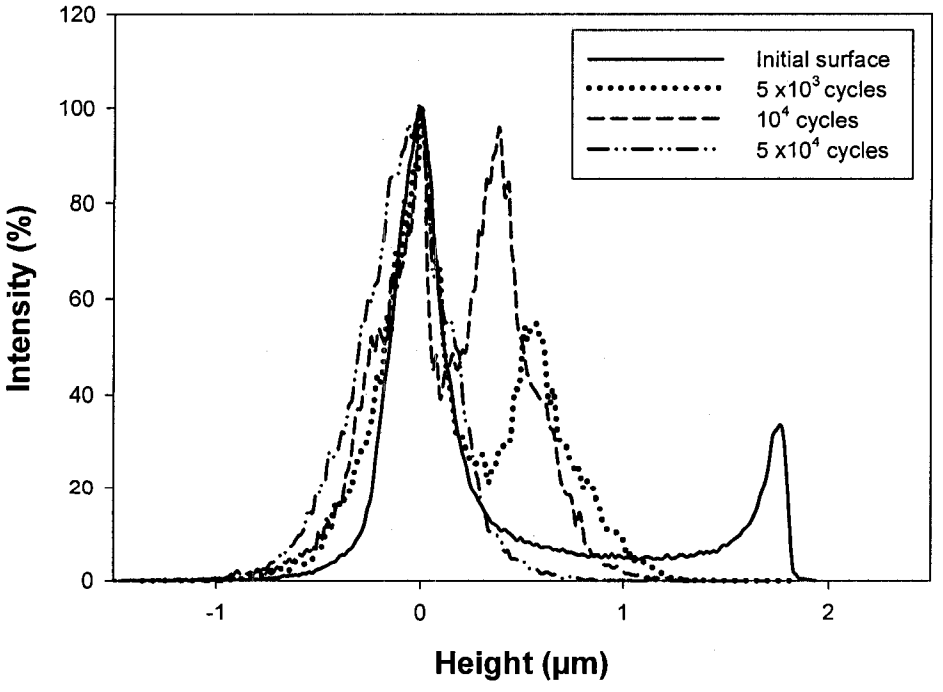
Initial surface
5 x10^3 cycles
10^4 cycles
5 x10^4 cycles
Intensity (%)
Height (μm)
120
100
80
60
40
20
0
-1
0
1
2

(b)

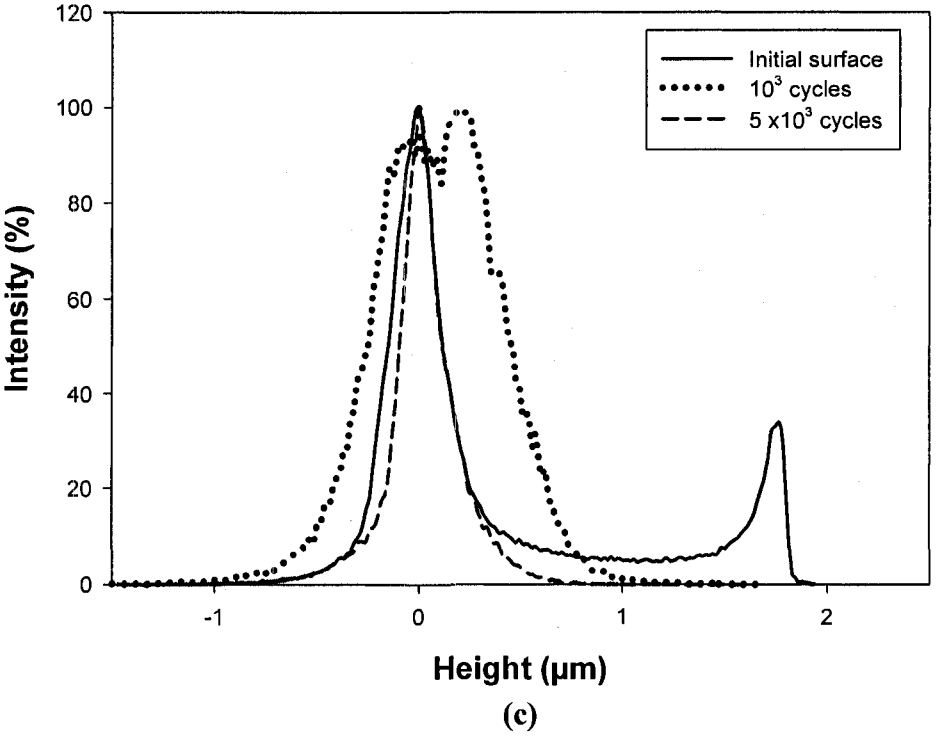

(c)

Fig. 6.17. The distribution frequency of surface topography on the Al-11% Si-F surfaces at various sliding cycles at **(a)** 0.5 N, **(b)** 1.0 N, and **(c)** 2.0 N

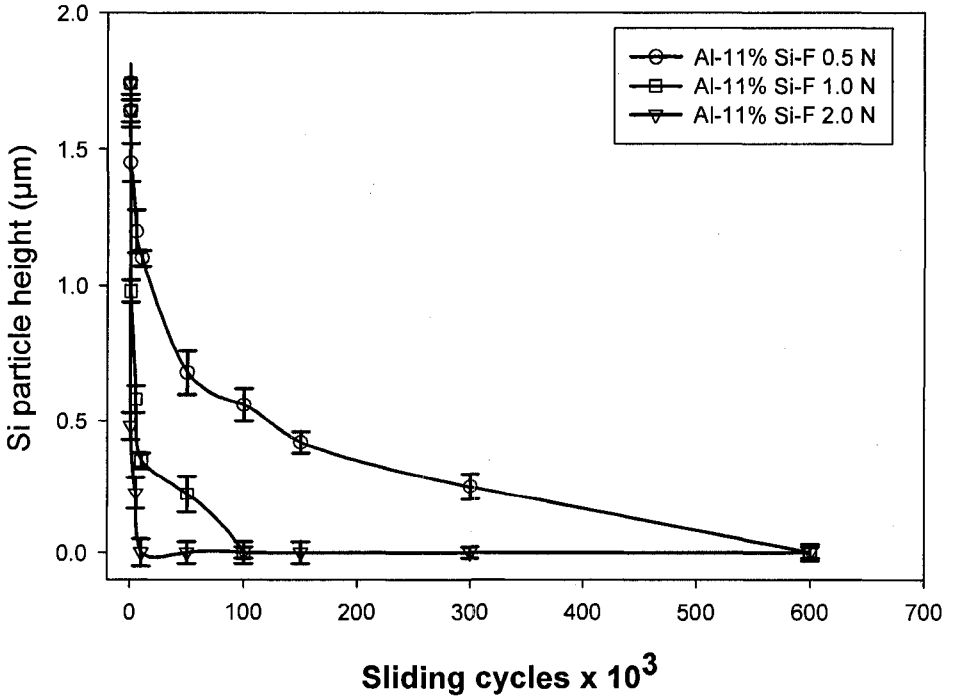

Fig. 6.18. Change in the silicon particle height projected above the aluminum matrix with the sliding cycles in Al-11% Si-F at applied loads of 0.5, 1.0, and 2.0 N.

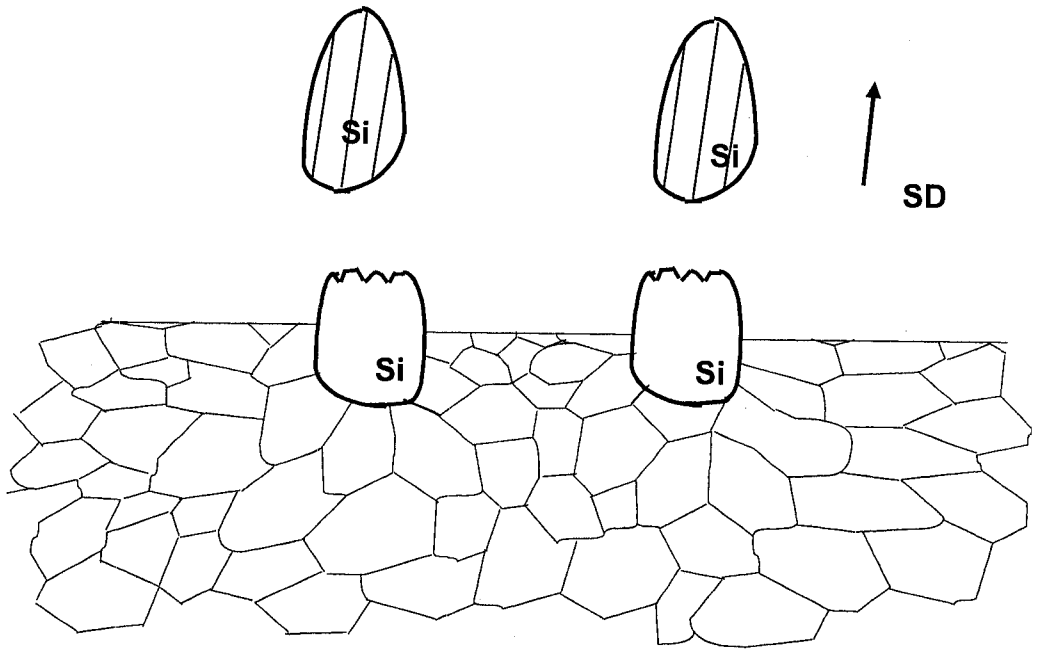

(a)

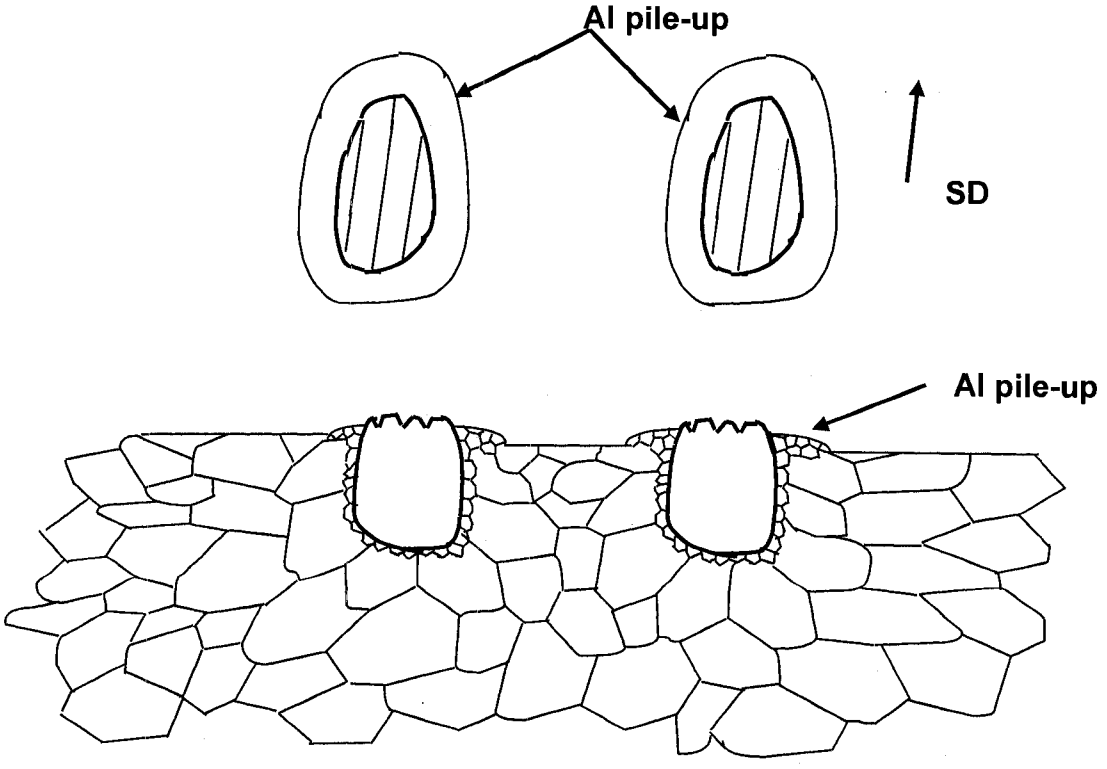

(b)

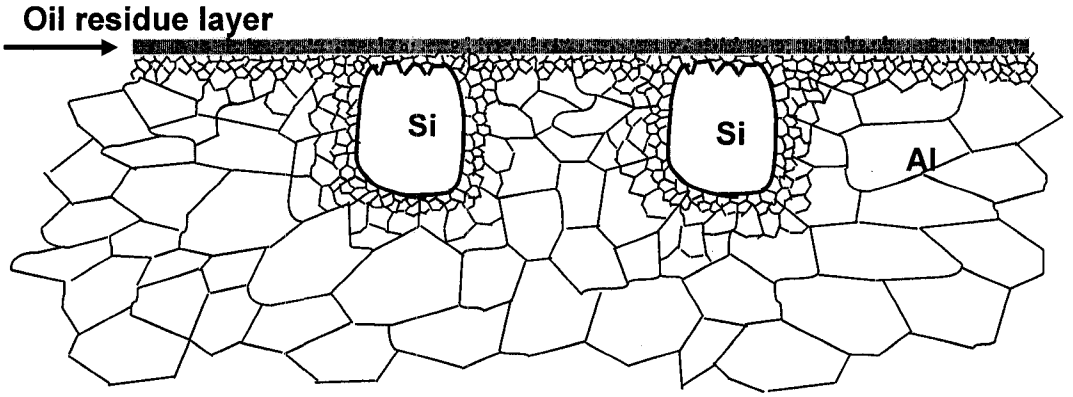

(c)

Fig. 6.19. Schematic illustration of the surface damage evolution in Al-Si alloys in UMW regime. **(a)** Si particles carry the applied load leading to the wear of the top Si surfaces; **(b)** Local plastic deformation in the forms of Si particle sinking-in and aluminum piling- up around the sunken-in Si particles, leading to the reduction in local aluminum grain size; **(c)** Formation of an oil residue layer supported by ultra-fine aluminum grains.

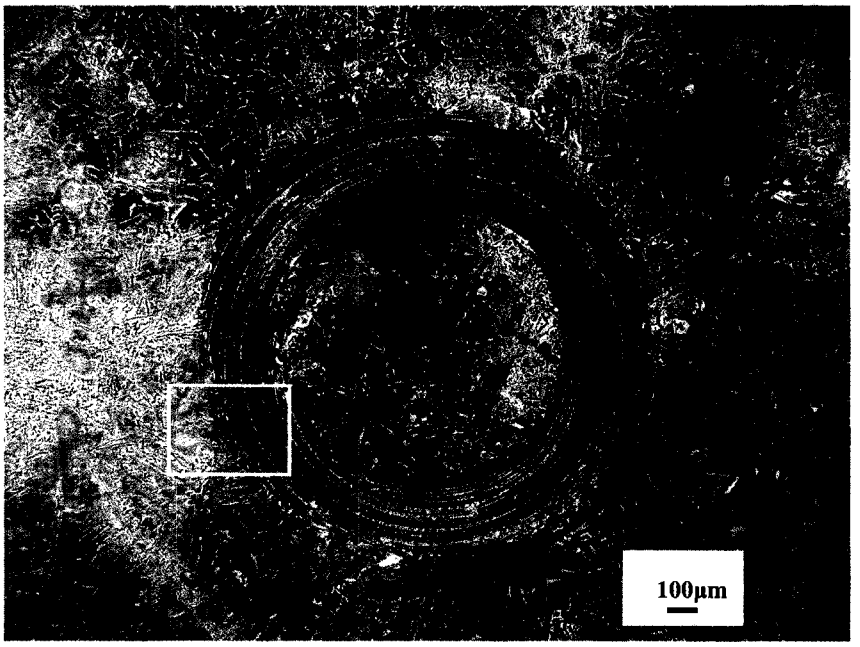

(a)

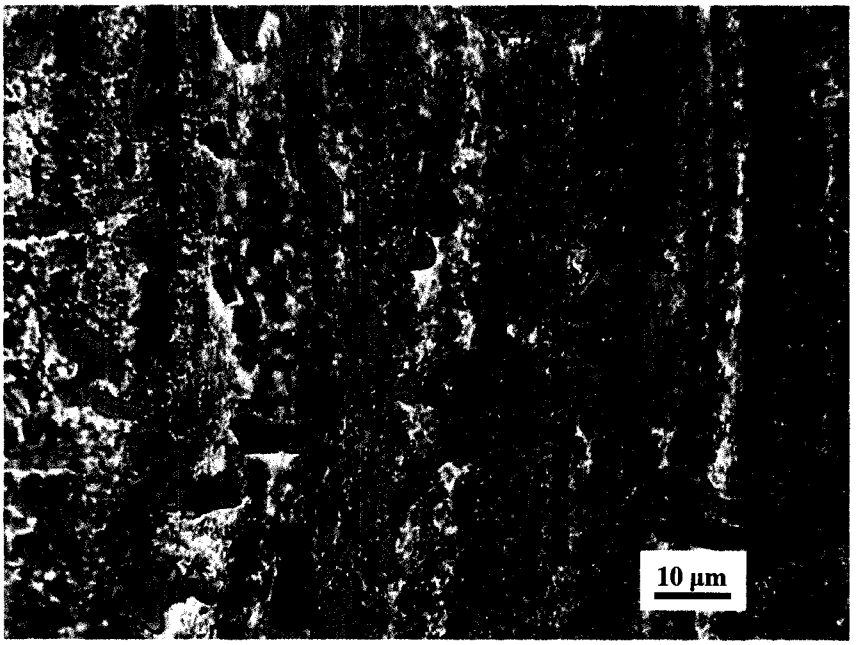

(b)

Fig. 6.20. Optical images showing surface damage on the wear track of Al-11% Si-C: **(a)** Low magnification image; **(b)** High magnification image from the inset in **(a)** after sliding for 2 x 10^6 cycles 2.0 N.

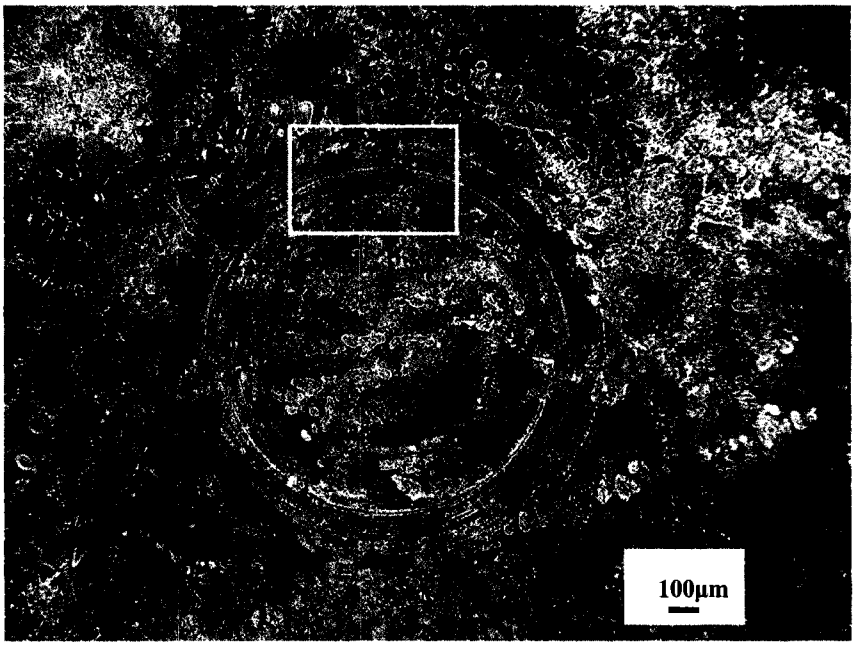

(a)

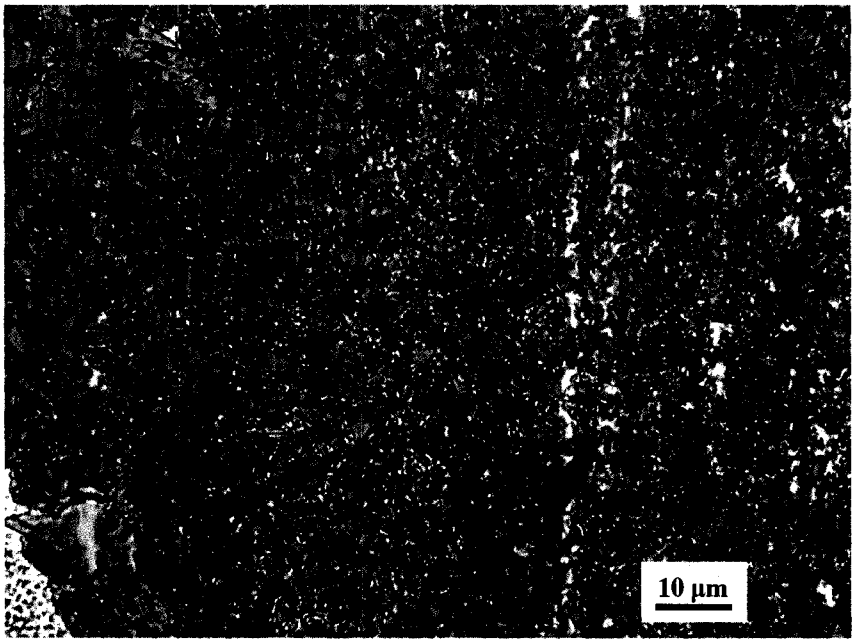

(b)

Fig. 6.21. Optical images showing surface damage on the wear track of Al-11% Si-F: **(a)** Low magnification image; **(b)** High magnification image from the inset in **(a)** after sliding for 2 x 10^6 cycles 2.0 N.

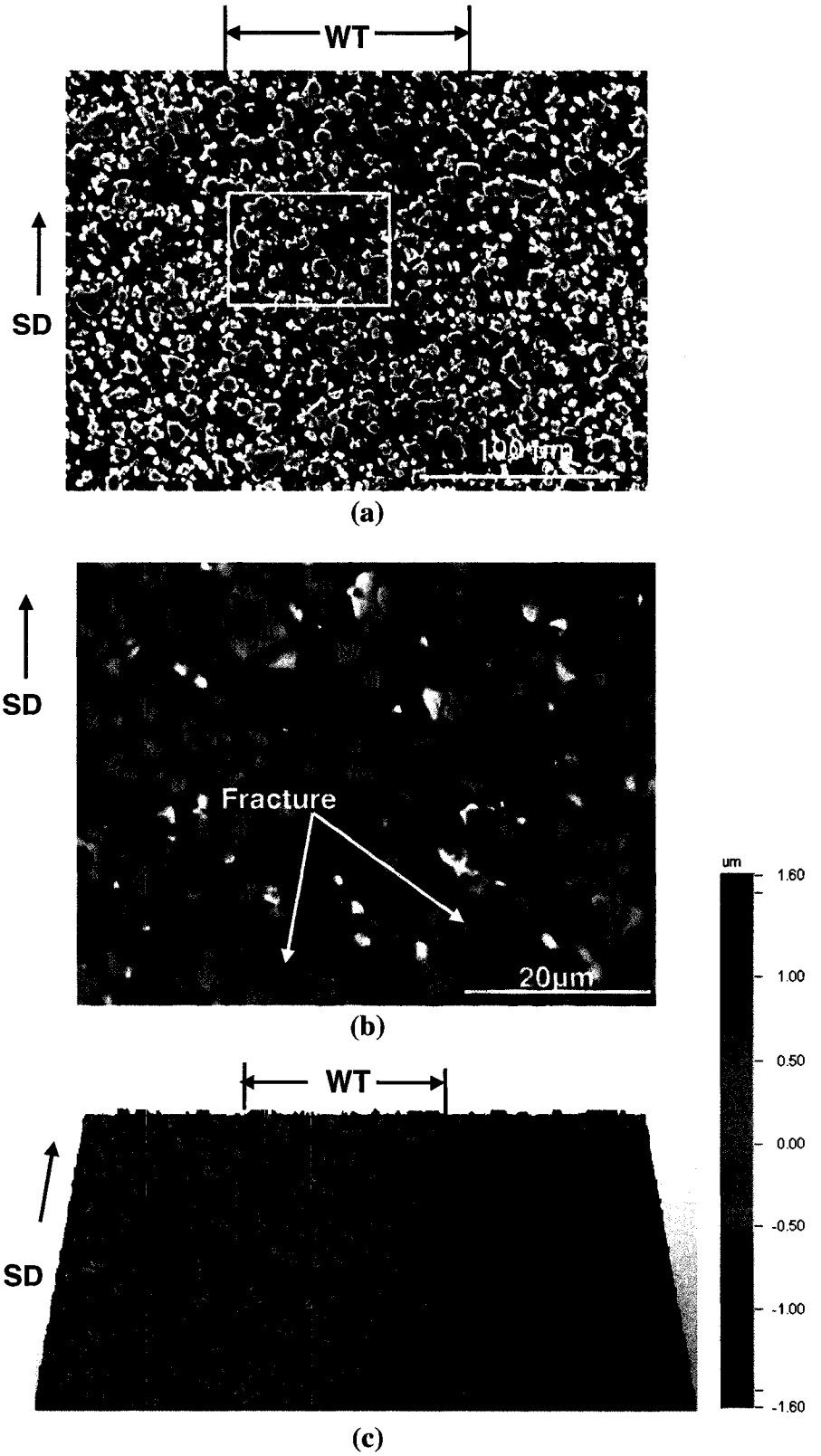

Fig. 6.22. **(a)** Secondary SEM image, **(b)** high magnification back scattered SEM image of inset 'X' in **(a)**, and **(c)** 3-D surface profile image showing surface damage on the top surfaces of silicon particles inside the wear track of Al-25% Si after sliding for 10^4 cycles 0.5 N.

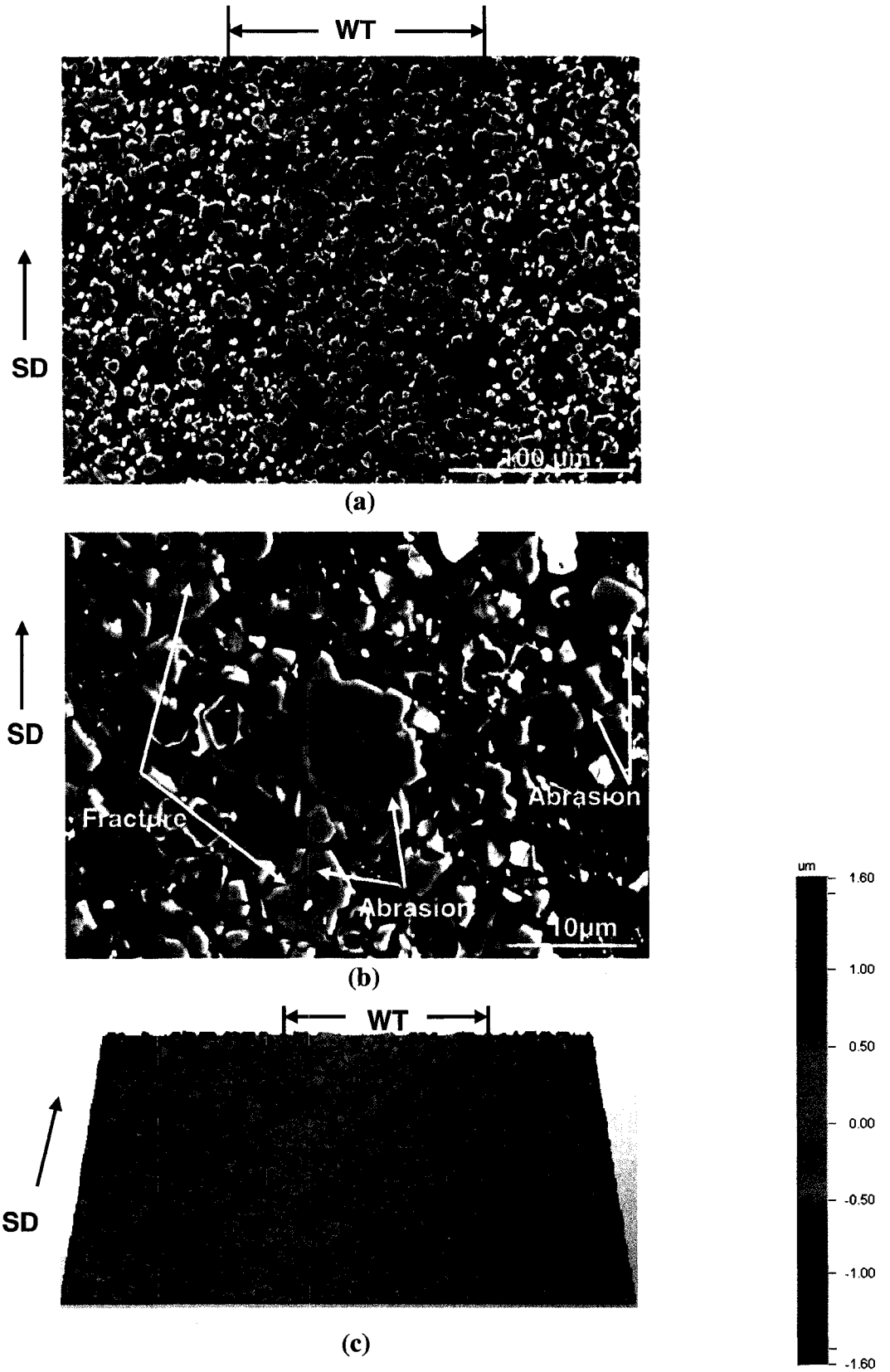

Fig. 6.23. **(a)** Secondary SEM image, **(b)** high magnification back scattered SEM image of inset 'X' in **(a)**, and **(c)** 3-D surface profile image showing surface damage on the top surfaces of silicon particles inside the wear track of Al-25% Si after sliding for 6 x 10^5 cycles 0.5 N.

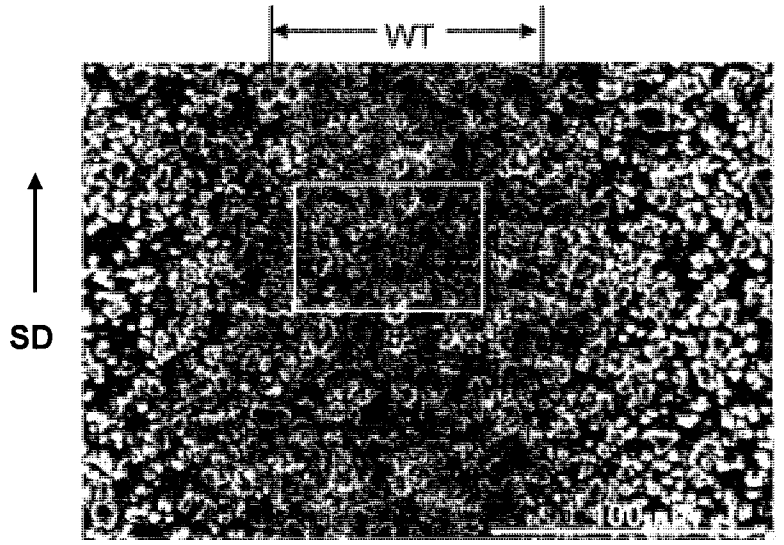

(a)

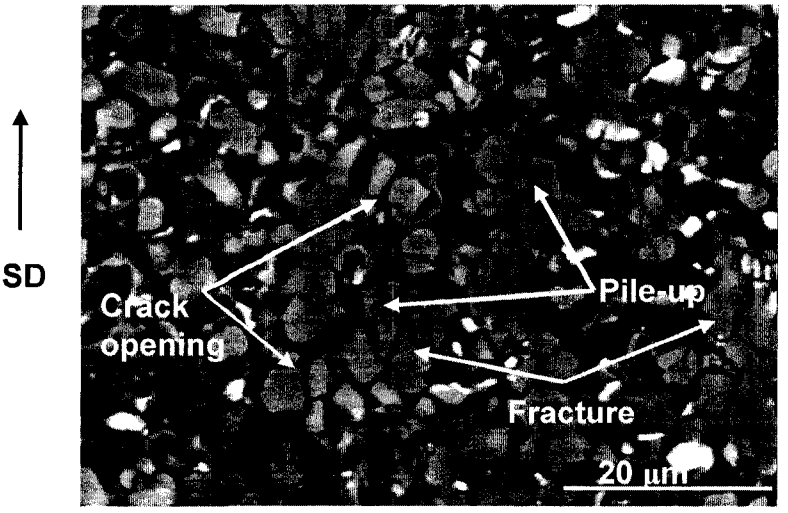

(b)

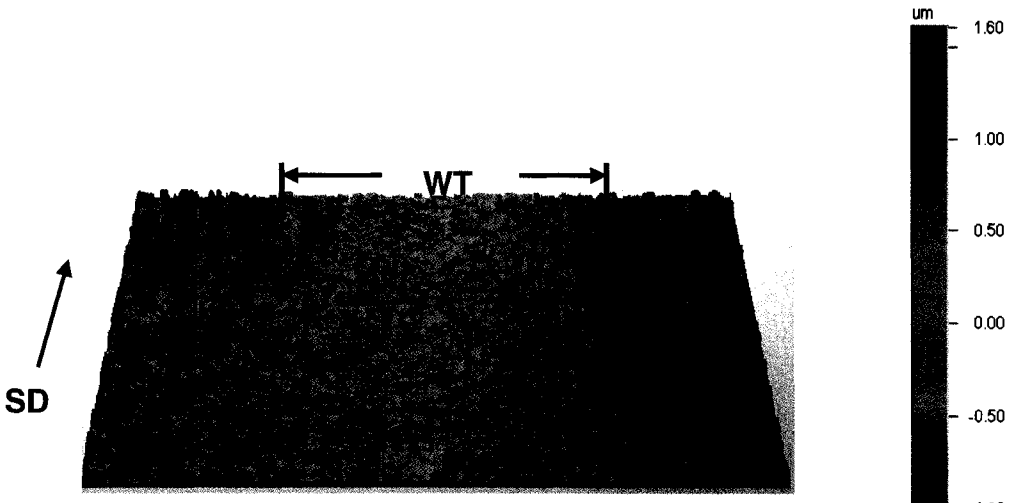

(c)

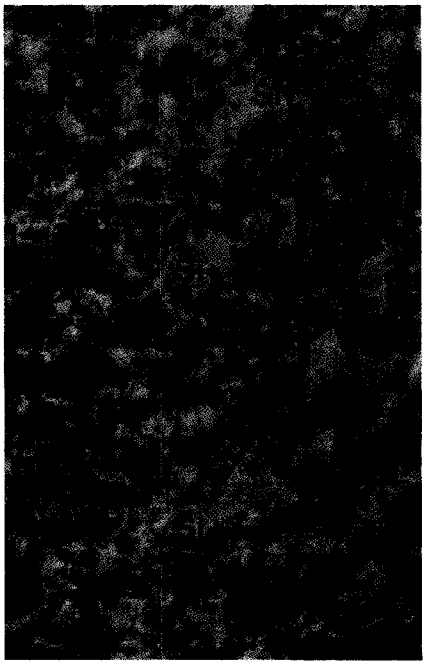

(d)

Fig. 6.24. (**a**) Secondary SEM image, (**b**) high magnification back scattered SEM image of inset in (**a**), (**c**) 3-D surface profile image, and (**d**) high magnification 3-D surface profile image of inset in (**c**) showing the evolution of surface damage in Al-25% Si, after sliding for 5 x 10^4 cycles at 1.0 N.

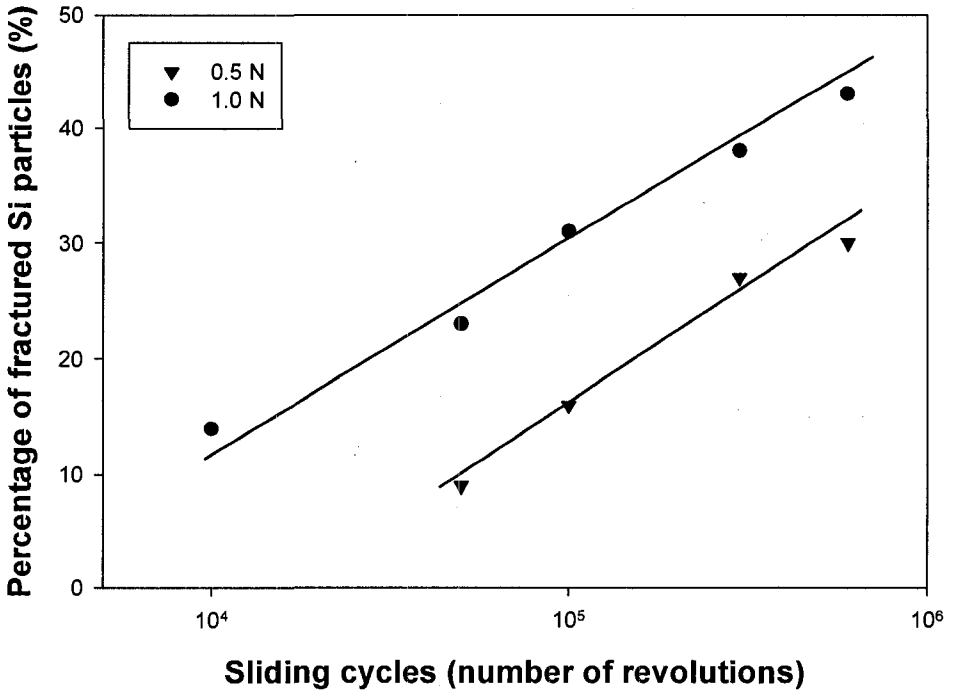

Fig. 6.25. The percentage of fractured Si particles inside the wear tracks at 0.5 and 1.0 N as a function of sliding cycles.

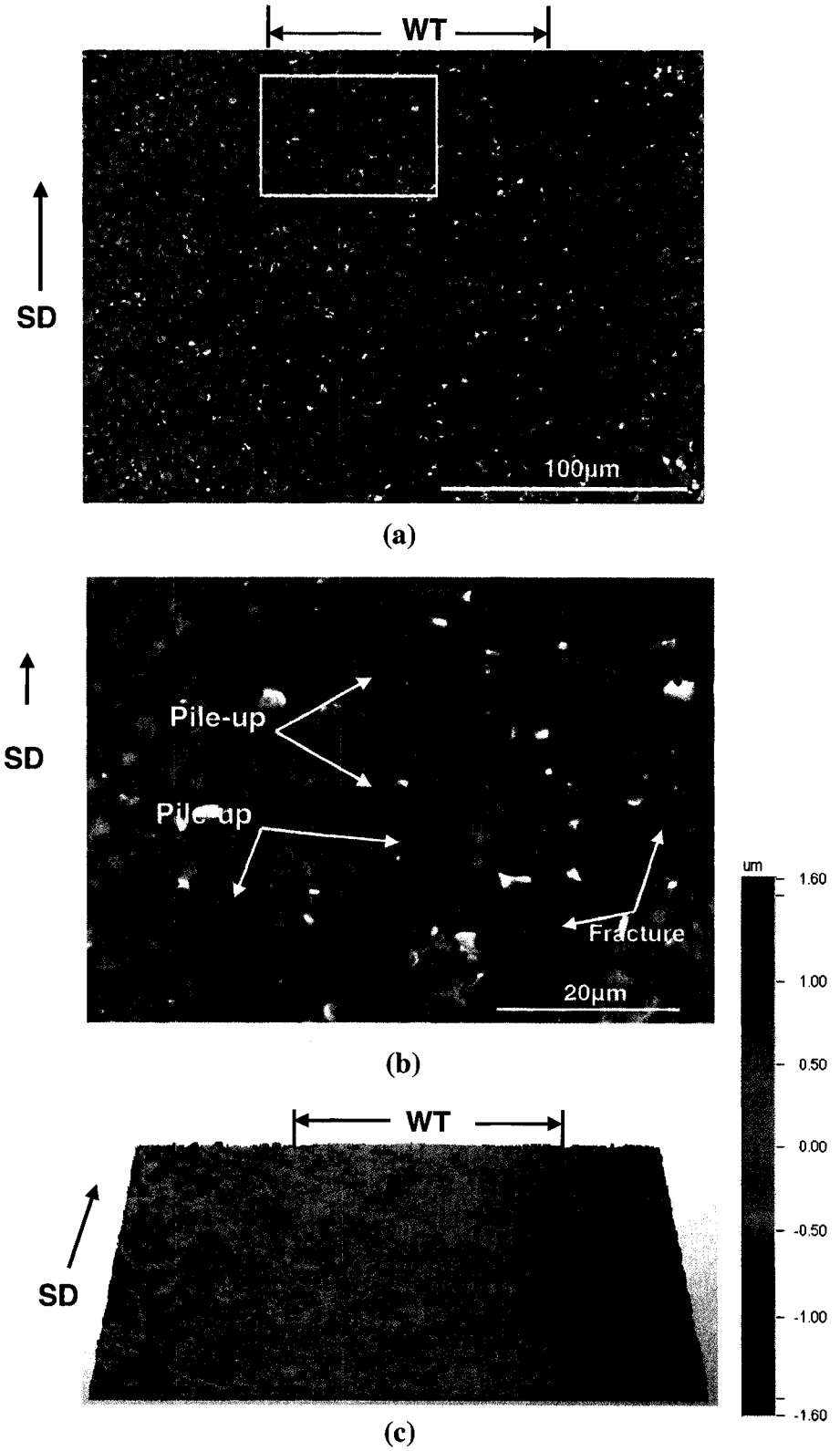

Fig. 6.26. **(a)** Secondary SEM image, **(b)** high magnification back scattered SEM image of inset in **(a)**, and **(c)** 3-D surface profile image showing the evolution of surface damage in Al-25% Si, after sliding for 6 x 10^5 cycles at 1.0 N.

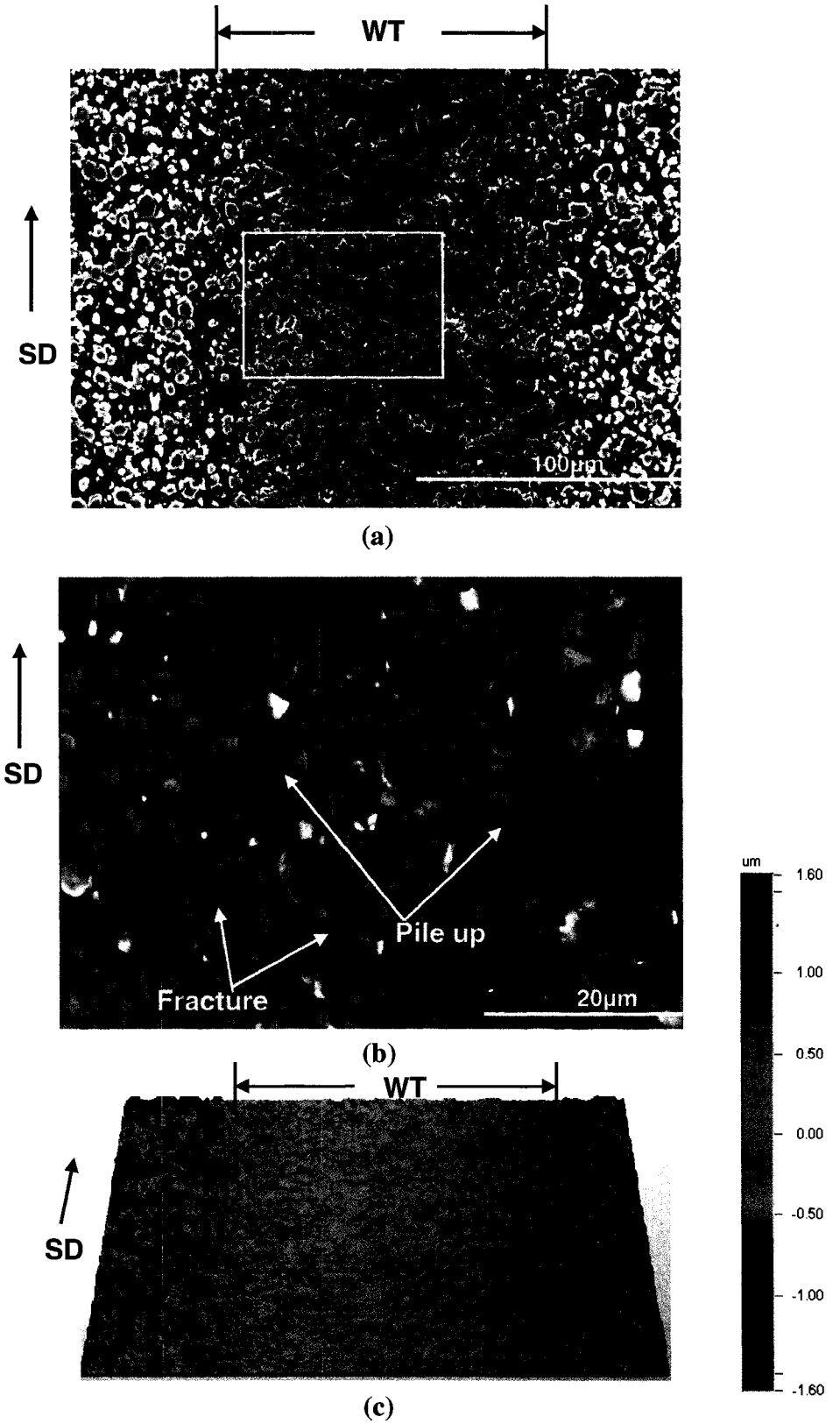

Fig. 6.27. Surface damage in Al-25% Si after sliding for 10^4 cycles at 2.0 N: **(a)** Secondary SEM image; **(b)** High magnification back scattered SEM image of inset in **(a)**; and **(c)** 3-D surface profile image showing slight damage on the aluminum matrix.

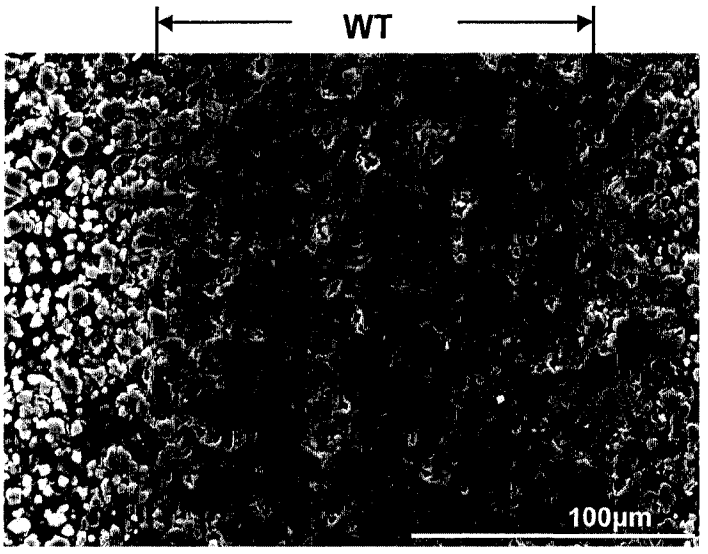

(a)

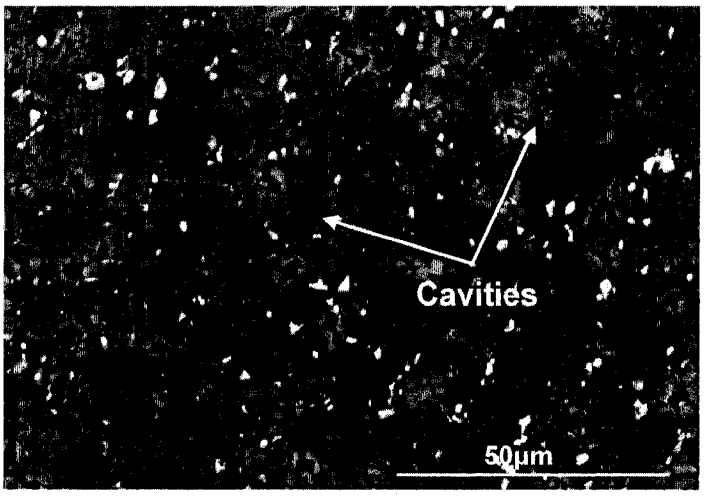

(b)

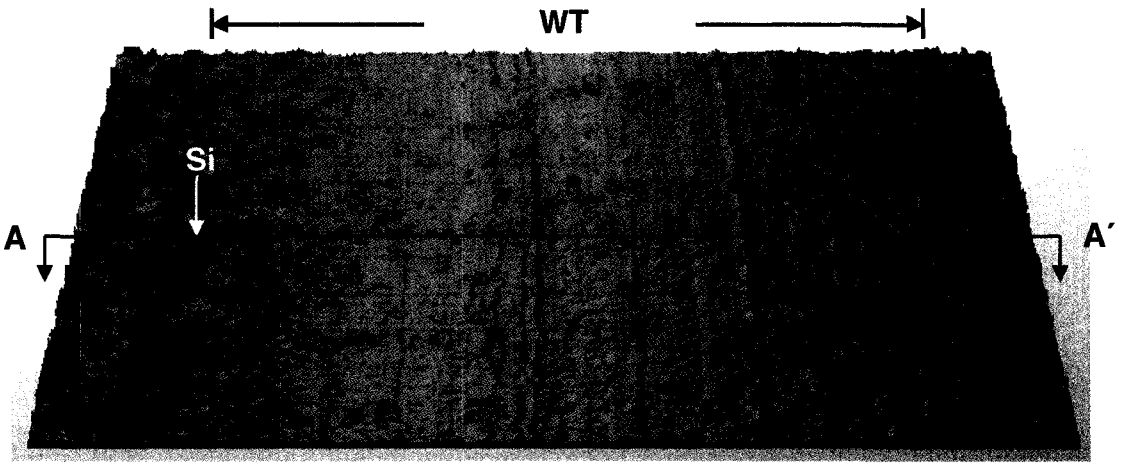

(c)

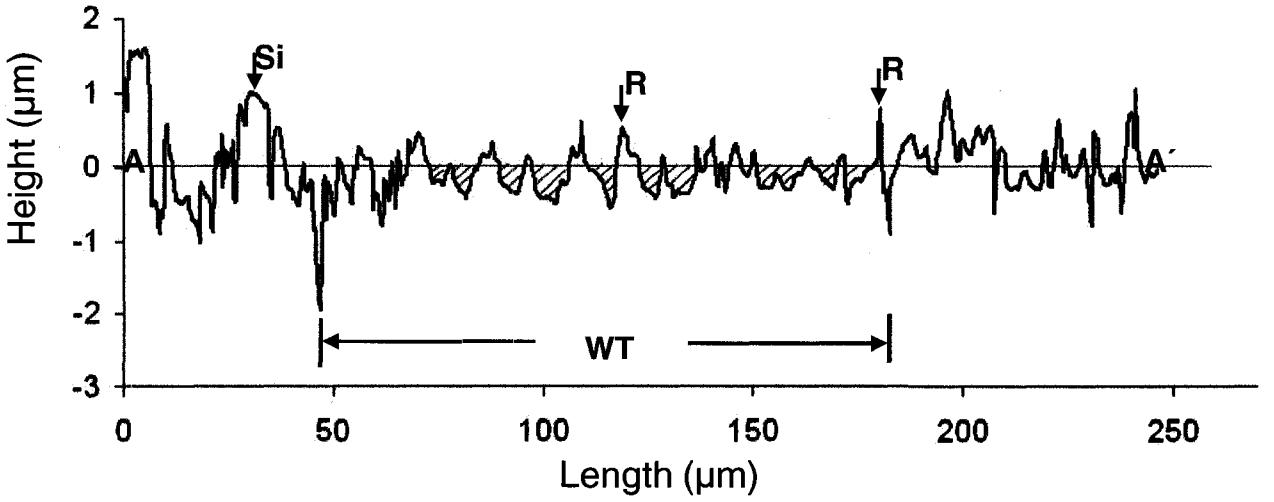

(d)

Fig. 6.28. Surface damage in Al-25% Si after sliding for 5 x 10^4 cycles at 2.0 N **:(a)** Secondary SEM image; **(b)** High magnification back scattered SEM image of inset in **(a)**; **(c)** 3-D surface profilometer image; and **(d)** 2-D surface profile scanned along the horizontal line (AA') indicated in **(c)** showing the material loss.

.

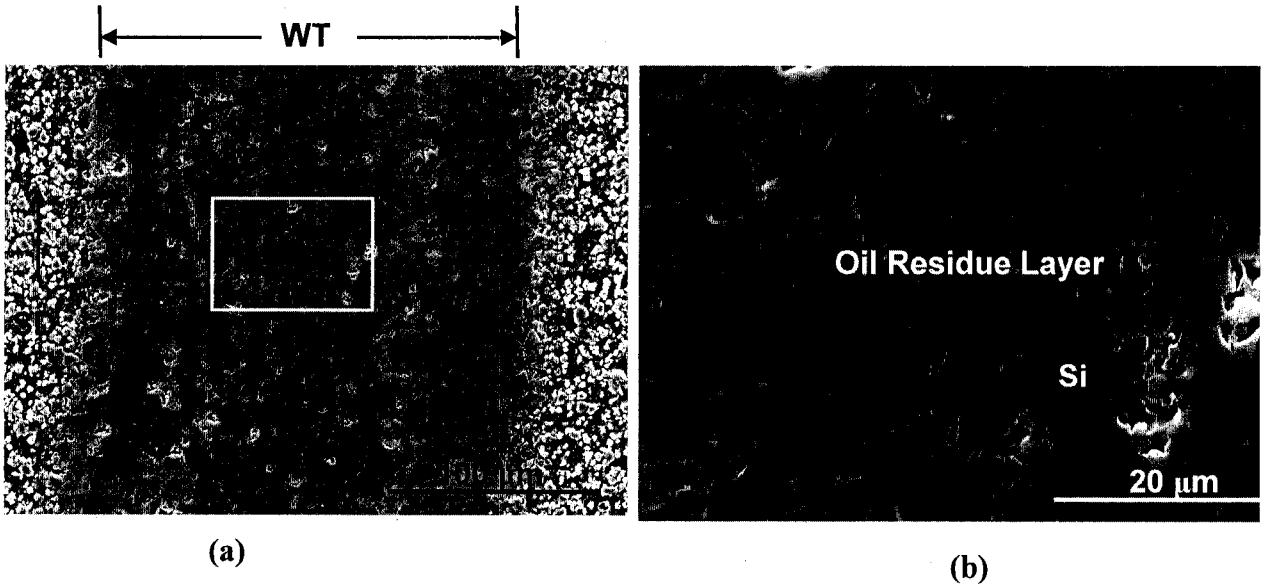

(a) (b)

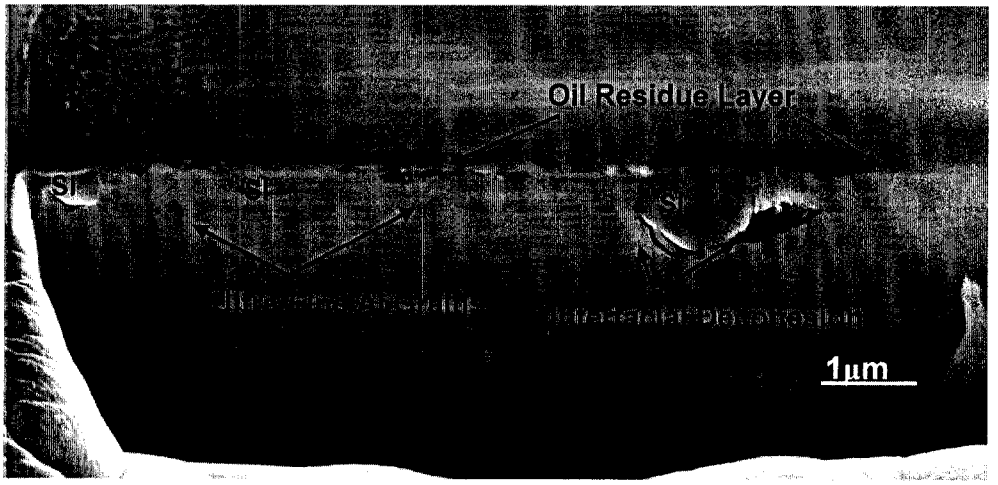

(c)

Fig. 6.29. Surface damage in Al-25% Si after sliding for 6 x 10^5 cycles at 2.0 N: **(a)** Secondary SEM image of the surface; **(b)** High magnification back scattered SEM image of the inset in **(a)** showing the wear track sparsely covered by a little amount of dark coloured layer; **(c)** Cross-sectional FIB secondary image (taken by Dr. Meng-Burany) of the wear track taken from the inset in **(a)** showing the oil residue layer generated locally on the contact surface.

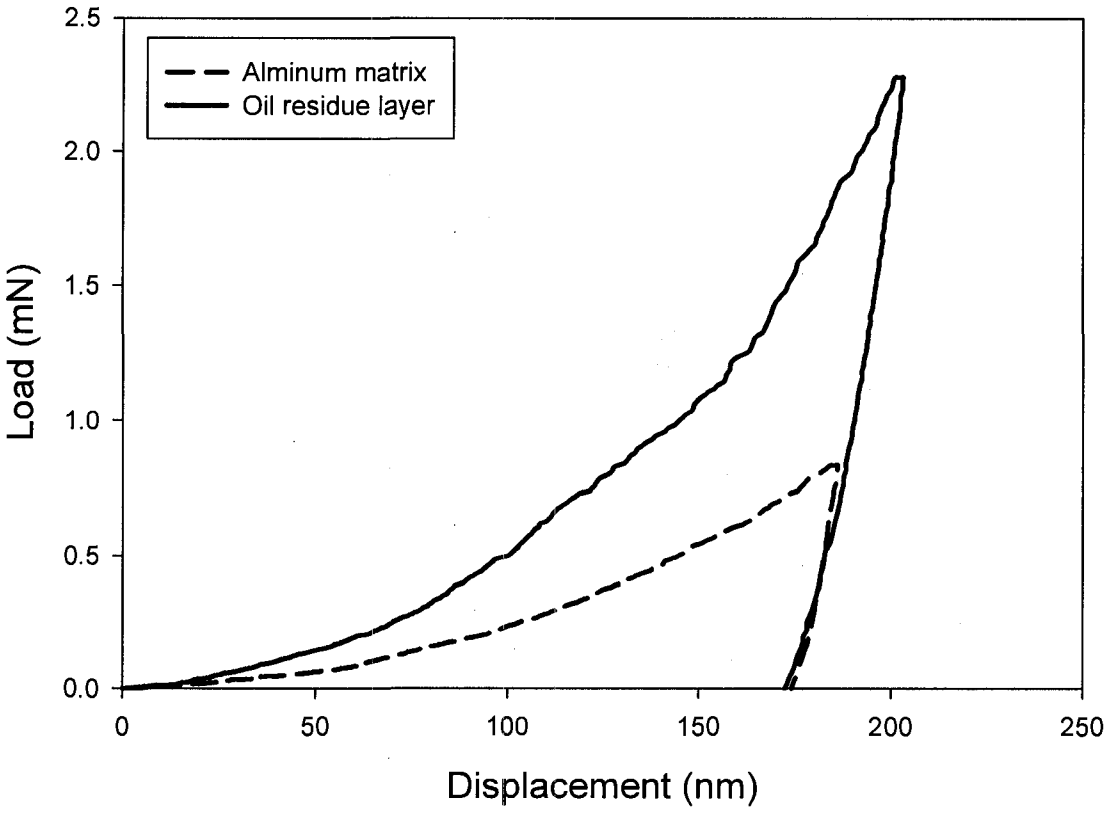

Fig. 6.30. The indentation displacement –load curves of the oil residue layer formed on the worn surface after sliding to 6 x 10^5 cycles at 2.0 N and aluminum matrix.

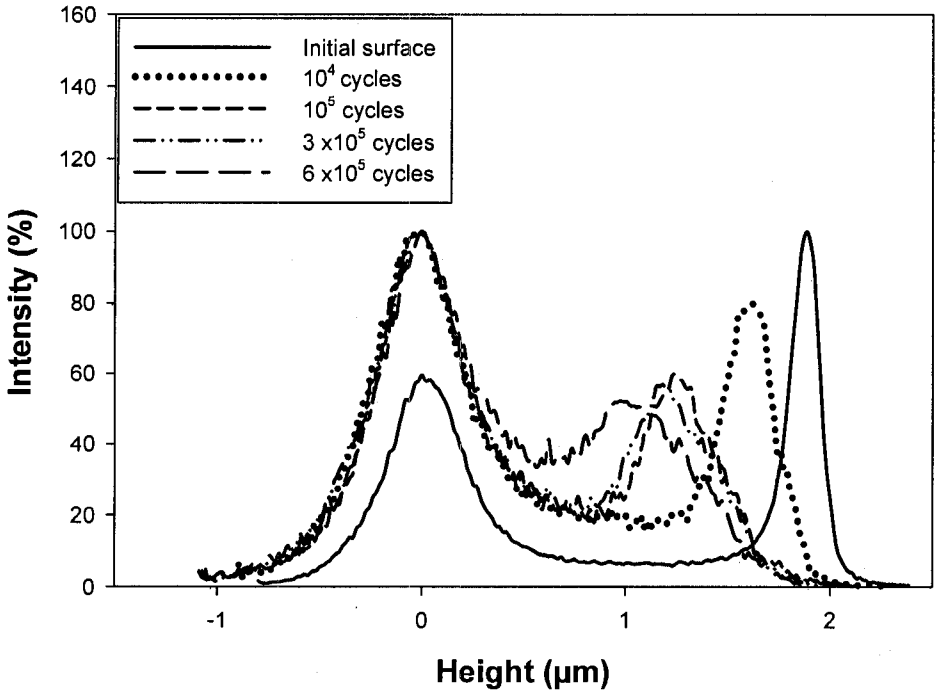
Initial surface
10^4 cycles
10^5 cycles
3 x10^5 cycles
6 x10^5 cycles
Intensity (%)
Height (μm)
160
140
120
100
80
60
40
20
0
-1
0
1
2

(a)

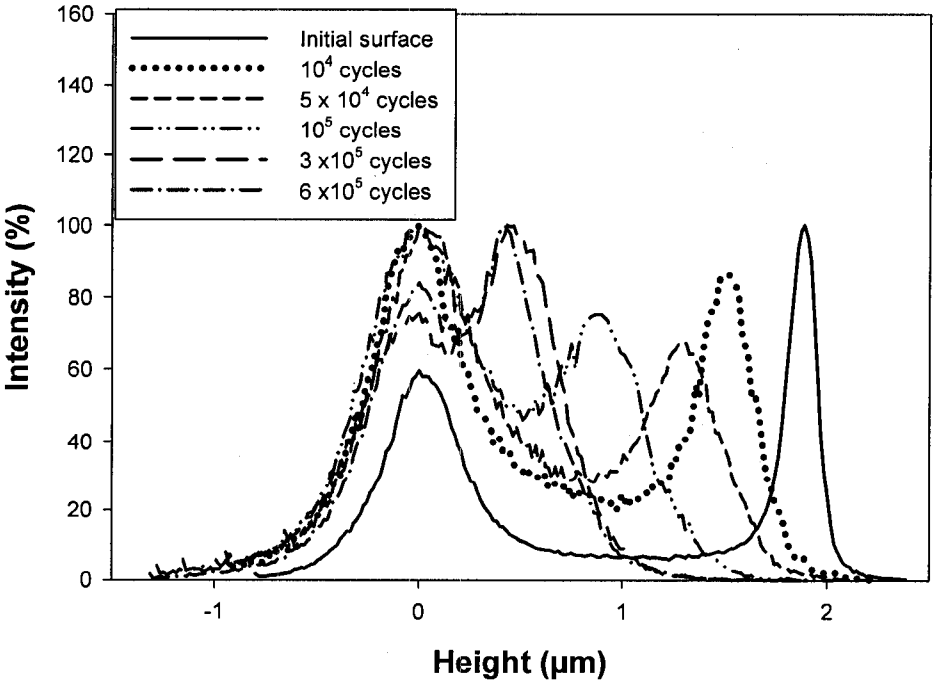
Initial surface
10^4 cycles
5 x 10^4 cycles
10^5 cycles
3 x10^5 cycles
6 x10^5 cycles
Intensity (%)
Height (μm)
160
140
120
100
80
60
40
20
0
-1
0
1
2

(b)

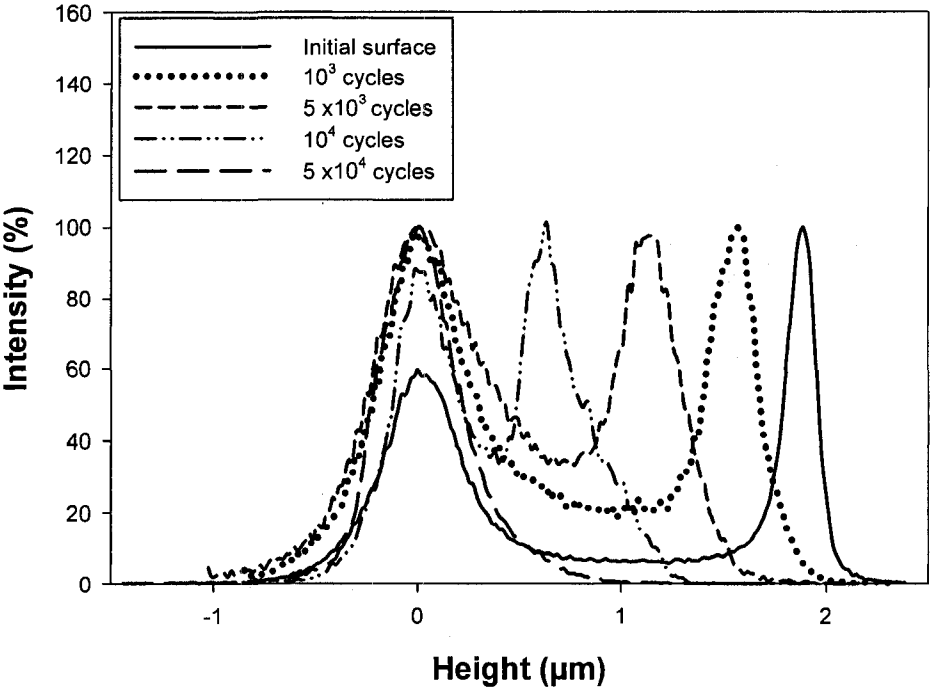

(c)

Fig. 6.31. The distribution frequency of surface topography on the Al-25% Si surfaces at various sliding cycles at **(a)** 0.5 N, **(b)** 1.0 N, and **(c)** 2.0 N.

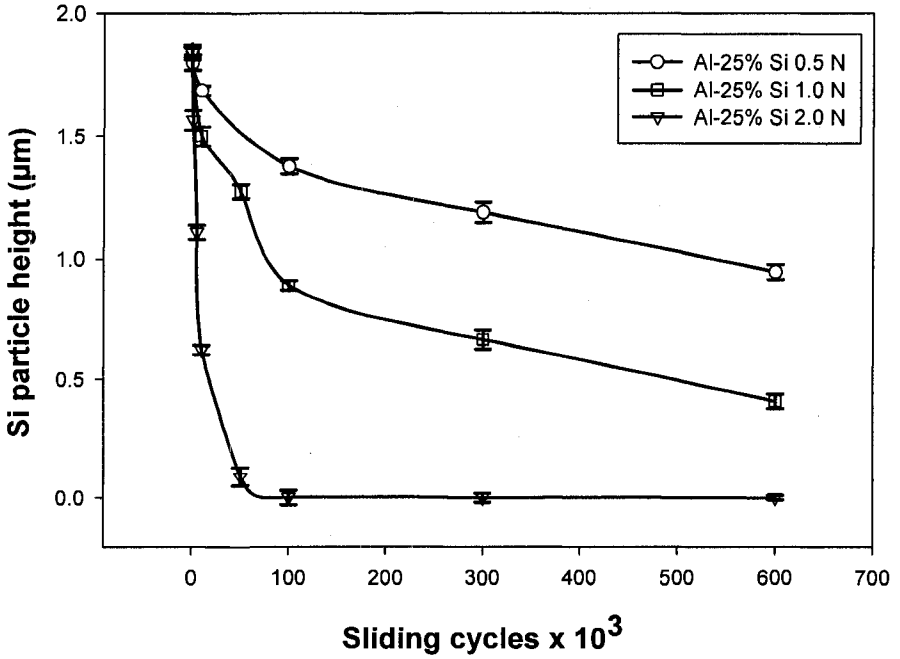

Fig. 6.32. Change in the silicon particle height projected above the aluminium matrix with the sliding cycles.

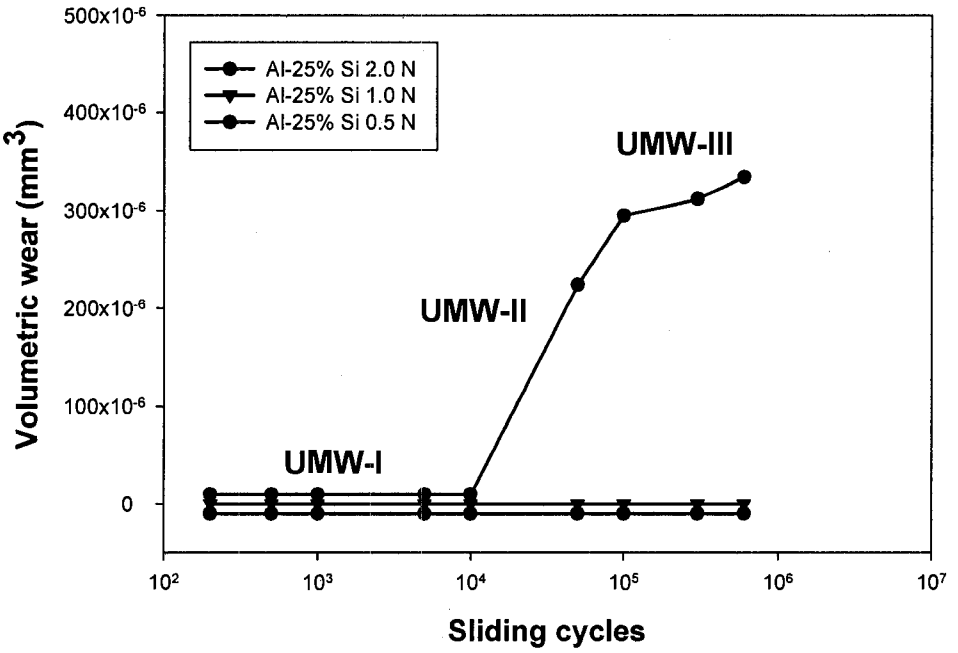

Fig. 6.33. Variation of the volumetric wear loss with the sliding cycles for the Al-25% Si. The plots at 0.5, 1.0, and 2.0 N with zero volume loss were shifted vertically for clarity.

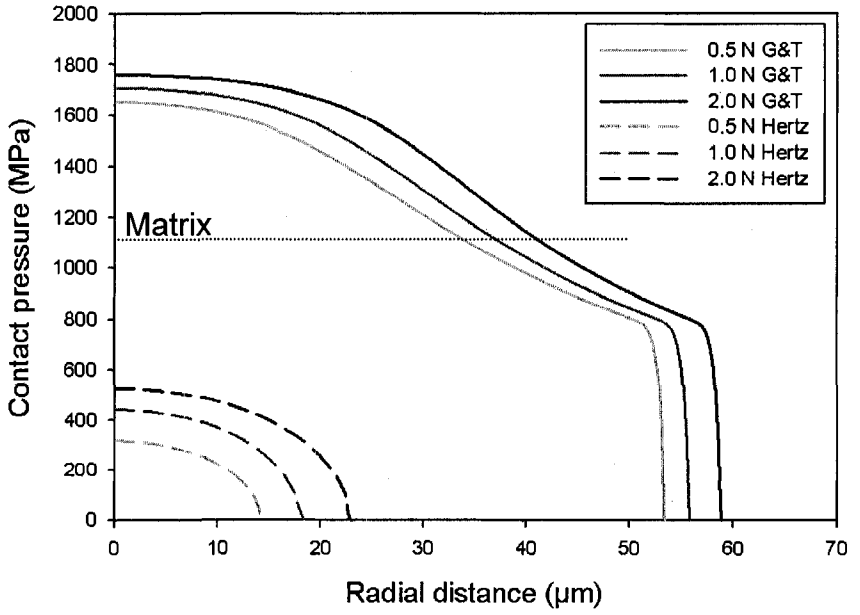

Fig. 6.34. Real contact pressure distribution applied to Al-25% Si at 0.5N, 1.0 N, and 2.0 N. The matrix hardness of the alloy is 1,090 MPa.

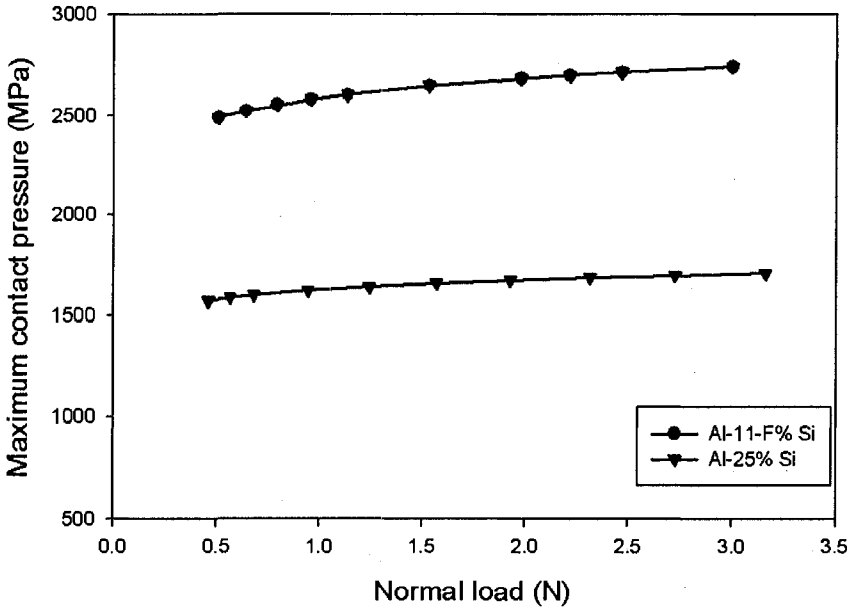

Fig. 6.35. Variation of the maximum real contact pressure applied on Al-25% Si and Al-11% Si-F.

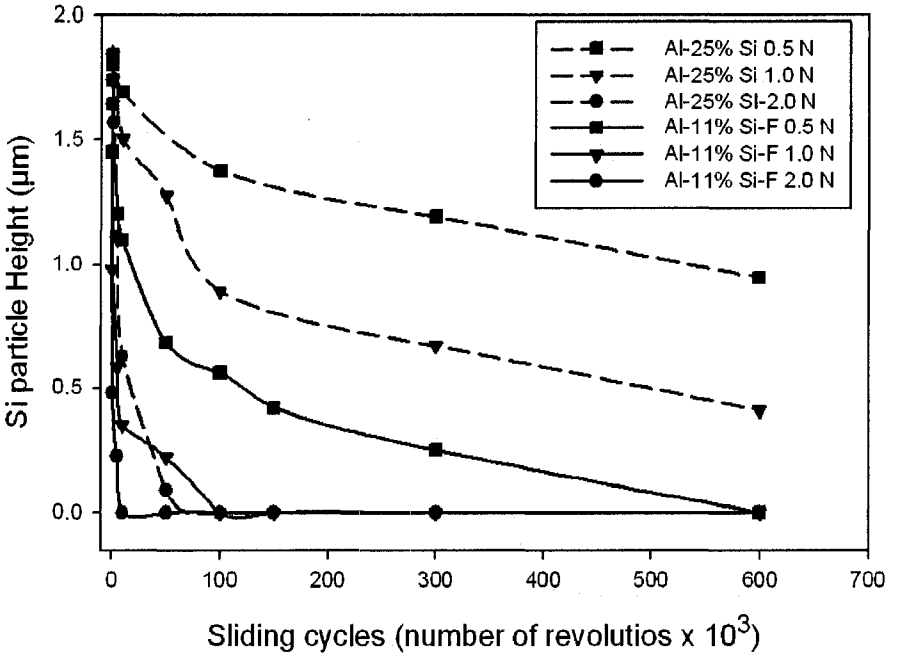

(a)

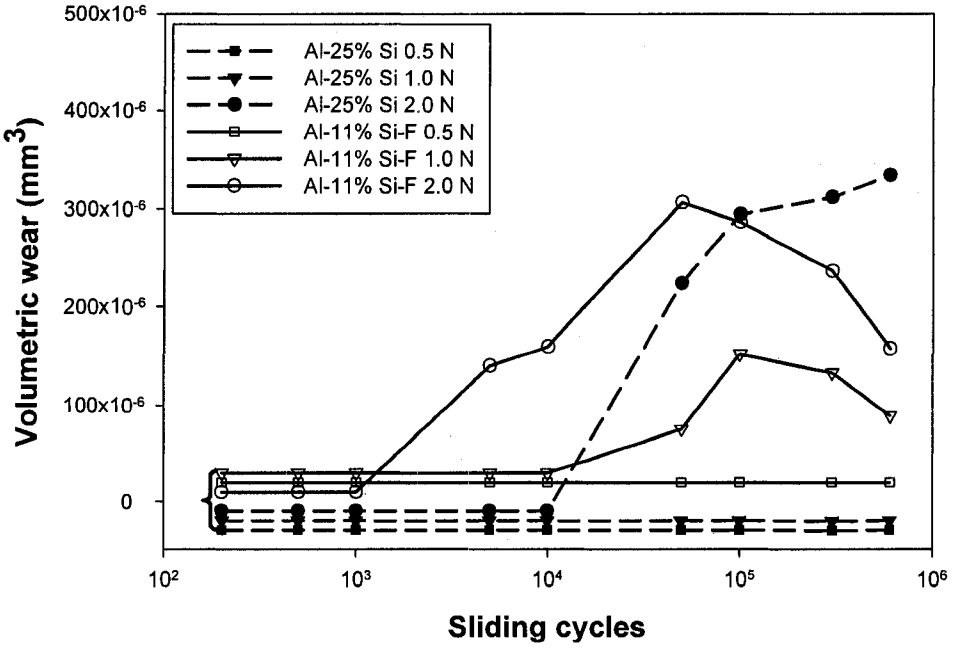

(b)

Fig. 6.36. Comparisons of **(a)** change in the silicon particle height projected above the aluminium matrix and **(b)** the variations of the volumetric wear loss with the sliding cycles in Al-11%-F Si and Al-25% Si. All the plots at 0.5, 1.0, and 2.0 N with zero volume loss were shifted purposely for clarity.

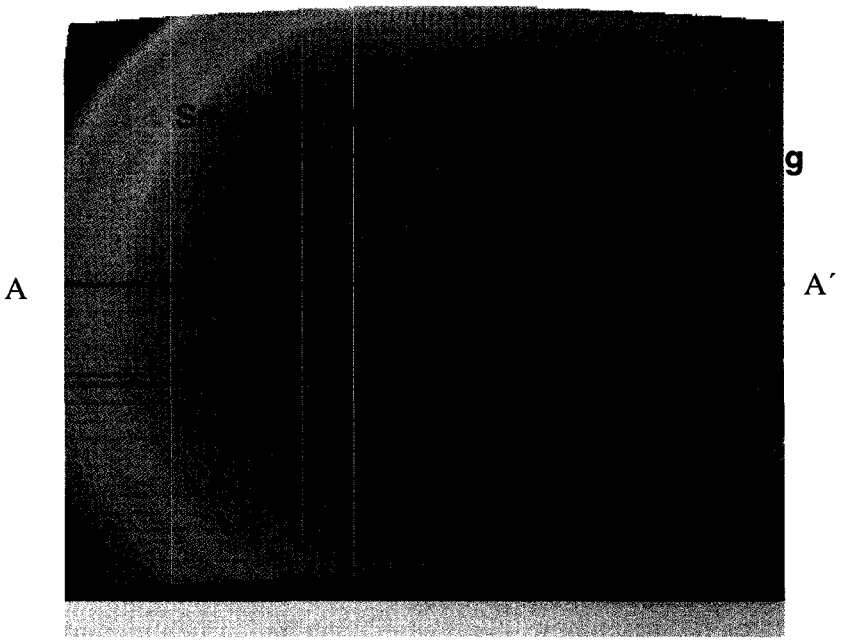

(a)

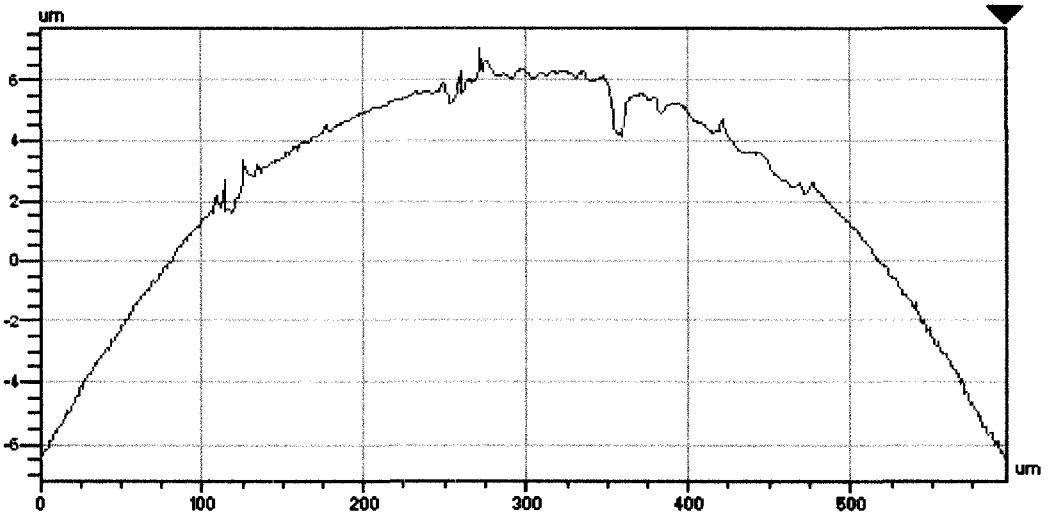

(b)

Fig. 6.37. (a) 3 D surface profile image of the ball surface sliding against Al-11% Si-F for 2 x10^6 cycles, and **(b)** 2 D surface profile scanned along the horizontal line (AA') indicated in **(a).**

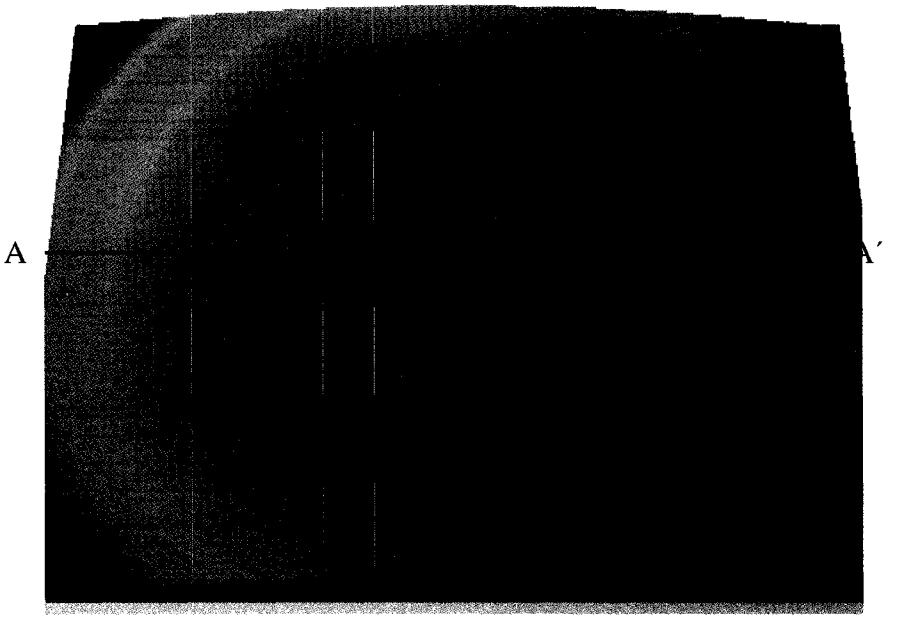

(a)

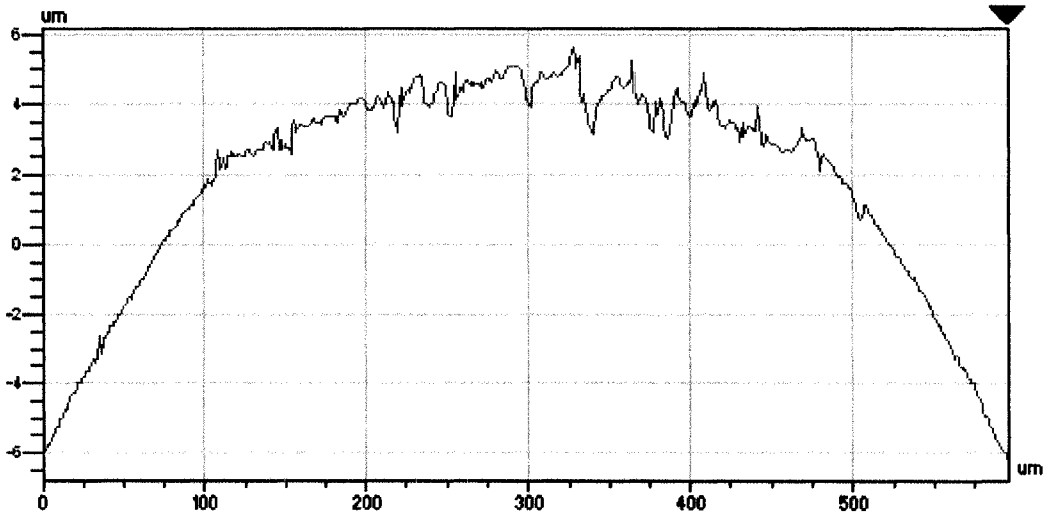

(b)

Fig. 6.38 (a) 3 D surface profile image of the ball surface sliding against Al-25% Si for 2 x10^6 cycles, and **(b)** 2 D surface profile scanned along the horizontal line (AA') indicated in **(a).**

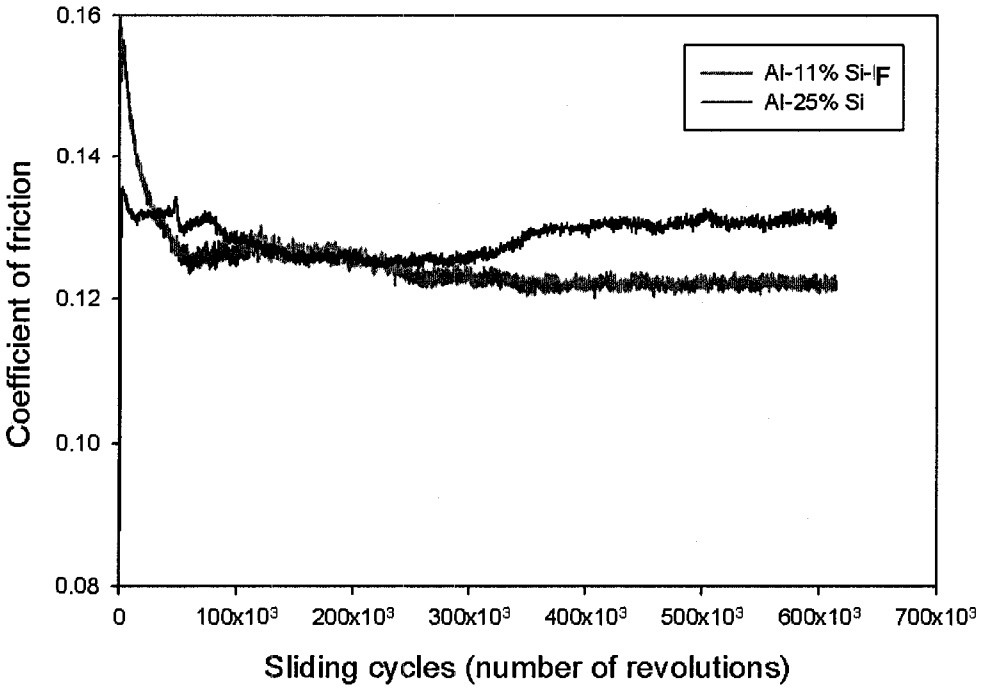

Fig. 6.39. Variation of the COFs of Al-25% Si and Al-11% Si-F with the sliding cycles at 2.0 N.

CHAPTER 7 SUMMARY AND CONCLUSIONS

1) The contact used in the experiments was modeled using both the Greenwood and Tripp formalism, and Hertzian contact mechanics, and the "real" asperity contact pressure was estimated as outlined by Greenwood and Tripp.

   i) The maximum average contact pressures distributed on the alloy with coarse Si particles were smaller than those applied on the alloy with fine Si particles. These pressures are smaller than the maximum Hertzian contact pressures at each load.

   ii) The maximum contact pressures applied on the exposed silicon particles, that is, the real contact pressure, were substantially higher than the maximum average contact pressures. These pressures are important in terms of understanding how the aluminum matrix supports the silicon particles.

   iii) The peak values of the real contact pressures occurred at the center of contact area and diminished with radial distance. Estimated distances where real contact pressure values reached zero were roughly the same as wear track widths of the alloys tested.

   iv) The maximum contact pressures applied on the Si particles were used to rationalize the mechanical response of Si particles. When they exceeded the matrix hardness of the tested alloys, the local plastic deformation in the form of Si particle sinking-in and aluminum piling-up around the sunken-in Si particles started to happen at the center of the wear tracks.

v) The maximum contact pressures applied on the alloys with coarse silicon particles (Al-12% Si, Al-11% Si-C, Al-18.5% Si) were smaller than those applied on the alloy with fine particle size (Al-11% Si-F, and Al-25% Si). The maximum contact pressures applied on the alloy with high areal density Si particles (Al-25% Si) was smaller than the one with small areal density of Si particles (Al-11% Si-F).

2) Surface damage that occurs in the UMW regime was simulated on the chemically etched (10% NaOH) contact surfaces of five Al-Si alloys namely, sand cast Al-12% Si, Al-11% Si-C, Al-11% Si-F, Al-18.5% Si, and spray formed Al-25% Si, through performing the sliding tests at low loads of 0.5, 1.0, and 2.0 N and under boundary lubricated conditions with synthetic engine oil as lubricant.

3) Quantitative evaluation of damage in UMW is made possible by statistically examining the morphological changes, including the relative changes in matrix and particle elevation distribution profiles, and volumetric loss from the elevated aluminum matrix. This methodology was effective to provide a quantitative measurement of a very small amount of wear.

4) Under the ultra-mild wear conditions sliding contact occurred on the tops of the elevated portions of the silicon particles standing above the aluminum matrix. The damage mechanisms leading to wear under UMW conditions consisted of the following steps:

i) Wear of the top surfaces of silicon particles by the counterface;

ii) Sinking of load bearing silicon particles into aluminum;

iii) Plastic deformation of the aluminum around silicon particles leading to the formation of aluminum pile-ups;

iv) Wear of the elevated portions of aluminum plateaus by the counterface.

5) UMW behaviours of Al-Si alloys were found to be strongly dependent on the matrix hardness and the microstructures of the alloys in terms of silicon particle morphology, size and their distribution.
   i) Increasing the silicon particle size and the matrix hardness, and using particles with low aspect ratio would improve the load carrying ability of the alloys, and thus would prevent aluminum matrix from being damaged.
   ii) Increasing the areal density of small spheroidized silicon particle and matrix hardness resists the silicon particle sinking-in and aluminum pile-up.
6) The morphological features of wear tracks changed with the applied load and at a given load level the surfaces evolved with the number of sliding contact cycles. At the point when the wear from plastically deformed aluminum became observable, the alloys entered a regime of high wear (UMW-II). However, the UMW-II regime was followed–up by a period of reduced wear rates at long sliding cycles when an oil residue layer was formed on the contact surface. The evolution of wear behaviour was dependent on the aluminum matrix and microstructural factors in terms of Si particle morphology, size, and distribution.
7) The transition to the UMW-II regime coincided with the formation of a contact morphology where the elevation difference between Si particles and aluminum matrix disappeared. That is to say that the transition to UMW-II started when the silicon particles were totally embedded into the aluminum matrix, leading to contact of the aluminum matrix with the counterface.
8) The microstructure factors in controlling the onset of the UMW-II regime were identified to be silicon particle size, morphology, distribution, and matrix

hardness. A comparison of sand cast Al -11% Si-F with Al-25% Si with similar small silicon size and morphology showed that the transition to UMW-II initiated at shorter sliding cycles and lower loads in the near-eutectic Al-Si alloy.

9) The aluminum grain size in the plastically deformed aluminum matrix adjacent to sunken-in silicon particles was generally less than 200 nm, indicating generation of large plastic strains and increase in local hardness.

10) An oil residue layer generated from the deformed aluminum matrix sliding contact with the counterface was observed on the contact surfaces. It had a hardness of 1.5-2.5 GPa. It appears to have been beneficial for delaying the transition to the UMW-II regime to a larger number of sliding cycles and higher loads, and reducing the wear rate in UMW-II leading to the attainment of UMW-III.

11) An oil residue layer was more easily to be formed in the Al-11% Si alloy with matrix hardness of 67 Hv and small Si particles, when compared to the alloys with either large silicon particles or with small silicon particles distributed at smaller interparticle distances and having a harder matrix. The preferable formation of a smooth and stable worn surface morphology of an oil residue that is supported by ultra-fine aluminum grains accounts for the optimal long term wear performance of this alloy.

REFERENCES

1. Edward P. Becker, Tribology International, 37 (2004) 569-575.
2. S. C. Tung, M. L. McMillan, Tribology International, 37(2004) 517-536.
3. W. S. Miller, L. Zhuang, J. Bottema, A. J. Wittebrood, P. De Smet, A. Haszler, A. Vieregge, Materials Science and Engineering, A 280 (2000) 37-49.
4. T.S. Eyre; "Wear of Aluminum Alloys", Microstructural Science, Stevens, Vander Voort, McCall, eds., Elsevier North Holland, Inc., 1980, New York, NY and Amsterdam, 8 (1980) 141-151.
5. R. Shivanath, B. Tech, P. K. Sengupta, M. Met. T. S. Eyre, The British Foundryman, (1977) 349-356.
6. M. Elmadagli, T. Perry, and A. T. Alpas, Wear, 262 (2007) 79-92.
7. A. Dyson, Proc. Inst. Mech. Eng. 190 (1976) 52–76.
8. P.K. Rohatgi, B.C. Pai, Wear, 28 (1974) 353–367.
9. K C. Ludema, Friction, Wear, Lubrication –a Text Book in Tribology, Boca Raton, FL, USA: CRC Press; (1996) 160-164.
10. E. W. Schneider, and D. H. Blossfeld, SAE International, 2004-01-2917.
11. H. Yu, "Tribological Failure Analyses of Automotive Engine Blocks Subjected Sliding Wear Damage", Master Thesis, University of Windsor, Windsor Ontario, Canada , 2006.
12. M. Elmadagli, and A.T. Alpas, Wear, 261 (2006) 823-834.
13. M. Dienwiebel, K. Pöhlmann, M. Scherge, Tribology International, 40 (2007) 1597-1602.
14. L. Pei, S. Hyun, J.F. Molinari,and Mark O. Robbins, Journal of the Mechanics and Physics of Solids, 53 (2005) 2385–2409.
15. W. R. Chang, I. Etsion, and D. B. Bogy, ASME J. Tribol. 110 (1987) 50–56.
16. A. Edrisy, T. Perry, and A.T. Alpas, Metallurgical and Materials Transactions A, 36 (2005) 2737-2750.
17. J. Zhang and A. T. Alpas, Materials Science and Engineering, A 160 (1993) 25-35.

18. J. L. Murray and A.J. McAllister, Bulletin of Alloy Phase Diagrams, 5 (1984)74-84.

19. L. Bäckrud, G. Chai, and J. Tamminen, Solidification Characteristics of Aluminum Alloys, v 2, "Foundry Alloys", Department of Structural Chemistry, Arrhenius Laboratory, University of Stockholm, Sweden, (1993) 179-215.

20. E. L. Roy, ASM Handbook, v 15, "Castings" 9th ed., ASM International, Materials Park, OH, (1992) 743 -769.

21. J. R. Davis & Associates, ASM Handbook, v 18, "Friction, Lubrication, and Wear Technology" 10th ed., ASM International, Materials Park, OH, (1992) 553-562.

22. J.R. Davis & Associates, B.S. Shabel; D.A. Granger, and W. G. Truckner, ASM Handbook, v 18, "Friction, Lubrication, and Wear Technology" 10^{th} ed., ASM International, Materials Park, OH, (1992) 786-794.

23. J.L. Jorstad, 6th International Society of Die Casting Engineers Congress, Cleveland, OH, Nov 16-19, 1970, Paper no. 105.

24. J.L. Jorstad, Modern Castings, 60 (1971) 59-64.

25. R.E. Green, Die Cast Engineer, 14 (1970) 12-14, 16, 18, 21-2, 24, 26.

26. R. M. German, Sintering Theory and Practice, John Willey & Sons, New York, (1996) 150-160.

27. E. Koya, Honda R & D Technical Review, 6 (1994) 126.

28. D. Casellas, A. Beltran, J. M. Prado, A. Larson, and A. Romero, Wear, 257 (2004) 730-739.

29. F. Kiyota, T. Fujit, T. Hirano, S. Horie, United States Patent 4,938,810; July 3, 1990.

30. A. Leatham, JOM, 51(1999)1-18.

31. V.C Srivastava, R.K. Mandal, S.N. Ojha, Materials Science and Engineering A, 304–306 (2001) 555–558.

32. F. Rueckert Franz Dr. Rieger Roland, Stocker Peter, United States Patent 5891273, 1999.

33. H. Santos, M. Serna, N. Lima, I. Costa, J. Rossi, Materials Research, 8 (2005) 181-186.

34. K. Hummert, B. Commandeu, A.G. Leatham, A.J.W. Ogilvy, and W. Hunt Jr., Proceedings of P/M Aluminum and Light Alloys for Automotive Applications Conference, Princeton, NJ: MPIF, (1998) 107-115.

35. S. C. Lim, and M. F. Ashby, Acta Metall., 35 (1987) 1-24.

36. S. K. Biswas and A. S. Reddy, J. Indian Inst. Sci. 75(1996) 15-35.

37. R. Shivanath, B. Tech, P. K. Sengupta, M. Met. T. S. Eyre, The British Foundryman, (1977) 349-356

38. J. Zhang and A. T. Alpas, Acta Materialia, 45 (1997) 513-528.

39. J. Clarke, and A. D. Sarkar, Wear, 69 (1981) 1-23.

40. B. K. Yen, and T. Ishihara, "Effect of humidity on friction and wear of Al-Si eutectic alloy and Al-Si alloy-graphite composites", Wear, 198 (1996) 169-175.

41. H. Goto, M Ashida, and K. Endo "The influence of oxygen and wear vapor on the friction and wear of an aluminum alloy under fretting conditions", Wear, 116 (1987) 141-155.

42. K. Razavizadeh and T. S. Eyre, Wear, 79 (1982) 325-333.

43. C. Beesley and T. S. Eyre, Tribology International, (1976) 64-69.

44. R. Antoniou and D. W. Borland, Materials Science and Engineering, 93 (1987) 57-72.

45. R. Antoniou and C. Subramanian, Scripta Metall., 22 (1988) 809-814.

46. Y. B. Liu, R. Asthana, and P.Rohatgi, Journal of Materials Science, 26 (1991) 99-102.

47. S. A. Reddy, B. N. Pramila Bai, K. S. S. Murthy, and S. K. Biswas, Wear, 171 (1994) 115-127.

48. S. Wilson, A.T. Alpas, Wear, 212 (1997) 41-49.

49. M. Elmadagli, and A. Alpas, Wear, 161 (2006) 367-381.

50. D. A. Rigney, Proceedings for Materials Solutions' 97 on Wear of Engineering Materials, 15-18 September 1997, Indianapolis, Indian.

51. D. A. Rigney, Wear, 245 (2000) 1-9.

52. X. Y. Li, and K. N. Tandon, Wear, 245 (2000) 148-161.

53. M. Acilar, F. Gul, Materials and Design, 25 (2004) 209-217.

54. W. M. Rainforth, Wear, 245 (2000) 162-177.

55. A. R. Riahi, A. T. Alpas, Wear, 251 (2001) 1396-1407.

56. X. Y. Li, and K. N. Tandon, Wear, 225-229 (1999) 640-648.

57. K. N. Tandon, and X. Y. Li, Script Materialia, 38 (2001) 1396-1407.

58. J. Li, M. Elmadagli, V. Y. Gertsman, J. Lo, A. T. Alpas, Material Science and Engineering A, 421 (2006) 317-327.

59. J. E. Hammerbergs, B. L. Holian, J. Roeder, A. R, Bishop, and S. J. Zhou, Physica D 123 (1998) 330-340.

60. R. Antoniou, and C. Subramanian, Scripta Metallurgica, 22 (1988) 809–814.

61. J. B. Andrew, M. V. Seneviatne, K. P. Zier, and T. R. Jett, WOM, 1980.

62. N. Bai Pramila, and S.K. Biswas, Wear, 120 (1987) 61-47.

63. J. Clark, and A. D. Sarkar, 54 (1979) 7-16.

64. K. Mohammed Jasim, and E. S. Dwaradasa, Wear, 119 (1987) 119-130.

65. F. Wang, H. Liu, Y. Ma, Y, Jin, Materials and Design 25 (2004) 163-166.

66. Elwin L. Rooy, ASM Handbook, 9th Edition, vol. 15, 751.

67. A. J. Clegg, and A. A. Das, British Foundryman, 70 (1977) 56-63.

68. G. K. Sigwroth, ASF Transactions, 91 (1983) 83-86.

69. M. Elmadagli, "Microstructural Studies of Wear Mechanisms in Cast Aluminum Alloys", Ph.D. Dissertation, University of Windsor, Windsor Ontario, Canada , 2005.

70. B. K. Prasad, K. Venkateswarlu, O. P. Modi, A. K. Jha, S. Das, R. Dasgupta, and A. H. Yegnsewaran, Metallurgical and Materials Transactions, 29A (1998) 2747.

71. A. R. Riahi, T. Perry, and A. T, Alpas, Materials Science and Engineering A343 (2003) 76-81.

72. A. R. Riahi, and A. T, Alpas, Materials Science and Engineering A441 (2006) 326-330.

73. F. Wang, Y. Ma, Z. Zhang, X. Cui, Y. Jin, Wear, 256 (2004) 342-345.

74. http:/www.motor-oil-engineere.com/motor%20oil%20engineers%20PDF.pdf.

75. H C. Freuler, Modified lubricating oil, US Patent Office 2,364, 284 (1994) 6.

76. M A. Nicholls, T. Do, P R. Norton, M. Kasrai, and G. Michael Bancroft, Tribology International, 38 (2005) 15-39.

77. A. Neville, A. Morina, T. Haque, and M. Voong, Tribology International, 40 (2007) 1680-1695.

78. E. N. Kaufmann (Edt.), Characterization of Materials, vol. 2, John Wiley & Sons, Inc., NJ, (2003) 835-1000.

79. S. Jahanmir, Journal of Tribology, 109 (1987) 577-586.

80. I M. Hutchings, Tribology: Friction and Wear of Materials, London: CRC Press; 1992.

81. G. Timmermans, and L. Froyen, Wear, 230 (1999) 105-117.

82. L. Hu, J. Chen, W. Liu, Q. Xue, C. Kajdas, Wear, 243 (2000) 60-67.

83. S. Das, and S. K. Biswas, Tribology Letters, 17 (2004) 623-628.

84. Y. Wan, L. Cao, and Q. Xue, Tribology International, 30 (1998) 767-772.

85. A. Neville, A. Morina, T. Haque, and M. Voong, Tribology International, 40 (2007) 1680-1695.

86. M. Kawamura, K. Fujita, Wear, 89 (1983) 99-105.

87. T. Konishi, E E. Claus, J L. Duda, Tribology Transactions, 39 (1996) 811-818.

88. M. Fuller, M. Kasrar, J S. Sheasby, G M Brancroft, K. Fyfe, and K H. Tan, Trobology Letters, 1 (1995) 367-378.

89. M A. Nicholls, P R. Norton, G M. Bancroft, M. Kasrai, Wear, 257 (2004) 311-328.

90. M. A. Nicholls, P. R. Norton, G. M. Bancroft, M. Kasrai, G. De Stasio, and L. M. Wiese, Tribology Letters, 18 (2005) 261-278.

91. M. Nakada, Tribology International. 27 (1994) 3–8.

92. J. R. Davis & Associates, "Friction and Wear of Internal Combustion Engine Parts", ASM Handbook, 10^{th} edition, 18 (1992) 553-562.

93. L. L. Ting, SAE, paper No. 852355, 1985.

94. S. D. Henry, "Friction, Lubrication and Wear Technology", ASM Handbook, The Materials Information Society, 18 (1992) 162-171.

95. K. C. Ludema, Wear, 100 (1984) 315-331.

96. S. D. Cramer, B. S. Covino, "Corrosion: Fundamentals, Testing and Protection", ASM Handbook, ASM International, ISBN 0-87170-705-5, 13, 2005.

97. S. M. El-Raghy, Corrosion, 40 (1984) 60-64.

98. Z. Ye, C. Zhang, Y. Wang, H. S. Cheng, S. Tung, Q. Wang, X. He, Wear, 257 (2004) 8-31.

99. M. Scherge, K. Pöhlmann, and A. Gerve, Wear, 254 (2003) 801-817.

100. H. Yamagata, The Science and Technology of Materials in Automotive Engines, Woodhead Publishing Ltd., Cambridge, England. 38-39.

101. B. J. Hamrock, S. R. Schmid and B. O. Jacobson, Fundamentals of Fluid Film Lubrication, Marcel Dekker, New York, (2004) 45-49.

102. I. M. Hutchings, Tribology: Friction and Wear of Engineering Materials, CRC Press, (1992) 68-70.

103. J. Li, T. Malis, and S. Dionne, Materials Characterizations, 57 (2006) 60-70.

104. W. C. Oliver and G. M. Pharr, J. Mater. Res. 7 (1992) 1564-1583.

105. K. L. Johnson, Contact Mechanics, Cambridge University Press, 396-420.

106. J. A. Greenwood, and J. B. P. Williamson, Proceedings of the Royal Society, London, 295 A (1966) 300-319.

107. J. A. Greenwood, and J. H. Tripp, ASME Journal of Applied Mechanics, 89 (1967) 153-159.

108. J. A. Greenwood, and J. H. Tripp, Proc. Instn. Mech. Engrs., 185 (1970-1971) 625-633.

109. D. Tabor, The hardness of metals, Oxford University Press, Oxford, (1951), 46-51.

110. G. W. Rowe, Principles of Metalworking, Edward Arnold, London, (1965) 95-97.

111. M. Aktary, M. T. McDermott, and G. A. McAlpine, Tribology Letters, 12 (2002) 155-162.

112. Y. Iwahashi, Z. Horita, N. Nemoto, T. G. Langdon, Acta Mater., 45 (1997) 4733-4741.

113. P. W. Bridgman, Studies in large flow and fracture, Harvard University press, Cambridge (1964) 279-289.

114. J. Lloyd, D. Kenny, Acta Metallurgica, 28 (1980) 639-649.

VITA AUCTORIS

The author obtained her Bachelor of Engineering in Metallurgy and Materials Engineering from the University of Chongqing in 1986. She was then honored as a Master of Science Degree candidate of Xi'an Jiaotong University without taking entrance examination, where she obtained a Master of Science in Materials Science and Engineering in 1989. After that she was accepted as a faculty member into the Department of Materials Science, Lanzhou University, China. From December 1998 to July 2000, she worked at the Laboratory of Tribology, School of Mechanical Engineering, Tohoku University, Japan, as a guest researcher supervised by Prof. Koji Kato. She joined the Materials Engineering PhD Program at the University of Windsor in September 2004 and hopes to graduate in September 2008.